Porous Polymer-derived Ceramics by Solution-based Freeze Casting

for Capillary Transport and Catalysis

Daniel Schumacher

Porous Polymer-derived Ceramics by Solution-based Freeze Casting for Capillary Transport and Catalysis

Vom Fachbereich Produktionstechnik

der

UNIVERSITÄT BREMEN

zur Erlangung des Grades

Doktor-Ingenieur

genehmigte

Dissertation

von

M.Sc. Daniel Schumacher

Gutachter:

Prof. Dr.-Ing. Kurosch Rezwan
Prof. Dr. rer. nat. Dirk Enke (Universität Leipzig)

Tag der mündlichen Prüfung: 15.06.2020

Danksagung

Diese Dissertation entstand im Rahmen meiner Tätigkeit als wissenschaftlicher Mitarbeiter in der Advanced Ceramics Group der Universität Bremen. Mein Dank gilt Herrn Prof. Dr.-Ing. Kurosch Rezwan für das entgegengebrachte Vertrauen, die Möglichkeit der experimentellen Arbeiten sowie der Unterstützung in der wissenschaftlichen Weiterbildung. Des Weiteren danke ich Prof. Dr. rer. nat. Dirk Enke für das Interesse an meiner Arbeit und die Bereitschaft, diese Dissertation als Zweitgutachter zu bewerten.

Mein herzlicher Dank gilt Dr. Michaela Wilhelm für ihre stetige Hilfsbereitschaft, unzählige Diskussionen, wertvolle Anregungen und ihr ausgezeichnetes, forderndes und förderndes Feedback. Ebenso danke ich Herrn Prof. Dr.-Ing. Michael Dreyer und Dawid Zimnik vom Zentrum für angewandte Raumfahrt (ZARM) für die konstruktive Zusammenarbeit und die Einführung in das Thema des kapillaren Transports. Des Weiteren danke ich Thomas Ilzig von der TU Dresden für die Hartnäckigkeit bei der Auswertung der µ-CT Daten und für die gelungene Kooperation.

Für die Einblicke in vielfältige wissenschaftliche Fragestellungen, das ehrliche Feedback und die Denkanstöße bedanke ich mich bei den Projektleiter*innen und Kolleg*innen aus dem Graduiertenkolleg MIMENIMA und der Advanced Ceramics Group. Besonders bedanken möchte ich mich bei Tina Kühn für die vielen, immer hilfreichen Hinweise im Labor. Vielen Dank an Christian Ellenberg für Unterstützung bei technischen Fragestellungen. Herzlichen Dank an meine Bürokolleg*innen Huxing Zhang, Nataliá Fontao, Pedro Braun und Marieke Hoog-Antink für die fachlichen Diskussionen, aber auch für die nötigen Pausen an langen Arbeitstagen.

Diese Arbeit wäre ohne die Mitwirkung von Studierenden nicht möglich gewesen. Sie haben in ganz unterschiedlicher Form etwas zum Gelingen meiner Forschung beigetragen. Ich bedanke mich für das Engagment bei Shamima Akhter, Farina Handels, Sebastian Neumann, Nantje Steinberg, Catherine Yokan , Mattheus Olivan, Pedro Braun, Gustavo Hamann, Tuoi Hoang, Matha Moeinkhah und Anil Pativada.

Auch außerhalb der Universität habe ich vielfältige Unterstützung erfahren. Ich bedanke mich bei meinen Eltern und meinem Bruder, die trotz der Entfernung immer Anteil genommen haben. Theresa, ganz besonders wertvoll war deine Bestätigung, Unterstützung, Aufmunterung und dein Verständnis – vor allem in enttäuschenden und zähen Phasen auf dem Weg zur Abgabe dieser Arbeit.

Contents

Zusammenfassung

Die präzise Kontrolle der Porenstruktur ist entscheidend für die Anwendung von porösen Strukturen. In der Literatur hat das Gefriergussverfahren gezeigt, dass es eine Vielzahl an Möglichkeiten besitzt, um die Porenstruktur und damit verknüpfte Eigenschaften, wie die Permeabilität und die mechanische Festigkeit, zu beeinflussen. Es eignet sich daher besonders für die Entwicklung von Porenstrukturen. Polymer-abgeleitete Keramiken haben in Untersuchungen bewiesen, dass sie eine einzigartige Kombination von Eigenschaften, wie eine niedrige Wärmeleitfähigkeit, einstellbare Oberflächeneigenschaften und die Möglichkeit die chemische Zusammensetzung einfach anpassen zu können, aufweisen. Folglich ist die Kombination des flexiblen Gefriergusses mit der gut einstellbaren polymer-abgeleiteten Keramik in hohem Maße vielversprechend, um den Herausforderungen unterschiedlichster Anwendungen poröser Monolithe zu begegnen.

Ziel dieser Arbeit ist die Entwicklung poröser polymer-abgeleiteter SiOC Monolithe für Anwendungen im kapillaren Transports und der heterogenen Katalyse. Anpassungen der Prozessparameter des lösungsbasierten Gefriergusses sowie Änderungen der Zusammensetzung der Polymerlösung stellen dabei die wesentlichen Variablen dar. *tert*-Butylalkohol und Cylcohexan werden als Lösemittel und Polysiloxane als präkeramische Polymere verwendet.

Im ersten Teil und als Ausgangspunkt für die folgende Konditionierung werden die grundlegenden Zusammenhänge zwischen der Zugabe von präkeramischen (SiOC) und keramischen (SiO_2, Al_2O_3) Füllern auf die Porenstruktur und Eigenschaften, wie Hydrophilizität, mechanische Festigkeit und spezifische Oberfläche, aufgeklärt. In Abhängigkeit der chemischen Zusammensetzung der präkeramischen Füller variiert die spezifische Oberfläche von 276 $m^2 \cdot g^{-1}$ bis 531 $m^2 \cdot g^{-1}$ und die Hydrophilizität von 0,13 bis 2,08. Die Kontrolle und sogar die Vorhersage der resultierenden Eigenschaften ist aufgrund der guten Übereinstimmung zwischen experimentellen Ergebnissen und der linearen Mischungsregel möglich. Die bemerkenswerte Steigerung der Druckfestigkeit um einen Faktor von bis zu 1,9 ist auf die Änderungen der Porenmorphologie zurückzuführen. Diese ist wiederum bedingt durch die Füllerzugabe und charakterisiert durch eine gesteigerte Isotropie. Bei niedrigen

Füllergehalten (1,7 vol%) führen Aluminiumoxid Platelets, die ein geringes Aspektverhältnis aufweisen, zu höheren Festigkeiten als sphärische Partikel. So ermöglicht die Zugabe von Füllern mit den beobachteten, verschiedenen Auswirkungen, die Porenstrukturen sehr flexibel und gezielt anzupassen. Besonders die verbesserte Festigkeit stellt einen bedeutenden Schritt in Richtung einer breiten Anwendung von porösen gefriergegegossenen SiOC Monolithen dar.

Das Wissen um die Möglichkeiten, die Porenstruktur durch Zugabe von Füllern zu beeinflussen, stellt eine breite Grundlage zur Herstellung von porösen Monolithen mit verschiedenen Strukturmotiven sowie zur Erprobung dieser Strukturen hinsichtlich ihrer Eigenschaften im kapillaren Transport dar. Das Verständnis der Zusammenhänge zwischen Porenstruktur und kapillarem Transport ist essentiell, um Komponenten für den kapillaren Transport effizient entwickeln zu können. Um unterschiedliche Porenmorphologien und –ausrichtungen zu erzeugen, werden im Rahmen dieser Arbeit neben unterschiedlichen Lösungsmitteln zwei Einfriermethoden untersucht: nicht unidirektional und unidirektional. Für den kapillare Transport bei Raumtemperatur zeigt sich, dass eine hohe Permeabilität zu einem schnelleren Transport führt. Obwohl die isotrop-dendritische und die prismatische Struktur sehr ähnliche Porenfenstergrößen und Porosität haben, führen Unterschiede in der Porenmorphologie und der Tortuosität zu höherer Permeabilität und damit auch zu schnellerem Transport in der isotrop-dendritischen Struktur bei nicht unidirektionalem Einfrieren. Der kapillare Transport in der dendritischen Porenstruktur mit geringer Porosität ist durch einen linearen Massenanstieg gekennzeichnet, der sich deutlich von dem idealtypischen gekrümmten Verhalten unterscheidet. Bei unidirektional gefrorenen Proben, die eine vollständig ausgerichtete Porenstruktur ohne Unterbrechung der Dendriten aufweisen, ist hingegen kein lineares Verhalten zu beobachten. Dies legt die Erklärungsansatz nahe, dass eine eingeschränkte Interkonnektivität zwischen den einzelnen ausgerichteten Porenbereichen der Grund für die Linearität ist. Erste, spezielle Auswertungen von µCT-Daten untermauern diesen Ansatz. Während das Einfrieren bei konstanter Einfriertemperatur in einem Gradienten der Porenfenstergröße resultiert, erzeugt eine konstante Einfriergeschwindigkeit eine homogene Porenstruktur. Wird die Einfriergeschwindigkeit von etwa 3,3 µm·s auf 6,8 µm·s reduziert, steigt die Porenfenstergröße um 14 % bis 67 % und damit auch die Geschwindigkeit des kapillaren

Transports. Die Vorhersage des kapillaren Transports anhand der Lucas-Washburn Gleichung stimmt nur bei Proben mit sehr spezifischen Eigenschaften (prismatisch, 60 % Porosität) mit den experimentellen Ergebnissen überein. Um den kapillaren Transport in den untersuchten komplexen dreidimensionalen Strukturen verlässlich vorherzusagen, sind die Annahmen der Lucas-Washburn Gleichung zu restriktiv. Zusammenfassend erlauben diese umfassenden Erkenntnisse zukünftig die gezielte Auslegung von lösungsbasierten, gefriergegossenen Komponenten für den kapillaren Transport.

Kontrolle über die Porenstruktur ist auch bei monolithischen Katalysatoren, die durch besseren Wärme- und Massetransport als konventionelle Festbettreaktoren charakterisiert sind, essentiell. Zunächst muss aber der inerte Träger mit katalytischer Aktivität ausgestattet werden. Dabei sind Trägermaterialien mit einer inhärenten katalytischen Aktivität aufgrund einiger Nachteile der kommerziell verwendeten Washcoat Beschichtung sehr interessant. In dieser Arbeit werden die zugrundeliegenden Prinzipien und Prozesse zur Erzeugung eines makroporösen metallhaltigen SiOC Monolithen aufgeklärt. Inhärent katalytisch aktive Monolithe werden mit Hilfe der neuartigen Kombination aus lösungsbasiertem Gefriergießen und dem bekannten Prinzip der in situ Bildung von Nickelpartikeln in SiOC Matrizes erfolgreich hergestellt. Unter vier Komplexierungs- und Vernetzungsmitteln stellt sich (3-amino)propyltriethoxysilan als am effektivsten heraus, um kleine und homogen verteilte Nickelpartikel zu erzeugen. Partikelgröße von (2.52 ± 0.82) nm können so erreicht werden. Die katalytische Aktivität wird in einem Festbettreaktor für die CO_2 Methanisierung bestimmt. Die Umsetzung von Kohlenstoffdioxid und die Selektivität gegenüber Methan nehmen mit sinkender Größe der Nickelpartikel ab und erreichen Maximalwerte von 0,49 und 0,74. Diese vielversprechenden Ergebnisse zeigen, dass metallhaltige makroporöse SiOC Monolithe, die durch das lösungsbasierte Gefriergussverfahren hergestellt werden, aussichtsreiche heterogene Katalysatoren sind.

Zusammenfassend beleuchtet diese Arbeit die grundlegenden Abhängigkeiten zwischen den Prozessparametern, wie z.B. die Zugabe von Füllern oder die Einfrierbedingungen und der entstehenden Porenstruktur von lösungsbasiertem Gefrierguss von PDCs. Ausgehend davon zeigt sie die erfolgreiche Anpassung und Entwicklung der Porenstruktur und/oder der chemischen Zusammensetzung hinsichtlich zweier relevanter Anwendungen: kapillarer Transport und heterogene Katalyse.

Abstract

The precise control of the pore structure is fundamental for the application of porous media. Freeze casting has proved to offer a great variety of possibilities to widely change the resulting pore structure and related properties such as the permeability and the mechanical strength. Consequently, it is very interesting for the development of pore structures. Moreover, polymer-derived ceramics (PDC) are reported to offer a unique combination of properties such as low thermal conductivity, tailorable surface characteristics and the possibility to easily modify the chemical structure. Consequently, the combination of the flexible freeze casting with the tailorable polymer-derived ceramics is very promising in tackling the challenges of various applications in the field of porous monoliths.

This work aims to develop porous polymer-derived SiOC monoliths for capillary transport and heterogeneous catalysis by adapting the processing parameters of the solution-based freeze casting and by altering the chemical composition of the starting solution. Hereby, *tert*-butyl alcohol and cyclohexane act as solvents and polysiloxanes are used as preceramic polymers.

In the first part and as base for the subsequent conditioning, the fundamental relationships between the addition of preceramic (SiOC) and ceramic (silica, alumina) filler particles and the resulting pore structure and properties such as hydrophilicity, strength and specific surface area are elucidated. Depending on the chemical composition of the preceramic filler particles, the BET surface area and the hydrophilicity vary in a wide range of $276\,\mathrm{m^2 \cdot g^{-1}}$ to $531\,\mathrm{m^2 \cdot g^{-1}}$ and 0.13 to 2.08, respectively. A linear rule of mixture shows very good agreement with the experimental results and enables the precise control and even the prediction of the resulting properties. The remarkable increase of the compressive strength by a factor of up to 1.9 is attributed to the change in the pore morphology. This change is caused by the filler addition and characterized by enhanced isotropy. At low filler concentrations of 1.7 vol%, the addition of alumina platelets which exhibit a low aspect ratio is more effective in improving the strength than the addition of spherical particles. The addition of filler particles and its influence on the pore structure represents a versatile toolbox which enables the precise adaption of pore structures.

Especially, the improved strength reflects an important step towards a broader application of freeze cast SiOC monoliths.

The knowledge of the possibilities to influence the pore structure by adding fillers is an excellent base to manufacture porous monoliths with different structural motifs and test these pore structures on their capillary transport ability. The understanding of relation between the pore structure and the capillary transport behavior is the key for an efficient design of capillary active components. To generate different pore morphologies and pore orientation, different solvents as well as two methods of freezing are used within this work: non unidirectional and unidirectional freezing. Isothermal wicking experiments at room temperature show that a high permeability results in fast wicking. Though having a similar pore window size of 5.5 µm to 7.0 µm and a similar porosity of 60.8 % to 63.5 %, the differences in pore morphology and tortuosity between the isotropic dendritic structure and the prismatic structure lead to a higher permeability and consequently faster wicking for the isotropic dendritic structure in non unidirectional freezing. The wicking of the dendritic structure with a lower porosity is characterized by a linear mass increase and deviates from the typical curved wicking behavior. The absence of a linear section in case of unidirectional freezing which provides a fully aligned pore structure without any interruption of the dendrites, supports the hypothesis of limited interconnectivity between aligned pore areas as reason for the linear section. A first particular analysis of µCT-data underpins this explanation. While constant freezing temperature conditions result in a graded pore window size, a constant freezing front velocity generates a homogeneous pore structure. Decreasing the freezing front velocity from approx. 3.3 µm·s to approx. 6.8 µm·s leads to an increase of the pore window diameter by 14 % to 67 % and consequently causes faster wicking. The prediction of the wicking by the Lucas-Washburn equation matches with the experimental data only for structures with a very specific set of properties (prismatic structure, 60 % porosity). The results clearly show that the assumptions made by the Lucas-Washburn equation are too restrictive to reliably predict the wicking in complex solution-based freeze cast structures. In summary, these comprehensive findings allow for a targeted design of components for capillary transport applications prepared by solution-based freeze casting in the future.

The control of the pore structure is also essential for monolithic catalysts which are characterized by superior heat- and mass transfer compared to packed-bed reactors. But before, catalytic activity has to be introduced to the initially inert support. Hereby, supports with an inherent catalytic activity are of interest due to some drawbacks of the commercially applied method of using a washcoat. Within this work, the underlying principles and processes of generating a macroporous metal containing PDC monolith are investigated. Inherent catalytic active monoliths are successfully prepared by the novel combination of solution-based freeze casting with the generally known principle of in situ formation of nickel particles in SiOC matrices. Among four complexing and cross-linking agents with amino functionality, (3-aminopropyl)triethoxysilane proofs to be most effective in creating small and well distributed metallic nickel particles of (2.52 ± 0.82) nm. Evaluation of the fundamental catalytic activity was performed in a packed-bed reactor using the CO_2 methanation as a probe reaction. Carbon dioxide conversion and the selectivity towards methane increase with decreasing nickel particle size with maximum values of 0.49 and 0.74, respectively. These encouraging results proof that metal containing macroporous SiOC monoliths prepared by solution-based freeze casting are very promising candidates for heterogeneous catalysis.

In conclusion, this work elucidates the fundamental relationships between the process parameters (e.g. the addition of fillers or the freezing conditions) and the resulting pore structure of monolithic solution-based freeze cast PDCs. Taking this as base, it demonstrates the successful adaption and conditioning of the pore structure and/or the composition for two relevant applications: capillary transport and heterogeneous catalysis.

Introduction

<div style="text-align: right; font-size: 3em;">1</div>

Porous ceramic monoliths are required in a wide range of industries. For applications such as water filtration, energy storage/conversion, gas adsorption, catalysis or even tissue engineering, a high permeability is a prerequisite to avoid mass transport limitations [1-5]. This requirement can be addressed by the introduction of open macroporosity. Several methods have been developed for the manufacturing of macroporous monoliths: direct foaming, replica method, additive manufacturing and sacrificial templating [6, 7].

Being able to precisely control the pore structure is crucial for the development of porous material in order to meet the requirements of the applications. Such development includes the adaption of parameters which are characterizing the porous structure itself: open porosity, pore window size, specific surface area, pore morphology and tortuosity. Additionally, further properties which are describing the interaction of the material with the environment have to be taken into account: surface characteristics, mechanical strength and reactivity with substances in the environment, e.g. catalytic activity.

Two applications of porous structures and their requirements on the pore structure should be considered within this work: capillary transport and heterogeneous catalysis. In the challenging niche application of liquid acquisition devices for spacecraft, porous screens are used for the separation of liquid from vapor to ensure gas free delivery of liquid propellants to the engine. The pore structure determines the pressure loss as well as the reliability under different thermal and gravitational conditions. The required pore size typically ranges from approx. 5 μm to approx. 100 μm and depends strongly on the specific operating conditions. To avoid thermal losses, materials with a lower heat conductivity than the currently used metallic meshes are of interest. A low heat conductivity of the porous structures would reduce boil-off of precious propellant which is a critical aspect in the context of cryogenic propellants. Additionally, the application of materials with a lower density than the currently used stainless steel reduces the system mass which is a crucial factor in aerospace. Most important when introducing new materials and processing methods, the basic relationships between the pore structure and the resulting capillary

performance need to be fully understood in order to enable an effective design of components.

The second application is the commercially important CO_2 methanation. While packed-bed reactors are the industrial standard, heterogeneous monolithic catalysts provide better heat conductivity which is especially important in strong exothermic reactions to avoid hot spots. The CO_2 methanation is such a reaction. The transformation of carbon dioxide to methane or other valuable chemicals is a key step in the power-to-gas technology. Conventionally, catalysts are prepared by a two-step process. A catalytic inactive ceramic support is coated with the metal containing washcoat. Besides the additional costs due to the coating step, ablation is a potential risk of the conventional coating process. Hence, it is of interest to develop inherent catalytic active materials which provide equal catalytic performance without the risk of ablation.

To meet the requirements of the two mentioned applications, solution-based freeze casting of polysiloxanes is used in this work to generate adapted porous SiOC monoliths. Freeze casting, which is a sacrificial templating method, enables to vary the properties of the pore structure in a wide range and allows to generate the required pore sizes [8, 9]. Pores are created by phase separation of a two-component system during freezing and subsequent sublimation of the liquid crystals followed by a heat treatment to consolidate the structure.

As a base for the development of structures, the fundamental possibilities to influence the properties of a pore structure are investigated in the first part of this work. Apart from properties which are characterizing the porous structure itself such as pore size and porosity, further properties which are relevant to the applications such as mechanical strength and surface characteristic need to be considered. Since prediction becomes more important in processing, also the reliability of predicting the properties is addressed.

The knowledge of the relation between the pore structure and the capillary transport behavior is of importance for an effective design of capillary active components. The second part of this work addresses important aspects of the correlation between pore structure and capillary transport. Major properties which need to be taken into account are the pore size, the porosity and the pore morphology. The impact of

changing these structural properties on the wicking behavior is investigated. In addition, the applicability of predicting the wicking performance of complex three dimensional structures is evaluated. Besides the influence of the mentioned structural parameters, the freezing conditions also strongly affect the capillary transport. In terms of the freezing conditions, two aspects need to be considered: the direction of freezing and the freezing velocity. Especially the differences between constant freezing temperature and constant freezing velocity are addressed.

Before applying the gained knowledge from the previous sections in order to adapt the pore structure of a monolithic catalyst, the underlying principles and processes of manufacturing a porous metal containing PDC monolith need to be fully understood and controllable. First, suitable complexing- and cross-linking agents need to be assessed. Second, the impact of further process parameters such as the nickel precursor and the ratio of complexing groups to nickel should be evaluated. The results of these investigations are shown in the third part of this work.

References

[1]   T. Fukasawa, M. Ando, T. Ohji, J. Ceram. Soc. Jpn. 110 (2002) 627 - 631.

[2]   N. MacDowell, N. Florin, A. Buchard, J. Hallett, A. Galindo, G. Jackson, C.S. Adjiman, C.K. Williams, N. Shah, P. Fennell, Energy Environ. Sci 3 (2010) 1645-1669.

[3]   S.D. Kenarsari, D. Yang, G. Jiang, S. Zhang, J. Wang, A.G. Russell, Q. Wei, M. Fan, RSC Advances 3 (2013) 22739-22773.

[4]   B.A. Haberman, J.B. Young, Int J Heat Mass Tran 47 (2004) 3617-3629.

[5]   J.R. Woodard, A.J. Hilldore, S.K. Lan, C.J. Park, A.W. Morgan, J.A.C. Eurell, S.G. Clark, M.B. Wheeler, R.D. Jamison, A.J.W. Johnson, Biomaterials 28 (2007) 45-54.

[6]   P. Colombo, C. Vakifahmetoglu, S. Costacurta, J. Mater. Sci. 45 (2010) 5425-5455.

[7]   A.R. Studart, U.T. Gonzenbach, E. Tervoort, L.J. Gauckler, J. Am. Ceram. Soc. 89 (2006) 1771-1789.

[8]   K. Araki, J.W. Halloran, J. Am. Ceram. Soc. 88 (2005) 1108-1114.

[9]   S. Deville, J. Mater. Res. 28 (2013) 2202-2219.

Scientific Background

2.1 Polymer-derived Ceramics (PDCs)

2.1.1 Processing of Polymer-derived Ceramics

Preceramic polymers are used to prepare polymer-derived ceramics via a polymer-to-ceramic conversion. To a huge extend, the macroscopic chemical and physical properties of PDCs can be adjusted by the chemical composition of the molecular precursor [1]. Besides the common structural feature which is the Si-based backbone, preceramic polymers can be varied in the additional backbone element (e.g. oxygen, carbon and nitrogen) and in the organic side group R. Figure 2.1 gives an overview over the large variety of preceramic polymers. Altering the additional backbone elements results in different classes of preceramic polymers e.g. polysiloxanes, poly-carbosilanes and polysilazanes [1].
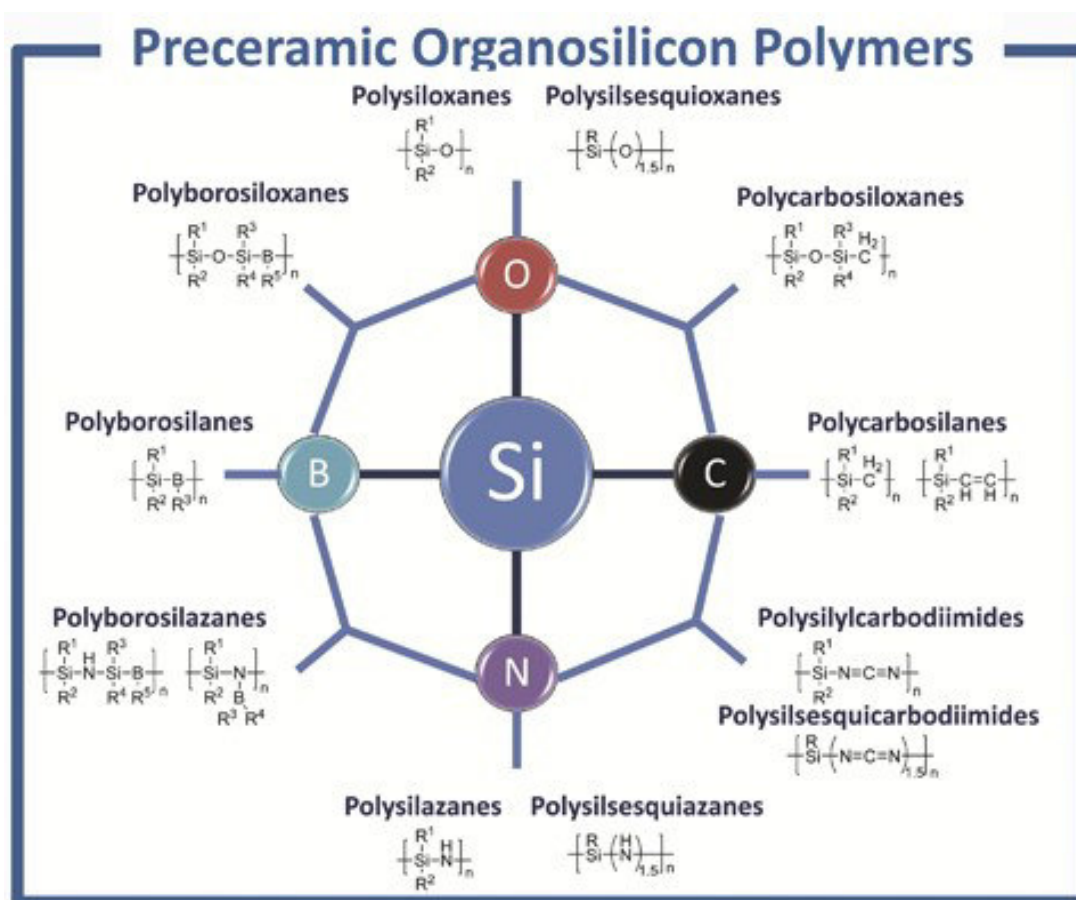
Figure 2.1   Overview over the variety of preceramic organosilicon polymers with R indicating variable organic side groups; Reprint with permission from Wiley [1].

Properties of the preceramic polymer such as the solubility, the rheological behavior, electronic and optical properties and the chemical and thermal stability can be changed by modifying the organic side group [1]. Hydrogen, aliphatic groups and aromatic organic side groups are most common as organic side groups [1]. Additionally, the carbon content is controlled by organic side groups. Due to their well-known chemistry, the synthesis of organosilicon polymers is promoted. This makes them the most representative class of preceramic polymers. [1]. Among a variety of possible educts, chlorosilanes R_xSiCl_{4-x} (x = 0–3) are mainly used as starting material due to their low cost and commercial availability [1]. The formation of a thermoset by thermal cross-linking below 200 °C after shaping is enabled by the incorporation of suitable functional groups (e.g. Si-OH or Si-H) which undergo condensation or addition (e.g. hydrosilylation) reactions [1]. In dependence on the amount of cross-linking active groups, a linear or branched polymeric network is formed. Also further cross-linking methods such as γ-radiation, UV-light, electron beam, oxidative curing and reactive gases have been reported [1]. In addition, suitable catalysts such as metal salts, acids or bases facilitate the cross-linking reaction [2]. Already mild conditions such as room temperature and the presence of oxygen or water might be sufficient for the cross-linking of polysilazanes or polysiloxanes, respectively. In the case of highly cross-linked preceramic polymers, a polymer-to-ceramic conversion is possible. As a result, organic moieties e.g. methyl, phenyl and vinyl groups decompose and convert [1, 3]. Besides other thermal and nonthermal processes, oven pyrolysis in flowing inert gas (nitrogen or argon) is most frequently applied for the polymer-to-ceramic conversion [1]. In dependence on the progress of the conversion, different products are obtained even from the same precursor. Figure 2.2 illustrates this issue exemplary on the conversion of polysiloxane.
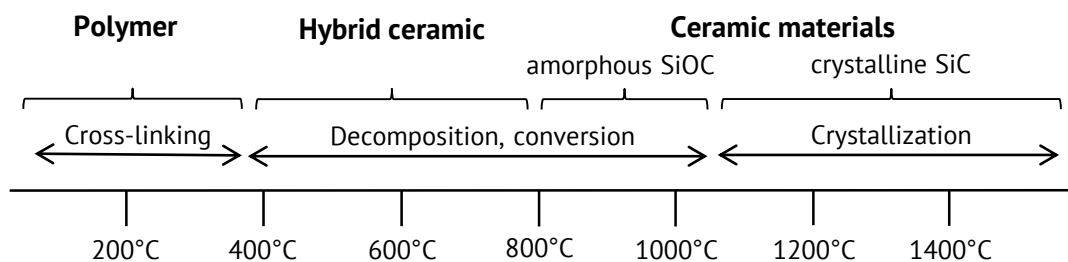
Figure 2.2 Products of polymer-to-ceramic conversion in dependence on pyrolysis temperature.

Decomposition takes place between 400 °C and 800 °C and results in the formation of a hybrid ceramic [4]. Additionally, Si-C and Si-O bonds rearrange and nanodomains composed of different SiOC species and free carbon form [5]. At temperatures above 800 °C decomposition is complete and the incorporation of carbon atoms into the Si-O network generates amorphous SiOC. Crystallization to silicon carbide is taking place at temperatures exceeding 1200 °C. The involved mechanisms are further rearrangement, phase separation and the release of CO formed by carbon from the matrix and oxygen [6].

Compared to oxidic ceramics prepared by the conventional powder based route, the PDC route offers several advantages:

- PDCs are additive free. Sintering additives which are necessary in the conventional powder based route may restrict technical applications due to the contamination of the ceramic material by decomposition products of additives [7].
- Properties such as surface characteristics and pore size are highly determined by the degree of decomposition during polymer-to-ceramic conversion [1].
- Polymer shaping techniques such as injection molding, extrusion, melt spinning, coating and polymer infiltration and pyrolysis (PIP) can be applied for PDCs. This enables the generation of complex shapes and shapes which are difficult to achieve by powder-based routes such as fibers, layers and composite materials. Additionally, the use of active fillers allow for near-net-shape ceramics as it is described in detail in section 2.1.3 on page 8 [8-11].
- The low synthesis temperature of 1100 °C to 1300 °C is of economic interest [12].
- Ternary compounds such as SiCN and SiOC can only be produced using the molecular approach of polymer-derived ceramics. The reason is that the corresponding binary compounds e.g. silicon carbide and silica cannot dissolve oxygen and carbon, respectively [1].
- Precursor-derived covalent ceramics generally exhibit enhanced thermo-mechanical properties with respect to creep, oxidation, crystallization and phase separation up to 1500 °C [1].
- Samples combining ceramic-like properties with polymer-like nanostructure can be prepared [13].

2.1.2 Porosity and Surface Characteristic of Polysiloxane-based PDCs

As a direct consequence of the decomposition/conversion of organic moieties during pyrolysis, porosity is generated. In the case of polysiloxanes, water and oligomers are released in the temperature range from 200 °C to 400 °C. Increasing temperature leads to the elimination of organic functional groups. In the range of 600 °C to 800 °C, polymethylphenylsiloxanes and polymethylsiloxanes release C_6H_6 and CH_4, respectively [14]. This gas evolution causes the formation of micropores (pore size < 2 nm) and/or mesopores (2 nm < pore size < 50 nm) and consequently results in very high BET surface areas of 400 $m^2 \cdot g^{-1}$ to 650 $m^2 \cdot g^{-1}$ [15]. The comparison between linear and branched alkoxy-substituted polycarbosilanes $Si(OR)_2CH_2$ shows, that only micropores form when using the linear polymer. In contrast, micro- and mesoporosity can be created in the case of the branched polymer [16]. Additionally, the pyrolysis conditions influence the formation of porosity. Fast pyrolysis of polysiloxanes induces crack formation and micropore collapse already at 600 °C, whereas slow pyrolysis preserves mesopores up to 1200 °C [15]. Collapse of the micro- and/or mesopores with diminishing BET surface area usually takes place at pyrolysis temperatures higher than 800 °C. Generally, high BET surface area and its control are crucial in many applications such as adsorption or catalysis.

The surface characteristic to which is referred in this work is mainly hydrophilicity/ hydrophobicity. While a water attracting surface is called hydrophilic, the term hydrophobic indicates the rejection of water. The underlying physical property which determines hydrophilicity/hydrophobicity is the surface energy of the material.

In general, the most frequently applied preceramic polymers are hydrophobic in the pristine as well as cross-linked state. As described above, the hydrophobic organic side groups such as methyl and phenyl groups decompose during pyrolysis. An extensive decomposition exposes the hydrophilic Si-O backbone and enables the tuning of the hydrophilicity by varying the pyrolysis temperature [17]. For poly-methylsiloxanes pyrolysis below 630 °C results in a hydrophobic surface, whereas pyrolysis above 700 °C creates a more hydrophilic surface [18]. Moreover, surface modifications such as plasma treatment are widely used to alter the surface characteristic of final ceramics. For a polydimethylsiloxane, the formation of a thin and brittle oxidation layer results in increased hydrophilicity after plasma treatment [19]. More effective in influencing the hydrophilicity/hydrophobicity is the

appropriate choice of the precursors and hydrophilic additives. Since the change in the surface characteristic is based on the decomposition of the organic side groups, the transition temperature can be influenced by altering the preceramic polymers. Furthermore, the usage of additives which add hydrophilic silica increases the hydrophilicity. Since the amino group of (3-aminopropyl)triethoxysilane (APTES) is almost completely decomposed already at 400 °C, blending a polymethylsiloxane with APTES leads to an increased hydrophilicity [20, 21].

Engineering the surface characteristic is crucial in many applications. For example, separation of oil from water is required in the case of oil spills. For the adsorption of hydrophobic hydrocarbons, a separation medium with a hydrophobic surface is needed [22]. Super-hydrophobic polysiloxane-based porous membranes proof an effective separation of an oil-in-water emulsion [23]. Also the contrary approach of using a hydrophilic membrane to reject the hydrophobic phase is used in oil-water-separation and desalination [24, 25]. In capillary transport applications, the prerequisite is the wetting of the solid by the liquid. Altering the plasma treatment of polyester fabrics and cotton fabrics result in a changed surface characteristics and significantly different wicking performance [26, 27]. Besides adjusting the pore network, controlling the surface characteristics is one of the main aspects when designing structures for capillary transport applications.

2.1.3 Effect of Filler Particle Addition

Fillers of various nature (ceramic, metallic, polymeric) and geometry (powders, platelets, nanotubes, nanofibers, chopped and long fibers) are added for different purposes to preceramic polymers. In general, the possibility to process preceramic polymers either as solution or in the molten state ensures a good dispersion of fillers [28]. Inert or passive fillers such as silicon carbide and silicon nitrite powders which do not react at all with the preceramic polymer are mainly used for reducing the shrinkage of the component during pyrolysis. By providing paths for the escape of gases generated upon ceramization, also the formation of macrodefects is avoided [29, 30]. Certain properties such as the magnetic characteristics and the electrical conductivity can be modified by the incorporation of functional fillers e.g. iron silicide [31].

In contrast, active fillers are reacting with mainly the gaseous products formed during pyrolysis. The transition of these metallic or intermetallic fillers to carbides, nitrides, oxides or silicides is accompanied with a large increase in volume (up to 50 vol%) which counterbalances the shrinkage of PDCs and allow for the production of near net shape components [32]. Additionally, cracks can be avoided and the density is increased [32]. However, some residual porosity typically remains. In order to modify electrical and/or mechanical properties, carbon nanofibers and nanotubes are added [33, 34]. For some fillers, the atmosphere during the heat treatment influences the properties of the fillers. While alumina fillers incorporated into polysiloxanes are inert in nitrogen and argon atmosphere, they are reactive in oxygen containing atmosphere. As a result of the reaction of γ-alumina fillers with the silica containing polysiloxane-derived matrix, mullite forms at very low temperatures of 1200 °C in oxygen containing atmosphere [35, 36]. This approach of generating compositions with a high degree of microstructural control is used for the synthesis of further ceramics such as SiAlON, wollastonite and cordierite [37, 38]. Polymeric fillers which decompose completely during pyrolysis can act as sacrificial templates for the generation of additional porosity. By choosing size and amount of the fillers the resulting porosity is adjusted. The usage of expandable polymeric microbeads which exhibit a four- to eightfold volume expansion during heating limits the amount of organics to be burned [39]. Hence, crack formation and noxious gases are reduced.

Though filler particles have been used for a variety of purposes, little research is done on the effect of filler particles on the surface characteristics of porous polymer-derived ceramics. As described above, several applications e.g. filtration, oil-water-separation and desalination require the precise control of the hydrophilicity. Besides well investigated techniques such as grafting or coating, the addition of filler particles with a different chemical composition represents a straightforward and simple approach to alter the surface characteristics of polymer-derived ceramics.

2.1.4 In situ Formation of Metal Particles

In contrast to the addition of metallic fillers, in situ formation of metal particles combines a small particles size in the nm-range with a very homogeneous dispersion. Different preceramic precursor show the ability to the in situ formation of metal particles. However, specific approaches for different preceramic polymers are required due to the differences in the reactive components of the preceramic polymers.

Iron atoms were added to the backbone of polysilanes by using ferrocene and ring opening polymerization of strained silaferrocenophanes [40, 41]. Soluble high molecular weight polyferrocenylsilanes which form ferromagnetic iron crystallites at a pyrolysis temperature of 1000 °C are synthesized. Pyrolysis of poly(ferrocene) obtained from spirocyclic ferrocenophane at 600 °C results in the formation of small superparamagnetic iron clusters, whereas at higher temperatures of 900 °C the clusters become larger and thus display ferromagnetic behavior [42].

In general, various metals can be incorporated into polymer-derived SiCN by modifying the preceramic polymer [43, 44]. The metal containing preceramic polymers are called single source precursors. Platinum was added to polysilazanes (poly(ureamethylvinyl)silazane) by effective reaction of the allyl group of the preceramic polymer with the platinum precursor (dimethyl(1,5-cyclooctadiene)-platinum) in the presence of a radical initiator (Dicumylperoxide) [45]. Well dispersed platinum particles with a size of 1 nm to 2 nm, a BET SSA of 44 $m^2 \cdot g^{-1}$ and a mean mesopore diameter of 11.0 nm are obtained. In the total oxidation of methane, the system achieved a conversion of almost 80 % at 600 °C without any sign of degradation.

Further metals which were incorporated into SiCN by means of the single source precursor approach are: iron, cobalt, copper, silver and gold [46]. For the metal modification of polysilazane, aminopyridinatocomplexes were used. These complexes show a distinct tendency for transferring the metal to the polymeric chain which is known to be a combination of a radical polymerization of vinyl functions with a hydrosilylation between vinyl and hydride groups [47].

While polysilazanes have highly reactive groups and can form covalent bonds to metal atoms, polysiloxanes are known to be less reactive. This requires a different approach to incorporate metals to the polymeric network. Two simple strategies to add copper, nickel, iron or cobalt are the addition of metal salts as powders and the mixing of dissolved preceramic polymers with dissolved metal salts and subsequent extraction of the solvent [48-52]. However, these approaches do not provide effective anchoring of the metal and consequently result in a inhomogeneous distribution of metal nanoparticles.

In solution, siloxanes with organofunctional groups such as amino groups or other nitrogen containing groups can complex metal ions. Reactions of functionalized (aminated or thiolated) siloxane which are covalently bound to e.g. a silica support with metal ions ensure the anchoring of metal ions on the surface [53]. This strategy can also be applied to incorporate metals into the network of polysiloxane-derived ceramics. During pyrolysis, gaseous decomposition products such as hydrogen and hydrocarbons reduce the metal ions to metallic nanoparticles. For example, metal alkoxides allow for introduction of metals such as aluminum, titanium and boron in a sol-gel process using polyorganosiloxanes [54]. Furthermore, platinum nanoparticles can be incorporated into polymethylsiloxane and polymethylphenyl-siloxanes. When pyrolyzed at 600 °C, these materials show a BET specific surface area between 432 $m^2 \cdot g^{-1}$ and 654 $m^2 \cdot g^{-1}$ and micro-/mesopores volume ratios in the range of 0.41 to 7.85 [4]. Additionally, nickel- and platinum-containing polysiloxanes can be used as precursor [55]. After mixing (3-aminopropyl)triethoxysilane with nickel acetate tetrahydrate in ethanol, the addition of phenyltrimethoxysilane provides further phenyl groups. Subsequent to cross-linking and drying, the precursors can be pyrolyzed at temperatures of 400 °C to 600 °C in nitrogen atmosphere. The resulting nano-sized metal particles with a size of 15 nm to 20 nm for nickel and 2 nm to 4 nm for platinum are homogeneously distributed through the matrix. The conversion in CO oxidation shows values up to 100 % at 230 °C. BET specific surface areas of up to 650 $m^2 \cdot g^{-1}$ can be achieved at a pyrolysis temperature of 600 °C.

Metals in the polymeric network often have an impact on the microstructure. The formation of carbon nanotubes during pyrolysis at 1000 °C is facilitated when Ni is present in the structure [50]. As a consequence, the electrical conductivity increases. The formation of whiskers which have the corresponding silicide of the metal on its

top is observed at higher pyrolysis temperatures in iron and cobalt containing PDCs [48, 49]. The mechanism of the whisker formation bases on reactions of gaseous decomposition products which are catalyzed by the metal.

In order to obtain macroporous solids, the combination of in situ formation of metal particles with a templating method is possible. Platinum containing hierarchically ordered macro/micro porous foams using polymethylphenylsiloxane and (3-amino-propyl)triethoxysilane, platinic acid as platinum precursor and expandable polystyrene beads with a diameter of 0.5 mm to 1 mm can be synthesized [56]. Cross-linking at 100 °C for 10 h is followed by pyrolysis at 500 °C for 4 h in nitrogen atmosphere. The resulting pore size is in the range of 1.4 mm to 1.5 mm. Furthermore, bimetallic catalytic nanoparticles have been investigated in micro-/ macroporous foam structures as schematically shown in Figure 2.3 [57].
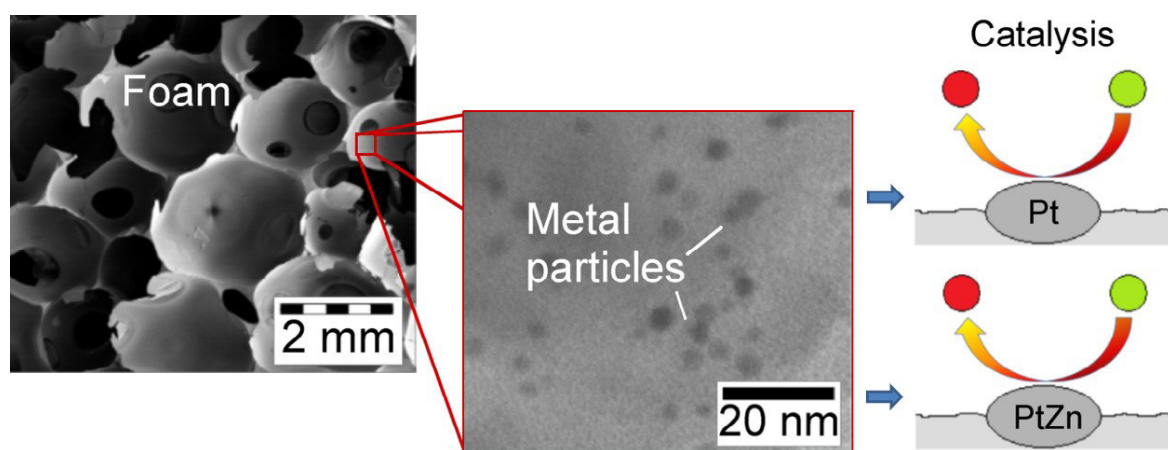
Figure 2.3 SEM image of the foam structure (left) and TEM image of the metallic particles in an amorphous SiOC matrix (middle) for platinum and zinc containing foams catalytic active in CO oxidation; Reprint with permission from Elsevier [57].

Platinum and zinc containing foams can be generated by low temperature pyrolysis at temperatures of 500 °C and 600 °C in nitrogen atmosphere using a mixture of poly-methylphenylsiloxane, (3-aminopropyl)triethoxysilane, platinic acid, zinc chloride and azodicarbonamide as blowing agent. BET specific surface area, pore size and the size of platinum particle varies from 300 $m^2 \cdot g^{-1}$ to 500 $m^2 \cdot g^{-1}$, 0.3 mm to 3.0 mm and 2.9 nm to 4.2 nm, respectively.

Until now, hierarchical macro- and microporous metal containing polymer-derived ceramics were only prepared by templating using polystyrene beads as described above. The required decomposition of the polystyrene causes several drawbacks such

as potential deposition of decomposition products on the pore walls covering the metal sites and crack formation due to intense gas evolution. Additionally, many applications such as monolithic catalysis usually demand structures with lower tortuosity. Hence, it is worthwhile to extend the range of possible macroporous pore morphologies for metal containing polymer-derived ceramics.

2.2 Macroporous Ceramic Structures

2.2.1 Fabrication by Sacrificial Templating Methods

In the last decades, an increasing number of applications which require porous ceramics have appeared. Especially for harsh conditions e.g. high temperature, extensive wear and corrosive media ceramics are promising. Exemplary applications are high temperature insulation, filtration of molten metals, filtration of hot corrosive gases and support for catalytic reactions [58-60]. By incorporating porosity to a ceramic component, properties such as low dielectric constant, low thermal mass, low thermal conductivity, controlled permeability and low density can be added or altered. The processing method has a huge impact on the resulting character of the porosity. Besides replica techniques, partial sintering, direct foaming, extrusion, additive manufacturing and weaving of ceramic fibers, sacrificial templating methods are widely used to generate porous ceramic components [61, 62].

Compared to other processes, the appropriate choice of the template in sacrificial templating allows to deliberately tailor important properties such as pore morphology, pore size and porosity. As porosity and pore size only depend on the volume fraction and the size of the template, a large range of porosity and pore size can be covered [62]. Figure 2.4 illustrates the flexibility of the sacrificial templating method in terms of porosity and pore size. A hierarchical pore structure and various porosity levels can easily be achieved by using templates of different size and different volume fraction of templates, respectively. Furthermore, the sacrificial templating method is very flexible regarding the chemical composition of the material [62]. A large variety of oxides (e.g. alumina, silica, calcium carbonate, hydroxyapatite and mullite) have been processed using starch particles as templates which can easily be dispersed in water and are highly available at different sizes and morphologies [63-66].
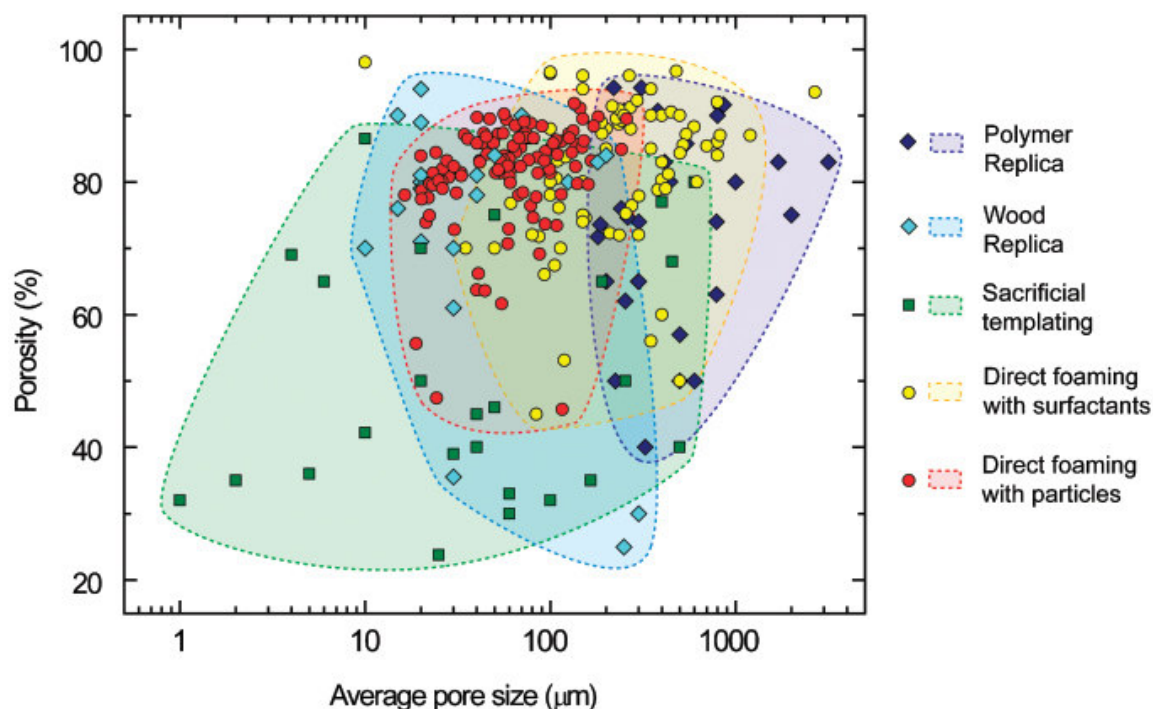
Figure 2.4 Typical porosity and average pore size achieved via the replica, sacrificial templating, and direct foaming processing routes; Reprint with permission from Wiley [62].

Sacrificial templating leads to a pore structure which is a negative replica of the sacrificial template. Usually, the homogeneously distributed sacrificial phase is dispersed in a continuous matrix of ceramic particles or a ceramic precursor and finally is extracted to form pores. Common ways to prepare this biphasic composite are the pressing of a two component powder mixture, the formation of a two phase suspension and the impregnation of previously consolidated preforms of the sacrificial template with a ceramic suspension or a preceramic polymer [62]. Prior to extraction, the continuous phase has to be solidified in order to avoid a collapse to the structure during extraction. Possible consolidation mechanisms are: sol-gel transition, the formation of a stiff attractive network of particles, cross-linking and the use of setting agents or binders [63, 67-69]. The method to extract the liquid mainly depends on the type of the template which can vary from natural and synthetic organics to liquids, metals, salts and ceramic compounds [62]. Salts, metallic and ceramic templates are usually extracted by chemical processes. Repeated washing with water easily removes salts [70]. In contrast, more aggressive media such as acidic leaching is necessary to extract metallic and ceramic particles [71, 72]. Pyrolysis at temperatures between 200 °C and 600 °C are applied to decompose synthetic and natural organics [73]. Main drawbacks of organic materials as sacrificial template are

crack formation due to a high amount of gaseous decomposition products and long heat treatment times to avoid crack formation. In order to overcome these drawbacks, liquid pore formers can be used. The removal of liquids such as water and oil is possible at mild conditions without the generation of toxic gases and pronounced stresses during the extraction [74, 75]. Also the extraction of solidified liquids by sublimation in the freeze casting process allows the removal under gentle conditions [76-78].

2.2.2   Solution- and Suspension-based Freeze Casting

In freeze casting, the sublimation of solidified liquids which act as sacrificial templates creates macroporous structures. Subsequent thermal treatment consolidates and densifies the walls [79]. Depending on the condition of the solid, two subcategories of freeze casting has to be separated: solution-based and suspension-based freeze casting. The process for both subcategories is schematically shown in Figure 2.5.

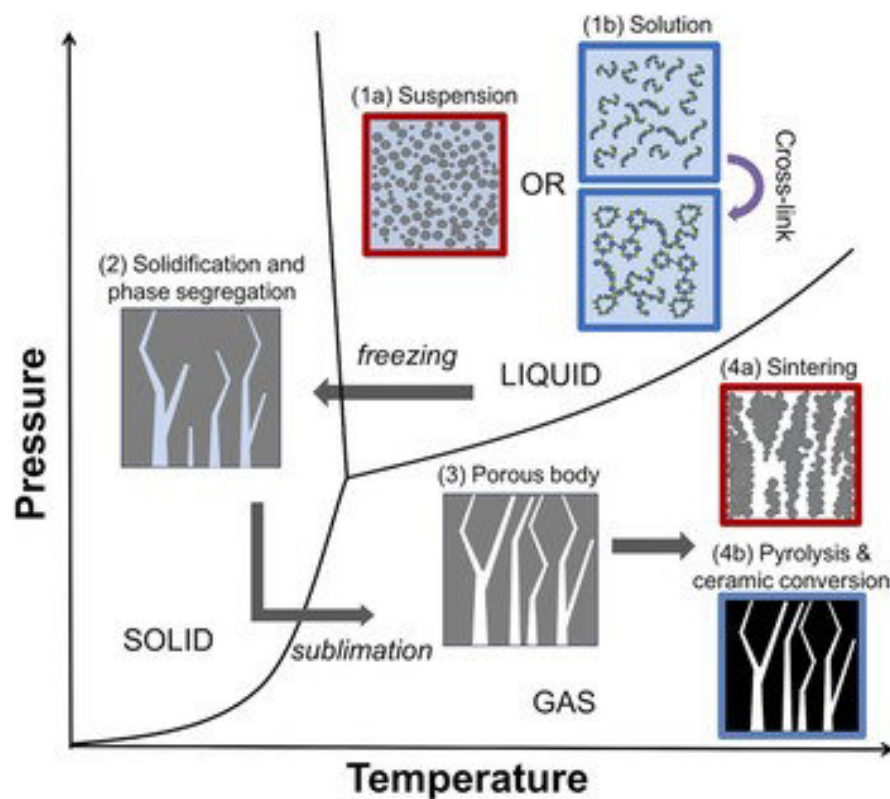

Figure 2.5   Schematic illustration of the freeze casting process for both suspension- and solution-based systems starting with a suspension (1a) or a solution (1b), respectively; Reprint with permission from Cambridge University Press [80].

While dispersed particles are used in suspension-based freeze casting, a homogeneous polymeric solution is present in solution-based freeze casting. In both cases, the starting point is the liquid state of a dispersion or a solution. Upon freezing the sample, liquid crystals nucleate and grow. In general, solidification of the suspension or solution is the critical stage where the characteristics of the future pore structure are determined.

In the case of suspension-based freeze casting, the dispersed particles are rejected by the moving solidification front. Further governing mechanisms are the breakdown of the solidification front to a nonplanar morphology and the concentration and entrapment of the particles in between the solidified crystals [81]. For all these mechanisms it is valid that the interactions of the particles with the solidification front are of physical nature and they determine the resulting structure.

The rejection of a particle from the advancing solidification front and the entrapment between the growing crystals is ensured if there is an overall increase of surface energy for the engulfment of the particle, i.e.,

$$\Delta\sigma = \sigma_{sp} - \left(\sigma_{lp} + \sigma_{sl}\right) > 0$$

(2.1)

where σ_{sp}, σ_{lp}, and σ_{sl} and are the interfacial free energies associated with the solid-particle, liquid-particle and solid-liquid interface respectively [79]. For $\Delta\sigma > 0$, a liquid film exists around the particle which enables the transport of molecules towards the growing crystal. With increasing freezing front velocity the thickness of this film decreases. At a critical velocity, the film is not thick enough to provide sufficient flow of molecules. Consequently, the particle becomes encapsulated by the crystal. The critical velocity depends on the viscosity of the liquid, the particle size and the variation of the free energy defined in Equation 2.1 [82]. A further requirement for the collection of particles between crystals is a nonplanar solidification front. In the case of a planar front, all particles are collected at one side of the sample. Thus, the morphology of the front dictates the architecture of the final pore structure. At the initial stage of freezing, the solidification front is planar and needs to transform towards an irregular morphology [79]. Two mechanisms are proposed in the literature. According to the first mechanism, instability is generated due to the reversal of the thermal gradient in the liquid ahead of the interface and behind the

particle [83, 84]. The second mechanism relies on the inherent instability of the interface, known as Mullins-Sekerka instability [85].

In contrast to suspension-based freeze casting, the separation mechanism in solution-based freeze casting bases on thermally induced phase separation [80, 86]. Especially, spinodal phase separation is thermodynamically preferred which results in a bicontinuous structure composed of a solvent-rich and a polymer-rich phase [87]. Clear polymer solutions which are observed ahead of the freezing front indicate that the solid-liquid phase separation is only occurring in conjunction with crystal growth at the freezing point of the solution [80]. However, the phase separation in the liquid state is still possible due to limited solubility in the case of poor solvents or high polymer concentrations [80]. In solution-based freeze casting, considerations on the morphology of the solidification front and on mechanisms causing a nonplanar solidification front such as the Mullins-Sekerka instability are equal to the ones in suspension-based freeze casting [88].

Since the pore structure is a replica of the original solvent crystals, variations of the solvent, the solidification conditions and the slurry/solution composition change the resulting pore structure. Most investigations on freeze casting have been performed on water-based systems. A lamellar pore morphology with lamellar channels between the ceramic walls is characteristic for water-based freeze casting. Basic crystallographic considerations and fundamental mechanisms of crystal growth explain the characteristic pore morphologies of different liquids. As an example, heavily anisotropic crystal growth of ice crystals results in significant differences of crystal growth along certain crystal axes. This leads to the formation of vertically lamellar crystals [79]. Similar considerations apply also for other liquids which are used in freeze casting. For example, the solidification of liquid camphene causes the formation of dendrites and a prismatic/honeycomb pore shape is obtained by using *tert*-butyl alcohol [89]. Figure 2.6 shows pore morphologies which can be generated by using different organic liquids.
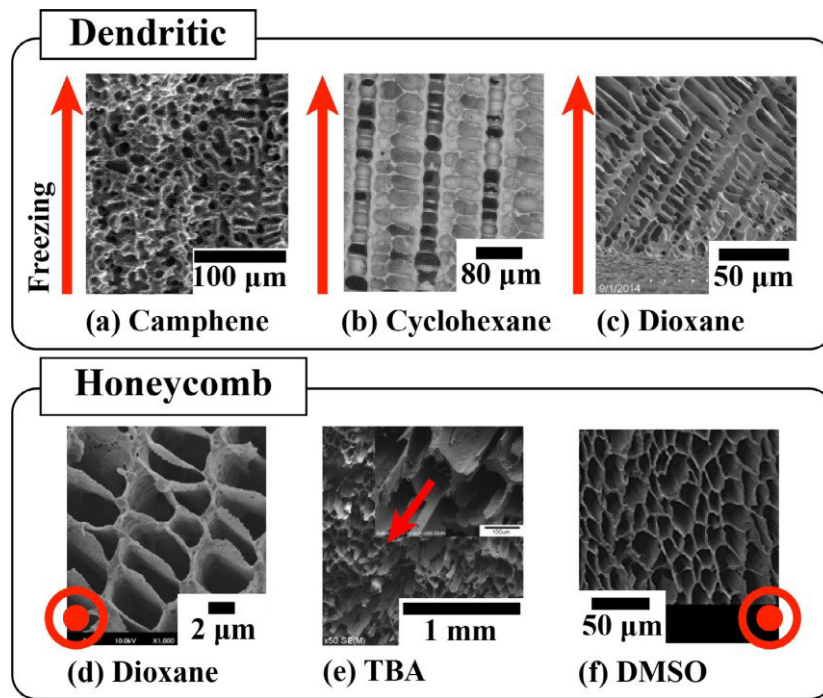
Figure 2.6 Overview of microstructures obtained using organic fluids under directional freezing conditions. Red arrows indicate the direction of freezing for cross sections taken parallel to the solidification direction; cross sections taken perpendicular to the solidification direction are marked with a circle [90]. Dendritic structures are shown in (a-c), where (a) is sintered, 50 vol% alumina templated with camphene [91], (b) is sintered, 20 wt% silicon oxycarbide (SiOC) obtained using cyclohexane [92], and (c) is polyurethane templated with dioxane [93]. Honeycomb structures are shown in (d-f), where (d) is 30 wt% polystyrene obtained with a fluid mixture of polyethylene glycol and dioxane [94], (e) is sintered 10 vol% alumina-zirconia obtained using *tert*-butyl alcohol [95], and (f) is poly (L-lactic acid) obtained using dimethyl sulfoxide (DMSO); Reprint with permission from Elsevier [96].

As a consequence, manipulating the crystal growth enables to adjust the final pore structure. Different approaches have been used e.g. mixtures of liquids, the use of cryoprotectants or the addition of alcohols or salts to water-based systems [97-101]. By this means, the pore morphology of water can be changed from originally lamellar to rectangular or cellular with distinctive faceted pores [97, 100, 101].

Furthermore, the direction of the thermal gradient governs the orientation of the pore channels. In contrast to random quenching which results in colonies of locally aligned pores without any long range order, controlling the direction of freezing allows to generate axial, radial or even mixed orientations [102, 103]. In the case of uniaxial freeze cast structures, pore channels run straight through the entire sample and result in a tortuosity close to 1. In addition, templating the cold surface to create specific topographies or locally manipulating the temperature gradient allows for an additional control of the crystal nucleation and consequently the lamella orientation

[101, 104, 105]. Solid loading and freezing front velocity are further parameters which drastically influence the microstructure. In general, faster freezing leads to smaller pores [15, 103, 106]. For water-based systems this can be empirically described with a simple power law. Since the liquid is removed in the sublimation step, the final porosity is directly related to the volume of liquid in the suspension or solution. Furthermore, the possible pore size depends on the solid loading. While small pore sizes can be obtained with all solid loadings, large pores are only possible with a low solid loading [107].

Combining the factors which influence the microstructure leads to a very large flexibility in terms of the pore structure. Porosity and pore size were found to be adjustable from 5.5 % [108] to 99.88 % [109] and from 0.01 µm [110] to 1200 µm [111], respectively. Furthermore, the physical nature of the pore forming mechanism allows to use a large variety of materials. Besides ceramics such as alumina, zirconia, silicon carbide, silicon nitride, mullite, hydroxyapatite, lead zirconate titanate, titania, chromium carbide, sialon, lithium iron phosphate, yttrium orthosilicate, cordierite, iron oxide and bioglass, metals such as titanium, nickel, copper, iron, tungsten, and various alloys or graphene and carbon nanotubes can be processed [90]. Also, composites containing different material classes have been prepared. Polymers which have been used in freeze casting are e.g. cellulose, chitosan, collagen, gelatin, PLLA, PU, PVA, PS and preceramic polymers [90]. In 2007, Yoon et al. firstly investigated solution-based freeze casting of preceramic polymers [112]. A polycarbosilane dissolved in camphene acts as preceramic polymer and lead to a highly aligned porous silicon carbide sample with a dendritic pore morphology as can be seen in Figure 2.7.
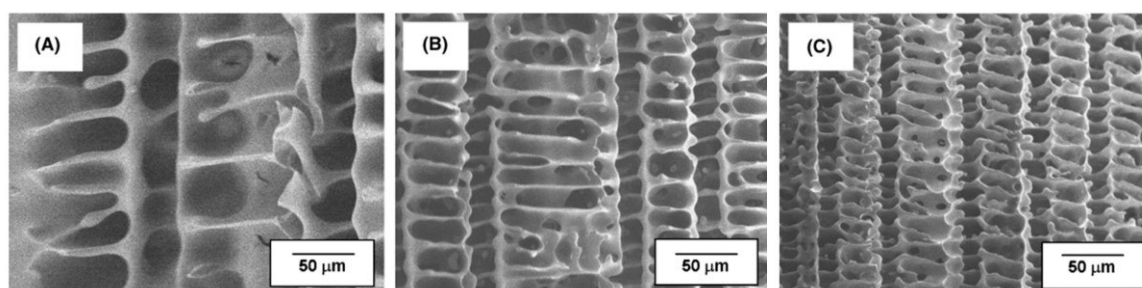

Figure 2.7   SEM images of porous polycarbosilane monoliths prepared at freezing temperatures of (A) 20 °C, (B) 0 °C, and (C) −20 °C at a solid loading of 10 wt%; adapted; Reprint with permission from Wiley [112].

Naviroj et al. changed the preceramic polymer to a polymethylsiloxane and obtained amorphous SiOC [88]. While the two solvents cyclohexane and camphene result in a dendritic structure, *tert*-butyl alcohol creates cellular pores. Furthermore, decreasing the solid loading increases the pore size. Porosity and pore size change from 61 % to 91 % and 4 µm to 32 µm, respectively.

Besides by solution-based freeze casting, polymer-derived ceramics were also prepared by suspension-based freeze casting. Zhang et al. pyrolyzed and ground a polymethylphenylsiloxane in order to increase the hydrophilicity. As a consequence, the received filler particles can be used together with silica sol as a binder in a water-based process [17]. Depending on the pyrolysis temperature and the freezing conditions, a hierarchically-ordered pore structure is obtained. While freezing at −150 °C leads to tubular pores also termed columnar pores, samples frozen at −80 °C and −20 °C display characteristic lamellar macropores. The pore size decreases with increasing freezing rate and ranges from less than 10 µm to 20 µm. Porosity between 45 % and 70 % is achieved by varying the solid loading from 40 wt% to 10 wt%. The presence of meso- and microporosity which results in relatively high BET specific surface area of 47 $m^2{\cdot}g^{-1}$ to 350 $m^2{\cdot}g^{-1}$ is due to the decomposition of the preceramic polymer during heat treatment and the use of silica sol. Details on the bakcground of processing and the characteristics of polysiloxane-based preceramic polymers are given in section 2.1 on pages 4 to 12.

In another study, Zhang et al. changed the preceramic polymer to polymethylsiloxane [20]. Rather than pre-pyrolysis, chemical modification with (3-aminopropyl)-triethoxysilane (APTES) is used to increase the hydrophilicity and enable water-based freeze casting. A ratio of MK:APTES = 1:1 increases the hydrophilicity most efficiently. Additionally, a heat treatment to partially decompose the precursor is necessary. This changes the surface charge from negative to positive which is compatible with the silica sol. A lamellar pore structure with the pore size ranging from 20 µm to 50 µm is obtained as can be seen in Figure 2.8. Depending on the chemical composition, the BET specific surface area and the pore size of the meso- and microporosity are 25 $m^2{\cdot}g^{-1}$ to 130 $m^2{\cdot}g^{-1}$ and 4 nm to 10 nm, respectively.
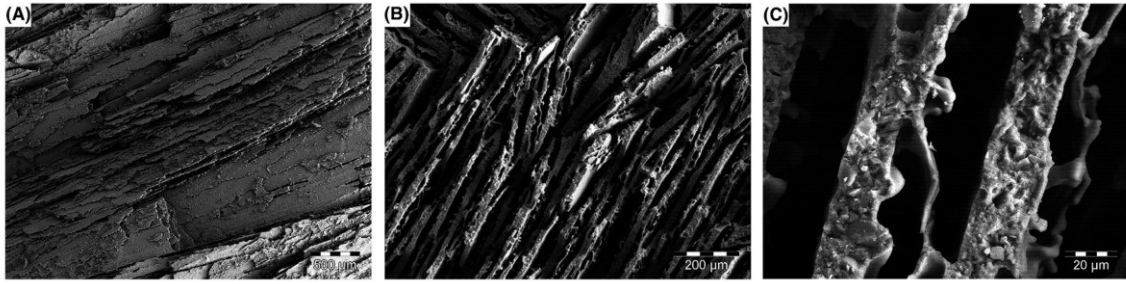
Figure 2.8 SEM images of SiOC monoliths prepared by water-based freeze casting using modified preceramic polymer fillers. (A) Cross section parallel to the lamellar pores, (B-C) cross sections perpendicular to the lamellar pores; adapted; Reprint with permission from Wiley [20].

In contrast to the very smooth pore walls in solution-based freeze casting (Figure 2.9 b), the pore walls in suspension-based freeze casting are rough since they are constructed from particles as can be seen in Figure 2.9 a and Figure 2.8 c.

The literature provides detailed descriptions on the mechanisms of the evolution of the pore structure both for suspension- and solution-based freeze casting of preceramic polymers. However, the impact of microstructural changes on the mechanical properties has only been discussed for suspension-based systems [113, 114]. Such investigations are crucial for the understanding of structure-property-correlations, but they are missing for solution-based freeze casting.
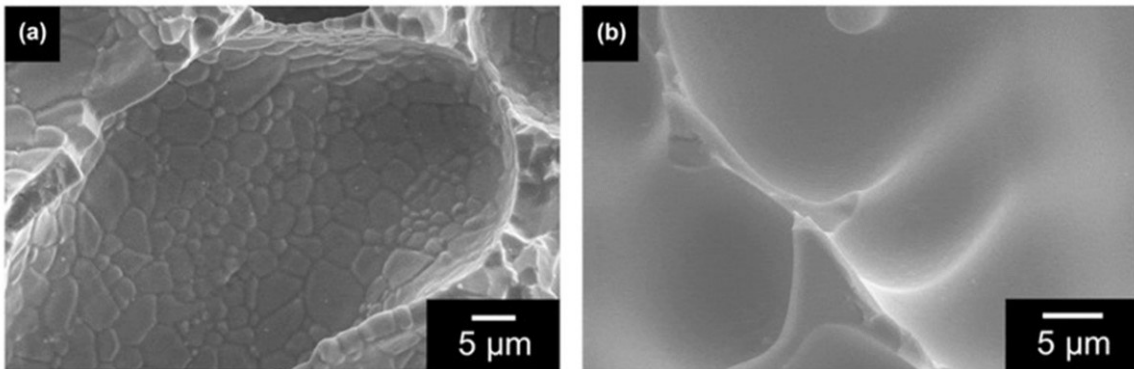
Figure 2.9 Surface morphology of pore walls of (a) sintered suspension-based alumina samples and (b) pyrolyzed solution-based preceramic polymer samples freeze cast with cyclohexane; adapted; Reprint with permission from Cambridge University Press [80].

2.3 Materials for Capillary Transport

2.3.1 Wicking in Porous Media

Many applications in science, industry and daily life rely on porous structures. Liquid flow driven by capillary forces represent such an application. Heat pipes, marker pens, candle wicks and sponges are examples for the wide use of capillary action in daily life as well as in technical settings. In general, imbibition is defined as the displacement of one fluid by another fluid which is immiscible and has a higher viscosity taking place in a porous medium [115].
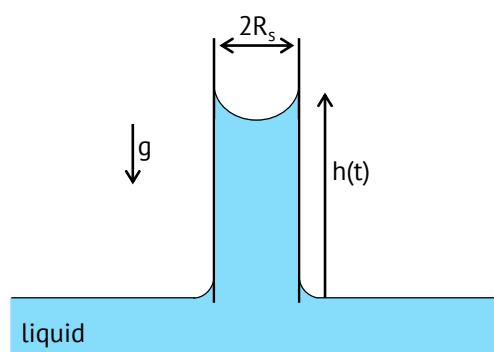
Figure 2.10 Liquid rise in a capillary tube of inner radius R_s. The gravity vector g is parallel to the tube. The height of the liquid column is a function of time and denoted $h(t)$.

If the driving force is the capillary pressure created at the liquid-air interfaces, such an imbibition is called wicking [116]. A schematic of this process is shown in Figure 2.10. Changes in the surface energy of the solid induced by wetting result in a capillary pressure and pull the invading liquid into the porous structure [117]. In general, wicking depends on time, the pore structure and the characteristics of the liquid and the solid [116]. Wettability which is the tendency of a liquid to be attracted by the surface of a solid phase is a main property causing wicking. To quantify wettability, contact angle measurements are performed with high angles indicating bad wettability. In dependence on the specific application and the operating conditions, the required pore size typically ranges from a few micrometers to a few hundred micrometers.

The well-known Young-Laplace equation for capillary pressure in a tube derives from the combination of the force balance of the meniscus in a capillary tube with the capillary pressure.

$$\Delta p = \frac{2\sigma \cos \theta}{R_s} \tag{2.2}$$

where θ is the contact angle, σ is the surface tension and R_s is the static radius which describes the radius of the capillary. Hereby, the capillary pressure originates from the differences in pressure across the interface of two immiscible fluids Δp. The estimation of the static radius might be challenging when using the Young-Laplace equation. Mostly, real porous structure are not composed of a straight bundle of capillaries. Moreover, they are characterized by a complex pore morphology and tortuous, interconnected fluid paths. Several methods to determine the static radius of a complex pore structure have been investigated. Capillary rise experiments are the most accurate method [118]. But also analysis of SEM images with different fitting principles such as fitting of circles into pores was used [119].

Since several hundred years, the maximum achievable height and correlations between time and height are investigated using mathematical as well as physical explanation [120, 121]. The first analytical explanation for the observed velocity of capillary rise was presented by Lucas and Washburn [122, 123]. Both authors provided an analytic solution giving the meniscus height as a function of time with the assumption of a bundle of capillary tubes.

The corresponding Lucas-Washburn equation with gravity effects is derived from the momentum conservation on a single capillary. The capillary pressure is balanced by viscous forces and hydrostatic pressure [116, 123]

$$\frac{2\sigma \cos \theta}{R_s} = \frac{\phi \mu_l \dot{h} h}{K} + \rho_l g h. \tag{2.3}$$

Where σ is the surface tension, θ the contact angle, R_s the static radius, Φ the porosity, μ_l the dynamic viscosity of the liquid, h the wicking height, $\dot{h}$ the interstitial velocity, K the permeability, ρ_l the density of the liquid and g the gravitational acceleration. To improve the consistency with real porous structures, studies on nonuniform capillary tubes e.g. varying in diameter have been conducted [124-126]. Further studies added missing or neglected terms to the momentum balance.

Apart from the Lucas-Washburn approach, another method to determine the viscous friction losses is proposed. This alternative bases on Darcy's law and is not using the capillary tube analogy [127]. The Darcy law is given as [128]

$$\frac{\Delta p}{\Delta L} = -\frac{\mu}{K} u_s.$$

(2.4)

with the pressure drop Δp, the length ΔL, the permeability K, the dynamic viscosity μ and the superficial velocity u_s. Wicking is seen as a single-phase flow through the porous medium [129]. An analytic model based on this approach shows good accordance of modeled wicking rates with wicking experiments on a metallic weave [130]. However, complex pore structures need to be described by only one constant. Merging several geometry parameters into a single constant which should reliably represent the structure is challenging.

Due to increasing performance of computers, it has become possible to numerically solve differential equations or to perform simulations of capillary transport. One example to model capillary transport is the control volume approach. This integral method allows to balance properties such as mass, energy and momentum inside the control volume [131, 132]. However, the boundary conditions need to be carefully selected, e.g. the assumption of constant fill level of the reservoir. Especially the consideration of the momentum balance enables to derive the governing equation of capillary motion. The resulting full linear momentum balance contains all known terms to describe the movement of the meniscus [133]. Following terms are represented in the full linear momentum balance: the local acceleration of the liquid inside the tube, the capillary pressure, the local acceleration of the liquid below the tube, the viscous losses below the tube, the convective flow losses at the entrance of the tube, the viscous losses in the tube, the hydrostatic pressure and a term describing the entrance function.

The high complexity of the control volume approach can be reduced by neglecting certain terms which only have a minor impact on the result for certain experimental conditions. For small capillary radii, entry effects can be neglected. As a consequence, the total viscous pressure loss is given by the Hagen-Poiseuille law and the viscous friction force can be simplified. Furthermore, a constant capillary pressure with a constant contact angle can be assumed. The viscous and local acceleration terms in the liquid reservoir can be neglected since they are typically small compared to the

losses in the tube. To conclude, in the simplified momentum balance, the capillary pressure is balanced by the sum of inertia, viscous and hydrostatic forces [133]. While inertia, viscous and hydrostatic forces depend on the wicking height, the capillary pressure is constant.

When investigating wicking not by means of simulation and modelling but experimentally, several potential sources of measurement errors have to be considered. Though the contact angle should be constant during the wicking, deviations were found involving spreading liquids and higher angles as expected during the experiment [134, 135]. Additionally to this issue, the microstructure of porous media can show great variations. While most models to describe capillary flow assume a capillary with constant diameter, this is only valid for a few experimental cases. Consequently, the determination of the correlation between porous medium and wicking rate is very challenging [136].

Most experimental research on capillary transport was conducted on metal weaves, fabrics and polymers. But also capillary action in porous nonmetallic inorganic materials was tested. For example, the capillary rise of liquid silicon in a carbonaceous preform with a pore size from 2 μm to 10 μm was investigated [137]. The evaluated effective pore radius is one to two orders of magnitude lower than the particle size, the particle spacing and the average pore size. When considering the varying pore sizes by using a two-sized single pore model, the predicted infiltration is consistent with the experiment. Additionally, the prediction of the effect of pore closure due to reactive capillary infiltration is in agreement with experimental data. Another study investigate the capillary rise of organic liquids into an interconnected capillary system made of 3D-stitched C-C preforms with an average pore size of 8.6 μm [138]. Since, the existing models for infiltration base on straight capillaries and are not able to predict imbibition into interconnected systems, a two-pore capillary infiltration model was proposed and validated by experimental data. This modified Washburn equation takes the bimodal pore size distribution obtained by the fabrication method into account. Experimentally determined kinetics of the infiltration with Si are in good correlation with the model. Furthermore, the formation of silicon carbide during infiltration was incorporated in the model [139]. Additionally, it was found that though the capillary pressure is governed by the larger pores and the infiltration is controlled by all pores.

Wicking in porous mullite obtained by an extrusion method and with average pore sizes of 10 μm and 16 μm shows a good agreement with a model which describes the viscous and gravitational time stage of wicking [140]. However, the effective pore radius is considerably smaller than the average pore radius measured by mercury intrusion porosimetry. Another study on a similar mullite structure found higher equilibrium heights and an increasing equilibrium height with decreasing pore size [141]. While the calculated effective pore radii are very similar, the calculated contact angle increases with decreasing pore size. As observed in the study described before, the effective pore size is significantly smaller than the experimentally obtained pore size.

In porous geopolymers with pore sizes from 0.5 μm to 2.5 μm, the capillary rise rate was found to increase with increasing fiber volume and higher fiber diameter [142]. Increasing fiber volume is thought to result in better connectivity of the cylindrical pores. Again, the effective pore radius is smaller than the experimentally obtained one. High tortuosity is supposed to cause the deviation between the pore sizes.

So far, only one study investigated wicking into porous polymer-derived ceramics. Grebenyuk et al. used cylindrical SiOC monoliths prepared by suspension-based freeze casting with water as dispersion liquid [143]. A radial orientation of the pores is created by the freezing process. The pore size of the anisotropic lamellar pore structure changes at a constant porosity from 12 μm to 20 μm. Further, increasing pore sizes increase the permeability. Additionally, the anisotropy of the pore structure leads to orientation dependent permeability and wicking rate. Furthermore, the influence of the anisotropy is larger for smaller pores. The comparison of the experimental wicking data with a theoretical prediction using the Lucas-Washburn equation with gravity effects shows a good agreement in both axial directions. Though this findings imply applicability of macroscopic modelling, it requires a precise directional characterization of the macroscopic parameters of a porous structure [143]. A drawback which was detected in this study is the poor mechanical stability of the suspension-based structures. The composition of only particles is thought to be the reason for the poor mechanical stability. Crack formation, spalling or even complete failure of the component is not acceptable since fragments of the structure can contaminate the liquid, cause blocking and hamper the wicking performance.

Although some research was already done on wicking, the influence of the pore morphology as well as the impact of varying the parameters of a complex pore structure are not sufficiently investigated yet. For the application of complex pore structures which are not reflected by the capillary bundle model, it is crucial to know the relation between pore structure and capillary performance. Furthermore, the improvement of the mechanical stability to a reasonable level is worthwhile to ensure a reliable liquid transport. Also other applications such as filtration would benefit from enhanced strength.

2.3.2 Cryogenic Wicking

Generally, the field of cryogenics is only loosely specified. However, usually a cryogenic liquid is defined as a substance which exists as liquid at very cold temperatures and as a gas at room temperature [144]. Since "cold" is a relative word, liquid nitrogen is normally used as the standard cryogenic liquid. Its boiling point is 77.4 K. Besides liquid nitrogen, liquid hydrogen, liquid oxygen and liquid methane are the fundamental cryogenic liquids. Compared to capillary action at room temperature, wicking at cryogenic temperature poses additional requirements on the materials. Besides the mass transport, the heat transport is a critical factor which needs to be considered. Hence, not only the pore structure but also thermal properties of the porous media are important for wicking at cryogenic conditions [133, 145].

One application of porous structures is the loop heat pipe which is a heat transfer device using two phases. As active structure, a wick in the evaporator circulates the working fluid. Loop heat pipes are required in the thermal management for various technical processes. Liquid oxygen was used as working fluid in a cryogenic loop heat pipe at temperatures between 65 K and 140 K for the investigation of the cooling performance [146]. The wick consists of stainless steel with a resulting pore size of 2.4 μm. 9 W are transported and reliable start as well as operation with the shrouds at room temperature is achieved. Furthermore, the wicking of sintered stacked layers of metallic meshes with a pore size of 5 μm was tested with liquid nitrogen in an open liquid nitrogen bath [147].

Another example for application of wicking at cryogenic conditions is fuel delivery in propellant management devices for spacecraft. Main difficulties are the necessity of large and thick walled tanks, costly insulation to avoid parasitic heat leakage and boil-off of precious propellant. Besides these aspects, vapor free liquid transfer from the propellant tank to the engine is a critical process in using liquid propellants. Low surface tension and the low boiling point complicate this task of separating vapor from liquid. Several structures have been developed in order to ensure vapor free propellant supply. For example, vanes and sponges are composed of an array of fins or plates made from ultra-thin, lightweight metal [144]. In contrast, screen channels are defined as closed channels with three solid walls and one porous wall as can be seen schematically in Figure 2.11 [144]. Typically, metallic meshes act as the capillary active component and a network of porous gallery arms runs through the tank. Compared to vanes and sponges, screen channels provide a much more robust phase separation over a wider range of thermal and gravitational conditions as well as larger possible flow rates [144].
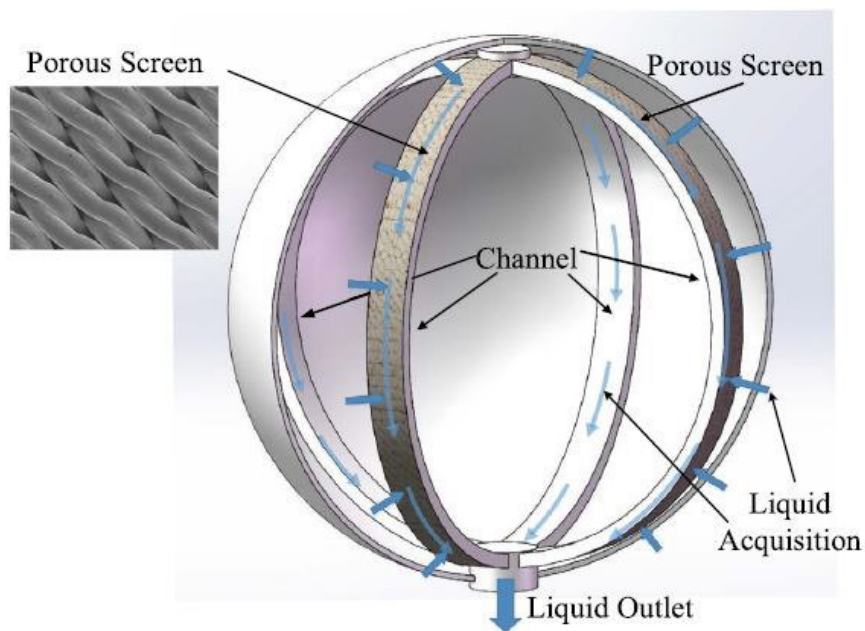

Figure 2.11 Illustration of a screen channel liquid acquisition device; Reprint with permission from Elsevier [148].

Generally, the screens are chosen according to the specific mission requirements such as gravitational and thermal environments and demanded flow rate. The properties of the screen such as the number of pores, the size and the manufacturing style are defined by the screen weave. Fine meshes ensure a good resistance to vapor ingestion, but tend to generate a large pressure loss. Usually, the pore sizes are tens of micrometers [130, 145, 149]. Channel design and channel mass are also affected by the applied metal. While coarse meshes can be produced with several metals such as titanium and aluminum, fine meshes are only available in heavier metals such as stainless steel. Often, a trade-off between performance and system mass is necessary.

The influence of different mesh sizes on the wicking performance of metallic wicks was investigated [130]. Pores in the range of 10 µm to 166 µm were obtained by changing the parameters of the weave. Another study compared cryogenic wicking into a metallic mesh with a pore size of 14 µm with modeled results and found good accordance between the experimental data and the Lucas-Washburn equation [149].

Although screens are the most performant liquid acquisition devices, some drawbacks have to be considered. Besides the delicacy reduce the reliability, fine meshes cannot be manufactured using light weight metals. Consequently, the necessity of large gallery arms leads to a very high system mass which is contradicting to light weight design in aerospace. Hence, materials with a lower density are discussed to replace the metallic meshes in cryogenic wicking. Additionally, properties such as the corrosion resistance are crucial for applications where the cryogenic liquid is in direct contact with the material. Consequently, ceramic materials which are characterized by high strength, low density, high corrosion resistance and low thermal conductivity begin to drawn attention to be used in capillary applications at cryogenic conditions [150]. The wicking performance of glass frits was tested on lab scale at cryogenic conditions with liquid nitrogen as test fluid [151]. For wicking into superheated samples, it the imbibition rate is greatly affected by the vapor flow. Due to the heat transfer between the liquid and the porous structure, vapor which is created above the wicking front slows down the imbibition. This effect gets more relevant with increasing size and superheating of the porous structure. These results suggest that the control of the heat transfer in porous structures highly affects the imbibition rate. Hence, materials with low thermal conductivity are fundamentally interesting to optimize the wicking performance.

2.4 Heterogeneous CO₂ Methanation

2.4.1 Thermodynamic and Kinetic Analysis

Sabatier and Baptiste first described the methanation of carbon dioxide [152]:

$$CO_2 + 4\,H_2 \rightleftharpoons CH_4 + 2\,H_2O \qquad \Delta_R H_{298} = -206\ \text{kJ·mol}^{-1}$$

$$\Delta_R G_{298} = -142\ \text{kJ·mol}^{-1}$$

(2.5)
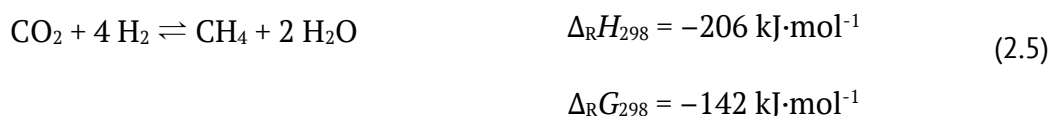
The reaction is strongly exothermic and shows a strong reduction in volume by 40 %. Hence, from a thermodynamic point of view and according to Le Chatelier's principle, high pressures and low temperatures are beneficial to obtain high carbon dioxide conversions. Besides the methanation reaction, several side reactions are possible involving the participating species. Methane dry-reforming, reverse water-gas-shift, Boudouard reaction, carbon dioxide reduction and chain growth are possible reactions forming further products such as carbon monoxide, carbon and hydrocarbons [153-156]. As a consequence, a complex gas-solid system has to be considered when investigating the CO₂ methanation. To find suitable operating conditions, usually numerical methods are applied to choose temperature, pressure and feed ratio. Concerning the feed ration, the carbon dioxide fraction in the product stream decreases with increasing feed ratio ($H_2:CO_2$) and approaches zero at the stoichiometric feed ratio of 4 [157]. At temperatures higher than 400 °C, the reverse reaction limits the carbon dioxide conversion into methane as can be seen in Figure 2.12.
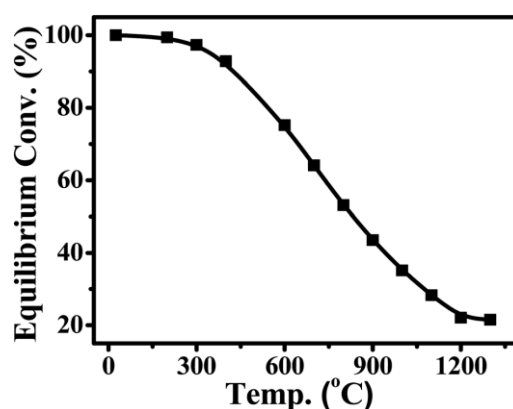

Figure 2.12 Equilibrium conversion of carbon dioxide in methanation at different temperatures; Reprint with permission from Royal Society of Chemistry [158].

Carbon monoxide formation which is relevant at temperatures higher than 600 °C reduces the carbon dioxide fraction [157]. In summary, a feed ratio of 4 should be maintained and when operating at 10 bar the temperature should be restricted to 400 °C [157]. Due to the strong volume contraction, reducing the pressure to 1 bar also lowers the maximum temperature to 300 °C [157]. Though thermodynamics do not predict carbon monoxide formation at low temperatures, dissociative adsorption of carbon dioxide at the surface may lead to the formation of carbon monoxide. Furthermore, the accumulation of solid carbon at feed ratios of 4 is thermo-dynamically not favorable due to the excess of hydrogen. However, pore diffusion effects which affect carbon dioxide more than hydrogen can result in locally depressed feed ratios during the reaction. At feed ratios below 3, the formation of solid surface carbon is thermodynamically favorable and leads to the deactivation of the catalysts [157].

Although the CO_2 methanation is exothermic as well as exergonic, kinetical limitations avoid that the reaction proceeds spontaneously. Thus, the use of catalysts is required to ensure acceptable reaction rates. In the course of the reaction, the transfer of eight electrons is necessary [159]. Though a lot of research was conducted, the mechanism of the CO_2 methanation is still not fully understood and two different routes were proposed [160, 161].

The dissociative mechanism assumes the dissociation of carbon dioxide at the metal-support interface to adsorbed carbon monoxide. The following steps are the reduction to surface carbon and subsequently the conversion to methane according to the steps of carbon monoxide methanation [162-165]. On the other hand, the associative mechanism proposes the formation of formates after non-dissociative adsorption of carbon dioxide at the support [166-168]. Hence, no carbon monoxide is generated as intermediate species. The published data suggest that the CO_2 methanation most likely proceeds according to the dissociative mechanism. However, contradicting results on the investigation of the rate-determining step and its relevant temperature range were published. Most studies found that the dissociation of adsorbed carbon monoxide is rate-determining [160, 169]. Sulfur poising and thermal sintering at temperatures higher than 500 °C are supposed to be the main deactivation mechanisms [160]. In contrast, deactivation by carbon formation on the surface of the catalysts is less likely.

2.4.2 Catalysts

The group VIII metals such as ruthenium, iron, nickel and cobalt are typical methanation catalysts. Regarding the activity, the following order is reported: Ru > Fe > Ni > Co [170]. In terms of the methane selectivity, the proposed order is: Ni > Co > Fe > Ru. Since nickel provides the best compromise between methane selectivity and activity on the one side and costs as well as availability on the other side, it is the preferred catalysts, especially for technological applications.

Besides the metal, three main factors are determining the catalytic performance: the metal-support interaction, the surface properties of the support and the metal particle size. The most used supports are: alumina, silica, zirconia, titania, ceria and zeolites [158]. The catalytic properties of heterogeneous catalysts are sensitive to the interaction between the oxidic support and the active metal [171-174]. The M^+ or O^{2-} sites of the support and metal sites of the active metal stabilize the key intermediates such as adsorbed carbon dioxide and formates [175]. Oxygen vacancies in ceria were found to activate the chemisorbed carbon dioxide and generate carbon monoxide intermediates in a ceria-supported nickel-based catalyst [176]. While ruthenium-supported on ceria shows a similar reaction mechanism with the formation of carbon monoxide via formates and carbonates, changing the support to alumina alters the reaction mechanism to carbon dioxide dissociation [177]. These results indicate that surface oxygen vacancies e.g. of ceria, allow the interaction with carbon dioxide and facilitate the hydrogenation reaction. Furthermore, the ability of a support to ensure an appropriate coverage and strong adsorption of carbon monoxide allows for hydrogen dissociation and consequently superior catalytic behavior [178]. Due to its reducibility, ceria is the most suitable support for ruthenium [178]. In contrast, irreducible alumina limits the co-adsorption of hydrogen and reducible zinc oxide only weakly adsorbs carbon monoxide which leads to the reverse-water gas shift reaction.

Not only the presence of oxygen vacancies and the reducibility are important. The special metal-support interaction between cobalt and zirconia enables the redistribution of cobalt on the surface of zirconia. This was reported to be the reason for Co/ZrO$_2$ catalysts being more active and more stable compared to Co/Al$_2$O$_3$ catalysts [179]. Besides the chemical composition of the supports, an influence of the phase composition was found for titania-supported catalysts. When rutile and

anatase are present, Ru particles tend to migrate towards the rutile phase during the reaction [180]. As a result, ruthenium is highly dispersed in the reduced phase and leads to a superior catalytic performance. A similar mechanism is documented for Ni/ TiO_2 catalysts [181].

Also the surface properties are affecting the methanation reaction. The adsorption capability towards carbon dioxide which can be influenced by the surface basicity is crucial for providing activated carbon dioxide molecules [158]. The addition of other transition and rare earth metals makes it possible to alter the surface basicity. Tungsten and lanthanum are reported to drastically improve the catalytic activity and stability of a Ni/MgO and Ni/Mg-Al catalyst, respectively [182, 183]. By increasing the surface basic sites, tungsten improves the carbon dioxide stabilization and promotes the reaction of adsorbed carbon dioxide to monodentate formate which is suggested to be the key intermediate. Additionally, it strengthens the interaction between nickel and magnesium [182]. Further metals which have been successfully used to enhance the basicity of nickel-based catalysts are lanthanum, cerium, samarium and praseodymium [184].

Finally, also the metal particle size is an important factor. Most studies report on higher selectivity towards methane with increasing nickel size [185-187]. For both, noble and non-noble metal-based catalysts, atom-scale structured catalysts tend to facilitate the reverse-water gas shift reaction. In contrast, larger metal particles favor methane formation. Investigations on Ir/CeO$_2$ catalysts reveal that small metal particles are partially oxidized and show selectivity towards carbon monoxide formation. On the other hand, large iridium particles resulting in a preference for methane generation. The metal particle size essentially influences the electrochemical state of the metal and consequently determines also the reaction route. However, there is also research reporting on higher carbon monoxide selectivity with increasing nickel size [188]. The proposed mechanism bases on the carbon monoxide dissociation at highly uncoordinated sites which are present on the steps of nickel [189]. Strong carbon monoxide adsorption at edges could enable direct methanation of carbon dioxide. Contrary, nickel faces mainly produce carbon monoxide due to the desorption of carbon monoxide before the hydrogenation to formates. As smaller nickel particles are supposed to exhibit a larger quantity of uncoordinated sites, their selectivity towards methane is higher.

2.4.3 Heterogeneous Monolithic Catalysis

Heterogeneous catalysts are composed of an active component which is typically deposited on an oxidic support. Usually, metals are acting as active components. The support ensures the stabilization of the nanometer-sized metal clusters and typically exhibits a high specific surface area of several $100 \, m^2 \cdot g^{-1}$. Nowadays, many technological applications rely on packed bed reactors which consist of mesoporous catalyst pellets or extrudates filled into the reactor tubes. Consequently, a random bed of loosely packed milli- or centimeter-sized catalysts pellets is created. The pellets provide easy handling of the catalysts. Size and shape of the pellets strongly influence heat, mass and momentum transport in the reactor. For example, small pellets create a higher pressure loss compared to large pellets.

Besides the pressure loss, the handling of significant heat and mass fluxes is necessary especially for exo- and endothermic reactions. Though heat and mass transport was improved by optimizing modern catalysts, several important catalytic reactions are still limited by either mass or heat transport. Due to their promising heat and mass transport properties, monolithic catalysts are of interest for optimizing catalytic performance.

In contrast to pellets, monolithic catalyst support have the same diameter as the reactor. Honeycombs, solid sponges and cross-flow structures are used as monolithic catalyst supports [190-193]. The difference between sponges and pellets in terms of geometry and dimension is illustrated in Figure 2.13. Depending on the specific application and the operating conditions, the pore size typically ranges from 100 µm to several millimeters and the porosity varies between 70 % and 95 % Metals as well as ceramics are used as monolithic catalyst supports. In contrast to metals, ceramics offer advantages such as better thermal stability, low thermal expansion coefficient and good coating adherence [194, 195]. While monolithic catalysts are already applied commercially for exhaust treatment, their application in the chemical industry is still part of intensive research. In order to increase the surface area, monolithic catalysts are usually covered with a micrometer-sized layer of a washcoat which exhibits a specific surface area in the order of several $100 \, m^2 \cdot g^{-1}$. γ-Alumina slurries are widely used as washcoat applied by different methods such as colloidal coating, slurry coating and sol-gel processes [196]. Several parameters of the coating process e.g. the particle size, the calcination temperature, the solid loading, intermediate layers,

additives/binders and the thermal or chemical pretreatment influence the adhesion of the washcoat [197-201]. Subsequently, the catalytic active metal is deposited onto the monolith by wet impregnation or deposition-precipitation [196] [202]. Usually, a dip coating process is used. Alternatively, mixing the active component into the washcoat allows for a one-step process.

Figure 2.13 Examples of catalysts supports in heterogeneous catalysis. Background: solid mullite sponges with decreasing pore window size from left to right. Foreground: alumina pellets [157].

Compared to pellets, a low pressure loss is provided by the regular geometry of honeycombs and the high porosity of solid sponges. In general, the continuous solid network of monolithic catalysts which have the same diameter as the reactor tube ensures high heat fluxes via thermal conduction. Sponges allow for increased fluid mixing which improves the transfer of heat between solid and liquid. Additionally, they exhibit higher specific surface area and enable radial flow compared to honeycombs. The separation of catalytic activity from heat and mass transport is a major advantage of coated monolithic catalysts. While the catalytic washcoat determines catalytic activity, selectivity and efficiency, the support influences heat and mass transport as well as pressure loss.

However, drawbacks of using a washcoat are the necessity of a two-step process with additional costs and the potential risk of spalling of the washcoat and crack formation. Especially for varying temperatures and differences in the thermal expansion coefficient between washcoat and support, flake-off of the catalytic layer has to be considered. Potential consequences are the degradation of the catalyst efficiency and the damage of downstream equipment [203-205]. Additionally, abrasive conditions such as high gas velocity or the presence of particles in the stream may lead to deactivation due to erosion of the washcoat [190].

A monolithic catalysts which consists of a high surface area material and has an inherent catalytic activity due to an incorporated active phase could overcome the problem of low washcoat adhesion. For zeolite-based monoliths, this approach was already investigated. In general, zeolites are the active component in applications such as adsorption, selective catalytic reduction of nitrogen oxides and petroleum-based catalytic applications e.g. hydrocracking and isomerization [196, 206]. Zeolite monoliths are typically prepared by the extrusion of a slurry and subsequent drying and sintering [207]. Adapted processing allows to waive the binder and thus avoid potential pore blocking due to excessive binder [208]. Lower susceptibility to abrasion was found for extruded zeolite structures compared to coated monoliths [209]. Besides zeolite structures, monolithic carbon materials have been produced by extrusion [210]. Carbon can act as adsorbents and as gas storage media [211]. Typically, a mixture of a carbon precursor, a binder and a plasticizer is extruded followed by drying and carbonization [212]. To improve the mass transfer and reduce the pressure drop, additional meso- and macroporosity can be introduced by adapting the extrusion process [213]. Pore sizes of 2 nm to 4 nm and 0.5 µm to 30 µm can be achieved. As alternative shaping route, the impregnation of sacrificial templates allows to further alter the pore structure. Porous silica monoliths and polymeric foams have been used as templates which form pore sizes in the range of 15 µm to 100 µm [214, 215]. Additionally, catalysts with a pore size of approx. 2 mm which contain oxides of titanium, vanadium and tungsten and sepiolite as an agglomeration agent were extruded and tested in selective catalytic reduction at industrial conditions [216, 217]. Also, a catalyst based on W/TiO_2, bentonite, glass fibers and small amounts of methylhydroxyethylcellulose and polyethyleneglycol was extruded and showed an average pore size of 9 µm [218].

As described, monolithic catalysts with inherent catalytic activity exhibit a high potential compared to coated structures under certain reaction conditions. Given the high potential, the investigation of such structures in reactions besides selective catalytic reduction, hydrocracking and isomerization is promising and would open up new applications. The CO_2 methanation is worthwhile to investigate as it plays a key role in using renewable energy in the power-to-X technology. In order to match the requirements of the desired reaction, the optimization in terms of the active component and the shaping method is necessary.

2.5 Characterization Methods

The following chapter provides background information on characterization methods which have been used in this work. Detailed descriptions of the procedures can be found in the corresponding experimental parts of chapter 4 to 7 (4.3.3 on page 68, 5.3.3 on page 92, 6.3.3 on page 124 and 7.3.3 on page 147). For information on common and widespread methods such as scanning electron microscopy (SEM), transmission electron microscopy (TEM), thermogravimetric analysis (TGA) and x-ray diffraction (XRD), the reader is referred to relevant literature.

2.5.1 Nitrogen Adsorption/Desorption

In general, the adsorption and desorption of gases is a volumetric method to determine the specific surface area. Besides other gases such as argon and krypton, nitrogen is the most frequently used adsorptive in adsorption/desorption measurements [219].

Starting from vacuum and at constant temperature of 77 K, multiple well defined doses of gaseous nitrogen are consecutively injected into the sample chamber. Depending on the pressure and the available surface area, nitrogen molecules partially adsorb on the sample surface. At equilibrium conditions, the amount of adsorbed nitrogen molecules is proportional to the gas pressure. The equilibrium pressure for each dose is recorded and the adsorbed volume of nitrogen is finally plotted versus the relative pressure as isotherm. The resulting plots are called isotherms. Usually, standard temperature and pressure (0 °C and 101.3 kPa) are used to plot the amount of adsorbed nitrogen. Hereby, the relative pressure is defined as the pressure divided by the saturated vapor pressure of nitrogen at 77 K.

According to the International Union of Pure and Applied Chemistry (IUPAC), 6 main classes and 2 subclasses of exemplary isotherms can be distinguished as shown in Figure 2.14 [219]. Type I isotherms are reversible and indicate microporous solids with a relatively small external surface. While the subclass I(a) results from microporous materials with narrow micropores (< 1 m), subclass I(b) is found for materials which have a wider range of pore sizes (< 2.5 nm). Nonporous or macroporous adsorbents cause reversible Type II isotherms. A sharp point B corresponds to the completion of monolayer coverage. However, no identifiable monolayer formation is obvious in

Type III isotherms. Hence, the adsorbent-adsorbate interactions are relatively weak and the nitrogen molecules are clustered at favorable surface sites. Type IV indicates mesoporous material. Followed by the initial monolayer-multilayer adsorption which is also present in Type II isotherms, pore condensation takes place. The presence of a hysteresis in Type IV isotherms depends on the adsorption system and the temperature. For nitrogen, following dependencies have been found: pores wider than 4 nm cause hysteresis (Type IV(a)) and smaller pores create complete reversible isotherms (Type IV(b)). Type V isotherms represent a combination of weak adsorbent-adsorbate interactions with molecular clustering at higher relative pressures. Furthermore, layer-by-layer adsorption on highly uniform nonporous surfaces causes Type IV isotherms. [219]
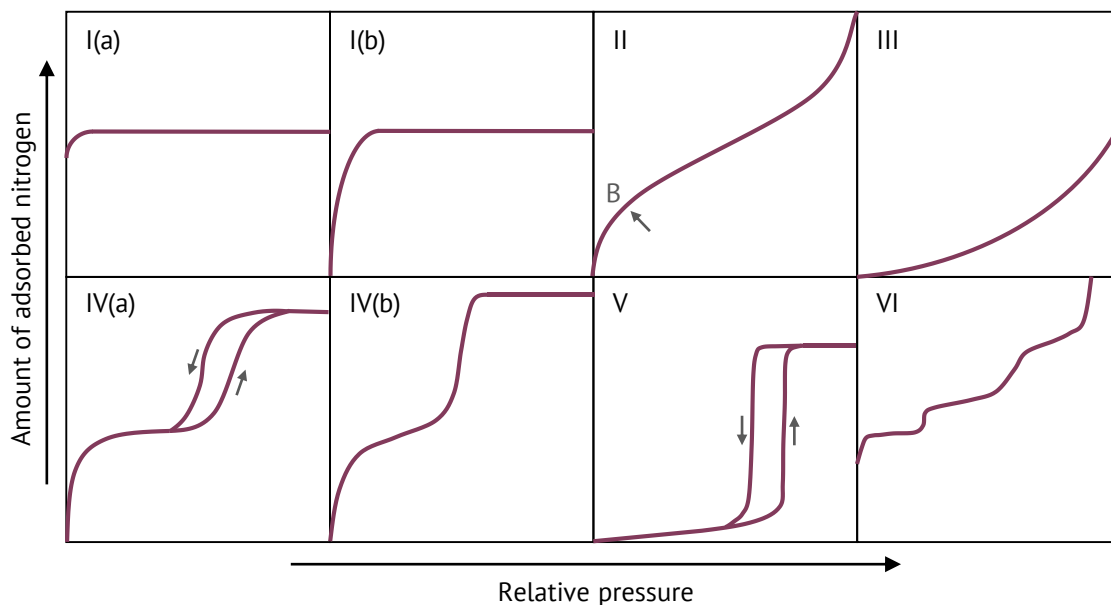
Figure 2.14   Classification of physisorption isotherms according to IUPAC.

Typically, nitrogen adsorption and desorption isotherms are used to calculate the specific surface area (SSA). The specific surface area is generally defined as the total surface area of a solid per unit of mass or volume. The method according to Brunauer-Emmet-Teller (BET) is widely applied to determine the specific surface area. Based on kinetic considerations of monolayer adsorption, this model describes a multi-layer adsorption of gas molecules on solid surfaces. Several assumptions have to be introduced to apply the concept of mono-layer adsorption to multi-layer adsorption. First, gas molecules are assumed to adsorb on the solid surface in an infinite number of layers. All higher layers are equivalent to the liquid state and for each layer the

theory of mono-layer adsorption is valid. Furthermore, single layers do not interact with each other as well there is no interaction between molecules within a layer. Additionally, the adsorption sites are independent of its neighbors [220]. In accordance with the described assumptions and for a constant temperature, the following equation correlates the adsorbed volume of gas with the relative pressure:

$$\frac{p}{v(p_0 - p)} = \frac{1}{v_m C} + \frac{C-1}{v_m C} \frac{p}{p_0} \tag{2.6}$$

where v is the specific adsorbed volume, v_m the specific volume of a mono-layer, C a constant which is associated with the heat of adsorption, p the pressure and p_0 the saturated vapor pressure of nitrogen. Plotting $\frac{p}{v(p_0-p)}$ versus the relative pressure $\frac{p}{p_0}$, the intercept is given by $\frac{1}{v_m C}$ and the slope is $\frac{C-1}{v_m C}$ [221]. Linear regression can yield the constant C as well as the specific volume of a monolayer v_m. The correlation of the specific volume of a monolayer with the density of nitrogen ρ_{N2}, the molecular mass of nitrogen M_{N2}, the average area which is occupied by an adsorbed nitrogen molecule $S_0 = 0.162$ nm^2 [222] and the Avogadro Constant N_A, leads to the specific surface area a_{spec}:

$$a_{spec} = v_m \frac{\rho_{N2}}{M_{N2}} N_A S_0 \tag{2.7}$$

For common adsorbents, including nitrogen the BET plot usually gives a good regression at relative pressures between 0.05 and 0.35. Nevertheless, the starting and ending point of the BET evaluation should be carefully selected depending on the material type [220, 222]. Details on the test parameters are presented in the sections 4.3.3 (see page 68) and 7.3.3 (see page 147).

2.5.2 Mercury Porosimetry

The volumetric pore size distribution over a wide range of pore sizes can be analyzed by means of mercury intrusion porosimetry [223]. Various materials can be tested with this method. Originally, the mercury porosimetry was developed to extend the evaluation of pore sizes from micro- and mesopores to the scale of macropores.

Since mercury has a high surface tension with a mean contact angle on ceramic surfaces of approx. 140°, it is considered a non-wetting liquid [222]. Thus, mercury does not spontaneously imbibe into porous media. The required external pressure

which is necessary to force mercury into the pores depends on physical properties of the mercury and the solid as well as on the pore size [224]. As a result of his studies on capillary flow and capillary forces, Edward Washburn described the relationship between pore size and pressure in the case of intruding mercury into a capillary as schematically shown in Figure 2.15 [123]. The evaluation of mercury intrusion data relies on this fundamental relation, called Washburn equation:

$$R = -\frac{2\sigma \cos \theta}{\Delta p} \tag{2.8}$$

where R is the pore size, σ the surface tension of mercury, θ the contact angle and Δp the external pressure. The Washburn equations includes several assumptions. First, cylindrical shape of the pores. Additionally, it is assumed that pores are filled in decreasing order of the size. In well interconnected pore networks this assumption might be valid. In contrast, low interconnectivity mostly results in this assumption to be invalid. In addition, narrow pore windows with wider pore diameter cause the overestimation of pore volume assigned to smaller pores. This aspect is called the ink-bottle effect [224, 225].
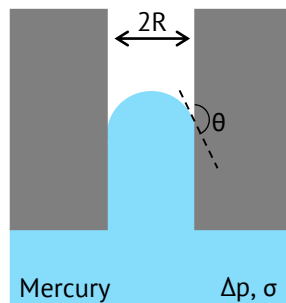
Figure 2.15 Schematic illustration of mercury penetration into a capillary and specification of the important physical parameters.

Further potential reasons for inaccuracy are the compressibility of mercury, the distortion of the measurement cell at high pressures and the compressibility and/or damaging of the sample. Additionally, the contact angle of mercury is strongly influenced by impurities, the material surface and whether it is penetrating or withdrawing. Hence, a range from 117° to 141° with a resulting uncertainty of 20 % on the pore size evaluation was found in literature [225, 226]. In this work, a constant contact angle of 140 ° was used. On the one hand, this ensures a good comparability of samples with similar chemical compositions as it is the case in this work. On the

other hand, the results presented in this work may differ from analysis which were performed at different conditions and/or with different devices. The sections 4.3.3 (see page 68), 5.3.3 (see page 92), 6.3.3 (see page 124) and 7.3.3 (see page 147) give more details on the applied device.

2.5.3 Vapor Adsorption

The chemical state of the surface and the presence of functional groups influence the interaction of the material with the environment. In this work, the interactions with water and heptane are taken as a measure for the surface characteristics. Usually, the hydrophilicity/hydrophobicity is characterized by means of contact angle measurements. However, a major drawback of the contact angle measurement is the sensitivity to the presence of pores and the roughness of the surface [227].

Vapor adsorption measurements with polar and unpolar liquids are an alternative to determine the hydrophilicity/hydrophobicity. This simple gravimetric method records the weight change of a dry sample which is put in contact with the vapor of a probe liquid at a certain pressure. The probe molecules adsorb on the surface and cause a weight gain. Polar liquids such as water are used as probe for hydrophilicity, whereas unpolar liquids such as *n*-heptane act as a measure of hydrophobicity. By comparing the adsorbed amount of probe molecules, the sample can be characterized to be more hydrophilic or more hydrophobic. Another way of evaluation is the normalization of the adsorbed amount of molecules on the BET specific surface area. Further details on the measurement procedure are given in sections 4.3.3 (see page 68) and 7.3.3 (see page 147).

2.5.4 Compressive Strength

Due to the brittle nature accompanied with weak tensile strength, structural ceramic components are usually applied under compressive conditions [228]. Hence, the mechanical properties are normally evaluated in bending and/or compression tests.

The fracture of porous ceramics can be generally described by the quasi-brittle behavior. Reasons for this classification are: the ultimate fracture is triggered by many local events and highly dissipative processes associated with plastic deformation are not present [229]. In porous ceramics, the mechanical behavior

depends on more than just the porosity. Experimental studies on the mechanical strength of porous ceramics have reported significant deviations from the widely used Gibson and Ashby model which correlates the relative strength to the relative density [229]. Especially, the number of connecting struts between the pores was found to highly impact on the mechanical response [229]. After breaking of the connecting struts, even increasing the strut thickness is not recovering the initial strength. As a consequence, factors such as the applied shaping method, the strut density and the pore morphology highly influence the mechanical properties.

A typical stress-strain curve of a porous ceramic material is schematically shown in Figure 2.16. Firstly, the material deforms elastically and follows the Hooke's law. This behavior is represented by the initial linear section. The yield point characterizes the ending of the linear-elastic behavior and in the case of brittle ceramics indicates the maximum stress. In porous ceramics, pore deflections takes place and causes a gradually decrease of the stress.
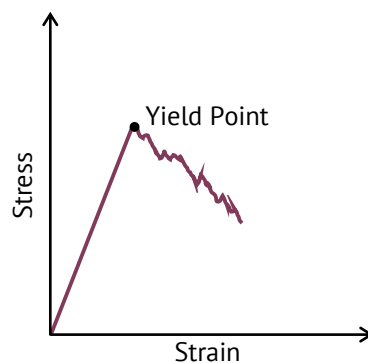
Figure 2.16   Schematic illustration of a typical stress-strain curve of a porous ceramic.

In general, the measured compressive strength of ceramic components is influenced to a large extend by the test parameters, e.g. strain rate and sample dimensions. For example, smaller sample dimensions result in increasing compressive strength according to the size effect of compressive strength. Furthermore, the geometry of the sample alters the crack propagation patterns and hence changes the measured compressive strength [230]. In addition, increasing strain rate leads to higher measured compressive strength values. This can be explained by the decreasing influence of defects with increasing strain rate [231]. Also the crack propagation is influenced by the strain rate. While high loading speeds limit the crack propagation, low strain rates result in enhanced crack growth. Thus, comparing the compressive

strength is only possible for identical test parameters. The section 4.3.3 (see page 68) provides details on the applied test parameters.

2.5.5 Isothermal Wicking

Isothermal wicking experiments are used to characterize the capillary action within a porous media. In general, imbibition is defined as the displacement of one fluid by another fluid which is immiscible and has a higher viscosity taking place in a porous medium [115]. If the driving force is the capillary pressure created at the liquid-air interfaces, such an imbibition is called wicking [116]. Changes in the surface energy of the solid induced by wetting result in a capillary pressure and pull the invading liquid into the porous structure [117]. A detailed description of the fundamentals of capillary action is given in section 2.3.1 (see page 22).

Isothermal wicking at room temperature is the simplest variation of wicking. Changing the conditions to cryogenic wicking introduces further influencing factors such as a superheated structure and vapor generation due to heat transfer between structure and liquid. These additional aspects complicate the assessment of the relation between pore structure and wicking performance. Therefore, the isothermal wicking at room temperature is most suited to study the basic correlations between pore structure and wicking. Details on the measurement parameters and the setup are presented in sections 5.3.3 (see page 92) and 6.3.3 (see page 124).

2.5.6 Constant Head Permeability Test

The permeability is the ability of a porous material to allow fluids to pass. In general, the permeability of a material depends on properties of the pore structure, e.g. porosity, pore size and pore morphology. The permeability K is part of the proportionality constant in Darcy 's law which describes the relation between flow rate and fluid physical properties (e.g. viscosity) to a pressure gradient which is applied to the porous media [128]:

$$\frac{\Delta p}{\Delta L} = -\frac{\mu}{K} u_s.$$

(2.9)

with the length of the sample ΔL, the dynamic viscosity μ, the superficial velocity u_s and the pressure drop Δp which is given by the hydrostatic pressure of the water

column h_{CHP}. A detailed derivation of the underlying equations is given in the appendix A.2.1 on page 195.

The Darcy's law considers only the viscous forces and assumes a linear dependence between superficial velocity and pressure gradient. Hence, several assumptions needs to be considered when applying the Darcy equation. Since the Darcy equation is only valid for slow superficial velocities, laminar flow regime has to be ensured. Further requirements are: no reaction of the fluid with the sample, incompressible fluid, single phase flow and continuous and steady flow. In contrast to Darcy's law, the Forchheimer equation includes the contributions of inertia and turbulence and can be applied in turbulent flow regime [59].

In literature, different methods are proposed to determine the permeability of a porous structure [232]. The constant head permeability test is widely used in the investigation of soils and rocks due to its simple procedure. Figure 2.17 illustrates the setup of the constant head permeability test. The pressure gradient is created by the hydrostatic pressure of the water column. Due to the low fluid flow and the high ratio between the radii of sample and water reservoir, the height of the water column can considered to be constant. The amount of penetrated water is gravimetrical evaluated. Details on the measurement procedure are presented in section 6.3.3 (see page 124).
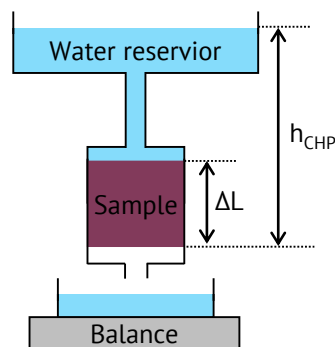

Figure 2.17 Schematic illustration of constant head permeability test and specification of the important physical and geometrical parameters.

2.5.7 Catalytic Test in a Packed-bed Reactor

The setup to evaluate the catalytic activity of a catalyst usually consists of a reactor where the reaction takes place at appropriate conditions and a device to analyze the product stream. Mostly, gas chromatography equipped with corresponding chromatography columns are applied to separate the single components from the product stream. The calibration of the detector allows for quantitative analysis of the products.

Most commercial catalytically activated gas-phase reactions are carried out in packed-bed reactors. A packed-bed or fixed-bed reactor consists of compact layers of catalysts pellets usually filled in a vertical tube as illustrated in Figure 2.18. Consequently, the reaction of gaseous reactants takes place over the stationary catalysts. Macroscopically, the catalysts bed acts like a porous media. In contrast to other reactor types or designs, e.g. homogeneous catalysts, packed-bed reactors are preferred due to their simple setup and ease of operation [233]. In industrial applications, packed-bed reactors are usually operated in a stationary mode over long production runs [234].

Due to the importance of temperature in influencing a chemical reaction, it is convenient to differentiate between reactors for adiabatic and nonadiabatic conditions. Adiabatic reactors are used when there is only one major reaction pathway and/or when the adiabatic temperature change is small. In contrast, reactions which are very temperature sensitive and reactions with a large heat of reaction require a reactor which can remove or provide heat. In these cases, multitubular packed-bed reactors are mostly applied. They are characterized by a heat carrier circulating around tubes which are filled with catalyst pellets.

Since several key requirements on reactor and catalyst design such as a good temperature control, a low pressure loss and a high catalyst concentration are to some extend contradictory, a large variety of different catalyst shapes and arrangements has been developed. Random packing of catalyst pellets in a tube as shown in Figure 2.18 represents the simplest form of a packed-bed.
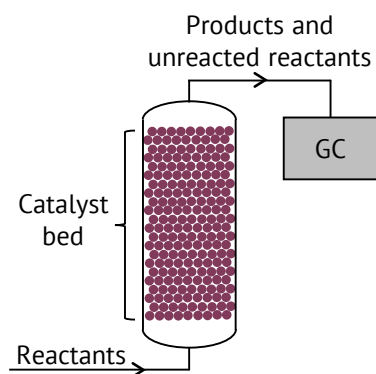
Figure 2.18   Illustration of an adiabatic packed-bed reactor with subsequent analysis of the product stream by gas chromatography (GC).

The mean pellet dimensions usually vary from 1 mm to 10 mm [234]. The upper limit is set the specific outer surface area for mass and heat transfer and the lower limit is defined by considerations concerning the pressure drop. Depending on the reaction conditions, different catalyst shapes are used: spheres, cylinders, rings, flat disk pellets or crushed material of a certain sieve fraction [234].

Due to the simple setup and the ease of operation, usually adiabatic packed-bed reactors with very small diameters of only a few millimeters are used in science for the assessment of a catalyst. Consequently, also the catalyst size reduces to hundreds of micrometers. A detailed description of the reactor and the measurement conditions which have been applied can be found in section 7.3.3 (see page 147).

References

[1]   P. Colombo, G. Mera, R. Riedel, G.D. Sorarù, J. Am. Ceram. Soc. 93 (2010) 1805-1837.

[2]   R.H. Baney, M. Itoh, A. Sakakibara, T. Suzuki, Chem. Rev. 95 (1995) 1409-1430.

[3]   P.H. Mutin, Journal of Sol-Gel Science and Technology 14 (1999) 27-38.

[4]   M. Wilhelm, C. Soltmann, D. Koch, G. Grathwohl, J. Eur. Ceram. Soc. 25 (2005) 271-276.

[5]   J. Brus, F. Kolar, V. Machovic, J. Svitilova, J. Non-Cryst. Solids 289 (2001) 62-74.

[6]   C.G. Pantano, A.K. Singh, H. Zhang, Journal of Sol-Gel Science and Technology 14 (1999) 7-25.

[7]   S. Sarkar, L. Zhai, Materials Express 1 (2011) 18-29.

[8]   S. Duperrier, C. Gervais, S. Bernard, D. Cornu, F. Babonneau, C. Balan, P. Miele, Macromolecules 40 (2007) 1018-1027.

[9]   S. Loginkin, L. Schlier, J. Harris, N. Travitzky, P. Greil, Adv. Eng. Mater. 18 (2016) 70-75.

[10]   Y. Zhu, Z. Huang, S. Dong, M. Yuan, D. Jiang, Ceram. Int. 34 (2008) 1201-1205.

[11]   R. Melcher, P. Cromme, M. Scheffler, P. Greil, J. Am. Ceram. Soc. 86 (2003) 1211-1213.

[12]   R. Riedel, G. Mera, R. Hauser, A. Klonczynski, J. Ceram. Soc. Jpn. 114 (2006) 425-444.

[13]   B.V. Manoj Kumar, Y.W. Kim, Sci Technol Adv Mater 11 (2010) 044303 - 044319.

[14]   M. Scheffler, T. Gambaryan-Roisman, T. Takahashi, J. Kaschta, H. Muenstedt, P. Buhler, P. Greil, Ceram Trans 115 (2000) 239-250.

[15]   H. Schmidt, D. Koch, G. Grathwohl, P. Colombo, J. Am. Ceram. Soc. 84 (2001) 2252-2255.

[16]   G.D. Soraru, Chemistry of Materials 10 (1998) 4047-4054.

[17]   H. Zhang, P. D'Angelo Nunes, M. Wilhelm, K. Rezwan, J. Eur. Ceram. Soc. 36 (2016) 51-58.

[18]   T. Prenzel, M. Wilhelm, K. Rezwan, Microporous Mesoporous Mater. 169 (2013) 160-167.

[19]   M.J. Owen, P.J. Smith, J. Adhes. Sci. Technol. 8 (1994) 1063-1075.

[20]   H. Zhang, C.L. Fidelis, A.L.T. Serva, M. Wilhelm, K. Rezwan, J. Am. Ceram. Soc. 100 (2017) 1907-1918.

[21]   T. Prenzel, M. Wilhelm, K. Rezwan, Chem. Eng. J. 235 (2014) 198-206.

[22]   S. Kizil, H. Bulbul Sonmez, J Environ Manage 196 (2017) 330-339.

[23]   B.-B. Dong, F.-H. Wang, M.-Y. Yang, J.-L. Yu, L.-Y. Hao, X. Xu, G. Wang, S. Agathopoulos, J. Membr. Sci. 579 (2019) 111-119.

[24]   K. Yamamoto, J. Ohshita, Polymer Journal 51 (2019) 1103-1116.

[25]   Y. Zhu, D. Wang, L. Jiang, J. Jin, NPG Asia Materials 6 (2014) e101-e101.

[26]   F. Ferrero, Polym. Test. 22 (2003) 571-578.

[27]   S. Inbakumar, R. Morent, N. De Geyter, T. Desmet, A. Anukaliani, P. Dubruel, C. Leys, Cellulose 17 (2009) 417-426.

[28]   Y. Li, L.a. Fernandez-Recio, P. Gerstel, V. Srot, P.A.v. Aken, G. Kaiser, M. Burghard, J. Bill, Chemistry of Materials 20 (2008) 5593-5599.

[29]   H. Tian, Q.-s. Ma, Y. Pan, W.-d. Liu, Ceram. Int. 38 (2012) 5039-5043.

[30]   K.B. Schwartz, D.J. Rowcliffe, Communications of the American Ceramic Society 69 (1986) 106-108.

[31]   L. Biasetto, A. Francis, P. Palade, G. Principi, P. Colombo, J. Mater. Sci. 43 (2008) 4119-4126.

[32]   P. Greil, J. Eur. Ceram. Soc. 18 (1998) 1905-1914.

[33]   M. Shibuya, M. Sakurai, T. Takahashi, Composites Science and Technology 67 (2007) 3338-3344.

[34]   Y. Katsuda, P. Gerstel, J. Narayanan, J. Bill, F. Aldinger, J. Eur. Ceram. Soc. 26 (2006) 3399-3405.

[35]   D. Suttor, H.-J. Kleebe, G. Ziegler, J. Am. Ceram. Soc. 10 (1997) 2541-2148.

[36]   F. Griggio, E. Bernardo, P. Colombo, G.L. Messing, J. Am. Ceram. Soc. 91 (2008) 2529-2533.

[37]   E. Bernardo, E. Tomasella, P. Colombo, Ceram. Int. 35 (2009) 1415-1421.

[38]   E. Bernardo, P. Colombo, S. Hampshire, J. Eur. Ceram. Soc. 29 (2009) 843-849.

[39]   Y.-W. Kim, S.-H. Kim, H.-D. Kim, C.B. Park, J. Mater. Sci. 39 (2004) 5447-5652.

[40]   R. Petersen, D.A. Foucher, B.-Z. Tang, A. Lough, N.P. Raju, J.E. Greedan, I. Manners, Chemistry of Materials 7 (1995) 2045-2053.

[41]   B.-Z. Tang, R. Petersen, D.A. Foucher, A. Lough, N. Coombs, R. Sodhib, I. Manners, J. Chem. Soc., Chem. Commun. (1993) 523-525.

[42]   M.J. MacLachlan, M. Ginzburg, N. Coombs, T.W. Coyle, N.P. Raju, J.E. Greedan, G.A. Ozin, I. Manners, Science 287 (2000) 1460-1463.

[43]   M. Zaheer, T. Schmalz, G. Motz, R. Kempe, Chem Soc Rev 41 (2012) 5102-16.

[44]   M. Zaheer, G. Motz, R. Kempe, Journal of Materials Chemistry 21 (2011) 18825 - 18831.

[45]   M. Kamperman, A. Burns, R. Weissgraeber, N.v. Vegten, S.C. Warren, S.M. Gruner, A. Baiker, U. Wiesner, Nano Lett 9 (2009) 2756-2762.

[46]   T. Schmalz, T. Kraus, M. Günthner, C. Liebscher, U. Glatzel, R. Kempe, G. Motz, Carbon 49 (2011) 3065-3072.

[47]   S. Deeken, S. Proch, E. Casini, H.F. Braun, C. Mechtler, C. Marschner, G. Motz, R. Kempe, Inorg. Chem. 45 (2006) 1871-1879.

[48]   C. Vakifahmetoglu, E. Pippel, J. Woltersdorf, P. Colombo, J. Am. Ceram. Soc. 93 (2010) 959-968.

[49]   C. Vakifahmetoglu, P. Colombo, S.M. Carturan, E. Pippel, J. Woltersdorf, J. Am. Ceram. Soc. 93 (2010) 3709-3719.

[50]   M. Scheffler, P. Greil, A. Berger, E. Pippel, J. Woltersdorf, Materials Chemistry and Physics 84 (2004) 131-139.

[51]   A. Idesaki, P. Colombo, Adv. Eng. Mater. 14 (2012) 1116-1122.

[52]   P. Colombo, T. Gambaryan-Roisman, M. Scheffler, P. Buhler, P. Greil, J. Am. Ceram. Soc. 10 (2001) 2265-2268.

[53]   A.M. Liu, K. Hidajat, S. Kawi, D.Y. Zhao, Chem Commun (2000) 1145-1146.

[54]   C. Gervais, F. Babonneau, N. Dallabonna, G.D. Soraru, J. Am. Ceram. Soc. 84 (2001) 2160-2164.

[55]   M. Wilhelm, M. Adam, M. Bäumer, G. Grathwohl, Adv. Eng. Mater. 10 (2008) 241-245.

[56]   M. Adam, S. Kocanis, T. Fey, M. Wilhelm, G. Grathwohl, J. Eur. Ceram. Soc. 34 (2014) 1715-1725.

[57]   M. Adam, M. Bäumer, M. Schowalter, J. Birkenstock, M. Wilhelm, G. Grathwohl, Chem. Eng. J. 247 (2014) 205-215.

[58] R.W. Rice, *Porosity of Ceramics*. 1998, New York: Marcel Dekker Inc.

[59] M. Scheffler, P. Colombo, *Cellular Ceramics: Structure, Manufacturing, Properties and Applications*. 2005, Weinheim: Wiley-VCH.

[60] L.J. Gauckler, M.M. Waeber, C. Conti, M. Jacob-Duliere, Journal of Metals 37 (1985) 47-50.

[61] P. Colombo, Philos Trans A Math Phys Eng Sci 364 (2006) 109-24.

[62] A.R. Studart, U.T. Gonzenbach, E. Tervoort, L.J. Gauckler, J. Am. Ceram. Soc. 89 (2006) 1771-1789.

[63] Lyckfeldt, J.M.F. Ferreira, J. Eur. Ceram. Soc. 18 (1998) 131-140.

[64] A.F. Lemos, J.M.F. Ferreira, Mater. Sci. Eng., C 11 (2000) 35-40.

[65] M.H.P.d. Silva, A.F. Lemos, I.R. Gibson, J.M.F. Ferreira, J.D. Santos, J. Non-Cryst. Solids 304 (2002) 286-292.

[66] R. Barea, M.I. Osendi, P. Miranzo, J.M.F. Ferreira, J. Am. Ceram. Soc. 88 (2005) 777-779.

[67] P. Colombo, E. Bernardo, L. Biasettot, J. Am. Ceram. Soc. 87 (2004) 152-154.

[68] K.M. Lindqvist, E. Carlström, J. Eur. Ceram. Soc. 25 (2005) 3539-3545.

[69] Y. Hotta, Mater. Sci. Forum 439 (2003) 186-191.

[70] T.J. Fithgerald, V.J. Michaud, A. Mortensen, J. Mater. Sci. 30 (1995) 1037-1045.

[71] H. Kim, C.d. Rosa, M. Boaro, J.M. Vohs, R.J. Gorte, J. Am. Ceram. Soc. 85 (2002) 1473-1476.

[72] H. Wang, I. Sung, X. Li, D. Kim, Journal of Porous Materials 11 (2004) 265-271.

[73] Y. Hotta, P.C.A. Alberius, L. Bergström, Journal of Materials Chemistry 13 (2003) 496-501.

[74] A. Imhof, D.J. Pine, Nature (Lond.) 389 (1997) 948-951.

[75] I. Akartuna, A.R. Studart, E. Tervoort, L.J. Gauckler, Advanced Materials 20 (2008) 4714-4718.

[76] T. Fukasawa, M. Ando, J. Am. Ceram. Soc. 84 (2001) 230 - 232.

[77] T. Fukasawa, Z.-Y. Deng, M. Ando, J. Mater. Sci. 36 (2001) 2523 - 2527.

[78] D. Koch, L. Andresen, T. Schmedders, G. Grathwohl, Journal of Sol-Gel Science and Technology 26 (2003) 149 - 152.

[79] S. Deville, Adv. Eng. Mater. 10 (2008) 155-169.

[80] M. Naviroj, P.W. Voorhees, K.T. Faber, J. Mater. Res. 32 (2017) 3372-3382.

[81] R. Liu, T. Xu, C. Wang, Ceram. Int. 42 (2016) 2907-2925.

[82] A.W. Rempel, M.G. Worster, J Cryst Growth 205 (1999) 427 - 440.

[83] L. Hadji, The European Physical Journal B - Condensed Matter 37 (2003) 85-89.

[84] L. Hadji, A.M.J. Davis, J Cryst Growth 191 (1998) 889-896.

[85] W.W. Mullins, R.F. Sekerka, J Appl Phys 35 (1964) 444-451.

[86] P.v.d. Witte, P.J. Dijkstra, J.W.A.v.d. Berg, J. Feijen, J. Membr. Sci. 117 (1996) 1-31.

[87]   C.-y. Gao, A. Li, L.-x. Feng, X.-s. Yi, J.-c. Shen, Polym. Int. 49 (2000) 323-328.

[88]   M. Naviroj, S.M. Miller, P. Colombo, K.T. Faber, J. Eur. Ceram. Soc. 35 (2015) 2225-2232.

[89]   R. Chen, C.-A. Wang, Y. Huang, L. Ma, W. Lin, J. Am. Ceram. Soc. 90 (2007) 3478-3484.

[90]   K.L. Scotti, D.C. Dunand, Prog. Mater Sci. 94 (2018) 243-305.

[91]   K. Araki, J.W. Halloran, J. Am. Ceram. Soc. 88 (2005) 1108-1114.

[92]   M. Naviroj, M.M. Wang, M.T. Johnson, K.T. Faber, Scripta Mater. 130 (2017) 32-36.

[93]   S. An, B. Kim, J. Lee, J Cryst Growth 469 (2017) 106-113.

[94]   R. Okaji, S. Sakashita, K. Tazumi, K. Taki, S. Nagamine, M. Ohshima, J. Mater. Sci. 48 (2012) 2038-2045.

[95]   H.J. Choi, T.Y. Yang, S.Y. Yoon, B.K. Kim, H.C. Park, Materials Chemistry and Physics 133 (2012) 16-20.

[96]   Y. Chu, Z. Lu, J. Li, Y. Zhu, S. Zhang, J. Chen, Polym. Adv. Technol. 26 (2015) 606-612.

[97]   S. Deville, C. Viazzi, J. Leloup, A. Lasalle, C. Guizard, E. Maire, J. Adrien, L. Gremillard, PLoS One 6 (2011) e26474-e26474.

[98]   J. Zeng, Y. Zhang, K.-c. Zhou, D. Zhang, Trans. Nonferrous Met. Soc. China 24 (2014) 718-722.

[99]   M.N. Rahaman, Q. Fu, J. Am. Ceram. Soc. 91 (2008) 4137-4140.

[100] Q. Fu, M.N. Rahaman, F. Dogan, B.S. Bal, Biomed Mater 3 (2008) 025005-025012.

[101] E. Munch, E. Saiz, A.P. Tomsia, S. Deville, J. Am. Ceram. Soc. 92 (2009) 1534-1539.

[102] J.-W. Moon, H.-J. Hwang, M. Awano, K. Maeda, Materials Letters 57 (2003) 1428 - 1434.

[103] S. Deville, E. Saiz, A.P. Tomsia, Acta Mater. 55 (2007) 1965-1974.

[104] J.L. Holbrough, J.M. Campbell, F.C. Meldrum, H.K. Christenson, Cryst. Growth Des. 12 (2012) 750-755.

[105] S. Algharaibeh, A. J.Ireland, B. Su, J. Eur. Ceram. Soc. 39 (2019) 514-521.

[106] S. Deville, Science 311 (2006) 515 - 518.

[107] S. Deville, S. Meille, J. Seuba, Sci. Technol. Adv. Mater. 16 (2015) 43501-43516.

[108] T.Y. Yang, S.W. Lyu, Y.M. Park, S.Y. Yoon, R. Stevens, H.C. Park, Key Engineering Materials 336-338 (2007) 2583-2585.

[109] N. Ni, S. Barg, E. Garcia-Tunon, F. Macul Perez, M. Miranda, C. Lu, C. Mattevi, E. Saiz, Sci Rep 5 (2015) 13712-13726.

[110] B. Wang, J. Ji, K. Li, Nat Commun 7 (2016) 12804-12812.

[111] L. Hu, Y. Zhang, S. Zhang, Y. Zhou, Materials Letters 82 (2012) 152-155.

[112] B.-H. Yoon, E.-J. Lee, H.-E. Kim, Y.-H. Koh, J. Am. Ceram. Soc. 90 (2007) 1753-1759.

[113] H. Zhang, C.L. Fidelis, M. Wilhelm, Z. Xie, K. Rezwan, Mater. Des. 134 (2017) 207-217.

[114] P.M. Hunger, A.E. Donius, U.G. Wegst, Acta Biomater 9 (2013) 6338-48.

[115] M. Alava, M. Dubé, M. Rost, Adv Phys 53 (2004) 83-175.

[116] R. Masoodi, K.M. Pillai, P.P. Varanasi, AlChE J. 53 (2007) 2769-2782.

[117] R. Masoodi, K.M. Pillai, Journal of Porous Media 15 (2012) 775-783.

[118] T. Dang-Vu, J. Hupka, Physicochemical Problems of Mineral Processing 39 (2005) 47-65.

[119] P.K. Chatterjee, B.S. Gupta, *Absorbent Technology*, ed. P.K. Chatterjee and B.S. Gupta. Vol. 13. 2002, Amsterdam: Elsevier Science

[120] P.S.d. Laplace, *Supplement au livre X du Traitée de méchanique céleste*. 1806, Paris: Couvreier.

[121] J. Jurin, Philosphical Transactions of the Royal Society 30 (1717-1719) 739-747.

[122] R. Lucas, Kolloid Z. 23 (1918) 15-22.

[123] E.W. Washburn, Phys. Rev. 17 (1921) 273-283.

[124] D. Patro, S. Bhattacharyya, V. Jayaram, J. Am. Ceram. Soc. 90 (2007) 3040-3046.

[125] M. Hemmat, A. Borhan, Phys. Fluids 7 (1995) 2111-2121.

[126] T.L. Staples, D.G. Shaffer, Colloids and Surface A 204 (2002) 239-250.

[127] R. Masoodi, K.M. Pillai, *Wicking in Porous Materials*. 2017, Boca Raton: CRC Press.

[128] H. Darcy, *Les Fontaines Publiques de la ville de Dijon*. 1856: Dalmont.

[129] K.M. Pillai, S.G. Advani, Journal of Colloid and Interface Science 183 (1996) 100-110.

[130] E.P. Symons, *Wicking of liquids in screens*. 1974, NASA Lewis Research Center: Cleveland, United States.

[131] M.E. Dreyer, *Free Surface Flows under Compensated Gravity Conditions*, in *Springer Tracts in Modern Pysics*. 2007, Springer: Berlin Heidelberg.

[132] S. Levine, P. Reed, E.J. Watson, G. Neale, *A theory of the rate of rise of a liquid in a capillary*, in *Colloid and Interface Science*, M. Kerker, Editor. 1976, Academic Press: New York.

[133] N. Fries. *Capillary transport processes in porous materials.* 2010. thesis in Produktionstechnik at Universität Bremen. Dr.-Ing.

[134] A. Siebold, M. Nardin, J. Schultz, A. Walliser, M. Oppliger, Colloids and Surface A 161 (2000) 81-87.

[135] E. Chibowski, R. Perea-Carpio, Adv. Colloid Interface Sci. 98 (2002) 245-264.

[136] J. Bear, J Fluid Mech 61 (1972) 206-208.

[137] E.O. Einset, J. Am. Ceram. Soc. 79 (1996) 333-338.

[138] S. Kumar, A. Kumar, A. Shukla, A.K. Gupta, R. Devi, J. Eur. Ceram. Soc. 29 (2009) 2643-2650.

[139] S. Kumar, A. Kumar, R. Devi, A. Shukla, A.K. Gupta, J. Eur. Ceram. Soc. 29 (2009) 2651-2657.

[140] K. Okada, S. Uchiyama, T. Isobe, Y. Kameshima, A. Nakajima, T. Kurata, J. Eur. Ceram. Soc. 29 (2009) 2491-2497.

[141] C. Popa, Y. Okayasu, K.-i. Katsumata, T. Isobe, N. Matsushita, A. Nakajima, T. Kurata, K. Okada, J. Mater. Sci. 48 (2013) 941-947.

[142] K. Okada, A. Imase, T. Isobe, A. Nakajima, J. Eur. Ceram. Soc. 31 (2011) 461-467.

[143] Y. Grebenyuk, H.X. Zhang, M. Wilhelm, K. Rezwan, M.E. Dreyer, J. Eur. Ceram. Soc. 37 (2017) 1993-2000.

[144] J. Hartwig, *Liquid Acquisition Devices for Advanced In-Space Cryogenic Propulsion Systems*. 2016, Amsterdam: Elsevier Inc.

[145] M. Zhang, *Capillary transport of cryogenic liquids in porous structure*. 2013, Göttingen: Cuvillier Verlag.

[146] D.K. Khrustalev, S.Y. Semenov, *Advances in Low-Temperature, Cryogenic, and Miniature Loop Heat Pipes*, in *V Minsk International Seminar "Heat Pipes, Heat Pumps, Refrigerators"*. 2003: Minsk, Belarus.

[147] T. Zhang, P. deBock, E.W. Stautner, T. Deng, C. Immer, Cryogenics 52 (2012) 301-305.

[148] Y. Ma, D. Zimnik, M. Dreyer, Y. Li, International Journal of Heat and Mass Transfer 141 (2019) 530-541.

[149] N. Fries, K. Odic, M. Dreyer. *Wicking of Perfectly Wetting Liquids into a Metallic Mesh*. in *2nd International Conference on Porous Media and its Applications in Science and Engineering*. 2007. Kauai, Hawaii, USA.

[150] X.Q. Cao, R. Vassen, D. Stoever, J. Eur. Ceram. Soc. 24 (2004) 1-10.

[151] Y. Grebenyuk, M.E. Dreyer, Cryogenics 78 (2016) 27-39.

[152] P. Sabatier, S.J. Baptiste, Comptes Rendus Hebdomadaires des seances de l'Academie des Sciences 134 (1902) 514-516.

[153] A. Swapnesh, V.C. Srivastava, I.D. Mall, Chem. Eng. Technol. 37 (2014) 1765-1777.

[154] J. Gao, Y. Wang, Y. Ping, D. Hu, G. Xu, F. Gu, F. Su, RSC Advances 2 (2012) 2358-2368.

[155] M.K. Nikoo, N.A.S. Amin, Fuel Process Technol 92 (2011) 678-691.

[156] Y. Li, Y. Wang, X. Zhang, Z. Mi, Int. J. Hydrogen Energy 33 (2008) 2507-2514.

[157] L. Kiewidt. *Solid Sponges as Support for Heterogeneous Catalysts in Gas-Phase Reactions*. 2017. thesis in Production Engineering at University of Bremen. Dr.-Ing.

[158] W. Li, H. Wang, X. Jiang, J. Zhu, Z. Liu, X. Guo, C. Song, RSC Adv. 8 (2018) 7651-7669.

[159] K.R. Thampi, J. Kiwi, M. Griitzel, Nature 327 (1987) 506-508.

[160] S. Rönsch, J. Schneider, S. Matthischke, M. Schlüter, M. Götz, J. Lefebvre, P. Prabhakaran, S. Bajohr, Fuel 166 (2016) 276-296.

[161] B. Miao, S.S.K. Ma, X. Wang, H. Su, S.H. Chan, Catal. Sci. Tech. 6 (2016) 4048-4058.

[162] J.L. Falconer, A.E. Zagli, J. Catal. 62 (1980) 280-285.

[163] F. Koschany, D. Schlereth, O. Hinrichsen, Applied Catalysis B: Environmental 181 (2016) 504-516.

[164] F.C. Patcas, G.I. Garrido, B. Kraushaar-Czarnetzki, Chemical Engineering Science 62 (2007) 3984-3990.

[165] S. Fujita, H. Terunuma, H. Kobayashi, N. Takezawa, React. Kinet. Catal. Lett. 33 (1987) 179-184.

[166] Q. Pan, J. Peng, S. Wang, S. Wang, Catal. Sci. Technol. 4 (2014) 502-509.

[167] C. Schild, A. Wokaun, R.A. Koeppel, A. Baiker, J. Phys. Chem. 95 (1991) 6341-6346.

[168] P.A.U. Aldana, F. Ocampo, K. Kobl, B. Louis, F. Thibault-Starzyk, M. Daturi, P. Bazin, S. Thomas, A.C. Roger, Catal. Today 215 (2013) 201-207.

[169] J. Sehested, J. Catal. 223 (2004) 432-443.

[170] G.A. Mills, F.W. Steffgen, Catalysis Reviews 8 (2006) 159-210.

[171] A.M. Abdel-Mageed, D. Widmann, S.E. Olesen, I. Chorkendorff, J. Biskupek, R.J. Behm, ACS Catalysis 5 (2015) 6753-6763.

[172] S. Sokolov, E.V. Kondratenko, M.-M. Pohl, A. Barkschat, U. Rodemerck, Applied Catalysis B: Environmental 113-114 (2012) 19-30.

[173] I. Rossetti, C. Biffi, C.L. Bianchi, V. Nichele, M. Signoretto, F. Menegazzo, E. Finocchio, G. Ramis, A. Di Michele, Applied Catalysis B: Environmental 117-118 (2012) 384-396.

[174] V. Nichele, M. Signoretto, F. Menegazzo, A. Gallo, V. Dal Santo, G. Cruciani, G. Cerrato, Applied Catalysis B: Environmental 111-112 (2012) 225-232.

[175] S. Kattel, P. Liu, J.G. Chen, J. Am. Chem. Soc. 139 (2017) 9739-9754.

[176] G. Zhou, H. Liu, K. Cui, H. Xie, Z. Jiao, G. Zhang, K. Xiong, X. Zheng, Int. J. Hydrogen Energy 42 (2017) 16108-16117.

[177] N.M. Martin, P. Velin, M. Skoglundh, M. Bauer, P.-A. Carlsson, Catal. Sci. Tech. 7 (2017) 1086-1094.

[178] J.A.H. Dreyer, P. Li, L. Zhang, G.K. Beh, R. Zhang, P.H.L. Sit, W.Y. Teoh, Applied Catalysis B: Environmental 219 (2017) 715-726.

[179] W. Li, X. Nie, X. Jiang, A. Zhang, F. Ding, M. Liu, Z. Liu, X. Guo, C. Song, Applied Catalysis B: Environmental 220 (2018) 397-408.

[180] A. Kim, D.P. Debecker, F. Devred, V. Dubois, C. Sanchez, C. Sassoye, Applied Catalysis B: Environmental 220 (2018) 615-625.

[181] Y. Lin, Y. Zhu, X. Pan, X. Bao, Catal. Sci. Tech. 7 (2017) 2813-2818.

[182] Y. Yan, Y. Dai, H. He, Y. Yu, Y. Yang, Applied Catalysis B: Environmental 196 (2016) 108-116.

[183] D. Wierzbicki, R. Debek, M. Motak, T. Grzybek, M.E. Gálvez, P. Da Costa, Catal. Commun. 83 (2016) 5-8.

[184] L. Xu, F. Wang, M. Chen, D. Nie, X. Lian, Z. Lu, H. Chen, K. Zhang, P. Ge, Int. J. Hydrogen Energy 42 (2017) 15523-15539.

[185] H.C. Wu, Y.C. Chang, J.H. Wu, J.H. Lin, I.K. Lin, C.S. Chen, Catal. Sci. Tech. 5 (2015) 4154-4163.

[186] J.H. Kwak, L. Kovarik, J. Szanyi, ACS Catalysis 3 (2013) 2449-2455.

[187] J.H. Kwak, L. Kovarik, J. Szanyi, ACS Catalysis 3 (2013) 2094-2100.

[188] G. Garbarino, P. Riani, L. Magistri, G. Busca, Int. J. Hydrogen Energy 39 (2014) 11557-11565.

[189] J. Engbæk, O. Lytken, J.H. Nielsen, I. Chorkendorff, Surf. Sci. 602 (2008) 733-743.

[190] P. Avila, M. Montes, E.E. Miró, Chem. Eng. J. 109 (2005) 11-36.

[191] D. Vervloet, F. Kapteijn, J. Nijenhuis, J.R. van Ommen, Chem. Eng. J. 233 (2013) 265-273.

[192] T.J. Schildhauer, K. Pangarkar, J.R. van Ommen, J. Nijenhuis, J.A. Moulijn, F. Kapteijn, Chem. Eng. J. 185-186 (2012) 250-266.

[193] F. Donsì, S. Cimino, A.D. Benedetto, R. Pirone, G. Russo, Catal. Today 105 (2005) 551-559.

[194] R.M. Hecka, S. Gulati, R.J. Farrauto, Chem. Eng. J. 82 (2001) 149-156.

[195] T.A. Nijhuis, A.E.W. Beers, T. Vergunst, I. Hoek, F. Kapteijn, J.A. Moulijn, Catalysis Reviews 43 (2001) 345-380.

[196] S. Govender, H. Friedrich, Catalysts 7 (2017) 62-91.

[197] D. Zhang, L. Zhang, B. Liang, Y. Li, Chem. Eng. J. 139 (2009) 430-435.

[198] C. Agrafiotis, A. Tsetsekou, J. Eur. Ceram. Soc. 20 (2000) 815-824.

[199] J. Zamaro, M. Ulla, E. Miro, Chem. Eng. J. 106 (2005) 25-33.

[200] B.P. Barbero, L. Costa-Almeida, O. Sanz, M.R. Morales, L.E. Cadus, M. Montes, Chem. Eng. J. 139 (2008) 430-435.

[201] L. Zhang, T. Li, M. Zhang, Y. Li, Journal of Rare Earths 29 (2011) 758-762.

[202] B. Kraushaar-Czarnetzki, S.P. Müller, *Shaping of solid catalysts*, in *Synthesis of Solid Catalysts*, K.P.d. Jong, Editor. 2009, Wiley: Weinheim, Germany. p. 173-199.

[203] A. Cybulski, J.A. Moulijn, *Structured Catalysts and Reactions*. 2006, Boca Raton: CRC/Taylor and Francis.

[204] V. Tomašić, F. Jović, Appl. Catal., A 311 (2006) 112-121.

[205] D. Wu, H. Zhang, Ind Eng Chem Res 52 (2013) 14713-14721.

[206] J. Weitkamp, Solid State Ionics 131 (2000) 175-188.

[207] Y.Y. Li, S.P. Perera, B.D. Crittenden, Chem. Eng. Res. Des. 76 (1998) 921-930.

[208] F. Akhtar, P.O. Vasiliev, L. Bergström, J. Am. Ceram. Soc. 92 (2009) 338-343.

[209] I.M. Lachman, M.D. Patil, *Method of Crystallizing a Zeolite on the Surface of a Monolithic Ceramic Substrate*, U.S. Patent, Editor. 1989.

[210] K.P. Gadkaree, Carbon 36 (1998) 981-989.

[211] D. Lozano-Castello, J. Alcaniz-Mongea, M.A.d.l. Casa-Lillo, D. Cazorla-Amorosa, A. Linares-Solano, Fuel 81 (2002) 1777-1803.

[212] T. Vergunst, M.J.G. Linders, F. Kapteijn, J.A. Moulijn, Catalysis Reviews 43 (2001) 291-314.

[213] A. Taguchi, J.-H. Smatt, M. Linden, Advanced Materials 15 (2003) 1209-1211.

[214] S. Alvarez, J. Esquena, C. Solans, A.B. Fuertes, Adv. Eng. Mater. 6 (2004) 897-899.

[215] A.-H. Lu, J.-H. Smått, S. Backlund, M. Lindén, Microporous Mesoporous Mater. 72 (2004) 59-65.

[216] J. Blanco, P. Avila, A. Bahamonde, M. Yates, J.L. Belinch6n, E. Medina, A. Cuevas, Catal. Today 27 (1996) 9-13.

[217] J. Blanco, P. Avila, M. Yates, A. Bahamonde, J. Belinchon, E. Medina, A. Cuevas. *The performance of a new monolithic SCR catalyst in a life test with real exhaust gases. Effect on the textural nature.* in *Eighth International Conference on Coal Science*. 1995.

[218] P. Forzatti, D. Ballardini, L. Sighicelli, Catal. Today 41 (1998) 87-94.

[219] M. Thommes, K. Kaneko, A.V. Neimark, J.P. Olivier, F. Rodriguez-Reinoso, J. Rouquerol, K.S.W. Sing, Pure and Applied Chemistry 87 (2015) 1051-1069.

[220] K. Sing, Colloids and Surface A 187-188 (2001) 3-9.

[221] S. Brunauer, P.H. Emmett, E. Teller, J. Am. Chem. Soc. 60.2 (1938) 309-319.

[222] H. Salmang, H. Schulze, *Keramik*. 7th ed. 2007, Berlin Heidelberg New York: Springer.

[223] S.J. Gregg, K.S.W. Sing, *Adsorption, Surface Area and Porosity*. 1982, London: Academic Press.

[224] J. Rouquerol, G. Baron, R. Denoyel, H. Giesche, J. Groen, P. Klobes, P. Levitz, A.V. Neimark, S. Rigby, R. Skudas, K. Sing, M. Thommes, K. Unger, Pure and Applied Chemistry 84 (2012) 107-136.

[225] F. Moro, H. Bohni, J Colloid Interface Sci 246 (2002) 135-49.

[226] S.P. Rigby, K.J. Edler, J Colloid Interface Sci 250 (2002) 175-90.

[227] A.B.D. Cassie, S. Baxter, Transactions of the Faraday Society 40 (1944) 546-551.

[228] A. Koller, *Structure and Properties of Ceramics*. 1 ed. Vol. 80. 1994, Amsterdam: Elsevier.

[229] V.R. Salvini, V.C. Pandolfelli, D. Spinelli, *Mechanical Properties of Porous Ceramics*, in *Recent Advances in Porous Ceramics*, U.M.B. Al-Naib, Editor. 2018, Intech Open: London.

[230] J.R. del Viso, J.R. Carmona, G. Ruiz, Cem. Concr. Res. 38 (2008) 386-395.

[231] J. Lankford, J. Am. Ceram. Soc. 64 (1981) C33-C34.

[232] H.W. Olsen, R.W. Nichols, T.L. Rice, Géotechnique 35 (1985) 145-157.

[233] H.A. Jakobsen, *Packed Bed Reactors*, in *Chemical Reactor Modeling*. 2009, Springer: Berlin, Heidelberg.

[234] G. Eigenberger, W. Ruppel, *Catalytic Fixed-Bed Reactors*, in *Ullmann's Encyclopedia of Industrial Chemistry*. 2012, Wiley: Weihnheim.

Aim and Approach

<div style="text-align: right; font-size: large;">3</div>

This work aims to develop porous polymer-derived SiOC monoliths for capillary transport and heterogeneous catalysis. As base for the subsequent development, the fundamental relationships between the process parameters and the resulting pore structure and properties such as hydrophilicity, specific surface area and mechanical strength need to be elucidated. To enable effective tailoring of capillary active components, the knowledge of the dependencies between the pore structure and the capillary transport performance is crucial for an effective design of capillary active components. And finally, the underlying principles and processes of producing a porous metal containing PDC monolith need to be fully understood in advance of optimizing the pore structure of a monolithic catalyst.

All approaches base on the common features of adapting the processing parameters of the solution-based freeze casting and/or altering the chemical composition of the starting solution. Hereby, *tert*-butyl alcohol and cyclohexane act as solvents and polysiloxanes are used as preceramic polymers. As illustrated in Figure 3.1, following approaches are pursued:

1. Determining the fundamental relationships between between the process parameters and the resulting pore structure and properties by evaluating the influence of the addition of preceramic (SiOC) and ceramic (silica, alumina) filler particles on the resulting pore structure and properties such as strength, hydrophilicity and specific surface area. First, the specific surface area and the hydrophilicity should be changed by the incorporation of chemical highly adjustable preceramic filler particles based on polymethylsiloxane and poly-methylphenylsiloxane. These fillers can be prepared exploiting the great chemical flexibility of polymer-derived ceramics. This flexibility enables to generate filler particles with varying specific surface area and hydrophilicity. As comparison in terms of hydrophilicity, silica particles should be used. Hence, it can be evaluated whether preceramic or ceramic filler particles are more effective in changing the surface characteristics. Second, the mechanical stability of the monoliths should be increased by the addition of alumina platelets with a high aspect ratio. Comparing the non spherical alumina

platelets with the spherical silica and preceramic fillers enables to study the influence of the particle shape on the resulting pore structure and the mechanical strength. Since non-spherical particles are known to strongly interfere the freezing process, the resulting pore structure is influenced. It was found, that these changes on the pore structure e.g. bridge formation between lamellas can improve the mechanical stability. Especially for the application in capillary transport, the increase of the mechanical strength is a key requirement.

2. Evaluation of the relationship between structural properties and the resulting wicking behavior by manufacturing varying pore structures and testing in isothermal wicking. Since there are no strict requirements given by the application, the flexibility of the freeze casting process should be used to cover a wide range of pore structures by preparing monoliths which differ as strongly as possible in their pore structures. First, porosity, pore window size and pore morphology should be altered by changing the solvent and the solid loading from cyclohexane to *tert*-butyl alcohol and from 20 wt% to 40 wt%, respectively. Second, the orientation of the pores should be changed by controlling the freezing conditions. Non unidirectional freezing is adapted towards unidirectional freezing. Third, gradients in pore size for unidirectional freezing should be avoided by changing from constant freezing temperature (CFT) conditions at -20 °C to constant freezing front velocity (CFV) conditions of 4 µm/s and 7 µm/s. The impact of these described changes in the pore structure on the permeability and the capillary transport is investigated by means of isothermal wicking at room temperature. Additionally, comparison of experimental data with predictions basing on the Lucas-Washburn equation is conducted to evaluate the applicability of predicting the wicking in a complex 3D structure.

3. Understanding the underlying principles and processes of producing a porous metal containing and catalytic active PDC monolith by solution-based freeze casting. First, the in situ formation of nickel particles known from reflux synthesis should be adapted to the solution-based freeze casting process. The selection of an effective complexing- and cross-linking is done by the screening of different complexing and cross-linking agents with amino functionality and

assessing their ability to generate small and well distributed nickel particles as well as providing sufficient cross-linking functionality. Small and well distributed nickel particles are beneficial for the catalytic performance as tested in the probe reaction of carbon dioxide methanation. Second, the catalytic performance should be improved by further reducing the nickel particle size. The influence of the following adaptions is assessed: increasing the ratio of complexing groups to nickel from 2 to 4, changing the nickel precursor from nickel(II) acetylacetonate to nickel(II) nitrate hexahydrate and decreasing the pyrolysis temperature from 600 °C to 500 °C.
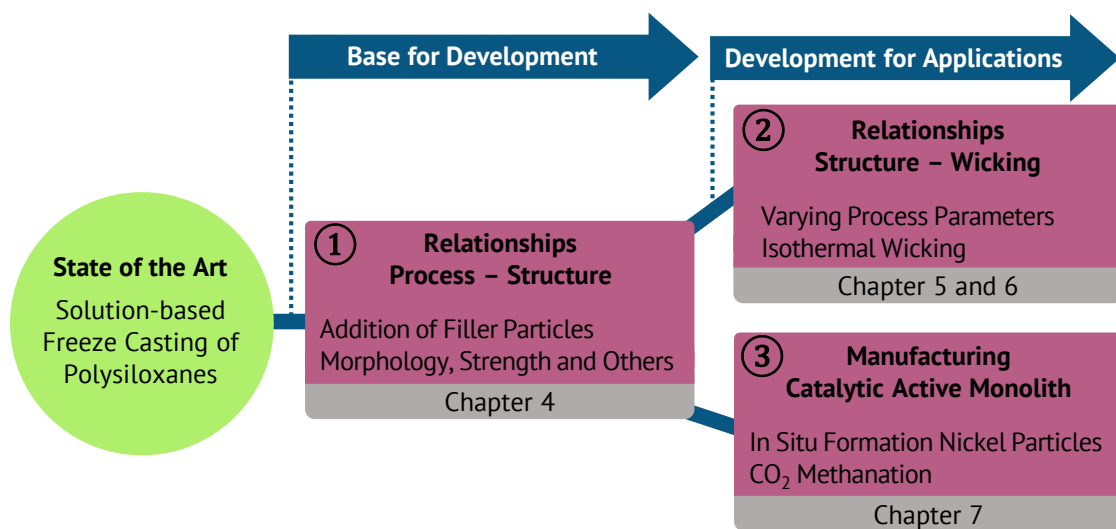

Figure 3.1 Illustration of the approaches to develop polymer-derived ceramic SiOC monoliths prepared by solution-based freeze casting for capillary transport and heterogeneous catalysis.

Influence of Filler Addition on the Pore Structure

4

Before developing a porous structure with regard to a specific application, the fundamental relationships between processing parameters and resulting properties needs to be known. The influence of the addition of filler particles on the pore structure and further properties is shown in the following chapter.

Several applications e.g. filtration, adsorption and capillary transport require the possibility to tailor specific properties. Additionally, the mechanical stability of the components is a crucial requirement. The limitation of the chemical composition in solution-based freeze casting excludes the possibility to alter the chemical composition of the preceramic polymer. Hence, the approach of adding filler particles to change properties such as specific surface area and hydrophilicity is pursued and illustrated in Figure 4.1. Furthermore, the impact of the filler particles on the pore morphology and the correlated mechanical strength is investigated. Although filtration is mentioned as potential application in the following chapter, the findings can also be directly transferred and utilized as base for the development of novel structures for capillary transport and heterogeneous catalysis.

The content of this section was published in the following article under the CC BY-NC-ND license. The style and numbering of the references, the figures, the tables and the nomination as well as further typographic aspects have been adapted to be consistent throughout the thesis and to fit the superordinate layout. Furthermore, the coloring of the figures was unified. The supplementary data can be found in the appendix A.1 on page 192.

4.1 Abstract

Applications such as filtration require not only control over the pore structure but also over properties like surface characteristics and mechanical strength. The addition of filler particles to solution-based freeze casting of preceramic polymers combines the flexibilities of freeze casting and preceramic polymers. Alumina platelets, silica spheres and preceramic filler particles with different compositions were frozen in solution-based freeze casting of preceramic polymers with cyclohexane as solvent. Polymethylsiloxane and polymethylphenylsiloxanes as well as (3-aminopropyl)-triethoxysilane were used as precursors and cross-linking agent, respectively. The compressive strength increases by factors of up to 1.9 (25 vol% preceramic filler) due to enhanced isotropy of the dendritic pore structure. At lower concentrations (1.7 vol%), alumina platelets are more effective in strengthening than spherical particles. In dependence on the composition of the preceramic filler, BET surface area and the ratio of vapor uptake between water and heptane change by factors of up to 1.19 and 16, respectively. Calculations according to a linear rule of mixture fit very well with the experimental data. In summary, the versatile approach to add differing filler particles to solution-based freeze casting allows for tailoring the pore structure as well as surface characteristics of macroporous monolithic samples.
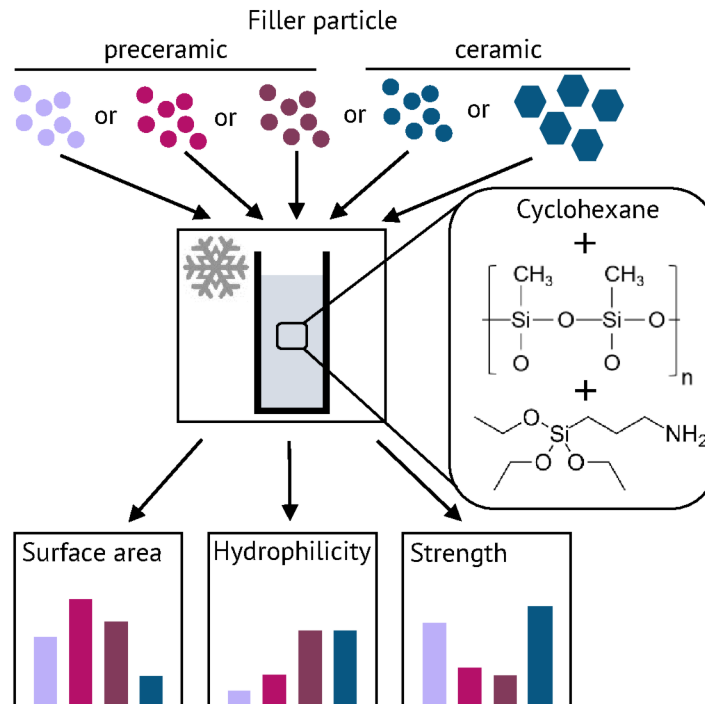
Figure 4.1 Schematic illustration of the addition of filler particles and their influence on pore structure and properties of solution-based freeze cast polymer-derived monoliths.

4.2 Introduction

Porous ceramic monoliths are required in a wide range of industries including energy and manufacturing. In order to avoid mass transport limitation, high permeability is a prerequisite for applications, such as catalysis, gas adsorption, water filtration, energy storage/conversion or even tissue engineering [1-7]. Introducing open macroporosity to the structure prevents this problem. Several techniques are available for the fabrication of macroporous monoliths, such as replica method, additive manufacturing, direct foaming and sacrificial templating [8, 9]. Tailoring the pore network, specifically the pore size, pore morphology and connectivity is crucial for adapting porous material in accordance with the requirements given by a specific application [10]. The process of freeze casting, which is a templating method, allows to vary the properties of porous structures in a wide range. Therefore, it has attracted considerable interest in recent years [11-14].

In freeze casting, pores are created by phase separation of a two-component system during freezing. At the beginning, a solid phase is uniformly dispersed in a liquid phase. Freezing of the suspension results in solidification of the liquid phase and rejection of the insoluble particles by growing crystals. Hence, the particles are assembled between the crystals. After completely frozen, sublimation removes the templating phase and thereby creates the porous structure which reflects the shape of the crystals. Various process parameters, such as particle size, particle shape and freezing front velocity influence the final pore structure [15-17]. To a great extent, the liquid phase determines the pore morphology, ranging from cellular to lamellar, dendritic or prismatic [18-21]. Although, most research is carried out using suspensions of dispersed particles, solutions of preceramic polymers can be used in freeze casting, too. Rather than rejection of particles, thermally induced phase separation is the segregation process in solution-based freeze casting [22].

Preceramic polymers offer some advantages over conventional powder based fabrication of ceramics, such as lower sintering/pyrolysis temperatures and versatility in shaping techniques [23]. Furthermore, incomplete decomposition of the organic groups at pyrolysis temperatures of 500 °C to 700 °C allows for the creation of micropores and the adjustment of hydrophilicity. Zhang et al. showed the influence of polymethylsiloxane and polymethylphenylsiloxanes precursors as well as the influence of different compositions and pyrolysis temperatures on BET surface area

and hydrophilicity [24, 25]. Thus, altering the precursor, the composition and the pyrolysis temperature changes the properties of polymer-derived ceramics. Recent research is ongoing on tailoring the surface characteristic, mostly by post-treatment e.g. impregnation, grafting for applications such as oil-water separation or waste-water filtration [26-30]. Using preceramic polymers would supersede costly post-treatment.

Very few research is conducted in the field of solution-based freeze casting of preceramic polymers. First, Yoon et al. prepared silicon carbide with dendritic pore structure based on polycarbosilane as preceramic polymer and camphene as solvent in solution-based freeze casting [31]. Naviroj et al. investigated solution-based freeze casting for cyclohexane and *tert*-butyl alcohol as solvents and polymethylsiloxanes, resulting in porous SiOC [22]. Precise control of cross-linking is required to prevent early gelation or poor mechanical stability in the green state. Hence, solution-based freeze casting strictly limits the composition and inhibits to make use of the great chemical flexibility of preceramic polymers.

For applications, such as filtration not only the pore structure, but also the strength is an important property. A mixture of alumina platelets and spherical particles enhance the mechanical properties of suspension freeze casting due to the formation of interlamellar bridges [17]. In solution-based freeze casting a nacre like structure with improved stiffness, strength and toughness was obtained by using alumina platelets in a chitosan/gelatin matrix [32]. Both studies were performed with water as solvent and a high concentration of alumina platelets, whereas nothing is known on the effect of platelet addition for other solvents such as cyclohexane or *tert*-butyl alcohol and for low platelet concentrations.

Not only platelets, but also spherical particles were used in solution-based freeze casting. Naviroj et al. investigated a combination of solution and suspension-based freeze casting for different solvents with polymethylsiloxanes and alumina particles and found an influence of the particle addition on the pore morphology [33]. Although, some studies already analyzed the influence of filler particles on the pore structure, so far, nothing is known on the influence of filler particles on the surface characteristics of porous monoliths. Since, the composition is strictly limited in solution-based freeze casting of preceramic polymers, the addition of filler particles

with different properties than the matrix would allow to alter the surface characteristics. Such surface characteristics are the BET surface area and hydrophilicity/hydrophobicity. The understanding of the several dependencies between filler composition and filler content on the one hand and the resulting properties on the other hand is crucial for an efficient design of materials according to specific applications.

In general, preceramic polymers offer the possibility to adjust their properties in a wide range by chemical modifications of the precursors. Additionally, preceramic fillers ensure a good compatibility between the preceramic matrix and the filler. So far no research was done on taking advantage of the chemical highly flexible preceramic filler particles in the freeze casting process. The addition of preceramic filler particles to solution-based freeze casting combines the flexibility of the freeze casting process regarding the macropore structure with the chemical flexibility of preceramic polymers. It has to be highlighted, that the investigated filler particles are only exemplary and were chosen to show the potential of this approach. The possible range of properties which can be altered by adapting the composition of the filler particles is much wider than presented here.

In this study, preceramic and ceramic filler particles are added to solution-based freeze casting of polymethylsiloxanes to overcome the chemical limitations of the process and hence enable adjusting structural and functional properties. We investigate the influence of adding filler particles on properties such as pore morphology, strength, BET surface area and hydrophilicity. The filler particles are either ceramic (alumina platelets and silica spheres) or preceramic (differing in composition). To alter the composition of the preceramic fillers, polymethylsiloxane or polymethylphenylsiloxane cross-linked with different concentrations of (3-amino-propyl)triethoxysilane (APTES) were used. After pyrolysis, porous monoliths with a dendritic pore structure were obtained. The following studies explore the effect of filler particles on the pore morphology as well as on surface characteristics. Furthermore, the reliability of predictions of BET surface area and hydrophilicity is assessed. Only good correlations between prediction and experimental data allow for efficient design of the material.

4.3 Materials and Methods

Porous ceramic monoliths were prepared by freeze casting, using filler particles in solution-based freeze casting. A commercial polymethylsiloxane (Silres® MK, Wacker Chemie AG, Germany) was used together with the solvent cyclohexane (Sigma-Aldrich) and (3-aminopropyl)triethoxysilane (APTES, abcr GmbH, Germany) as cross-linking agent. The chemical structures are displayed in Figure 4.2 on page 66 and comprehensivly listed on page 191. Two different classes of fillers were incorporated: ceramic and preceramic filler particles. As ceramic fillers alumina platelets (Alusion™, Antaria Ltd., Australia) with an average diameter of d_{50} = 7.5 µm and a thickness of 300 nm to 500 nm were used in addition to monodispersed silica particles (AngstromSphere, Fiber Optic Center Inc., USA) with a particle diameter of 1.0 µm. Alumina platelets and silica particles are labeled "A" and "S", respectively.

4.3.1 Preparation of Preceramic Filler

Preceramic fillers were synthesized using different preceramic polymers: poly-methylsiloxane (Silres® MK, Wacker Chemie AG, Germany) and polymethylphenyl-siloxane (Silres® H44, Wacker Chemie AG, Germany) (Figure 4.2). Just as in the freeze casting process, APTES acted as cross-linking agent. After homogenization of the preceramic polymer in ethanol for 30 min, APTES was added under stirring. To obtain fillers with different properties MK ("M1") or H44 were used and the amount of APTES was changed from 1 mol% ("H1") to 50 mol% ("H50") for fillers composed of H44. The compositions of the fillers are indicated in Table 4.1. The solid loading was kept constant at 30 wt%. Homogenization was followed by the evaporation of ethanol at room temperature for 18 h. For curing a multi-stage heat treatment in air with dwelling at 80 °C, 140 °C and 200 °C with dwelling times of 2 h and a heating rate of 60 K·min^{-1} was used. Dry ball milling at 350 r·min^{-1} for 6 h resulted in filler particles with a mean particle size d_{50} of 2.63 µm to 3.34 µm. The fillers were used without further processing in freeze casting.

4.3.2 Freeze Casting

The preparation of monolithic samples by freeze casting is illustrated in Figure 4.2. Filler particles were added to cyclohexane under vigorous stirring, followed by the addition of MK. The overall solid loading was kept constant at 40 wt% for all samples. Whereby, MK, APTES and filler particles counted as solid fraction. After 30 min of homogenization under stirring, APTES was added as cross-linking agent. Stirring was continued for 3 min to ensure a good distribution of AP. Subsequent degassing at 300 mbar for 30 s removed gas bubbles created during stirring. The solution was poured into a mold, which comprised a brass bottom and a PVC rod with an inner diameter of 40 mm and a height of 60 mm.

After casting the mold was transferred to a freezer at −20 °C. To enable easy demolding without changing the geometry of the sample, the mold remained at the freezer for 72 h. Due to the low temperature, cross-linking is slowed down. This results in a longer time which is necessary for cross-linking.
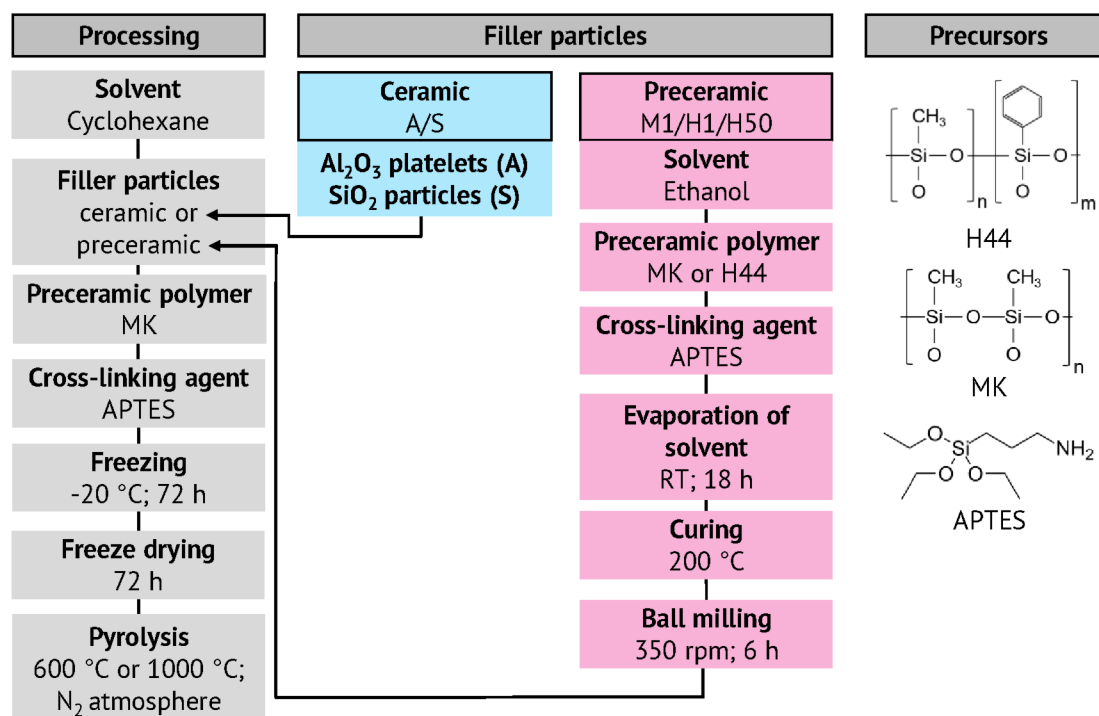

Figure 4.2   Process scheme of monolith preparation by freeze casting and the preparation of polymeric filler particles.

After demolding, the samples were dried in a freeze dryer for 72 h at −20 °C shelf temperature and a pressure of 1000 µbar. Finally, the samples were pyrolyzed at 600 °C and 1000 °C under the flow of nitrogen with a heating rate of 2 K·min⁻¹ and a

dwelling time of 4 h. The monoliths were given the nomenclature: [vol% of filler addition] [type of filler] / [pyrolysis temperature]. Sample Ref/xxx presents the reference without the addition of fillers. Table 4.1 gives an overview of all samples and their compositions.

Table 4.1 Denotation, composition and pyrolysis temperatures applied for all samples.

| Denotation | Preceramic filler particles | | | Ceramic filler particles | | Pyrolysis temperature |
	Content vol%	Polymer	Content AP mol%	Content vol%	Composition	xxx °C
25H1/xxx	25	H44	1	–	–	600
50H1/xxx	50	H44	1	–	–	600
50H50/xxx	50	H44	50	–	–	600
25S/xxx	–	–	–	25	SiO_2	600/1000
25H50/xxx	25	H44	50	–	–	600/1000
Ref/xxx	–	–	–	–	–	600/1000
25M1/xxx	25	MK	1	–	–	600/1000
50M1/xxx	50	MK	1	–	–	600/1000
1.7A/xxx	–	–	–	1.7	Al_2O_3	600/1000
3.5A/xxx	–	–	–	3.5	Al_2O_3	600/1000
1.7M1/xxx	1.7	MK	1	–	–	1000
3.5M1/xxx	3.5	MK	1	–	–	1000

4.3.3 Materials Characterization

The true density of the filler particles and the reference samples were measured with helium pycnometry (Accupyc 1330, Micromeritics, USA). Furthermore, the particle size of the preceramic filler particles was determined on diluted suspensions of filler particles in ethanol using laser diffraction (LA-960, Horiba Ltd.). To ensure comparability for all investigations, all specimens were taken from the center of the monolith at a height of ≈ 10 mm. The pore structure was investigated using scanning electron microscopy (SEM, field-emission SEM SUPRA 40, Zeiss, Germany) operating at 7.00 kV with specimens mounted on carbon tape. Samples were sputtered with gold (K550, Emitech, Judges Scientific Plc., UK) prior to the measurement. Pore size distribution and porosity were obtained by mercury intrusion porosimetry (Pascal 140/440, POROTEC GmbH, Germany). Compression tests were performed on cylindrical monolithic samples with a diameter of 9.5 mm to 9.6 mm and a height of 10 mm using a universal testing machine (Zwick/Roell 2005, Zwick, Germany). A constant displacement of 0.5 mm·min^{-1} was used and more than 9 samples of each composition were tested. The freezing direction was parallel to the cylinder axis. A steel half sphere with a diameter of 23 mm was placed on top of the specimen in order to minimize effects of superficial defects and misalignment. The force at the end of the elastic stage was used to calculate the compressive strength. Specific surface area was determined by evaluating nitrogen adsorption isotherms according to BET theory (Belsorp-Max, Bel Japan Inc., Japan). For nitrogen adsorption measurements the monolithic specimens were prepared by grinding and sieving with a 300 μm mesh. Furthermore, degassing of the powder at 120 °C for 3 h was carried out before starting the analysis. Measurements of vapor adsorption were performed by placing vessels with ≈ 1 g of monolithic samples in closed Erlenmeyer flasks filled with liquids. The liquids water and heptane were a measure of hydrophilic and hydrophobic surface characteristic, respectively. The liquids were at equilibrium with their vapor phase at 20 °C. Prior to the measurement, the samples were dried at 70 °C for 24 h. Weighing of the samples at the beginning and at the end of a 24 h measurement period allowed for determining the vapor uptake.

4.4 Results

4.4.1 Pore Morphology

4.4.1.1 Pore Structure

The pore structure depends heavily on the solvent and the freezing process. Figure 4.3 shows SEM images of the pore structure of samples without, with 25 vol% and 50 vol% of preceramic filler M1 pyrolyzed at 1000 °C. The images are representative for the samples with preceramic fillers and no differences in pore structure between pyrolysis at 600 °C and at 1000 °C were observed.
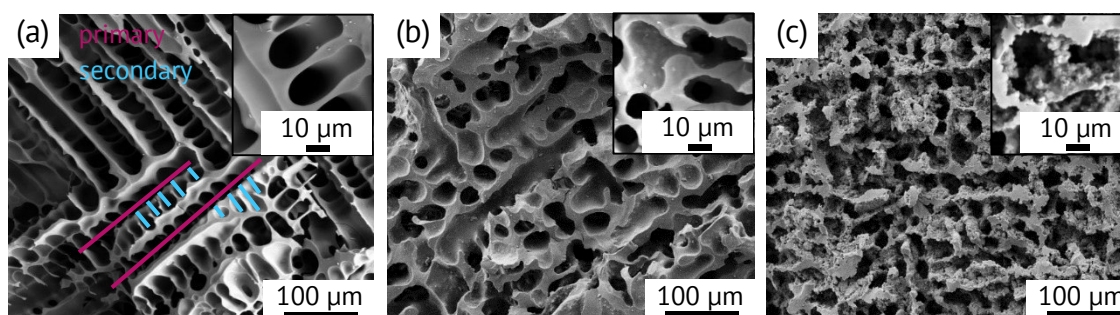

Figure 4.3 SEM images of the pyrolyzed monoliths at 1000 °C for increasing preceramic filler particle content, (a) Ref/1000, (b) 25M1/1000 and (c) 50M1/1000.

The preceramic filler particles are embedded in the pore walls in the case of the addition of 25 vol% filler. Whereas for increased filler content, the particles create rough pore wall surfaces. Since the size of filler particles observed in SEM and the measurement of particle size by laser diffraction is in good agreement, dispersion of the particles can be considered as good. Furthermore, no relevant sedimentation occurred during the time required for freezing the whole sample. Hence, dispersion and distribution of preceramic particles are assumed to be sufficient to prepare samples with homogeneous properties. In contrast, ceramic filler particles S and A lead to agglomeration of filler particles for 25S/600 and crack formation around platelets for 3.5A/1000, respectively (see Figure A.1.1 on page 192). Due to the decreasing viscosity of the solution with increasing filler content, the addition of 25 vol% and 50 vol% of alumina platelets results in sedimentation. Therefore, only 1.7 vol% and 3.5 vol% were investigated further. Furthermore, silica particles were used only as a reference with 25 vol%. Preceramic fillers H1 and H50 were added at contents of 25 vol% and 50 vol%. Since, the trend in results for 50 vol% matches very well with the one of 25 vol%, only the results of 25 vol% are reported here. With

intention to simplification and clarity only Ref, 25M1 and 50M1 are reported for a reduced pyrolysis temperature of 600 °C.
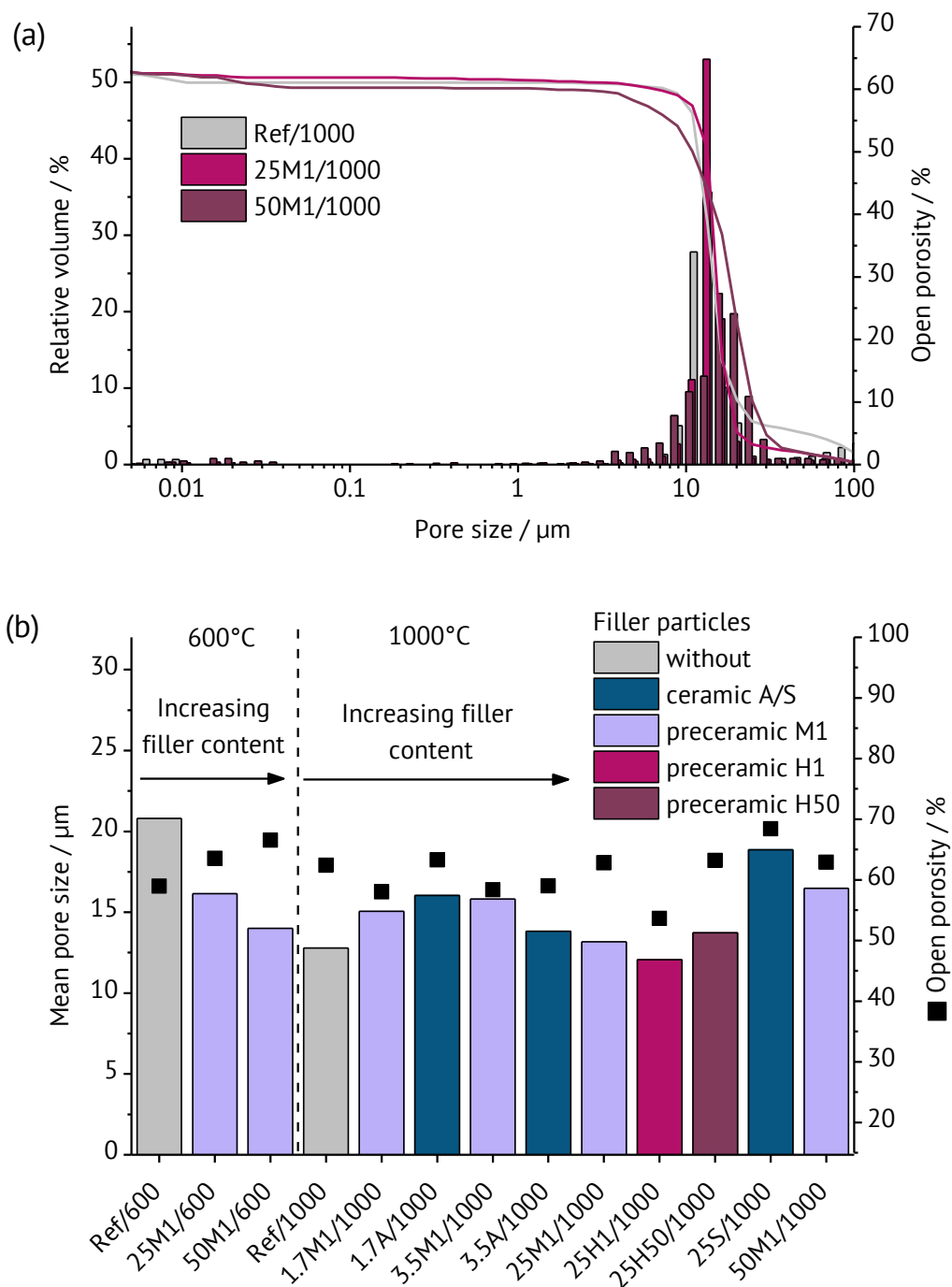

Figure 4.4 (a) Exemplary pore size distribution of Ref/1000, 25M1/1000 and 50M1/1000 as example for all other investigated samples; (b) mean pore size and open porosity for all samples investigated regarding strength.

The pore morphology is dendritic as it is characteristic for structures obtained using cyclohexane as solvent [22, 33]. In the structure without filler particles, primary and secondary dendrites can be easily identified. Whereas, with increasing content of filler particles the isotropy of the structure increases and the structure appears to be less ordered. Furthermore, the roughness of internal pore walls changes from smooth to very rough.

Besides SEM images, results of mercury intrusion porosimetry further characterize the pore structure. Figure 4.4 shows mean pore size and open porosity for all samples investigated regarding strength as well as representative pore size distributions in dependence of the filler particle concentration. Pore sizes range from 4 µm to 40 µm with a monomodal distribution for all samples. Whereas, the mean pore size and the open porosity is in the range of 13 µm to 21 µm and 60 % to 65 %, respectively. These almost constant parameters indicate no influence of the addition of filler particles on pore size distribution, mean pore size and open porosity.

4.4.1.2 Compressive Strength

In order to investigate the influence of the addition of filler on the mechanical properties of the samples, compression tests were performed. The results for different pyrolysis temperatures and different filler particles are shown in Figure 4.5. The same samples as in Figure 4.4 are reported here.

Independently on the addition of filler particles, strength drastically increases with increasing pyrolysis temperature. The strength of the reference sample rises from 6.5 MPa (600 °C) by a factor of 5.4 to 35 MPa (1000 °C). With enhancement factors of 6.6 and 11.4 the effect is even more pronounced for samples with 25 vol% and 50 vol% of preceramic M1 filler particles, respectively. Since the pore structure remains the same, the influence of the temperature on the material is supposed to be the reason for the difference. The increase in strength can be attributed to the higher density due to mineralization reactions in the temperature range from 600 °C to 1000 °C [34]. In mineralization reactions, carbon is inserted in the silica network via Si-C bonds leading to a densification of the SiOC(H) network, which enhances the mechanical strength [35]. Mechanical studies on dense SiOC material confirm this presumption [35].
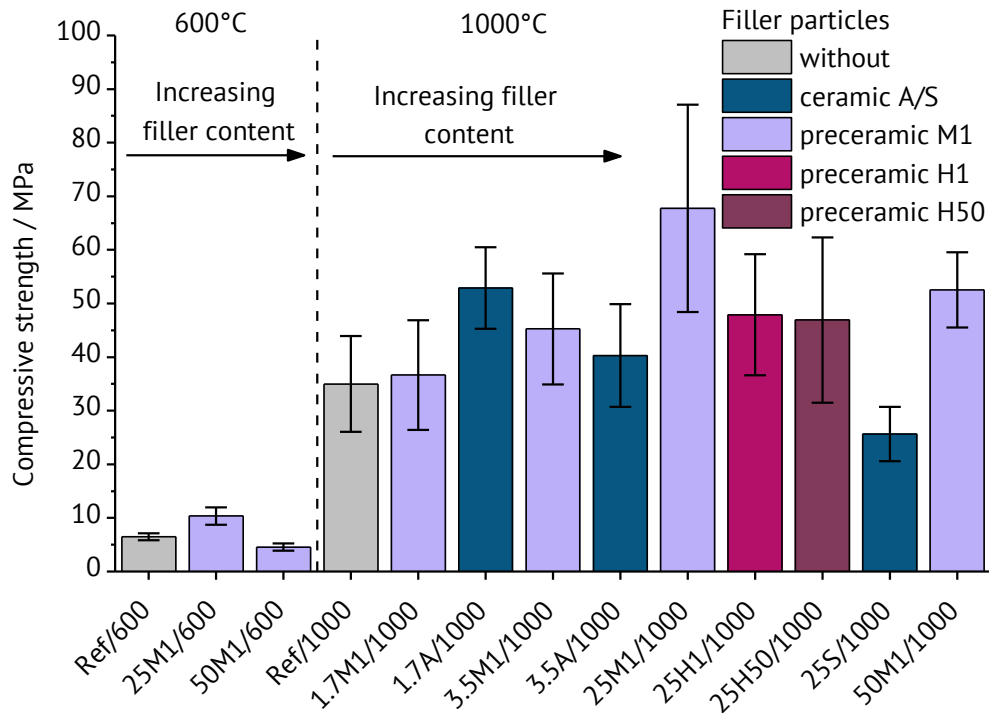
Figure 4.5 Compressive strength for samples without and with preceramic and ceramic filler particles pyrolyzed at different temperatures.

At both temperatures, the composition 25M1 shows the highest strength with factors of enhancement of 1.6 and 1.9 for 600 °C and 1000 °C, respectively. Whereas, an increase of filler particles to 50 vol% leads to a decrease of strength. Changing the composition of the preceramic filler particles from M1 to H1 and H50 reduces the strengthening effect to a factor of 1.3 at a filler content of 25 vol%. Due to differences in decomposition of H1 and H50 compared to the matrix, crack formation around the filler particles during pyrolysis is assumed to result in less enhancement. Weight loss at 1000 °C for the matrix and the filler H1 and H50 is 14.80 %, 25.09 % and 30.21 %, respectively. Since the matrix and filler M1 have the same composition, no cracks will form in 25M1 and 50M1.

With the ceramic filler S reducing the strength rather than increasing it, the preceramic filler M1 is the most effective at high filler concentrations. The reduced strength of samples with filler S is attributed to the formation of agglomerates. Due to its very hydrophilic surface characteristic, agglomerates of filler S prohibit the hydrophobic polymer solution to penetrate the interparticular volume. The resulting pores between the filler particles can be seen in Figure A.1.1 (a) on page 192. Those relatively large pores act as source of crack formation and reduce the strength.

Lowering the filler concentration to 1.7 vol% the ceramic filler A is more effective than M1. 1.7A/1000 has a factor of enhancement of 1.5, whereas 1.7M1/1000 does not show significant enhancement. No well-known strengthening/toughening mechanisms, such as crack deflection and crack bridging were observed for 1.7A/1000. Moreover, the pore morphology became more isotropic (see Figure A.1.2 on page 192). Slightly increasing the filler content from 1.7 vol% to 3.5 vol% leads to a reduction of strengthening effect to a factor of only 1.16 for 3.5A/1000. SEM images reveal cracks around the alumina platelets, as it can be seen in Figure A.1.1 (b) on page 192, while no cracks are observed for 1.7A/1000 and unpyrolyzed samples. Crack formation during pyrolysis can be explained by a difference in the coefficient of thermal expansion between the matrix ($\alpha_{SiOC} = 3.12 \times 10^{-6}\,K^{-1}$) and the alumina platelets ($\alpha_{Al2O3} = 7.2 \times 10^{-6}\,K^{-1}$ to $8.0 \times 10^{-6}\,K^{-1}$) of $\approx 4.5 \times 10^{-6}\,K^{-1}$ in the temperature range of RT to 1000 °C [36]. The induced stress during pyrolysis is proportional to the concentration of filler. It exceeds the strength of the matrix at platelet contents $\geqslant 3.5$ vol% leading to crack formation.

4.4.2 Control of Surface Functions

4.4.2.1 Specific Surface Area

With regards to the control of the surface characteristic, nitrogen adsorption isotherms were evaluated according to BET theory (Figure 4.6). Silica particles were used only as a reference with 25 vol%. Preceramic fillers were investigated only at contents of 25 vol% and 50 vol%. With intention to simplification and clarity only Ref and 50H1 are reported for an increased pyrolysis temperature of 600 °C.

Type II isotherms are observed for ceramic filler particles and samples pyrolyzed at 1000 °C, revealing a macroporous/non porous material without micropores. For pyrolysis temperatures of 600 °C nitrogen isotherms are of type I, indicating the presence of micropores (see Figure A.1.3 on page 193). Due to micropores, which are formed during pyrolysis by decomposition of organic groups, H1, H50 and Ref/600 show very high BET surface areas of $607 \pm 3\ m^2 \cdot g^{-1}$, $546 \pm 1\ m^2 \cdot g^{-1}$ and $451 \pm 1\ m^2 \cdot g^{-1}$, respectively. The phenyl group in the polymethylphenylsiloxane H44 decomposes below 600 °C, whereas the methyl group in H44 and MK is not decomposed at 600 °C [37]. Therefore, the use of phenyl containing H44 results in higher BET surface areas

compared to polymethylsiloxane MK [38, 39]. Furthermore, pure APTES has a BET surface area of 350 m² g⁻¹ and a negative effect on the BET surface area was found for the addition of APTES to MK [24]. Thus, it is possible to tailor the BET surface area of preceramic fillers by adapting their compositions. Since Ref/600 has the same composition as M1, addition of M1 to Ref/600 has no influence on the BET surface area.
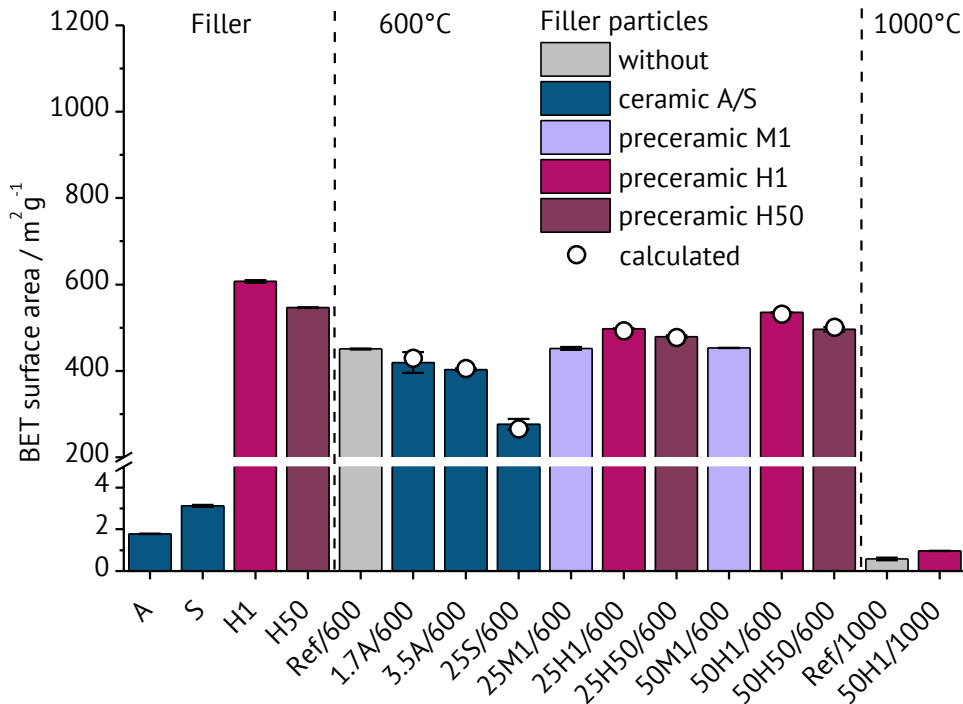
Figure 4.6 BET surface area for filler particles and samples with different filler particle content at different pyrolysis temperatures.

For samples with the ceramic fillers, H1 and H50, calculations of the expected BET surface area BET_{calc} were performed prior to the experiment (Equation 4.1). A linear rule of mixture was assumed using the volume fraction of the filler x and the BET surface areas of the matrix BET_{Ref} and of the filler BET_{Filler}:

$$BET_{calc} = (x - 1)\, BET_{Ref} + x\, BET_{Filler} \tag{4.1}$$

Calculated values are in the range of deviation for all samples. Hence, the addition of 50 vol% H1 increases the BET surface area with 18.8 % the most. On the other hand, adding 1.7 vol% and 3.5 vol% of filler A and 25 vol% of filler S reduces the BET surface area to 419 ± 24 m²·g⁻¹, 403 ± 3 m²·g⁻¹ and 276 ± 12 m²·g⁻¹, respectively. Due to the absence of microporosity the ceramic filler particles show very low BET surface areas,

which are reducing the overall BET surface area in the monolithic samples. At elevated pyrolysis temperatures of 1000 °C the micropores in the preceramic filler as well as in the matrix material collapse and the BET surface area is determined only by the macropores obtained by the freeze casting. Therefore, only very low BET surface areas of around 0.58 ± 0.05 m²·g⁻¹ are observed for Ref/1000.

4.4.2.2 Surface Characteristics

The addition of filler particles influences not only the BET surface area but also the surface characteristic regarding hydrophobicity/hydrophilicity. Figure 4.7 depicts the vapor adsorption ratio of water to heptane for filler particles and samples with different filler particle concentrations. Samples with ratios > 1 are considered to be more hydrophilic. The same samples as in Figure 4.6 are reported here.
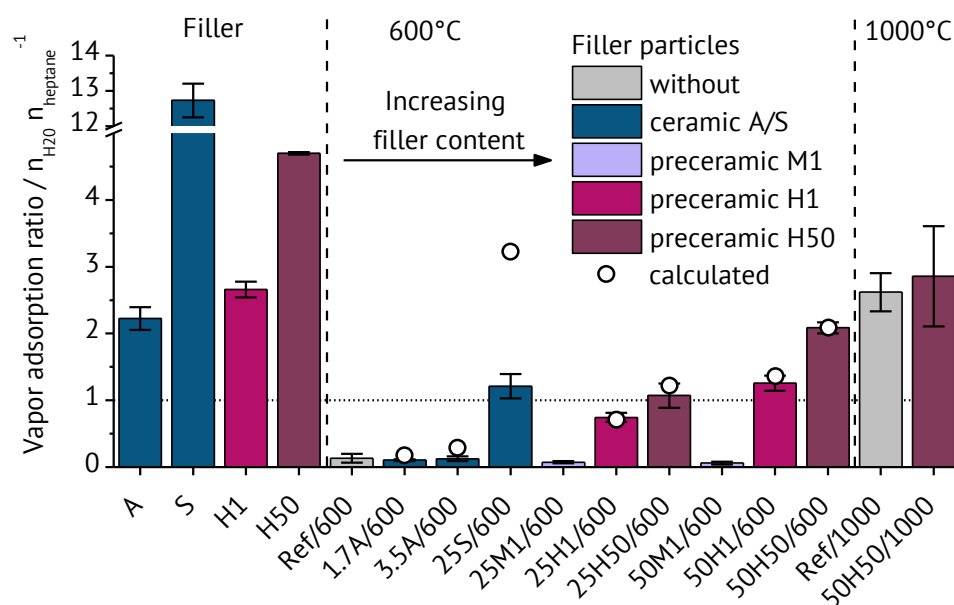
Figure 4.7 Vapor adsorption ratio water to heptane at 22 °C for filler particles and samples with changing content of filler particles at different pyrolysis temperatures.

All filler particles excluding M1, which has the same composition as Ref/600, show a more hydrophilic behavior. The ceramic oxidic fillers A and S are known to be hydrophilic, especially the silica filler S with a ratio of 12.7 ± 0.5. Due to the decomposition of the hydrophobic phenyl groups at 600 °C, also the preceramic fillers H1 and H50 show hydrophilic behavior [1, 37]. Additionally, an increase of APTES concentration in the filler particles enhances the hydrophilicity. Almost all amino

groups of APTES are decomposed at 600 °C, leading to the formation of hydrophilic silica [24]. In contrast to H1 and H50, M1 is not composed of phenyl groups, but of methyl groups which are thermally more stable and do decompose at 600 °C to a lower extent [37]. Hence, M1 retains its hydrophobic surface character at 600 °C with a ratio of 0.13 ± 0.06.

The addition of M1 shows no influence on the vapor adsorption ratio, since the composition of M1 and the matrix is identical. However, when adding 25 vol% H1 and H50 the hydrophilicity strongly increases to ratios of 0.74 ± 0.07 and 1.07 ± 0.18, respectively. The same observation applies for higher filler concentrations with ratios of 1.25 ± 0.11 and 2.08 ± 0.08 for 50 vol% of H1 and H50, respectively. Thus, H50 is the most effective preceramic filler for increasing the hydrophilic surface character with a ratio of water to heptane adsorption of roughly 1 already at 25 vol%. A linear rule of mixture was applied to calculate expected values for the vapor adsorption ratio, as it was done for the BET surface area, too (Equation 4.1). The calculated results are in the range of deviation for all samples except of 3.5A/600 and 25S/600. 3.5A/600 shows only a slight variation between experiment and calculation. Whereas 25S/600 differs strongly with a factor of 2.6 from the expected ratio. It reaches a ratio of 1.21 ± 0.18, which is only slightly higher than the most effective preceramic filler H50 at the same concentration. Elevated pyrolysis temperature of 1000 °C results in the complete decomposition of all organic groups, leading to hydrophilic SiOC structures without significant influence of the compositions of preceramic filler particles.

4.5 Discussion

4.5.1 Pore Morphology and Strength

The pore morphology can be widely changed when using the freeze casting process. Freezing front velocity has an influence on the pore size. Whereas solid loading affects not only the pore size, but also the overall porosity. Furthermore, the choice of the solvent greatly influences the pore morphology due to differences in the morphology of the growing solvent crystals. Possible morphologies ranges from lamellar for water, prismatic for *tert*-butyl alcohol [18], honeycomb for DMSO [19], cellular for benzoic acid [20] to dendritic for cyclohexane [21]. Even a greater variety of structures is possible when also considering additives which manipulate the crystallization behavior or mixtures of solvents [21, 40-42]. Also, the introduction of filler particles

to a solution-based freeze casting process changes the pore morphology, as it can be seen in Figure 4.3. With increasing amount of particles, the structure becomes more isotropic. Naviroj et al. assume that suspended particles are disrupting the dendritic solidification structure by inducing *noise* ahead of the freezing front [33]. The solidification microstructure can be affected by sufficient amount of noise ahead of the freezing front which disrupts the growth of the dendrite tips [43]. Hence, fractal patterns are created instead of regular ones. On the one hand, fluctuations in the thermal or solute field ahead of the solid-liquid interface can be considered as noise. On the other hand, also particles located at the dendritic tip can act as noise by creating small temperature fluctuations and direct contact. Naviroj et al. hypothesized, that particles with a size of 1 % of each dendrite tip will destabilize and break down the dendrite tips [33]. Since in the present case, the size of the filler particles is ≈ 20 % of the dendrites, it can be assumed that the decrease in anisotropy is caused by the addition of filler particles. Furthermore, the addition of filler particles can adjust the roughness of the pore walls. One application of porous media which is not investigated in this research is deep bed filtration. Increased pore wall roughness is supposed to be beneficial for deep bed filtration by increasing the impact possibility with the collector surface especially for particles in the range of 20 μm to 80 μm [44]. In addition, surface roughness hinders rolling, which is the dominant mechanism of detachment of spherical particles [45]. Therefore, surface roughness improves both, the probability of attachment and the resistance to detachment. It is worthwhile mentioning, that though the pore morphology and surface roughness greatly change, other properties of the pore structure like the pore size and the open porosity are kept constant.

Besides porosity and pore size, the pore morphology directly influences the mechanical properties of freeze cast samples [46]. Preliminary test revealed that the prismatic pore structure of *tert*-butyl alcohol shows a compression strength of only 5 MPa. Water as solvent with a lamellar structure leads also to low strength with values at around 6 MPa [47]. Since the prismatic structure of *tert*-butyl alcohol is less interconnected than the dendritic structure of cyclohexane the strength is reduced. Whereas, water is very sensitive to the formation of defects like ice lenses [48].

Similar considerations apply for the strengthening effect of filler addition. Since the mean pore size and porosity are kept constant in a narrow range for all samples, their

influence on the strength is negligible (Figure 4.4). Hence, the increase in strength is attributed to a change in the pore morphology showing enhanced isotropy. Another aspect is the reduction of elongated pores as a structural feature of filler addition. Assuming a discrepancy between the axis of pores and the axis of the applied load, the resistance against load out of crystal axis is increased by both of these structural properties. Load out of crystal axis results in shear stress between single pore channels. In filler free samples, the pore walls between elongated pore channels are rather thin leading to a low resistance. In contrast, addition of filler reduces this weak points by enhancing the isotropy and diminishing elongated pores. For high particle contents the formation of irregular shaped pore walls with notches in between the filler particles overbalance the strengthening effects. Additionally to notches, which can cause crack initiation, the pore wall thickness varies heavily as it can be seen in Figure 4.3. According to the principle of the weakest link, locations with low pore wall thickness reduce the overall strength. Since the strengthening effect is based on changes in the pore morphology, it should be independent on the pyrolysis temperature, which is confirmed by Figure 4.5. At both temperatures the strength is increased by a factor of 1.63 and 1.75, respectively.

Comparing the influence of the platelet shaped filler A and the preceramic filler M1 at concentrations of 1.7 vol%, it becomes obvious that the addition of platelets is more effective than the addition of spherical particles for increasing the strength at low particle concentrations. Hence, the platelets manipulate the pore morphology to a greater extend at the same concentration. They have a slightly higher particle size, but especially a highly different shape compared to the spherical fillers. It can be assumed, that the platelet like shape creates more *noise* at the freezing front, resulting in higher disruption of the dendrite tips. Moreover rejection of platelets by growing crystals is more difficult due to spherical reasons and larger particle size [49].

Recent research on the strengthening effect of platelets in water based freeze cast structures found, that addition of platelets changes the pore structure by creating bridges between lamellar pore walls [50]. Although the effect of changing the pore morphology reported in the current work is not as pronounced as for research done with lamellar structures, the influence on the strength is emphasized.

4.5.2 Control of Surface Functions

Besides the pore morphology, also functional properties can be altered using filler particles with different functional properties compared to the matrix material. Figure 4.6 shows a significant influence of the filler composition on the BET surface area. Considering as well the good correlation between experimental data and calculations, it can be stated that the filler particles are accessible. Due to the microporous matrix material, filler particles are not sealed by the surrounding matrix. Thus, highly precise tailoring of the BET surface area in a wide range between 276 $m^2 \cdot g^{-1}$ and 535 $m^2 \cdot g^{-1}$ is possible by adjustment of the filler concentration as well as the filler composition.

Filler particles not only differ in BET surface area, but also in their hydrophilicity. As shown in Figure 4.7 the hydrophilicity depends on the chemical composition of the filler as well as on the pyrolysis temperature. The influence of the filler particles on the vapor adsorption reveals that the particles are not sealed or covered by the surrounding matrix. In fact, they are accessible and influence the surface characteristic of the monolithic sample. The comparison of experimental data with calculations reveal a good agreement for all samples except of sample 25S/600. While 25S/600 exhibits a discrepancy between calculation and experiment in hydrophilicity, no difference was observed for BET surface area. In contrast to the measurement of the BET surface area, the adsorption measurement investigated only the surface but not the volume of the pore walls. Hence, the concentration of the filler particles at the surface must be the same as in the volume to obtain a good agreement between calculation and experiment for the vapor adsorption. However, SEM images show that agglomerates of filler particles are present in 25S/600 (see Figure A.1.1 on page 192). Compared to the assumption of homogeneous distribution, more filler particles are embedded in the pore walls where they are not accessible in the vapor adsorption measurement. Therefore, the deviation between experiment and calculation can be explained by a heterogeneous distribution of filler particles in 25S/600 with less particles at the pore wall surface. Nevertheless, the addition of filler particles allows for adjusting the hydrophilicity very precisely in case of homogeneous distribution of particles. In dependence of the filler composition and concentration, ratios of water to heptane adsorption between 0.07 and 2.08 are possible.

4.5.3 Overview: Dependence of Properties on Filler Particles

The current work shows, that single properties can nicely be altered by adding specific filler particles. However, for designing a material focusing on a defined application, the influence of the filler on all other properties has to be taken into account as well. Figure 4.8 gives assistance to overview the influence of filler particles on the compression strength, the BET surface area and the vapor adsorption ratio of water to heptane by providing plots for (a) the ceramic filler particles and (b) preceramic filler particles with regard to the investigated properties. Figure 4.8 (c) depicts the investigated properties with regard to the filler particles.
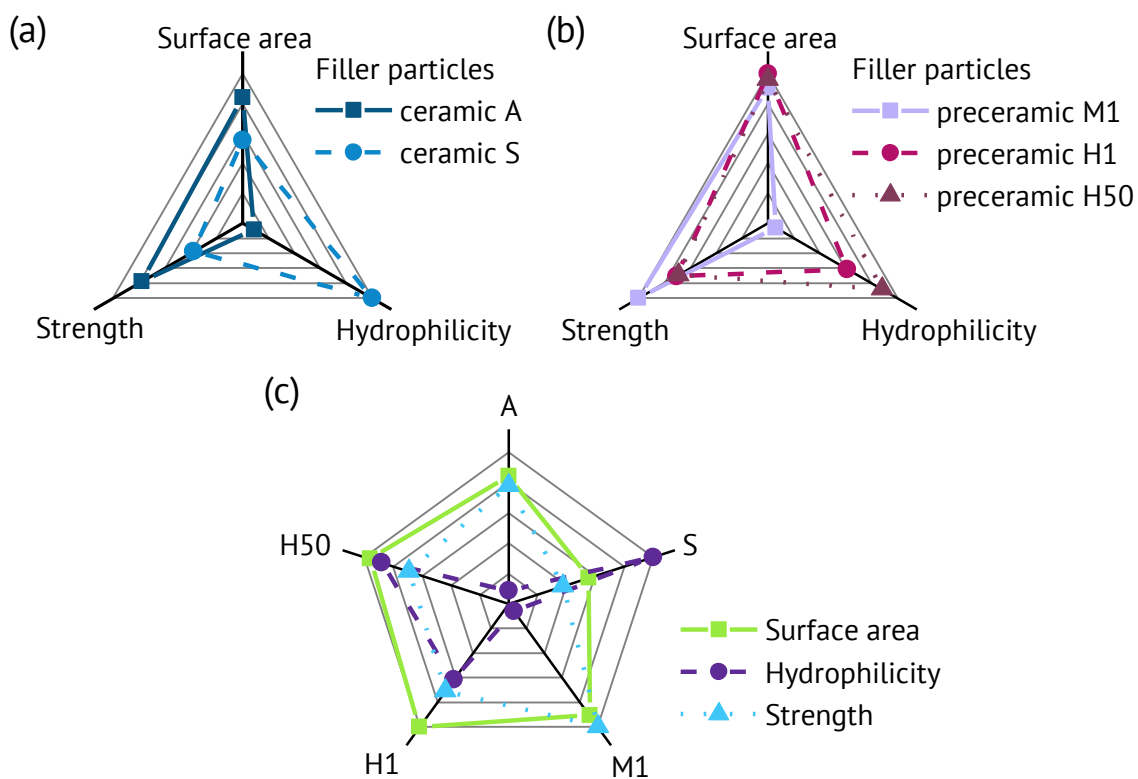
Figure 4.8 Radarplots at filler concentrations of 25 vol% for M1, H1, H50 and S and 1.7 vol% for A at a pyrolysis temperature of 600 °C for BET surface area and hydrophilicity and 1000 °C for strength showing the investigated properties as a percentage of the maximum value (a) for ceramic filler particles and (b) for preceramic filler particles with regard to the investigated properties; (c) surface area, strength and hydrophilicity as a percentage of the maximum value with regard to the filler particles.

Though less effective than calculated, the ceramic filler S is most efficient to increase the hydrophilicity at 600 °C closely followed by the preceramic filler H50. M1 shows the highest strengthening effect at 25 vol%, but at lower concentrations A is more effective to enhance the strength. Whereas, H1 increases the BET surface area the most with values up to $535 \pm 1\ m^2 \cdot g^{-1}$.

4.6 Conclusion

The addition of filler particles allows for adjusting several parameters in dependence on the filler composition and concentration: pore morphology, compressive strength, BET surface area and hydrophilicity. During freezing, filler particles create small temperature fluctuations and direct contact at the dendrite tips and therefore disrupt the growth of the solvent crystals. As a result, the pore morphology changes from anisotropic for pure solution-based to more isotropic for the addition of filler particles. The increase in compressive strength by a factor of 1.9 is attributed to the modified pore morphology. Less anisotropy and reduced elongated pores lead to enhanced resistance against load out of axis. The shape of the particles was found to influence their effect on the pore structure. Hence, platelet shaped filler particles are more effective to modify the structure at low concentrations compared to spherical ones.

The temperature difference between the decomposition of methyl and phenyl groups in the preceramic fillers enables the adjustment of BET surface area as well as hydrophilicity. Especially for H1, enhanced decomposition without the collapse of micropores leads to higher BET surface areas. Moreover, reduction of the organic hydrophobic groups by decomposition results in increased hydrophilicity which is most pronounced for H50. The prediction of properties by a linear rule of mixture is very precise for homogeneously distributed filler particles. This is a prerequisite for efficient design of materials. Whereas, the agglomeration of filler particles S leads to deviations in hydrophilicity between calculation and experiment. Nevertheless, the ceramic filler S is very effective in increasing the hydrophilicity. The main criterion to allow for adjusting functional properties is the accessibility of the filler particles, which was confirmed to exist. Therefore, highly accurate adjustments of BET surface area and hydrophilicity over a wide range are possible. The gained knowledge of the several dependencies between filler composition and filler content on the one hand and their effect on the properties on the other hand allows for an efficient design of materials. The results show, that optimization of one property by filler addition leads to changes of other properties. With the presented results it is possible to tackle this problem in its entirety.

The versatile approach to add filler particles to solution-based freeze casting enables to tailor macroporous monolithic samples according to the requirements of specific

applications. For filter applications, the possibility to add pore wall roughness and simultaneously change the hydrophilicity is promising to adapt the filter to the medium and enhance the filter efficiency. Furthermore, the combination of different filler particles or the incorporation of other functionalities create even more freedom in tailoring the material.

Acknowledgments

References

[1]   F. Xue, K. Zhou, N. Wu, H. Luo, X. Wang, X. Zhou, Z. Yan, I. Abrahams, D. Zhang, Ceram. Int. 44 (2018) 6293-6299.

[2]   T. Fukasawa, M. Ando, T. Ohji, J. Ceram. Soc. Jpn. 110 (2002) 627 - 631.

[3]   N. MacDowell, N. Florin, A. Buchard, J. Hallett, A. Galindo, G. Jackson, C.S. Adjiman, C.K. Williams, N. Shah, P. Fennell, Energy Environ. Sci 3 (2010) 1645-1669.

[4]   S.D. Kenarsari, D. Yang, G. Jiang, S. Zhang, J. Wang, A.G. Russell, Q. Wei, M. Fan, RSC Advances 3 (2013) 22739-22773.

[5]   B.A. Haberman, J.B. Young, Int J Heat Mass Tran 47 (2004) 3617-3629.

[6]   J.R. Woodard, A.J. Hilldore, S.K. Lan, C.J. Park, A.W. Morgan, J.A.C. Eurell, S.G. Clark, M.B. Wheeler, R.D. Jamison, A.J.W. Johnson, Biomaterials 28 (2007) 45-54.

[7]   S. Heidenreich, Fuel 104 (2013) 83-94.

[8]   A.R. Studart, U.T. Gonzenbach, E. Tervoort, L.J. Gauckler, J. Am. Ceram. Soc. 89 (2006) 1771-1789.

[9]   P. Colombo, C. Vakifahmetoglu, S. Costacurta, J. Mater. Sci. 45 (2010) 5425-5455.

[10]   E.C. Hammel, O.L.R. Ighodaro, O.I. Okoli, Ceram. Int. 40 (2014) 15351-15370.

[11]   K. Araki, J.W. Halloran, J. Am. Ceram. Soc. 88 (2005) 1108-1114.

[12]   S. Deville, Adv. Eng. Mater. 10 (2008) 155-169.

[13]   S. Deville, J. Mater. Res. 28 (2013) 2202-2219.

[14]   R. Liu, T. Xu, C. Wang, Ceram. Int. 42 (2016) 2907-2925.

[15] S. Deville, E. Saiz, A.P. Tomsia, Acta Mater. 55 (2007) 1965-1974.

[16] T. Waschkies, R. Oberacker, M.J. Hoffmann, Acta Mater. 59 (2011) 5135-5145.

[17] D. Ghosh, M. Banda, H. Kang, N. Dhavale, Scripta Mater. 125 (2016) 29-33.

[18] R. Chen, C.-A. Wang, Y. Huang, L. Ma, W. Lin, J. Am. Ceram. Soc. 90 (2007) 3478-3484.

[19] Y. Chu, Z. Lu, J. Li, Y. Zhu, S. Zhang, J. Chen, Polym. Adv. Technol. 26 (2015) 606-612.

[20] J. Yue, B. Dong, H. Wang, P. Colombo, J. Am. Ceram. Soc. 94 (2011) 1989-1991.

[21] K.L. Scotti, D.C. Dunand, Prog. Mater Sci. 94 (2018) 243-305.

[22] M. Naviroj, S.M. Miller, P. Colombo, K.T. Faber, J. Eur. Ceram. Soc. 35 (2015) 2225-2232.

[23] P. Colombo, G. Mera, R. Riedel, G.D. Sorarù, J. Am. Ceram. Soc. 93 (2010) 1805-1837.

[24] H. Zhang, C.L. Fidelis, A.L.T. Serva, M. Wilhelm, K. Rezwan, J. Am. Ceram. Soc. 100 (2017) 1907-1918.

[25] H. Zhang, P. D'Angelo Nunes, M. Wilhelm, K. Rezwan, J. Eur. Ceram. Soc. 36 (2016) 51-58.

[26] Q. Wang, B. Dai, J. Bai, Z. Yang, S. Guo, Y. Ding, L. Yang, P. Lei, J. Han, J. Zhu, Mater. Des. 111 (2016) 9-16.

[27] J. Rong, T. Zhang, F. Qiu, J. Xu, Y. Zhu, D. Yang, Y. Dai, Mater. Des. 142 (2018) 83-92.

[28] G. Godeau, C.R. Szczepanski, T. Darmanin, F. Guittard, Mater. Des. 92 (2016) 911-918.

[29] Z. Chen, G. Li, L. Wang, Y. Lin, W. Zhou, Mater. Des. 141 (2018) 37-47.

[30] O.A. Al-Harbi, M. Mujtaba Khan, C. Özgür, Mater. Des. 96 (2016) 296-303.

[31] B.-H. Yoon, E.-J. Lee, H.-E. Kim, Y.-H. Koh, J. Am. Ceram. Soc. 90 (2007) 1753-1759.

[32] P.M. Hunger, A.E. Donius, U.G. Wegst, J Mech Behav Biomed Mater 19 (2013) 87-93.

[33] M. Naviroj, P.W. Voorhees, K.T. Faber, J. Mater. Res. 32 (2017) 3372-3382.

[34] L. Bois, J. Maquet, F. Babonneau, H. Mutin, D. Bahloul, Chem. Mater. 6 (1994) 796-802.

[35] S. Walter, G.D. Soraru, H. Bréquel, S. Enzo, J. Eur. Ceram. Soc. 22 (2002) 2389-2400.

[36] T. Rouxel, G. Massouras, G.-D. Soraru, J. Sol-Gel Sci. Technol. 14 (1999) 87-94.

[37] M. Scheffler, T. Gambaryan-Roisman, T. Takahashi, J. Kaschta, H. Muenstedt, P. Buhler, P. Greil, Ceram Trans 115 (2000) 239-250.

[38] T. Prenzel, M. Wilhelm, K. Rezwan, Chem. Eng. J. 235 (2014) 198-206.

[39] T. Prenzel, M. Wilhelm, K. Rezwan, Microporous Mesoporous Mater. 169 (2013) 160-167.

[40]   C. Guizard, J. Leloup, S. Deville, M.A. White, J. Am. Ceram. Soc. 97 (2014) 2020-2023.

[41]   J. Zeng, Y. Zhang, K.-c. Zhou, D. Zhang, Trans. Nonferrous Met. Soc. China 24 (2014) 718-722.

[42]   M.N. Rahaman, Q. Fu, J. Am. Ceram. Soc. 91 (2008) 4137-4140.

[43]   E. Brener, H. Muller Krumbhaar, D. Temkin, Phys Rev E 54 (1996) 2714-2722.

[44]   F. Heuzeroth, J. Fritzsche, E. Werzner, M.A.A. Mendes, S. Ray, D. Trimis, U.A. Peuker, Powder Technol. 283 (2015) 190-198.

[45]   S.K. Das, R.S. Schechter, M.M. Sharma, J. Colloid Interface Sci. 164 (1994) 63-77.

[46]   S. Deville, S. Meille, J. Seuba, Sci. Technol. Adv. Mater. 16 (2015) 43501-43516.

[47]   H. Zhang, C.L. Fidelis, M. Wilhelm, Z. Xie, K. Rezwan, Mater. Des. 134 (2017) 207-217.

[48]   A. Lasalle, C. Guizard, E. Maire, J. Adrien, S. Deville, Acta Mater. 60 (2012) 4594-4603.

[49]   U.G. Wegst, M. Schecter, A.E. Donius, P.M. Hunger, Philos Trans A Math Phys Eng Sci 368 (2010) 2099-2121.

[50]   D. Ghosh, H. Kang, M. Banda, V. Kamaha, Acta Mater. 125 (2017) 1-14.

Relationship between Pore Structure and Wicking

<div style="text-align:right">5</div>

The knowledge of the possibilities to influence the pore structure by adding fillers which was shown in the previous chapter is an excellent base to manufacture porous monoliths with different structural motifs and test these pore structures on their capillary transport ability. In contrast to ceramic fillers, preceramic filler particles proofed to enable crack free monoliths. Several applications such as heat pipes and propellant management devices rely on the resulting macroporous structure and its capillary transport ability. The knowledge of the relation between the pore structure and the capillary transport behavior is of importance for an effective design of capillary active components. The high flexibility in terms of the pore structure in solution-based freeze casting enables to generate a variety of pore structures with variations in the pore morphology, the porosity and the condition of the external surface. In the following chapter, the impact of these structural changes on the wicking behavior is investigated by means of isothermal wicking at room temperature as can be seen schematically in Figure 5.1. Additionally, the applicability of predicting the wicking performance of complex 3D structures with the Lucas-Washburn equation is evaluated.

Daniel Schumacher[†], Dawid Zimnik[†], Michaela Wilhelm, Michael Dreyer, Kurosch Rezwan; Solution-based freeze cast polymer-derived ceramics for isothermal wicking - relationship between pore structure and imbibition; Science and Technology of Advanced Materials 20 (2020) 1207-1221, DOI: 10.1080/14686996.2019.1699766

[†] Equal authorship

5.1 Abstract

Besides conventional applications for porous monoliths such as filtration, open porosity enables capillary transport. For this application, porous polymer-derived ceramic monoliths (SiOC) with different pore morphology and porosity were obtained by solution-based freeze casting. Polymethylsiloxane and (3-aminopropyl)triethoxy-silane were used as precursor and cross-linking agent, respectively. *Tert*-butyl alcohol and cyclohexane acted as solvents and created prismatic and dendritic pore morphology. Additionally, differences in solid loading and the addition of preceramic filler particles changed the open porosity from 62 % to 79 %, the mean pore window diameter from 11 µm to 21 µm and the isotropy. The lateral surface of the monoliths is mainly closed due to the use of a Si-coated film as an intermediate layer which prevents nucleation. Within the parameters characterizing the pore structure, open porosity and pore window diameter were found to be most influencing on wicking tested by the Washburn-Sorption method. The permeability was obtained by constant head experiments and from the viscous-dominated part of the wicking curve. Furthermore, predictions of wicking using the Lucas-Washburn equation with gravity effect which bases on the assumption of capillary bundles were conducted. Wicking experiments showed that describing a real porous structure by macroscopic parameters may not be sufficient for structures deviating strongly from the assumption of capillary bundles. The combination of prediction with the knowledge of main influencing factors allows for tailoring the pore structure of SiOC monoliths prepared by solution-based freeze casting for capillary transport applications.
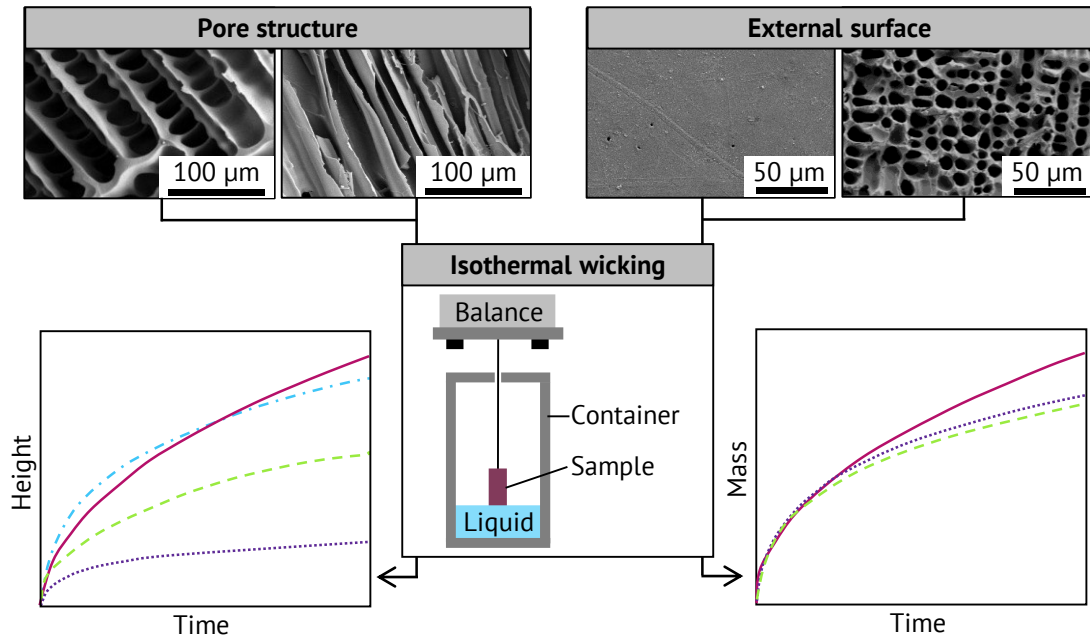
Figure 5.1 Illustration of the influence of variations in pore structure and the external surface on the wicking behavior at room temperature.

5.2 Introduction

Porous monolithic materials are required in a wide range of industries including energy and manufacturing. In order to enable mass transport, high permeability is a prerequisite for applications, such as catalysis, gas adsorption, water filtration, energy storage/conversion or even tissue engineering [1-7]. Besides these applications, the aerospace industry uses porous materials in propellant management devices or liquid acquisition devices for phase separation to ensure gas-free liquid delivery to the engines [8, 9]. The liquid is transported by the capillary pressure in the pores of the porous material to rewet parts of the screen that dry out. A saturated porous medium prevents the penetration of gas, as long as the bubble point pressure is not exceeded. Imbibition is commonly defined as the displacement of a non-wetting fluid by a wetting fluid in a porous medium. Wicking is used to make a statement about the capillary-driven transport ability in porous materials.

Nowadays, metallic screens are used as porous materials in propellant management devices with a structured porous structure. But nonmetallic inorganic materials for transport processes may offer advantages compared with the metallic screens. Properties such as chemical and thermal stability, corrosion resistance, controllable surface characteristics, relatively low density and low thermal conductivity make the

application of porous ceramics for capillary transport a potential alternative. Moreover, the lower thermal conductivity compared to metals reduces the risk of diminished wicking behavior due to evaporation in non-isothermal cryogenic conditions [10, 11]. Furthermore, it is possible to adjust the pore structure of ceramic parts, e.g. the pore size, the porosity and the pore morphology by applying different pore shaping methods like replica processes, additive manufacturing, sacrificial templating, direct foaming and phase separation [12, 13]. Additionally, even the production of parts in final shape is possible, which can reduce the production and maintenance costs.

Some research was already done on the wicking of porous nonmetallic inorganic material. Einset [14] investigated the capillary rise in carbonaceous porous media of similar pore structure using various liquids. The height over time was measured by an optical method and was used to determine the infiltration of the porous material. Capillary rise of organic liquids into 3D-stitched fibrous carbon preforms with the same pore structure was investigated by Kumar et al. [15] using the optical measurement to obtain the increasing liquid front in the porous ceramic. They measured the flow rate of water through the porous material and calculated the permeability of it. In a second paper, Kumar et al. [16] investigated the capillary infiltration rates of silicone into fibrous carbon preforms. Okada et al. investigated the capillary rise properties of porous mullite ceramics [17] and geopolymers [18] prepared by an extrusion method using water as test liquid. The investigated mullite ceramics showed a fair alignment of cylindrical pores running parallel to the extrusion direction. The liquid rise within the sample was recorded with an optical measurement. Popa et al. [19] also investigated the capillary rise properties of porous mullite ceramics prepared by an extrusion method. The capillary rise height was measured by optical observation, using water as the test liquid.

Compared to conventional ceramics such as alumina, titania and mullite polymer-derived ceramics offer some advantages. Significantly reduced thermal conductivity ensures benefits in capillary transport at cryogenic conditions and lower pyrolysis/sintering temperatures provide advantages in terms of environment and costs [20]. Furthermore, incomplete decomposition of the organic groups at low pyrolysis temperatures results in the creation of micropores and allows for the adjustment of the surface characteristic, e.g. hydrophilicity. The unique adjustment

of micropores and hydrophilicity by pyrolysis temperature enables additional possibilities to adapt the material to specific capillary transport applications. In contrast to conventional powder-based fabrication methods preceramic polymers offer a great versatility in shaping techniques. Also, shaping methods assigned to polymers such as solution-based freeze-casting can be used [21].

The process of freeze casting, which is a templating method, allows to vary the properties of porous structures in a wide range. Hence, it has attracted considerable interest in recent years [22-25]. Though most research is carried out on dispersed particles (suspension-based freeze casting), solution-based freeze casting of preceramic polymers shows great potential in creating promising pore structures. Rather than rejection and entrapment of particles, thermally induced phase separation is the segregation mechanism in solution-based freeze casting [26]. Generally, pores are created by phase separation of a two-component system during freezing and the subsequent sublimation of the solvent crystals. At the beginning of solution-based freeze casting, a soluble phase e.g. preceramic polymer, is dissolved in a liquid phase. Freezing of the solution results in crystallization of the liquid phase and depletion of liquid phase around growing crystals. Consequently, the volume between the solvent crystals depletes completely in the liquid phase and enriches in the solid phase. After completely frozen, sublimation removes the solidified liquid phase and thereby creates the porous structure which reflects the shape of the crystals. To a great extent, the liquid phase defines the pore morphology, ranging from cellular to lamellar, dendritic or prismatic [25, 27-29].

Very little is known about wicking in porous polymer-derived SiOC ceramics. Grebenyuk et al. [30] investigated the influence of pore size on the wicking of SiOC ceramics prepared by suspension-based freeze casting using water as dispersing medium. The sample weight was monitored to record the penetrated liquid into the porous structure. Increasing permeability for increasing pore size was observed. Additionally, a good agreement with theoretical predictions according to Lucas-Washburn equation was found for all samples. While the impact of important parameters characterizing the pore structure on the wicking behavior was investigated for porous materials which can be described by the fractal theory [31, 32]. Pore morphology, anisotropy and open porosity are properties which are supposed to have a great influence on wicking.

In this study, the investigation of the influence of different pore structures on isothermal wicking of porous SiOC monoliths prepared by solution-based freeze casting was conducted. Solution-based freeze casting of preceramic polymers enables to adjust important pore structure-related parameters independently in a wide range and hence allows to study the impact of parameter variations. Furthermore, the effect of different lateral surface conditions on wicking can be investigated by using solution-based freeze casting. The intention of the closed lateral surface is preventing dry out of the structure in capillary transport applications.

5.3 Experimental Section

5.3.1 Materials

Porous ceramic monoliths were prepared by freeze casting. All filler free samples were prepared by solution-based freeze casting, whereas a modified solution-based freeze casting process was used for the samples containing preceramic filler particles. Details to this process can be found elsewhere [33]. A commercial polymethylsiloxane (Silres® MK, Wacker Chemie AG, Germany) was used together with (3-aminopropyl)-triethoxysilane (APTES, abcr GmbH, Germany) as a cross-linking agent. Cyclohexane (CH, > 99 %, Sigma-Aldrich Chemie GmbH, Germany) and *tert*-butyl alcohol (TBA, > 99 %, Thermo Fisher GmbH, Germany) acted as solvents. The chemical structures are displayed in Figure 5.2 on page 91 and comprehensivly listed on page 191. All raw materials were used without further treatment or purification. The preceramic filler particles were prepared using the same composition as the matrix. After homogenization and drying, the fillers were cross-linked and ball milled to a mean particle size of $d_{50} = 2.63\,\mu m$ to $3.34\,\mu m$. A detailed description of the filler preparation can be found elsewhere [33].

5.3.2 Freeze Casting

The preparation of monolithic samples by solution-based freeze casting is depicted in Figure 5.1. In case of filler containing samples, filler particles were added first to the solvent under vigorous stirring. To ensure the liquid state of the solvent, TBA ($T_m = 23\,°C$ to $26\,°C$) was heated to $50\,°C$ in an oil bath. Whereas, CH ($T_m = 6.5\,°C$) was used at room temperature without any external heating. After the addition of MK and homogenization for 30 min under stirring, APTES was added as a cross-linking agent

at an amount of 1 mol%. Stirring was continued for 3 min to ensure a good distribution of AP. Subsequent degassing at 300 mbar for 30 s removed gas bubbles created during stirring. The solution was poured into a mold, which consists of a brass bottom and a PVC rod with an inner diameter of 20 mm and a height of 60 mm. A silicon-coated PET film (Hostaphan RN 30 2SLK, Mitsubishi Polyester Film GmbH, Germany) was used as a separation layer between solution and rod.
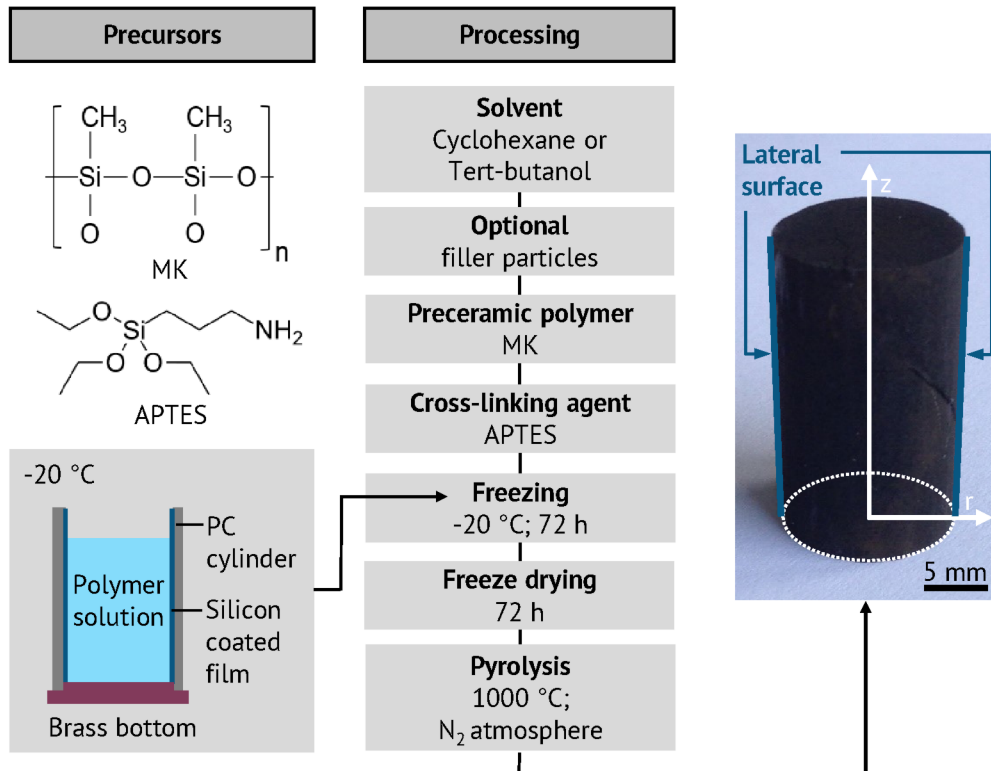
Figure 5.2 Process scheme of monolith preparation by solution-based freeze casting of polymeric solutions.

After casting, the mold was transferred to a freezer at −20 °C. The mold remained at the freezer for 72 h to enable easy demolding without changing the geometry of the sample. Cross-linking is slowed down due to the low temperature and hence longer times are necessary for sufficient cross-linking. After demolding, the solvent was sublimated in a freeze dryer for 72 h at −20 °C shelf temperature and a pressure of 1000 μbar. Finally, the monoliths were pyrolyzed at 1000 °C under the flow of nitrogen with a heating rate of 2 K·min^{-1} and a dwelling time of 4 h. For wicking experiments the both ends in z-direction were removed to ensure an open and flat cross section as inlet available. After complete characterization of the as prepared

specimens, the outside layer of the lateral surface was removed by a file. Subsequently, cleaning using compressed air and an ultrasonic bath removes grinding remainings. Due to the very low thickness of the dense outside layer, the sample radii before and after removing the dense outside layer were considered to be equal.

The labeling "EC" (experimental closed) and "EO" (experimental open) refers to the condition of the sample and depicts the as prepared lateral surface and the lateral surface after removal of the outside layer, respectively. Furthermore, "N" indicates results obtained by numerical calculations. The samples were given the nomenclature: [solvent] [solid loading in wt%] / [preceramic filler content in vol% of solid] _ [condition of sample]. Whereby, the polymeric precursor, the cross-linking agent and the filler particles counted as solid fraction. Table 1 gives an overview of all samples and their compositions.

Table 5.1 Labeling and composition for studied samples.

Sample labeling	Solvent	Solid loading	Filler loading	Condition of sample[a]
		wt%	vol%	XXX
CH20/0_XXX	Cyclohexane	20	0	EC/EO/N
CH40/0_XXX	Cyclohexane	40	0	EC/EO/N
TBA40/0_XXX	*Tert*-butyl alcohol	40	0	EC/EO/N
CH40/50_XXX	Cyclohexane	40	50	EC/EO/N

[a] EC = experimental closed; EO = experimental open, N = numerical results

5.3.3 Characterization

The pore structure was investigated using a scanning electron microscope (SEM, field-emission SEM SUPRA 40, Zeiss, Germany) operated at 10 kV with specimens mounted on carbon tape. Samples were sputtered with gold (K550, Emitech, Judges Scientific Plc., UK) prior to the measurement. Pore window diameter distribution and effective open porosity ϕ were obtained by mercury intrusion porosimetry (Pascal 140/440, POROTEC GmbH, Germany). To ensure comparability, the specimens were taken from the position $r = 0$ mm and $z = 10$ mm referring to the coordinate system depicted in Figure 5.2. Three specimens of each sample were tested. For the evaluation of the wicking results, the static radius R_s was considered to be equal to the average pore window diameter $R_{merc} = R_s$.

The Washburn sorption method was used to study the wicking process in porous media. The whole cylindrical samples were used for this characterization. To ensure a homogeneous and well accessible pore structure at the top and bottom, 2 mm were cut from the top and bottom. While the top and bottom are open for fluid flow, the outer side was closed or open. During the measurement, the temporal mass increase was recorded. Figure 5.3 shows the experimental setup for the wicking experiment.
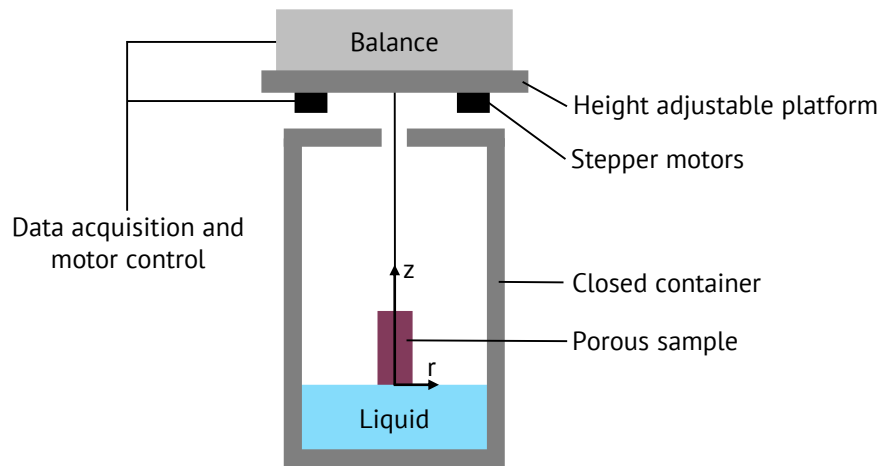
Figure 5.3 Schematic representation of the experimental wicking device.

The weight of the porous samples was measured using a high precision balance (LA310S, Sartorius AG, Germany) with a precision of ± 0.0001 g. The balance was mounted on a height-adjustable platform. This platform could be moved in the vertical direction with two stepper motors (VRDM566/50, Berger Lahr/Schneider Electric). The porous sample was attached to a sample holder, which is attached to the balance from beneath over a metallic wire. The porous sample was placed inside a container with a diameter of 9.5 cm. The lid of the container has a small hole allowing for a frictionless movement of the sample. The container was partially filled with a hydrofluoroether (HFE-7500, 3M Fluorinert™). The liquid properties of HFE-7500 are summarized in Table 5.2. It shows perfect wetting characteristic with different materials. Therefore, a zero contact angle was assumed with the used material, giving $\cos(\theta) = 1$ [10].

Table 5.2 Liquid properties of HFE-7500 and water at 298.15 K and 101325 Pa. Source: Product data sheet of supplier 3M.

Liquid	Surface tension σ 10^{-3} $N{\cdot}m^{-1}$	Density ρ $kg{\cdot}m^{-3}$	Dynamic viscosity μ 10^{-3} $Pa{\cdot}s$
HFE-7500	16.2	1614	1.24
Water	–	998	1.00

The vertically oriented sample was brought into contact with the liquid using the height-adjustable platform. The immersion process was stopped on the first contact with the liquid surface. This leads to the fact that only the bottom of the sample was in contact with the liquid. Wicking begins immediately at the first contact between the porous sample and liquid. The liquid imbibes into the porous material, which increases the mass of the porous sample. This increasing mass was recorded by the balance cell with a sample rate of 20 Hz. This process continues until an equilibrium state was reached or the porous sample appears to be completely saturated. A constant weight signals complete saturation of the porous structure m_{sat}. Subsequently, the porous sample was driven approx. 5 mm out of the liquid to lose contact with the liquid. All experiments were carried out under room temperature and ambient pressure.

Based on the weight measurement, some corrections are needed to make a statement about the pure mass increase during the wicking experiment. These corrections include the decreasing liquid level in the container during the experiment as well as the buoyancy and the Wilhelmy effect. The liquid level decrease due to the imbibition of the liquid into the sample could be eliminated by using the geometry of the sample and the experimental container. Furthermore, the buoyancy force and the Wilhelmy effect have to be considered. In order to account for these effects, a correction of the weight measurement was used, which is has already been used by Grebenyuk et al. [30, 34]. For this purpose, the weight of the completely saturated sample, but partially submerged sample is subtracted from the weight of the completely saturated sample.

Permeability

Permeability K is the ability of a porous material to allow fluids to pass through it. It is a property of the porous material and is commonly defined by the Darcy law [35]. Both methods which are used in this work to determine the permeability base on the Darcy law, which is given by

$$\frac{\Delta p}{\Delta L} = -\frac{\mu}{K} u_s.$$
(5.1)

To facilitate an overview, all symbols used in equations are listed on page 189.

Different methods are proposed to determine the permeability of a porous structure in literature. Thus, the permeability can be determined, for example by constant head permeability measurements

$$K = \frac{\mu h_s}{\Delta p} \frac{m}{\rho \frac{\pi}{4} D^2 t}.$$
(5.2)

or as a fitting parameter of the viscous dominated part of the wicking experiment [10, 30, 36].

$$\frac{m^2}{t} = \frac{4\sigma \, \cos\theta \rho_l^2 A^2 \phi}{\mu_l} \frac{K}{R_s}.$$
(5.3)

This equation is also called Lucas-Washburn equation for porous media. A detailed derivation of Equation 5.3 can be found in the appendix A.2.1 on page 195. With knowledge of the parameters of the porous structure and liquid parameters, the permeability can be determined using this equation. For this, the knowledge of $m^2{\cdot}t^{-1}$ is required, which can be determined from the wicking experiment. Both methods base on the Darcy law.

Permeability measurements

Both approaches used to flow through the porous medium in the z-direction in order to determine the permeability. The permeability according to constant head measurements K_{Darcy} was evaluated on cylindrical samples with a radius R_{Darcy} of 5 mm and a height H_{Darcy} of 5 mm to 6 mm. Freeze cast monoliths were cut to obtain suitable cylindrical samples. Samples from the lateral surface with an axial orientation in r-direction were prepared as well as samples from the center of the freeze cast

monolith with an axial orientation in the z-direction. The orientations are depicted in Figure 5.2. Both, samples from the lateral surface as well as samples from the bulk were taken at the axial position of z = 10 mm. Compressible silicon sample holders were used to minimize bypass flow. The mass of the permeated water $m_{w, Darcy}$ at a pressure difference Δp_{Darcy} of 15 kPa and a time t_{Darcy} of 300 s was recorded. To characterize the lateral surface, samples in r-direction were only tested for water flux through the lateral surface per time and cross section. With the dynamic viscosity of water at 20 °C μ_w = 1.00 mPas and the density of water at 20 °C ρ_w = 998 kg·m^{-3}, the permeability K_{Darcy} can be calculated according to Equation 5.2. To reduce deviations due to intake losses, the specimens were soaked with water prior to measurement. Additionally, an initialization time of 120 s was waited to reach steady state flow conditions before starting the measurement. Each sample was tested three times and the average permeated mass of water was used for further calculations. After testing the samples from the lateral surface with the as prepared closed lateral surface ("EC"), the outside layer of the surface was removed and the samples were tested again three times ("EO").

The method, proposed by Fries et al. [10], was used to calculate the permeability from the viscous-dominated part of the wicking experiment using Equation 5.3. This Lucas-Washburn equation is only valid for short times. With increasing time, gravity has to be taken into account. According to Fries and Dreyer [37], the Lucas-Washburn equation can be used in the vertical wicking setup up to 10 % of the maximum achievable wicking height, in order to neglect the influence of gravity. The height can be recalculated into mass (see Appendix A.2.1.; Equation A.2.10 on page 196). The values of the equilibrium mass are given in Table 5.3 (see page 104). In this study, values from the wicking experiment up to a mass of 1 % of the maximum achievable wicking mass were used to obtain squared mass over time. Corrections were applied as described on page 94. The resulting error is < 1 % and can, therefore, be neglected. The plot of the squared mass over time shows a constant slope which can be approximated by linear regression. Using this fit, the macroscopic parameters given in section 5.4, and the physical parameters of the fluid in Table 5.2 (see page 94), the permeability K could be calculated using Equation 5.3 (see page 95). The results of the permeability by constant head experiments and by fitting the wicking curves are summarized in Table 5.3 (see page 104).

5.4 Results

5.4.1 Pore Structure

Figure 5.4 a-d depicts SEM images of the characteristic resulting internal pore structure obtained by solution-based freeze casting. The insets represent a schematic representation of the pore structures. The pore structure depends closely on the solvent, the composition and the freezing process. Two pore morphologies can be distinguished, depending on the solvent. Dendritic pores are created in case of using cyclohexane in samples CH20/0, CH40/0 and CH40/50 and prismatic pores when using *tert*-butyl alcohol in sample TBA40/0. This is in accordance with the literature, describing the observed pore structures as characteristic for the corresponding solvents [26, 38]. Furthermore, the internal pore walls are smooth for the samples without filler addition. In pure solution-based compositions, the solvent crystals grow according to the segregation process of thermally induced phase separation [39, 40]. This enables a crystal shape which is close to the energetically most favorable shape and hence to very smooth pore wall surfaces. In contrast, the addition of 50 vol% filler particles results in a very rough pore wall surface, as it can be seen in the inset of Figure 5.4 d. The particles are not completely embedded in the pore walls and hence creating roughness. Since the chemical composition and therefore the decomposition during processing is equal for matrix and filler particles, no detachment or debonding is expected. This expectation is confirmed by the absence of any cracks around filler particles.

Furthermore, also the pore morphology is affected by the addition of filler particles as it becomes more isotropic. Figure 5.4 b shows a dendritic anisotropic pore structure obtained by particle free freeze casting. In contrast, particle content of 50 vol% being the only difference the pore structure depicted in Figure 5.4 d is more isotropic. In case of increased isotropy, the differentiation between primary and secondary dendrites becomes more difficult, leading to a structure which looks less arranged and hardly shows any elongated primary dendrites (see insets of Figure 5.4 b and d). It is assumed that suspended particles are disrupting the regular solidification structure by inducing *noise* ahead of the freezing front [39]. The solidification microstructure can be influenced by a sufficient amount of noise ahead of the freezing front which disrupts the growth of crystal tips [41]. Hence, fractal patterns are formed instead of regular ones. Fluctuations in the thermal or solute field ahead of the solid-liquid

interface can be considered as noise. But also particles located at crystal tips can act as noise by creating small temperature fluctuations and direct contact.
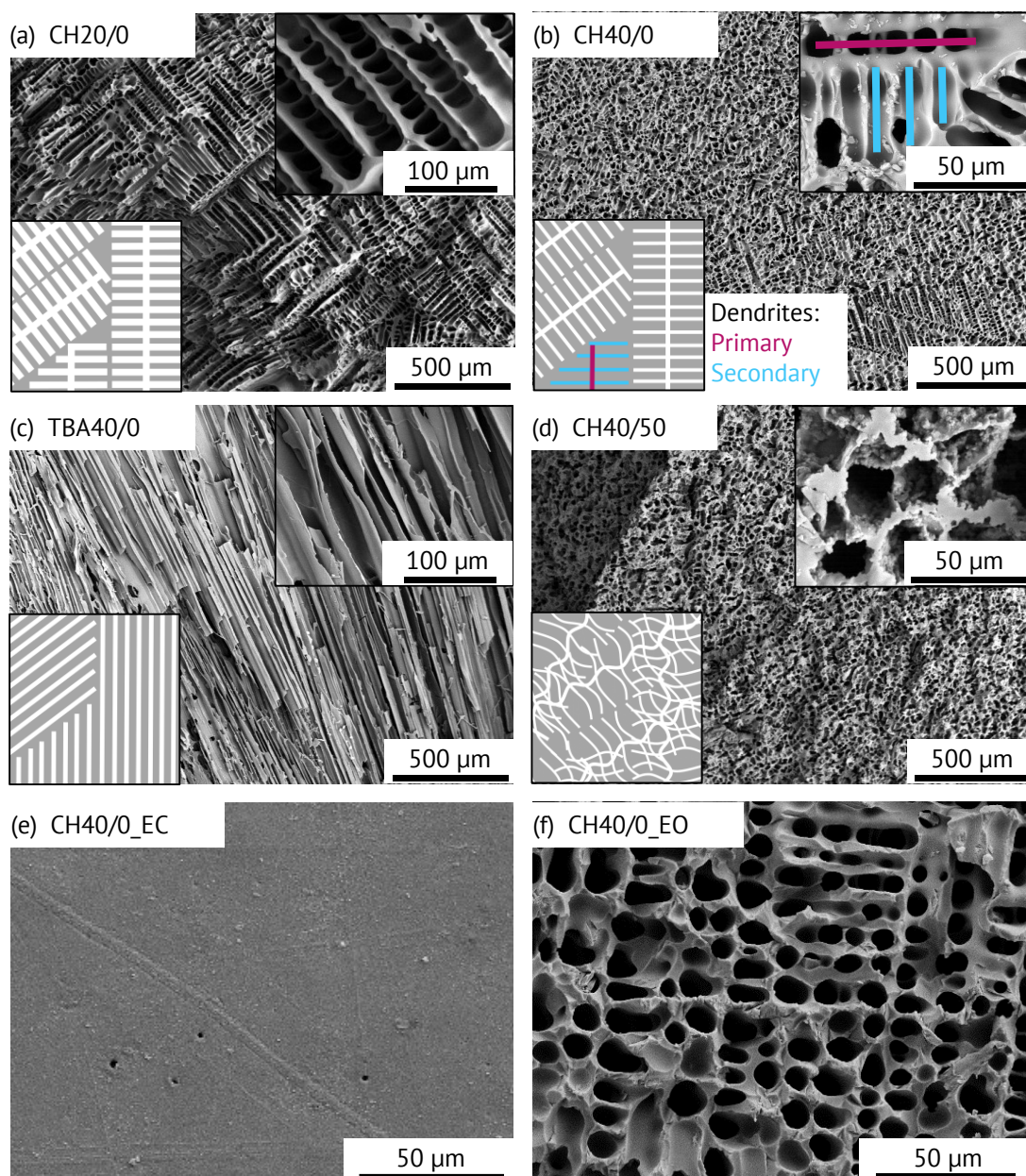
Figure 5.4 Characteristic cross sectional SEM images of the pore structure of pyrolyzed monoliths and simplified schemes of the pore structure for (a) CH20/0, (b) CH40/0, (c) TBA40/0 and (d) CH40/50; SEM images of the lateral surface of sample CH40/0 (e) as prepared (to a great extend closed) and (f) after removing the dense layer (open lateral surface).

Since porosity and pore morphology are only dependent on solid loading and solvent, both properties can be considered as constant throughout one sample. The pore size is influenced by the freezing velocity. The freezing occurs mainly in the radial direction, and as the freezing length in the radial direction is relatively short, no

significant changes in pore size can be assumed. Additionally, radial freezing leads to the valid assumption of constant pore size in the axial direction. The observed pore structures are in accordance with reported structures in literature for all investigated compositions [26, 39].

In contrast to Figure 5.4 a-d, Figure 5.4 e and f do not depict the internal pore structure but the top view of the lateral surface of sample CH40/0. The as prepared state of the lateral surface is shown in Figure 5.4 e with hardly any pores visible on the surface indicating an almost completely closed lateral surface. The thickness of the layer is 1 µm to 5 µm. Very similar observations can be found for all other samples. However, the as prepared lateral surface becomes slightly more open in the order of CH40/0 – TBA40/0 – CH40/50 – CH20/0. This reveals, that anisotropy of the pore structure and decreasing porosity are beneficial for the formation of closed lateral surfaces. Details on the mechanism of the formation of the closed lateral surface can be found in the appendix A.2.2 on page 197. Figure 5.4 f shows the lateral surface of sample CH40/0 after the outside layer was removed. No major differences can be observed when comparing with the internal pore structure of sample CH40/0 depicted in Figure 5.4 b. This observation applies to all investigated samples. In addition, no grinding remainings, such as abraded particles were found in the structure, indicating a successful complete cleaning of the sample. The absence of abraded particles ensures permeability and wicking experiments without the influence of abraded particles hindering flow by blocking pore channels.

The mathematical description of the capillary driven liquid transport in a volume averaged porous medium requires the knowledge of macroscopic parameters. These are the open porosity ϕ, the static radius R_s and the permeability K. Figure 5.5 depicts open porosity ϕ and mean pore window diameter $2R_{merc}$ for all investigated samples measured by mercury porosimetry. The detailed pore window diameter distribution can be found in the supplementary data.

As it can already be assumed assessing the SEM images in Figure 5.4 a-d, CH20/0 shows the highest open porosity ϕ as well as the highest mean pore window diameters $2R_{merc}$ with values of (21.2 ± 1.1) µm and (79.3 ± 0.3) %, respectively. In contrast, CH40/0, TBA40/0 and CH40/50 exhibit almost constant open porosity ϕ with values of (60.8 ± 2.3) %, (63.5 ± 0.3) % and (63.1 ± 0.2) %, respectively. Moreover, also the

mean pore window diameter $2R_{merc}$ of (13.9 ± 1.1) µm, (10.9 ± 0.3) µm and (11.1 ± 0.4) µm shows no significant deviation.

Monomodal pore window diameter distributions were observed for all investigated samples covering a range of 15 µm to 50 µm (CH20/0) and 6.5 µm to 35 µm (CH40/0, TBA40/0, CH40/50). When further analyzing the SEM images of the pore structure in Figure 5.4 a-d with regards to the difference of pore size and pore window diameter it becomes obvious that pore size equals pore window diameter for TBA40/0 due to its prismatic pore morphology. On the contrary, CH20/0 and CH40/0 exhibit dendritic pore morphology with distinct primary and secondary dendrites and different corresponding pore window sizes. Ratios of around 2 were found for both samples with pore window diameters of primary dendrites being the larger ones. Comparison with mercury porosimetry results clearly reveals that the smaller pore windows of the secondary dendrites are dominant in the mercury porosimetry measurement. Thus, more volume is accessible through pore windows of the secondary dendrites compared with primary dendrites for CH20/0 and CH40/0 [26]. Yet, this is only valid for anisotropic dendritic pore structure since there are no distinct primary and secondary dendrites for increased isotropy caused by particle addition.

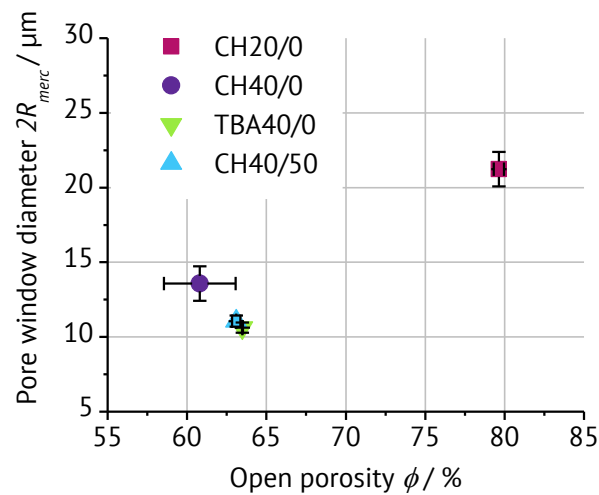**Figure 5.5** Open porosity φ and mean pore window diameter 2Rmerc for all studied samples obtained by mercury intrusion.

It can be stated, that in this study only the solid loading influences the open porosity ϕ and mean pore window diameter $2R_{merc}$. While in suspension-based freeze casting the solid loading is reported to have only influence on the open porosity ϕ, it is known

that in solution-based freeze casting solid loading also affects the mean pore window diameter [24, 26, 42]. For the compositions and freezing conditions which were investigated in this study other parameters such as solvent and particle addition do not alter the open porosity ϕ and the mean pore window diameter $2R_{merc}$. As a result, the pore structure can be changed in terms of pore morphology, anisotropy and pore wall roughness without changing influential properties for capillary transport such as open porosity and mean pore window diameter.

5.4.2 Water flux through lateral surface

To characterize the water flux through the lateral surface, constant head permeability tests were conducted. Figure 5.6 shows the water flux j of the lateral surface in dependence of the condition of the lateral surface, where "EC" indicates the as prepared state and "EO" describes the state after removal of the outside layer. In Table 5.3 (see page 104) the results are summarized. In accordance with the SEM images in Figure 5.4 e and f it can be clearly seen, that the water flux j for the open lateral surface is significantly higher than for closed lateral surface for all samples. Ratios of 2.3 to 5.9 are found, being CH40/50 the sample with the lowest and CH20/0 the one with the highest ratio. The lowest water flux j with a value of 3.32×10^{-5} kg·s^{-1}·m^{-2} is observed for the closed lateral surface of CH40/0. In contrast, CH20/0 exhibits with 3.88×10^{-4} kg·s^{-1}·m^{-2} the highest water flux j for closed lateral surface conditions. TBA40/0 and CH40/50 show very similar values of 1.29×10^{-5} kg·s^{-1}·m^{-2} and 1.47×10^{-5} kg·s^{-1}·m^{-2}, respectively. The significant different water flux j indicates an influence of the composition on the condition of the as prepared lateral surface. When comparing the results for the closed lateral surface, lower water flux j, meaning a larger degree of closed lateral surface, can be achieved by using a high solid loading, cyclohexane as solvent and a filler particle free composition. Further, it can be stated, that the solid loading has the greatest impact on the condition of the lateral surface.
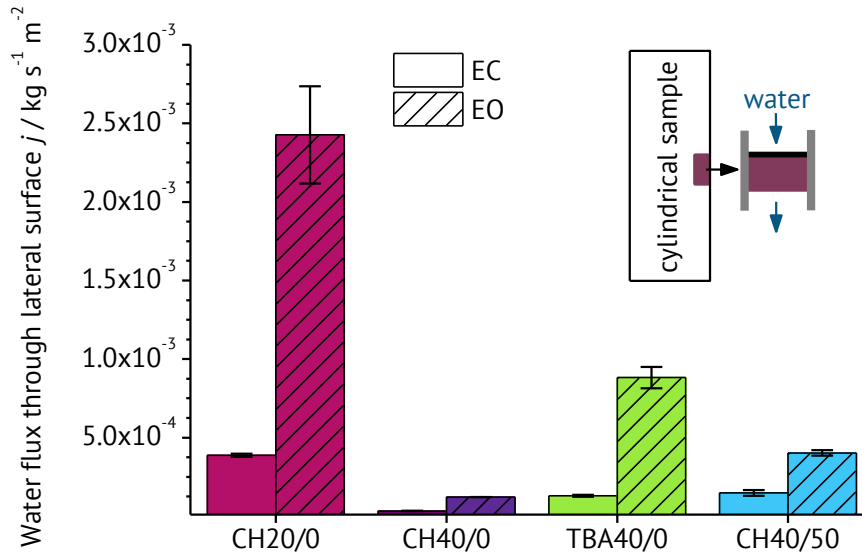
Figure 5.6 Water flux through the lateral surface j obtained by constant head permeability measurements for all studied samples as prepared and after removing the dense outside layer.

Analyzing the samples with open lateral surface, the water flux j is not limited anymore by the denser outside layer. As a result, the water flux j of the samples with open lateral surface is influenced mainly by the internal pore structure. As for the closed lateral surface, solid loading with its strong influence on open porosity ϕ and pore window diameter $2R_{merc}$ has the largest influence. Hence, the sample with the lowest solid loading (CH20/0) shows the highest water flux j of 2.43×10^{-3} kg·s^{-1}·m^{-2}. TBA40/0 and CH40/50 with altered pore morphology and anisotropy exhibit intermediate water flux j with values of 8.82×10^{-4} kg·s^{-1}·m^{-2} and 4.02×10^{-4} kg·s^{-1}·m^{-2}, respectively. On the other hand, the dendritic most anisotropic pore structure of CH40/0 leads to the smallest water flux j of 1.22×10^{-4} kg·s^{-1}·m^{-2}. The same dependences between pore structure and permeability are observed in permeability measurements of samples from the bulk in z-direction. Previous investigations of samples with the same conditions as presented here confirm especially the difference in permeability of CH40/0 and CH40/50 though pore size and porosity are similar. This indicates that also the pore morphology strongly influences the permeability.

5.4.3 Wicking experiments and theoretical prediction using macroscopic parameters

Besides the knowledge of the open porosity ϕ and the static radius R_s, the permeability K needs to be evaluated in order to calculate the capillary driven liquid transport in a porous medium. The values are given in Table 5.3 (see page 104). An additional macroscopic parameter which has to be known to solve the differential equation describing wicking is the static radius R_s. It describes an equivalent capillary pore radius. It can be calculated from the equilibrium between capillary pressure and hydrostatic pressure, as long as the equilibrium condition is known. The equation is given as

$$\frac{2\sigma \, \cos \theta}{R_s} = \rho g h_{eq}. \tag{5.4}$$

This approach was used by Lucas [43] and is known as Jurin's height. Due to the limited sample height of our investigated samples, the equilibrium could not be reached experimentally and the static radius R_s could not be determined. The estimated wicking height and mass were calculated using Equation 5.4. Additionally, Equation A.2.10 which is given in appendix A.2.1. on page 196, is necessary.

Wicking height and mass are summarized in Table 5.3 (see page 104). Therefore, the mean pore radii R_{merc} from the mercury porosimetry measurement were used as the characteristic pore sizes for further calculations. The corresponding mean pore radii R_{merc} are given in Table 5.3 (see page 104). The last macroscopic parameter, which has to be known is the permeability. The method, proposed by Fries et al. [10], was used to calculate the permeability from the viscous-dominated part of the wicking experiment using Equation 5.3.

	H 10^{-3} m	D 10^{-3} m	ϕ	R_{merc} 10^{-6} m	$K_{Wicking}$ 10^{-14} m^2	K_{Darcy} 10^{-14} m^2	$j(EC)$ 10^{-4} kg·s^{-1}·m^{-2}	$j(EO)$ 10^{-4} kg·s^{-1}·m^{-2}	h_{eq} m	m_{eq} kg
CH20/0	32.9 ± 0.1	13.7 ± 0.1	0.793 ± 0.003	10.5 ± 0.6	48.4 ± 3.2	6.43 ± 1.07	3.88 ± 0.10	24.3 ± 3.10	0.195	0.037
CH40/0	25.9 ± 0.1	13.6 ± 0.2	0.608 ± 0.023	7.0 ± 0.5	3.9 ± 0.8	0.10 ± 0.04	0.33 ± 0.01	1.22 ± 0.04	0.292	0.041
TBA40/0	22.9 ± 0.1	14.7 ± 0.1	0.635 ± 0.003	5.5 ± 0.1	9.8 ± 1.3	1.31 ± 0.73	1.29 ± 0.06	8.82 ± 0.68	0.372	0.064
CH40/50	25.2 ± 0.2	14.6 ± 0.1	0.631 ± 0.002	5.5 ± 0.2	12.9 ± 0.6	3.98 ± 0.44	1.47 ± 0.18	4.02 ± 0.17	0.372	0.063

Table 5.3   Geometrical characteristics and macroscopic parameters of the investigated samples.

Figure 5.7 shows the squared mass over time for the investigated samples. Different wicking rates can be seen for the investigated samples. Permeability is a structure parameter and should be similar despite different approaches. Nevertheless, the permeability calculated from the wicking experiment shows a 3 to 39 times higher permeability compared to the permeability obtained from the constant head measurement. A possible explanation for this could be inlet losses, which, due to the low height of 5 mm to 6 mm, have an influence on the resulting pressure drop. An increased pressure loss results in a low permeability. Such an inlet pressure drop was not considered in the calculation of the permeability.
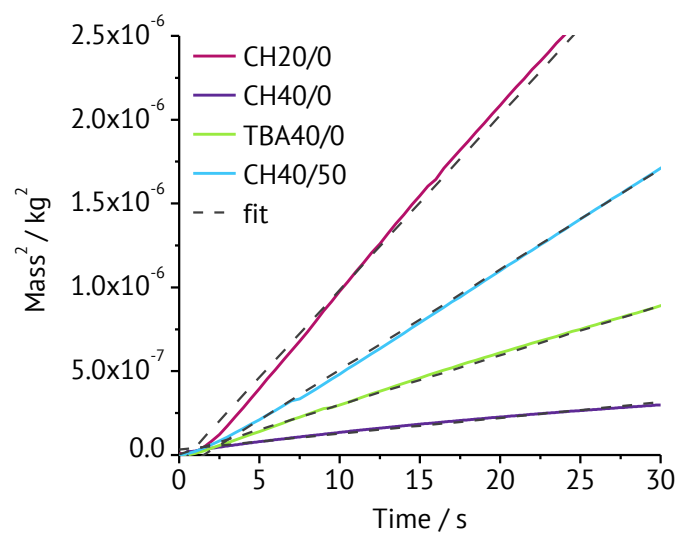
Figure 5.7   The squared height over time for the investigated samples. Equation 5.3 was fitted to the experimental line.

The sample CH20/0 shows the highest permeability value of 48.4×10^{-14} m^2 for the wicking experiment and 6.43×10^{-14} m^2 for the constant head permeability approach of all investigated samples. It can be related to the highest characteristic pore radius of 10.5 µm. It also shows the highest porosity with a value of 79.3 %. All other samples show a porosity of about 60 %. Among them, CH40/0 shows the lowest permeability value of 3.9×10^{-14} m^2 or 0.1×10^{-14} m^2, respectively. TBA40/0 and CH40/50 show a similar porosity and characteristic pore radius. However, the permeability varies between them. This can only be attributed to the different pore morphologies. As mentioned, TBA40/0 shows a prismatic pore structure, whereas CH40/50 exhibits a dendritic pore morphology.

The capillary model was used for the theoretical prediction of the wicking behavior, which reduces the complex porous structure to a simple bundle of aligned capillary tubes of the same radii. The equation for the capillary model is derived from the momentum conservation equation on a single capillary. The driving force for the wicking process is the capillary pressure, which is the result of the curvature of the free surface. The capillary pressure is balanced with viscous forces and hydrostatic pressure [30, 44-46]:

$$\frac{2\sigma \cos \theta}{R_s} = \frac{\phi \mu_l \dot{h} h}{K} + \rho_l g h. \tag{5.5}$$

This equation is also called the Lucas-Washburn equation with gravity effects. Furthermore, the relative influence of gravity and viscous friction on the wicking can be described using the simplified form of the wicking process, using the following parameters

$$b = \frac{\phi R_s}{K} \frac{\mu_l}{2\sigma \cos \theta} \tag{5.6}$$

and

$$c = R_s \frac{\rho_l g}{2\sigma \cos \theta} \tag{5.7}$$

The same parameters were used by [10, 30, 34, 37]. This results in

$$1 = b\dot{h}h + ch \tag{5.8}$$

The parameter b is the relative influence of the viscous friction on the wicking, while c is the relative influence of the gravity on the wicking process. The prerequisite for the application of Equation 5.5 is the knowledge of the macroscopic parameters. They were determined in the previous sections and are summarized in Table 5.3 (see page 104). Using the macroscopic parameters and the thermophysical liquid properties of HFE-7500 from Table 5.2 (see page 94), a prediction for each sample type was compiled.

The permeability obtained by the Darcy approach was used for prediction, which is given in the graphs of Figure 5.8 (see page 108) as solid red line. The fitting permeability, obtained from the experiment was used for the *prediction* given as solid blue line. The imbibed mass is scaled by the saturated mass, which was obtained from the completely saturated porous material with the lateral closed surface. The results of the prediction using the theoretical model are plotted in Figure 5.8. The theoretical prediction using the macroscopic parameters with permeability, obtained by the Darcy experiment $K_{Darcy,}$ underestimates the wicking experiment. Thus, it can be concluded that, despite independently determined macroscopic parameters, the wicking equation does not predict the imbibition rate correctly.

As seen in Figure 5.8, the *prediction* using $K_{wicking}$ for TBA40/0, CH20/0 and CH40/50 shows a good accordance with the experimental data. This can be attributed to the fact, that the permeability is a fitting parameter determined from the first mass increase of the imbibed mass of the wicking experiment. Thus, a match in the first wicking area can be ensured. Furthermore, the wicking equation assumes a porous material to be a bundle of straight capillaries of the same radii. It can be seen that the assumption holds for TBA40/0, CH20/0 and CH40/50 in the investigated time frame. The sample CH40/0 behaves differently compared to the *prediction*. The experimental curve does not show the typical Lucas-Washburn behavior. After a first mass increase within the sample, further progression is characterized by a linear mass increase. The deviation in the CH40 sample is due to the fact, that $K_{wicking}$ was determined from the first mass increase of the experiment. This results in a large $K_{wicking}$ and thus to a large deviation between prediction and experiment in the further course.

In order to investigate the influence of different pore structures on capillary transport, wicking experiments were performed. The imbibed mass was extracted from the wicking data introduced in section 5.3.3 (see page 92). The comparison between the wicking behavior with a laterally closed and laterally open surface is shown in Figure 5.8. The dotted line indicates the experiment with the lateral closed surface, whereas the open lateral surface is shown as dashed line.
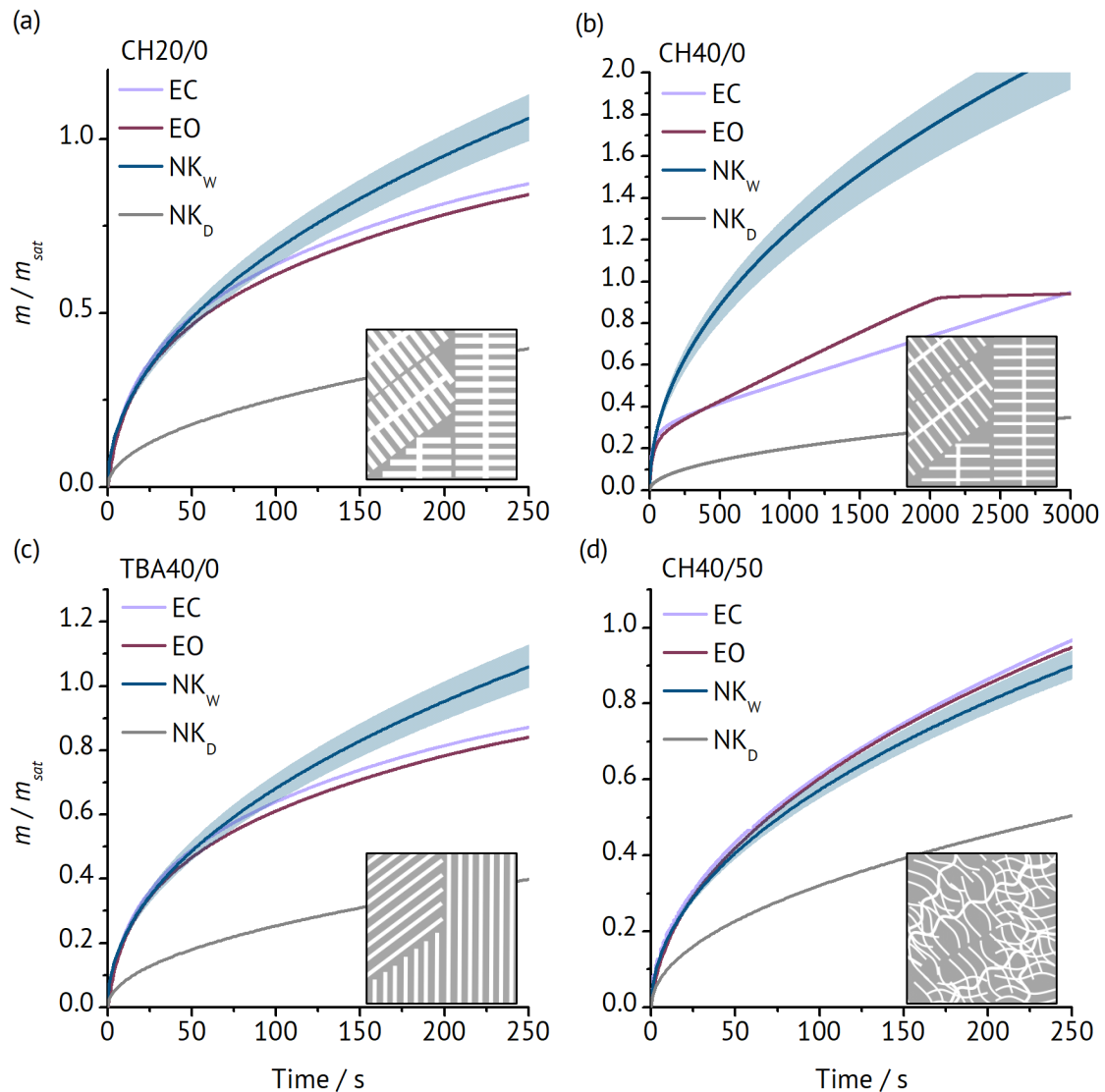
Figure 5.8 Wicking results of the samples with a lateral open and lateral closed surface compared with the calculated wicking results of Equation 5.5; the grey areas represent the deviation of the calculation caused by the measurement error of the macroscopic parameters.

The samples TBA40/0, CH20/0 and CH40/50 have no deviations between the laterally closed and open surface, which leads to the conclusion that there is no influence of a closed surface on the wicking behavior. Furthermore, the samples follow the typical Lucas-Washburn curve. Only the sample CH40/0 shows unexpected wicking behavior. After the first mass increase the slope of the imbibed mass changes. In the further course, the imbibed mass increases linearly with time until the sample is completely saturated. Previous wicking tests on samples with the same composition as CH40/0 confirm the peculiar wicking behavior. Furthermore, CH40/0 shows a 20 % higher imbibition rate after removing the closed lateral surface. The lateral open surface favors the imbibition of the liquid into the porous sample [30, 44-46].

5.5 Discussion

5.5.1 Influence of lateral surface on wicking

The influence of the lateral surface on the wicking behavior was investigated by comparing wicking experiments with closed ("EC") and open ("EO") lateral surface. As shown in Figure 5.7 (see page 105), the samples TBA40/0, CH20/0 and CH40/50 show a similar mass increase after the removing of the closed lateral surface. This result was expected, but a different wicking behavior was found for CH40/0. The change in the slope of the wicking curve, the linear wicking behavior and the increasing the imbibition rate after removing the lateral closed surface leads to the assumption that an additional force within the sample reduces the wicking behavior of the sample. Removing the outer closed surface, the force is reduced, which enables the liquid to rise faster, but still linearly inside the sample.

The linear wicking behavior does not match the classic Lucas-Washburn curve. A linear wicking curve could be observed in Grebenyuk and Dreyer [34]. They investigated the wicking behavior of liquid nitrogen with a superheated porous structure. The linear course was explained by an additional pressure created by the evaporating liquid, which could not escape fast enough from the sample. However, in the case studied in this work, there is no evaporation, creating an additional pressure. Therefore, the behavior may be explained by the pore structure. At higher magnifications of SEM images in Figure 5.4, it can be observed, that some pores of CH40/0 seem to be closed. In contrast, the samples TBA40/0, CH20/0 and CH40/50 show an unstructured, but connected pore structure. Thus, only a reduced number of transport routes for the liquid are available in the CH40/0. A smaller amount of remaining connected pores act like a throttle for the liquid, which causes the linear behavior. The higher mass increase after removing the outer surface and the reason for the linear course for CH40/0 could not be conclusively clarified in this work.

As a result, the lateral surface can be designed to be closed without significantly changing the wicking behavior for most of the samples. This opens up different possibilities: Structures with capillary transport functionality can be lateral encapsulated to prevent interactions with the environment such as contamination of the environment or the structure. In addition, dry out of capillary active structures and thus interruption in capillary transport can be prevented. So far, an additional coating process is necessary to provide encapsulation. In the case of CH40/0, an

encapsulated structure offers an additional option to adjust the wicking behavior to a certain application. Furthermore, a less porous lateral surface facilitates the subsequent deposition of a dense or functional coating [47, 48]. However, when the wicking conditions change from isothermal at room temperature to non-isothermal at cryogenic temperature, a pronounced difference in wicking behavior in dependence on the porosity of the lateral surface is expected.

5.5.2   Influence of pore structure on wicking

Figure 5.9 shows the comparison of the investigated samples in terms of increasing height over time for the samples with a lateral open surface. As depicted in Figure 5.9, the wicking behavior depends on the pore structure. The first time steps are mostly influenced by the viscous force, whereas for longer times the influence of the gravity becomes more significant [37]. The fastest wicking can be seen in the sample CH20/0, which is due to the highest permeability K. It can be also explained in terms of the parameters in Equation 5.6 and 5.7. The value of b, which describes the relative influence of the viscous force is smaller for CH20/0 compare to the other samples. It means that the resistance is smaller and it is easier for the liquid to flow through the structure. The wicking permeability was used to calculate the parameter b. After a first rapid increase, the curve of CH20/0 shows the biggest change in the slope among the investigated samples. For longer times, the gravity term becomes more dominant. The parameter c of Equation 5.7 describes the relative influence of gravity on wicking.

It can be seen in Table 5.4 that CH20/0 has the highest value for c, which indicates the highest influence of gravity among the investigated sample. It results in the biggest change in the slope of CH20/0. In contrast to CH20/0, CH40/0 shows a shallow liquid rise inside the sample, indicating a smaller permeability K or a higher value for the relative influence of the viscous force. TBA40/0 and CH40/50 show the same values for the relative influence of gravity, which is due to the fact that the parameter c only requires the characteristic pore size of the porous medium.
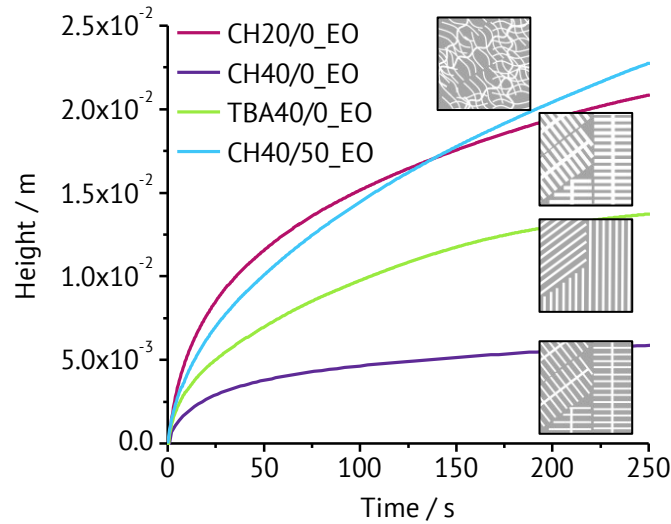
Figure 5.9 Wicking curves for all investigated pore morphologies of samples with open lateral surface.

Table 5.4 Scaled parameters of Equation 5.8 describing wicking.

	b	c
	10^5	
	$s \cdot m^{-2}$	m^{-1}
CH20/0	6.6	5.13
CH40/0	41.8	3.42
TBA40/0	13.6	2.69
CH40/50	10.3	2.69

However, the relative influence of the viscous force differs among the two samples, which is due to the different permeability of the samples, because the characteristic pore size and the porosity are similar for both samples. Comparing both wicking curves in Figure 8, CH40/50 shows a higher wicking rate compared with TBA40/0. Despite the similar porosity and pore size, the permeability of CH40/50 is over 30 % higher compared to TBA40/0. This implies that the dendritic pore morphology has a higher ability of liquid flow through a porous structure than the prismatic pore morphology.

Generally, it turns out that the sample with the highest viscous resistance has the slowest imbibition rate, while the smallest viscous resistance results in a high imbibition rate. In addition, the samples with the highest influence of gravitation have the biggest change in the slope during wicking (CH20/0). It turns out that the characteristic pore radius has the greatest influence on the wicking behavior among the investigated parameters. Furthermore, it can be seen in Figure 5.8, that the reduction of a complex porous structure to the three macroscopic parameters is not sufficient to describe the wicking behavior for all investigated samples. The wicking equation uses the open porosity ϕ, static radius R_s and permeability K to simplify the porous structure to a bundle of straight capillaries [49]. As in Figure 5.8 depicted, the wicking behavior can be predicted for the samples TBA40/0, CH20/0 and CH40/50, but it does not apply to CH40/0. The *prediction* curve, using $K_{wicking}$ overestimates the wicking behavior for CH40/0. Possible reasons for the difference between the experimental results and the prediction of the Lucas-Wasburn equation with gravity effect for CH40/0 are the lack of connections between the pores in the porous material and slow filling of secondary dendrites. Further studies to enlighten the reason for the peculiar wicking behavior of CH40/0 are ongoing. The used model, does not take into account the interconnectivity of the pores within a real porous structure and the presence of secondary dendrites. It bases, as mentioned before, on a bundle of straight, not connected capillaries. Therefore, it is not able to predict three-dimensional wicking flow.

5.6 Conclusions

In this study, we investigated the influence of four different pore structures on the isothermal wicking behavior. Porous polymer-derived ceramic monoliths (SiOC) were prepared by solution-based freeze casting. This process enables to adjust important pore structure-related parameters independently in a wide range and hence allows to study the impact of parameter variations. Furthermore, the effect of different lateral surface conditions on wicking was investigated. Polymethylsiloxane and (3-amino-propyl)triethoxysilane were used a as precursor and cross-linking agent, respectively. *Tert*-butyl alcohol or cyclohexane was used as solvents to obtain a prismatic or dendritic pore morphology. Differences in solid loading and the addition of preceramic filler particles change the porosity from 60 % to 79 % and the mean pore

window diameter from 11 µm to 21 µm. A silicon-coated film prevents nucleation on the lateral surface, resulting in a dense lateral surface. The samples with such a dense layer showed 2.3 to 5.9 times lower water flux of the lateral surface compared with an open surface.

To characterize the capillary transport within the samples, vertical wicking experiments were performed using the Washburn-Sorption method. The weight measurement technique was used to obtain the imbibed mass. The permeability was determined by two different approaches: on the one hand from the constant head permeability and on the other hand as a fit from the viscous-dominated part of the wicking experiment. The permeability from the wicking experiment showed a 3 to 39 times higher permeability compared to the permeability obtained by the constant head approach. One potential explanation for this behavior is the presence of inlet losses which are not considered in the permeability determined by wicking. Further, it turns out that the capillary transport in porous media depends on the macroscopic parameters as well as on the pore morphology. The prismatic pore morphology shows a higher imbibition rate compared to a dendritic pore morphology.

In order to predict the wicking experiments, the Lucas-Washburn equation with gravity effect was used. A good agreement between the experimental curves could be found for most of the investigated samples using the permeability obtained from the wicking experiment. Only the CH40/0 sample shows a deviation of the typical Lucas-Washburn behavior, which cannot be predicted by the wicking equation. The reason for such a behavior could not be clarified ultimately in this work. Reduced connectivity between aligned pore areas and slow filling of secondary dendrites are potential explanations and will be investigated in upcoming studies. Furthermore, CH40/0 also showed an over 20 % higher mass increase after removing the closed lateral surface. The encapsulation provides an additional way to change the wicking behavior in CH40/0 sample, while the removing of the closed lateral surface has no influence for the other samples. It allows to encapsulate these structures without influencing the wicking. Besides avoiding contamination of the structure or the environment the accessibility of the structure can be tailored.

The wicking equation is a simple tool to predict the wicking behavior in porous structures as long as the porous structure can be assumed as a bundle of straight capillaries. However, it could be shown that the simplification of a real three dimensional porous structure to the macroscopic parameter is not sufficient to accurately describe the wicking behavior for all investigated samples.

Acknowledgments

References

[1]   T. Fukasawa, M. Ando, T. Ohji, J. Ceram. Soc. Jpn. 110 (2002) 627 - 631.

[2]   B.A. Haberman, J.B. Young, Int J Heat Mass Tran 47 (2004) 3617-3629.

[3]   S.D. Kenarsari, D. Yang, G. Jiang, S. Zhang, J. Wang, A.G. Russell, Q. Wei, M. Fan, RSC Advances 3 (2013) 22739-22773.

[4]   N. MacDowell, N. Florin, A. Buchard, J. Hallett, A. Galindo, G. Jackson, C.S. Adjiman, C.K. Williams, N. Shah, P. Fennell, Energy Environ. Sci 3 (2010) 1645-1669.

[5]   J.R. Woodard, A.J. Hilldore, S.K. Lan, C.J. Park, A.W. Morgan, J.A.C. Eurell, S.G. Clark, M.B. Wheeler, R.D. Jamison, A.J.W. Johnson, Biomaterials 28 (2007) 45-54.

[6]   F. Xue, K. Zhou, N. Wu, H. Luo, X. Wang, X. Zhou, Z. Yan, I. Abrahams, D. Zhang, Ceram. Int. 44 (2018) 6293-6299.

[7]   S. Heidenreich, Fuel 104 (2013) 83-94.

[8]   R.N. Eberhardt, G.R. Cunnington, W.A. Johns, *Conceptual design and analysis of orbital cryogenic liquid storage and supply systems*. 1981, Martin Marietta Cooperation Denver Aerospace.

[9]   J. Hartwig, *Liquid Acquisition Devices for Advanced In-Space Cryogenic Propulsion Systems*. 2016, Amsterdam: Elsevier Inc.

[10]   N. Fries, K. Odic, M. Conrath, M. Dreyer, J Colloid Interface Sci 321 (2008) 118-29.

[11]   E.P. Symons, *Wicking of liquids in screens*. 1974, NASA Lewis Research Center: Cleveland, United States.

[12]   P. Colombo, C. Vakifahmetoglu, S. Costacurta, J. Mater. Sci. 45 (2010) 5425-5455.

[13]   A.R. Studart, U.T. Gonzenbach, E. Tervoort, L.J. Gauckler, J. Am. Ceram. Soc. 89 (2006) 1771-1789.

[14]   E.O. Einset, J. Am. Ceram. Soc. 79 (1996) 333-338.

[15]   S. Kumar, A. Kumar, A. Shukla, A.K. Gupta, R. Devi, J. Eur. Ceram. Soc. 29 (2009) 2643-2650.

[16]   S. Kumar, A. Kumar, R. Devi, A. Shukla, A.K. Gupta, J. Eur. Ceram. Soc. 29 (2009) 2651-2657.

[17]   K. Okada, S. Uchiyama, T. Isobe, Y. Kameshima, A. Nakajima, T. Kurata, J. Eur. Ceram. Soc. 29 (2009) 2491-2497.

[18]   K. Okada, A. Imase, T. Isobe, A. Nakajima, J. Eur. Ceram. Soc. 31 (2011) 461-467.

[19]   C. Popa, Y. Okayasu, K.-i. Katsumata, T. Isobe, N. Matsushita, A. Nakajima, T. Kurata, K. Okada, J. Mater. Sci. 48 (2013) 941-947.

[20]   H. Zhang, C.L. Fidelis, M. Wilhelm, Z. Xie, K. Rezwan, Mater. Des. 134 (2017) 207-217.

[21]   P. Colombo, G. Mera, R. Riedel, G.D. Sorarù, J. Am. Ceram. Soc. 93 (2010) 1805-1837.

[22]   K. Araki, J.W. Halloran, J. Am. Ceram. Soc. 88 (2005) 1108-1114.

[23]   S. Deville, Adv. Eng. Mater. 10 (2008) 155-169.

[24]   R. Liu, T. Xu, C. Wang, Ceram. Int. 42 (2016) 2907-2925.

[25]   K.L. Scotti, D.C. Dunand, Prog. Mater Sci. 94 (2018) 243-305.

[26]   M. Naviroj, S.M. Miller, P. Colombo, K.T. Faber, J. Eur. Ceram. Soc. 35 (2015) 2225-2232.

[27]   R. Chen, C.-A. Wang, Y. Huang, L. Ma, W. Lin, J. Am. Ceram. Soc. 90 (2007) 3478-3484.

[28]   Y. Chu, Z. Lu, J. Li, Y. Zhu, S. Zhang, J. Chen, Polym. Adv. Technol. 26 (2015) 606-612.

[29]   J. Yue, B. Dong, H. Wang, P. Colombo, J. Am. Ceram. Soc. 94 (2011) 1989-1991.

[30]   Y. Grebenyuk, H.X. Zhang, M. Wilhelm, K. Rezwan, M.E. Dreyer, J. Eur. Ceram. Soc. 37 (2017) 1993-2000.

[31]   J. Cai, B. Yu, Transport Porous Med 89 (2011) 251-263.

[32]   J. Cai, B. Yu, M. Zou, L. Luo, Energ Fuel 24 (2010) 1860-1867.

[33]   D. Schumacher, M. Wilhelm, K. Rezwan, Mater. Des. 160 (2018) 1295-1304.

[34]   Y. Grebenyuk, M.E. Dreyer, Cryogenics 78 (2016) 27-39.

[35]   H. Darcy, *Les Fontaines Publiques de la ville de Dijon*. 1856: Dalmont.

[36]   J.F. Siau, *Transport processes in wood*. 1984, Berlin: Springer.

[37]   N. Fries, M. Dreyer, J. Colloid Interf. Sci. 320 (2008) 259-263.

[38]   S. Deville, S. Meille, J. Seuba, Sci. Technol. Adv. Mater. 16 (2015) 43501-43516.

[39]   M. Naviroj, P.W. Voorhees, K.T. Faber, J. Mater. Res. 32 (2017) 3372-3382.

[40] B.-H. Yoon, E.-J. Lee, H.-E. Kim, Y.-H. Koh, J. Am. Ceram. Soc. 90 (2007) 1753-1759.

[41] E. Brener, H. Muller Krumbhaar, D. Temkin, Phys Rev E 54 (1996) 2714-2722.

[42] S. Deville, Materials 3 (2010) 1913-1927.

[43] R. Lucas, Kolloid Z. 23 (1918) 15-22.

[44] E.W. Washburn, Phys. Rev. 17 (1921) 273-283.

[45] R. Masoodi, K.M. Pillai, P.P. Varanasi, AlChE J. 53 (2007) 2769-2782.

[46] R. Masoodi, K.M. Pillai, P.P. Varanasi. *Role of Hydraulic and Capillary Radii in improving the Effectiveness of Capillary Model in Wicking*. in *Proceedings of FEDSM2008 2008 ASME Fluids Engineering Conference*. 2008.

[47] J. Seuba, J. Leloup, S. Richaud, S. Deville, C. Guizard, A.J. Stevenson, J. Eur. Ceram. Soc. 37 (2017) 2423-2429.

[48] J.-W. Moon, H.-J. Hwang, M. Awano, K. Maeda, Materials Letters 57 (2003) 1428 - 1434.

[49] R. Masoodi, K.M. Pillai, *Wicking in Porous Materials*. 2013, Boca Raton: CRC Press.

Influence of Freezing Conditions and Templating Solvent on Wicking

<div style="text-align:right">

6

</div>

In chapter 5 the impact of changes in the pore morphology, the porosity and the condition of the external surface on isothermal wicking at room temperature was described. The pore morphology and the porosity significantly influence the wicking behavior. Nevertheless, relevant variables have not been taken into consideration. The pore structure of a freeze cast monolith highly depends on the templating solvent and the freezing conditions such as freezing direction and freezing front velocity. Hence, the following section focuses on the influence of the freezing conditions and the templating solvent on pore structure, permeability and capillary transport as schematically shown in Figure 6.1. In contrast to chapter 5, the freezing direction is changed from radial-uncontrolled to uniaxial-controlled and two different freezing conditions are used: constant freezing temperature (CFT) or constant freezing velocity (CFV). Additionally, two different templating solvents are considered. As for section 5 (see pages 85 to 116), experimental results are compared with predictions of wicking obtained by the Lucas-Washburn equation.

The content of this section was published in the following article. The style and numbering of the references, the figures, the tables, the nomination as well as further typographic aspects have been adapted to be consistent throughout the thesis and to fit the superordinate layout. Furthermore, the coloring of the figures was unified. The supplementary data can be found in the appendix A.3 on page 199.

6.1 Abstract

Porous SiOC monoliths were prepared by solution-based freeze casting of poly-siloxane at constant freezing temperature or constant freezing front velocity. Dendritic and prismatic pore structures were obtained by using cyclohexane and tert-butyl alcohol as solvent, respectively. Gradients in freezing velocity lead to gradients in pore window size, whereas a constant freezing velocity ($3.3\,\mu m \cdot s^{-1}$ to $6.8\,\mu m \cdot s^{-1}$) generates homogeneous pore structures. The water permeability varies from $1.12 \times 10^{-13}\,m^2$ to $1.03 \times 10^{-11}\,m^2$ and correlates with the pore window diameter ($10\,\mu m$ to $59\,\mu m$) and the porosity (51 % to 82 %). In wicking tests, the gradient in pore window size is clearly reflected by a pronounced decrease of the wicking speed. Contrary, a homogeneous pore structure results in wicking curves which are closer to the prediction according to the Lucas-Washburn equation. However, this theoretical approach based on the three parameters, pore window size, porosity and permeability, is insufficient to describe complex three dimensional pore structures. Besides the porosity, the pore morphology was found to be a major influencing factor on the wicking. The filling of secondary dendrites slows down the wicking into the dendritic structure. Fastest wicking was observed for a prismatic pore structure at low freezing front velocity (6.6 µm/s) and high porosity (78 %), whereas slowest wicking occurred into the dendritic structure with high porosity (76 %) and constant freezing temperature ($-20\,°C$). The knowledge of the relationship between structural properties and the resulting wicking behavior can address a variety of pivotal applications in chemical engineering for capillary transport.
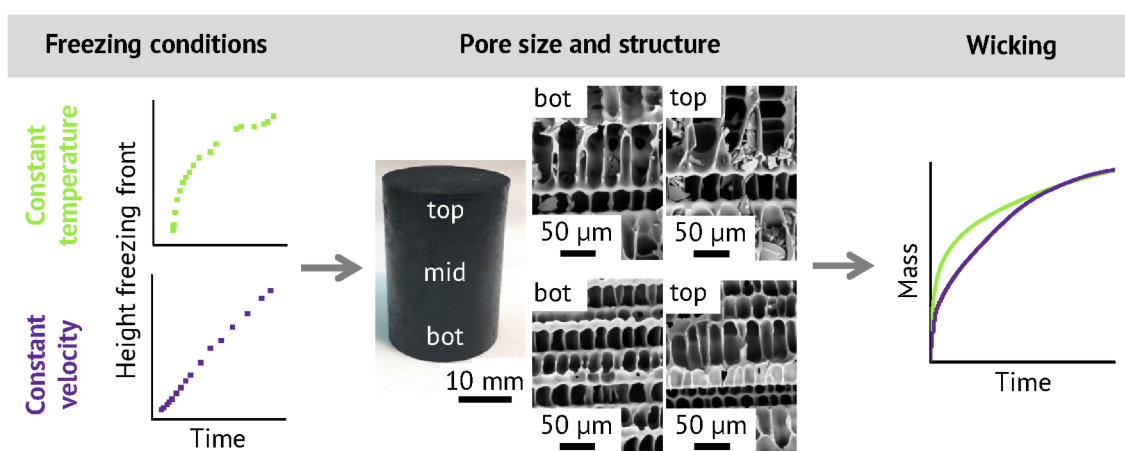

Figure 6.1 Schematic illustration of the impact of the freezing conditions on the pore structure and the wicking behavior.

6.2 Introduction

A wide range of industries such as power generation and storage rely on porous monolithic materials, where mass transport is a crucial property. For a large variety of applications including gas adsorption, water filtration, energy conversion/storage, catalysis and even bone tissue engineering, the control of the permeability is of great interest [1-4].

Aside from these applications, porous materials are used by the aerospace industry in, e.g., liquid acquisition devices and propellant management devices [5]. At pressures below the bubble point, a saturated porous medium prevents the penetration of gas/vapor and guarantees a gas-free delivery of, e.g., propellant to the engine. Capillary pressure is the driving force for the liquid transport [6]. Hence, pore window size and porosity highly influence the ability of a porous material to provide phase separation and liquid transportation properties. Nowadays, woven metallic screens are the standard materials in propellant management devices. The properties of nonmetallic inorganic materials such as low thermal conductivity, thermal and chemical stability, corrosion resistance and low density make them an interesting alternative to metals [7].

Some studies were already conducted on the wicking of porous nonmetallic inorganic material. Wicking of various liquids including silicone oil and organic liquids into 3D-stitched C–C preforms, carbonaceous porous samples and mullite was investigated [8-10]. They found a good agreement of experimental infiltration heights with a model based on pore radii of two sizes.

In contrast to oxidic ceramics such as alumina, titania and mullite, polymer-derived ceramics can provide some benefits. Particularly, the reduced thermal conductivity is suggested being advantageous in the capillary transport of cryogenic liquids [11]. Considering the surface characteristics and its influence on the interaction between liquid and solid, polymer-derived ceramics offer the possibility to adjust properties such as hydrophilicity and specific surface area by adapting the pyrolysis temperature [12]. Besides extrusion, injection molding, additive manufacturing and reactive methods, solution-based freeze casting of preceramic polymers allows for the versatile formation of a large variety of pore window sizes, porosities and pore morphologies [13-16].

The freeze casting process which can be considered as a templating method has attracted considerable interest in recent years [17]. Although the majority of studies focus on suspension-based freeze casting (dispersed particles), solution-based freeze casting of preceramic polymers has considerable potential to create unique and promising pore structures. The segregation mechanism in solution-based freeze casting bases on thermally induced phase separation of a two-component system [16]. After phase separation during freezing, the sublimation of the solvent crystals creates the pore structure. Since the final pore structure reflects the shape of the solvent crystals, the liquid phase determines the pore morphology which can range from dendritic to prismatic, cellular or lamellar [17-19]. In order to obtain homogeneous pore structures, controlling the freezing conditions is crucial. Especially the freezing front velocity highly influences the resulting pore structure, mainly the pore window size [20]. With regard to polymer-derived ceramics, SiOC structures have so far been produced with a constant freezing rate using the solution-based method, but systematic investigation of the orientation of the pore structures is lacking for this substance class [21].

Though freeze casting is able to create a large variety of pore structures and polymer-derived ceramics offer unique properties, very little is known on wicking in porous polymer-derived SiOC. In previous works of the working group, Grebenyuk et al. prepared SiOC monoliths by suspension-based freeze casting with water as dispersing medium and investigated the influence of pore window size on the wicking [22]. A comparison of experimental wicking data with predictions according to the Lucas-Washburn equation showed good agreement. Schumacher and Zimnik et al. found that predictions using the Lucas-Washburn equation differ from experimental wicking on SiOC monoliths due to a significant deviation of the pore morphology from the capillary bundle model [23]. Despite the research already conducted on porous SiOC for wicking, the influence of the freezing conditions was not yet addressed.

In this study, the influence of different freezing conditions on isothermal wicking of porous SiOC monoliths prepared by unidirectional solution-based freeze casting was investigated. Unidirectional solution-based freeze casting of preceramic polymers at constant freezing temperature or constant freezing velocity was applied for monolith preparation and enables to study the impact of the homogeneity of the pore structure. Additionally, variations of solid loading and solvent allow for the identification of distinctions between different pore structures. Furthermore, experimental wicking data were compared with a prediction based on the Lucas-Washburn equation.

6.3 Experimental Section

6.3.1 Materials

Porous ceramic monoliths were prepared by solution-based freeze casting. A commercial polymethlysiloxane (Silres® MK, Wacker Chemie AG, Germany) was used with (3-aminopropyl)triethoxysilane (APTES, abcr GmbH, Germany) which served as cross-linking agent. Tert-butyl alcohol (TBA, > 99 %, Thermo Fisher GmbH, Germany) and cyclohexane (CH, > 99 %, Sigma-Aldrich Chemie GmbH, Germany) acted as solvents. The chemical structures are displayed in Figure 6.2 on page 122 and comprehensivly listed on page 191. All materials were used without further treatment or purification.

6.3.2 Solution-based Freeze Casting

The preparation of porous monolithic samples by solution-based freeze casting is shown in Figure 6.2. In order to enable the reliable correlation of findings regarding the pore structure, the permeability and the wicking with the freezing conditions, all characterization was done on one sample for each composition. Heating to 50 °C in an oil bath ensured liquid state of the pure solvent TBA (T_m = 23 °C to 26 °C). In contrast, CH (T_m = 6.5 °C) was used at room temperature. Subsequent to the addition of MK and homogenization for 30 min under vigorous stirring, APTES was added at an amount of 1 mol%. After stirring was continued for 3 min, degassing at 300 mbar for 30 s removed gas bubbles created during stirring. The solution was poured into a mold, which consists of a brass bottom and a transparent polycarbonate cylinder with

an inner diameter of 40 mm and a height of 90 mm. A silicone-coated polyethylene-terephthalat (PET) film (Hostaphan RN 30 2SLK, Mitsubishi Polyester Film GmbH, Germany) was used as a separation layer between solution and cylinder. The use of the separation layer guaranteed easy demolding without damaging the frozen sample. The samples were frozen on a cold finger, which allows to control the temperature of the brass bottom. One end of a copper cold finger is immersed in liquid nitrogen and the other end is equipped with a resistance heater. A thermocouple positioned at the center of the brass bottom detects the temperature at the interface between the brass bottom and sample.
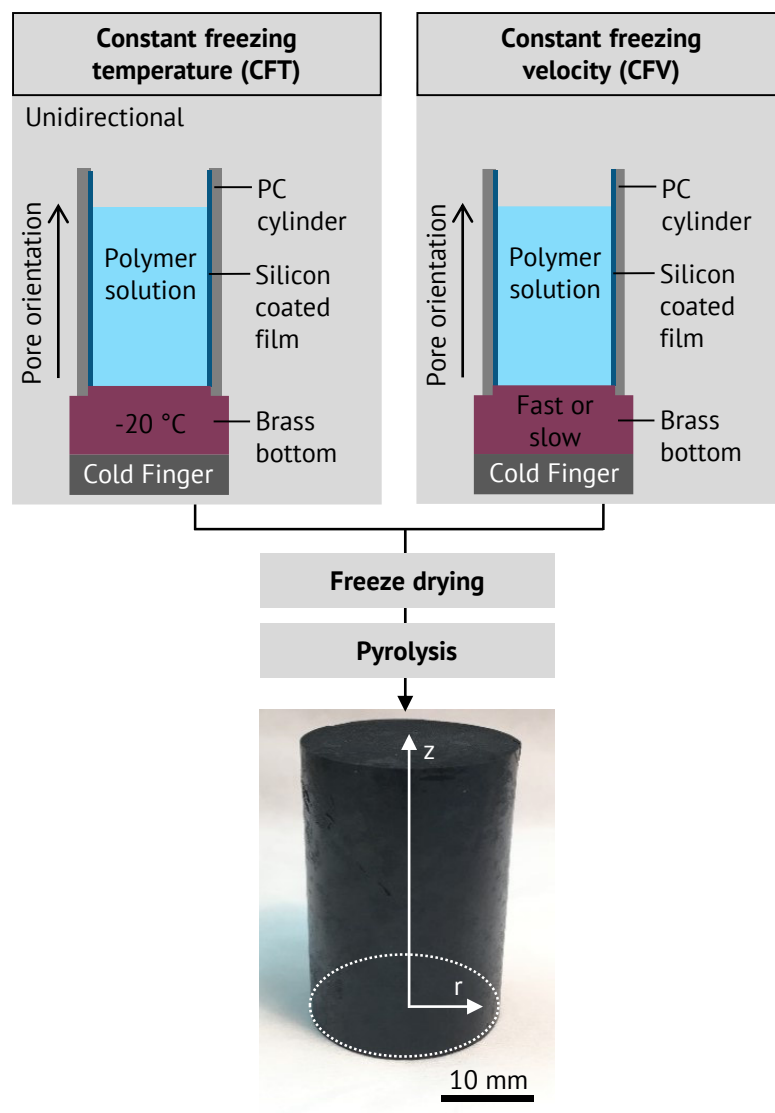

Figure 6.2   Process scheme of monolith preparation by solution-based freeze casting of polymeric solutions.

Three different freezing conditions were used: constant freezing temperature (CFT) at −20 °C and constant freezing velocity (CFV) at two different speeds (fast and slow, see Table 6.1). The starting conditions for CFT samples were set to 0 °C for 3 min. The data obtained by recording the freezing velocity in CFT condition were used as input to adapt the cooling ramps and empirically ensure CFV conditions. Under the assumption of a linear correlation between the cooling rate and the freezing front velocity, the local deviation of the freezing front velocity in CFT conditions from the constant freezing front velocity was taken as a parameter for changing the cooling ramps. The starting conditions for CFT samples were set to 0 °C for 3 min.

After complete freezing, the mold was transferred to a freezer at a temperature of −20 °C for 72 h to enable sufficient cross-linking. Subsequently, the solvent was sublimated in a freeze dryer for 72 h at a shelf temperature of −20 °C and a pressure of 1000 µbar. Lastly, the samples were pyrolyzed at 1000 °C under flowing nitrogen with a heating rate of 2 K·min^{-1} and a dwelling time of 4 h. Before characterization, 2 mm of the bottom end was removed to ensure an open access to the pore structure and a flat cross section. Additionally, cutting all samples to a total height of 25 mm guarantees comparability in wicking experiments. After the wicking tests, the monoliths were cut horizontally to obtain samples for the height dependent investigation of pore window size, porosity and permeability. Three positions were taken into account: bottom, middle and top. The middle positions correspond to a height of 12.5 mm and all samples were taken from identical positions.

The samples were given the nomenclature: [solvent] [solid loading in wt%] [freezing condition]. Whereby, the polymer and the cross-linking agent counted as solid fraction. Table 6.1 gives an overview of all samples and their compositions.

Table 6.1 Denotation, composition, freezing conditions and experimental freezing front velocity.

Denotation	Solvent	Solid loading wt%	Freezing condition	Experimental freezing front velocity μm/s
CH20-20	Cyclohexane	20	CFT[a] − 20 °C	–
CH40-20	Cyclohexane	40	CFT[a] − 20 °C	–
TBA20-20	Tert-butyl alcohol	20	CFT[a] − 20 °C	–
TBA40-20	Tert-butyl alcohol	40	CFT[a] − 20 °C	–
CH20fast	Cyclohexane	20	CFV[b] fast	6.8
CH40fast	Cyclohexane	40	CFV[b] fast	6.6
TBA20fast	Tert-butyl alcohol	20	CFV[b] fast	6.6
TBA40fast	Tert-butyl alcohol	40	CFV[b] fast	6.8
CH20slow	Cyclohexane	20	CFV[b] slow	4.6
CH40slow	Cyclohexane	40	CFV[b] slow	4.2
TBA20slow	Tert-butyl alcohol	20	CFV[b] slow	4.6
TBA40slow	Tert-butyl alcohol	40	CFV[b] slow	3.3

[a] CFT = Constant Freezing Temperature
[b] CFV = Constant Freezing Velocity

6.3.3 Characterization

The freezing front axial advance of one sample for each composition was recorded during the freezing process by a CCD-camera in order to evaluate the freezing front velocity. The pore structure at the positions bottom, middle and top was investigated using a scanning electron microscope (SEM, Camscan Series2, Obducat CamScan Ltd.) with samples mounted on carbon tape. Before acquisition, specimens were sputtered with gold (K550, Emitech, Judges Scientific Plc., UK). Pore window diameter distribution and open porosity ϕ at the positions bottom, middle and top were obtained by mercury intrusion porosimetry (Pascal 140/440, POROTEC GmbH, Germany).

The permeability $K = K_{Darcy}$ at the positions bottom and top was evaluated in axial z-direction according to Darcy's law in constant head measurements on cylindrical samples with a diameter D_{Darcy} of 10 mm and a height H_{Darcy} of 5 mm to 9 mm. Suitable cylindrical samples were cut from the center of the corresponding cross sections. Bypass flow was minimized by using a compressible silicone sample holder. The mass

of the permeated water $m_{w, Darcy}$ at a pressure difference Δp_{Darcy} of 10 kPa and a time t of 300 s was recorded. With the dynamic viscosity of water at 20 °C μ_w = 1.00 mPa·s and the density of water at 20 °C ρ_w = 998 kg·m^{-3}, the permeability $K = K_{Darcy}$ was calculated according to Equation 6.1. Soaking the specimens with water before the measurement should reduce deviations due to intake losses. Each sample was tested minimum five times and the average was calculated. In order to obtain reliable results, the validity assumptions of the Darcy equation have been verified. Since calculated Reynolds numbers range from 2 to 1450, the presence laminar flow regime is indicated. Further requirements such as no reaction of the fluid with the sample, incompressible fluid, single phase flow and continuous and steady flow can be considered as fulfilled. Thus, the applicability of the Darcy equation is ensured.

$$K = K_{Darcy} = \frac{\mu_W H_{Darcy}}{\Delta p_{Darcy}} \frac{m_{W,Darcy}}{\rho_W \frac{\pi}{4} D_{Darcy}^2 t_{Darcy}}. \tag{6.1}$$

The Washburn sorption method was used to investigate wicking into porous media when in contact with a liquid. Figure 6.3 shows a schematic drawing of the wicking device.
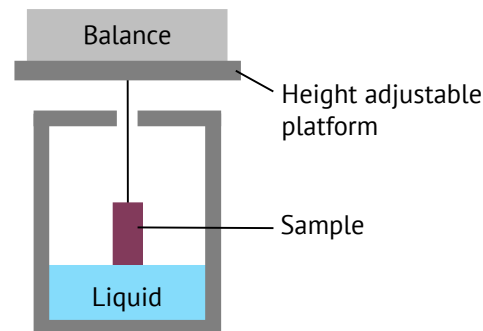
Figure 6.3 Schematic drawing of the device for isothermal wicking at room temperature.

The mass increase in the sample caused by imbibing liquid was recorded by a balance (LA310S, Sartorius AG, Germany) with a precision of ± 0.0001 g and a sample rate of 20 Hz. The scale was mounted on a height-adjustable platform which allows for bringing the sample in contact with the liquid. The specimen was attached to a sample holder and connected by a metallic wire with the balance. The surrounding container has a diameter of 0.095 m and its lid has a small hole allowing for a frictionless

movement of the sample. Hydrofluoroether (HFE-7500, 3M™ Novec™) was used as test liquid, because it shows excellent wetting properties for a wide range of materials. Hence, a contact angle of $\theta = 0°$ was assumed [7]. Once the sample had contact with the liquid, the immersion process was stopped. After wicking to complete saturation indicated by a constant mass signal m_{sat}, the monolith was lifted approx. 5 mm to lose contact with the liquid. All wicking tests were performed under room temperature and at ambient pressure. The geometry of the device leads to the assumption of negligible decreasing liquid level, whereas buoyancy and the Wilhelmy effect result in the necessity of raw data corrections. The Wilhelmy effect describes the mass change due to surface tension. Following previous studies, the weight of the completely saturated, but partially submerged sample was subtracted from the weight of the completely saturated sample [22, 24].

Besides the experimental approach, wicking can be evaluated by calculating the liquid transport. The capillary bundle model was used for the theoretical prediction of the wicking. The capillary pressure, which results from the curvature of the surface, is the driving force for the wicking. Viscous forces and hydrostatic pressure balance the capillary pressure [22, 23, 25-27]:

$$\frac{m^2}{t} = \frac{4\sigma_l \, \cos\theta \, \rho_l^2 A^2 \phi}{\mu_l} \frac{K}{R_s}. \qquad (6.2)$$

This equation gives the imbibed mass m per time t and is called the Lucas-Washburn equation with gravity effects for porous media with σ_l being the surface tension of the liquid, θ the contact angle, R_s the static radius, ϕ the open porosity, μ_l the dynamic viscosity of the liquid, K the permeability, ρ_l the density of the liquid, g the gravitational acceleration and A the cross section of the sample. According to the product sheet of the supplier, the surface tension σ_l, the dynamic viscosity μ_l and the density ρ_l of HFE-7500 are 16.2×10^{-3} N·m^{-1}, 1.24×10^{-3} Pa·s and 1614 kg·m^{-3}, respectively [28]. As already mentioned, the contact angle θ can be assumed to be 0°.

Wicking can be predicted with the knowledge of the macroscopic properties describing the porous structure such as the static radius R_s, the open porosity ϕ and the permeability K. The static radius R_s describes an equivalent capillary pore radius and can be calculated from the equilibrium between capillary pressure and hydrostatic pressure. Due to the limited height of the samples in this study, the

equilibrium was not reached and the static radius R_s could not be calculated. Instead, the mean pore window radius R_{merc} determined by mercury intrusion porosimetry was used as static radius.

6.4 Results and Discussion

6.4.1 Freezing Process

To evaluate the freezing front velocity, the axial advance of the freezing front was monitored during freezing as shown in Figure 6.3.
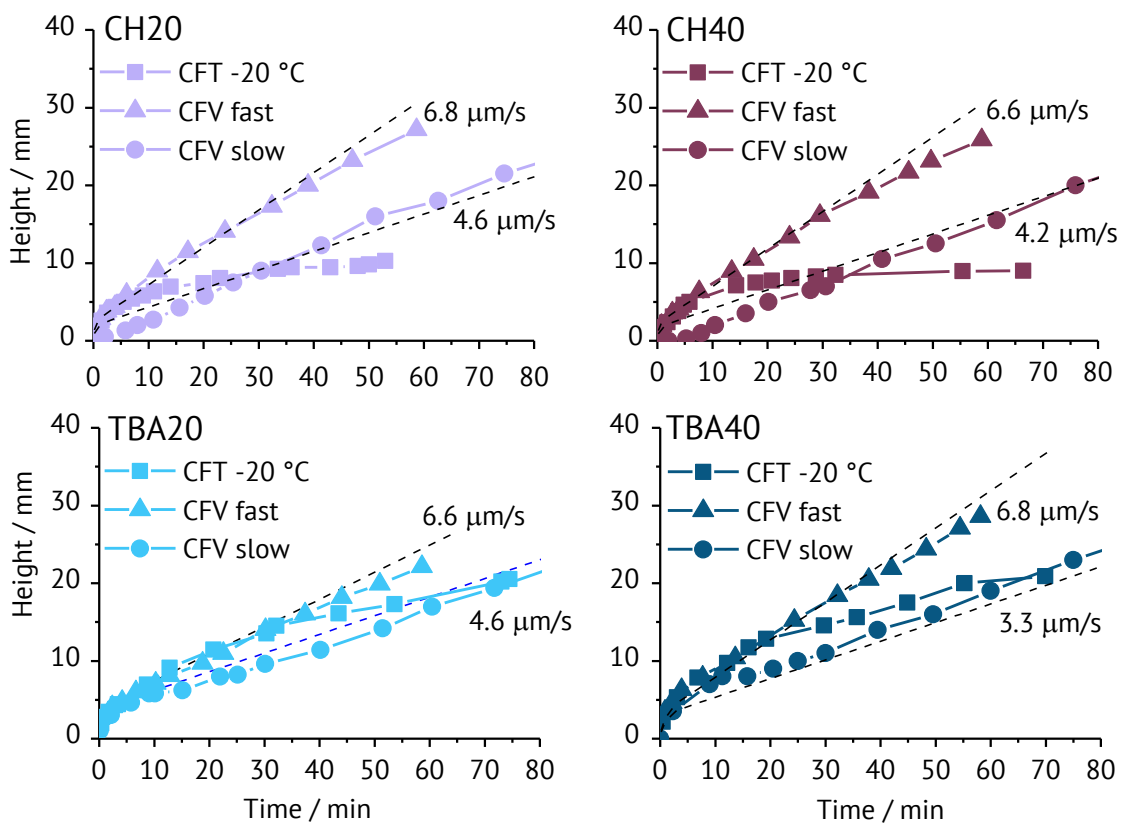
Figure 6.4 Position of freezing front during freeze casting in dependence on solvent, solid loading and freezing conditions; the theoretical constant freezing front velocity is symbolized by the dashed lines.

Constant freezing temperature conditions (CFT) are characterized by a clear decrease in freezing front velocity with time. The thermal resistance increases with progressing freezing front leading to a decrease in the thermal gradient at the freezing front. Since the freezing front velocity is mainly influenced by the thermal gradient, it decreases with time [29]. While the solid loading (20 wt% or 40 wt%) does not affect the freezing front velocity at CFT conditions (rectangles in Figure 6.4), the solvent

clearly has an impact. At the same conditions, the freezing front reaches only half of the height in cyclohexane samples compared to samples with *tert*-butyl alcohol. One reason is the higher temperature difference between freezing temperature and melting point for TBA which translates into a higher undercooling. Though the thermal conductivity of the solid solvent is supposed to be an influencing factor, no estimation is possible due to the lack of data for TBA. The thermal conductivity of CH at −25 °C was reported to be 0.14 W·(m·K)$^{-1}$ [30]. In the liquid state, CH and TBA exhibit a similar thermal conductivity with values of 0.117 W·(m·K)$^{-1}$ (27.68 °C) and 0.1076 W·(m·K)$^{-1}$ (27.8 °C), respectively [31, 32].

When adapting the temperature program, two different constant freezing front velocities were achieved indicated by an almost constant slope in Figure 6.4. The theoretical velocity is symbolized by the dashed lines. The empirical approach which uses the data of CFT conditions to obtain CFV conditions proofs to be efficient for the investigated parameters. Due to the initial freezing stage at 0 °C for 3 min, the theoretical velocity as well as the experimental data starts with a nonlinear section. The realized freezing front velocities were influenced by the composition and differ from 3.3 µm·s^{-1} to 6.8 µm·s^{-1}. Constant freezing front velocities over the complete height of the sample are easier to achieve for slow freezing front velocities. Especially at low freezing front velocities the freezing front velocity during the initial freezing stage deviates from the average velocity. Depending on the solvent, the freezing front velocity deviates to higher or lower velocities. Due to different melting points of TBA (T_m = 23 °C to 26 °C) and CH (T_m = 6.5 °C), the thermal gradient at initial freezing (0 °C) is higher for TBA compared to CH, which is why TBA20slow and TBA40slow show faster initial freezing. In contrast, CH20slow and CH40slow froze significant slower at the initial stage. Furthermore, precise evaluation of the position of the freezing front is difficult resulting in scattered data. The formation of ice on the outer surface of the mold and the meniscus-shaped solidification front which is generated by the heat transfer from the bottom through the cylindrical mold to the solidification front are main difficulties.

6.4.2 Pore Structure

The influence of the freezing front velocity on the pore structure was height-dependently investigated at three positions: bottom, middle and top. Figure 6.5 shows representative cross sectional SEM images of the pore structure parallel to the freezing direction and schematic representations of one dendrite along the complete sample height.

Due to the unidirectional freezing, the pore structure is orientated from bottom to top. The characteristic dendritic and prismatic pore morphology is present for cyclohexane and *tert*-butyl alcohol, respectively [16]. Investigations by mercury intrusion porosimetry enable a detailed characterization of the pore structure. The mean pore window diameters (a) and open porosities (b) are shown in Figure 6.6.
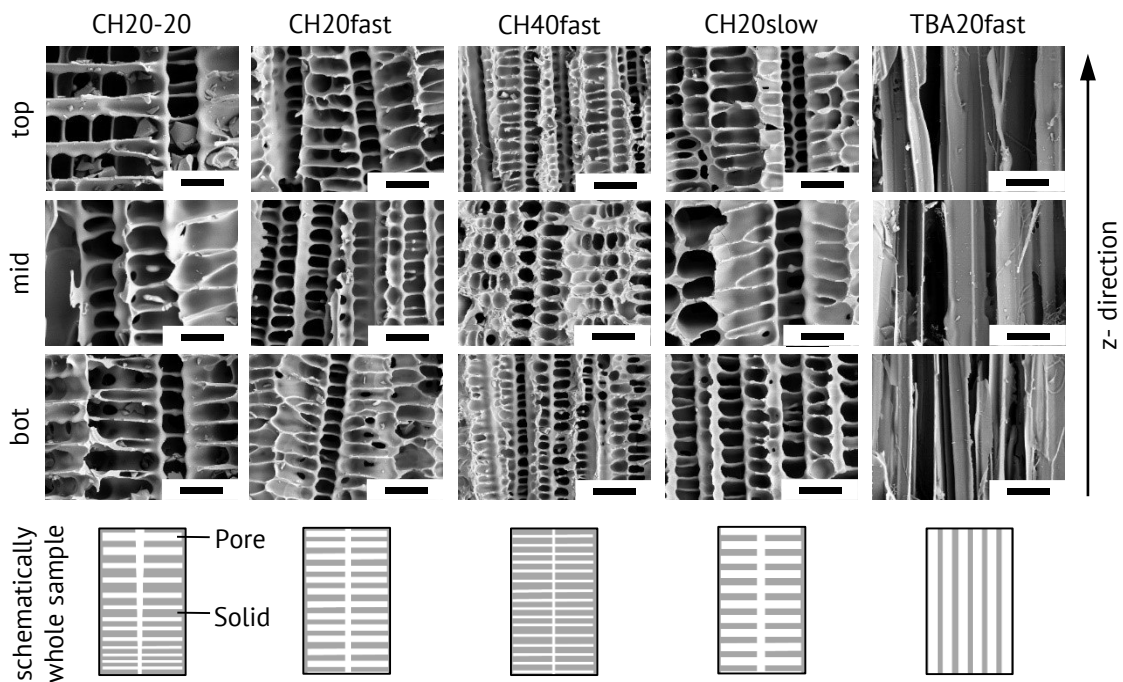
Figure 6.5   Exemplary cross sectional SEM images of the pore structure for bottom, middle and top position in dependence on solvent, solid loading and freezing conditions; scale bar: 50 µm.

(a) Mean pore window diameter $2R_{merc}$ / µm
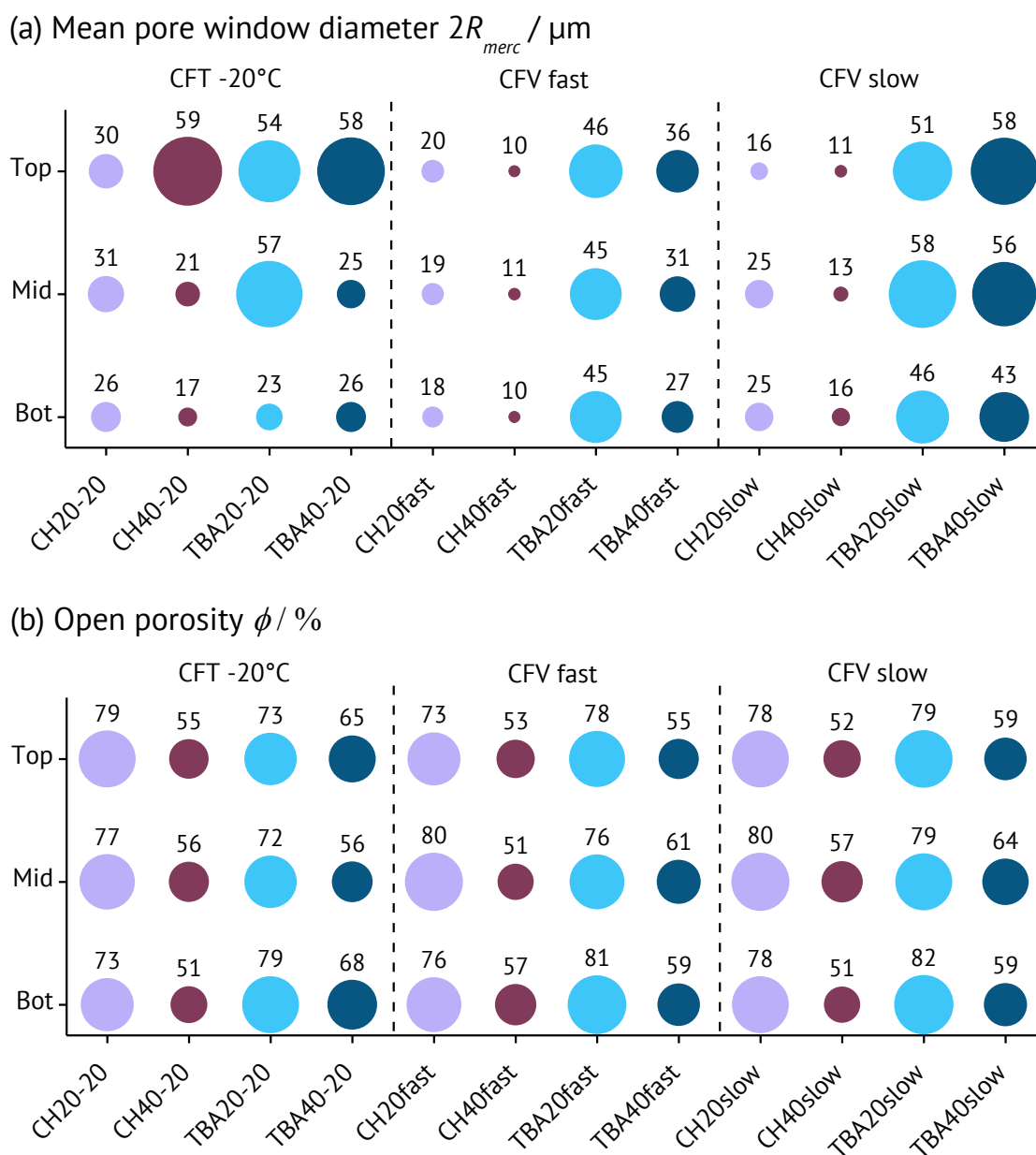
(b) Open porosity ϕ / %

Figure 6.6 Mean pore window diameter (a) and open porosity (b) in dependence on the position obtained by mercury intrusion.

The porosity is almost constant within one sample. The solid loading is the main influencing factor on porosity with higher porosity at lower solid loading as it is described in literature [33]. The porosity ranges from 51 % to 82 %. Regarding the pore window size, lower solid loading results in slightly larger pore window diameters. In general, the pore window size distribution is mainly monomodal as it can be seen exemplarily in Figure A.3.2 on page 200. In addition to the solid loading, the solvent influences the pore window size with the prismatic pore morphology (TBA) leading to larger pore window sizes compared to the dendritic (CH) one. All samples frozen at

CFT conditions exhibit an increasing pore window size from bottom to top of factors between 1.2 and 3.5. This is in accordance with SEM images since Figure 6.5 shows the same trend.

Comparison with the recorded freezing front velocity indicates a strong relation between freezing front velocity and pore window size. Hence, a gradient in freezing front velocity leads to a gradient in pore window size with slow freezing resulting in large pores. This correlation was also reported in the literature for suspension-based freeze casting using water as liquid phase [20]. In contrast, a constant freezing front velocity generates a homogeneous pore window size as it can be observed for most of the samples frozen at CFV conditions. Significant deviations from constant pore window sizes in CFV conditions for example in TBA40slow and CH20slow are caused by locally different freezing front velocities. In Figure 6.4 faster and slower freezing than the average freezing front velocity during the course of freezing are obvious for CH20slow and TBA40fast, respectively. By adapting the freezing front velocity, the generation of samples with different homogeneous pore window sizes is possible. This is valid for both solvents.

Decreasing the freezing front velocity from CFV slow to CFV fast conditions results in an increase in the pore window diameter by 16 %, 29 %, 14 % and 67 % for CH20, CH40, TBA20 and TBA40, respectively. Hence, samples with higher solid loading are more sensitive to variations in freezing front velocity and allow for a larger range of achievable pore window sizes. At large pore window sizes, the thermodynamics of crystal growth are assumed to slow down the increase in pore window size with decreasing freezing front. While small pore window sizes at low solid loading are difficult to achieve due to the dependence of the pore window size from the solid loading, decreasing the freezing front velocity to obtain larger pores at high solid loading is easily possible. The combination of the different influencing factors on the pore window size such as solid loading, solvent and freezing front velocity with CFV freezing conditions enables the preparation of samples with a homogeneous pore structure. The pore window size can be adjusted in the range of 10 μm to 69 μm. Besides creating a homogeneous pore structure, the knowledge of the relation between freezing front velocity and resulting pore window size also allows for the generation of defined gradients in pore window size by adapting the freezing front velocity.

6.4.3 Permeability

The permeability K of bottom and top positions and the ratio between top and bottom position are shown in Figure 6.7.
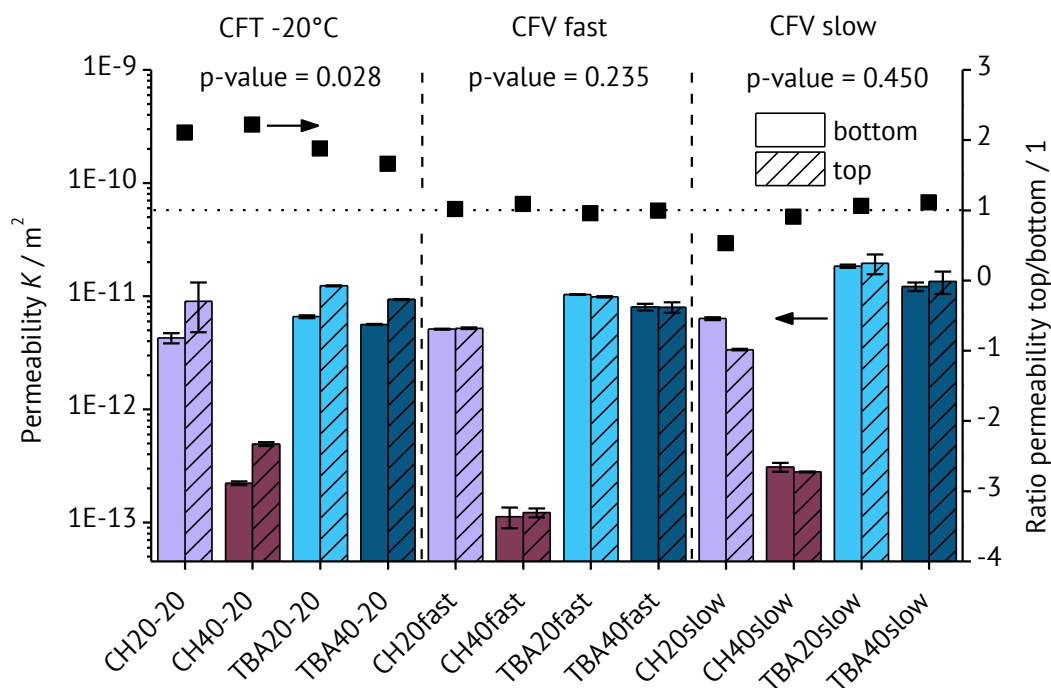
Figure 6.7   Permeability of top and bottom position and ratio between permeability of top and bottom position depending on solvent, solid loading and freezing condition.

Permeabilities in the range of 1.12×10^{-13} m^2 to 1.03×10^{-11} m^2 were measured. In general, decreasing permeability with decreasing porosity obtained by higher solid loading is observed for all freezing conditions and both solvents [34]. All samples with cyclohexane as liquid exhibit lower permeability compared to samples prepared at the same conditions with *tert*-butyl alcohol. This can be mainly attributed to the smaller pore window sizes of CH samples compared to TBA samples. The relation between permeability K and pore structure is usually modeled based on [35]:

$$K = c_{geo}\, \phi\, R^2,$$ (6.3)

where R is the pore radius, ϕ is the porosity and c_{geo} is a geometric factor that describes the shape, connectivity and aspect ratio of the pores. Equation 6.3 indicates that the permeability is very sensitive to the pore radius. The trend of pore window sizes obtained by mercury intrusion is in good accordance with the resulting permeability. Furthermore, for CFT conditions a gradient in pore window sizes is present which is reflected by higher permeability of all CFT samples at the top position. Hence, the

ratio between the permeability of top and bottom positions is larger than one. In contrast, CFV conditions with the homogeneous pore window sizes result in ratios close to one. Only CH20slow shows a non constant permeability with a significant lower permeability at the top compared to the bottom position. Statistical analysis on the significance of the differences between top and bottom positions revealed p-values of 0.028, 0.235 and 0.450 for CFT, CFV fast and CFV slow conditions, respectively. As the p-value for CFV fast and CFV slow conditions is larger than the significance level of 0.05, the difference in permeability can be considered to be statistically not significant for CFV fast and CFV slow conditions. In contrast, CFT exhibits statistically significant differences between top and bottom position (p-value < 0.05).

When comparing this finding with the pore window size, it becomes clear that the change in permeability is caused by differing pore window sizes. In contrast, the decrease in pore window size for CH40slow from bottom to top is assumed to be too low to significantly influence the experimentally obtained permeability. While TBA20 shows the highest permeability for all freezing conditions, CH40 exhibits the lowest permeability. Again, this can be clearly attributed to the different pore window sizes. For the same conditions, TBA generates larger pores compared to CH as can be seen in Figure 6.6. The geometric factor c_{geo} was calculated according to Equation 6.3. 0.0611 ± 0.0160, 0.0086 ± 0.0013, 0.0358 ± 0.0135 and 0.0427 ± 0.0176 were obtained for CH20, CH40, TBA20 and TBA40, respectively. For samples prepared with TBA, the change in solid loading has no significant influence on the c_{geo} value. This indicates no influence of the solid loading on structural parameters such as pore shape, pore connectivity and aspect ratio. In contrast, the c_{geo} value of samples with a dendritic pore structure (CH) depends on the solid loading. Hence, structural parameters describing the pore structures change with solid loading for a dendritic pore morphology. Lower solid loading accompanied with a higher porosity and a larger pore window size induces a high c_{geo} value in CH samples. This suggests that describing and predicting the permeability of the dendritic pore structure is more complex compared to the prismatic pore structure. In the literature, permeability, porosity and pore window size results which lead to a c_{geo} value of 0.0508 were reported for a dendritic pore structure obtained by a similar process [36]. This c_{geo} value is close to the one of CH20 and indicates comparable pore structures.

Investigations on c_{geo} values of granular material such as sandstone and volcanic rock reveals values of 0.012 and 0.0022, respectively [35]. The deviation of the c_{geo} values for freeze cast structures from c_{geo} values reported for granular material can be explained by considerable differences in the pore morphology. Only the c_{geo} value of CH40 is in the range of granular material.

It has to be mentioned that especially the permeability measurement of TBA20 is prone to bypass flow due to the low mechanical stability of the sample and potential crack formation when mounting the sample to the sample holder. As a consequence, the permeability of TBA20 samples is potentially overestimated.

6.4.4 Wicking and Theoretical Prediction of Wicking

The results of isothermal wicking experiments grouped by composition are shown in Figure 6.8. While at short times the viscosity of the liquid is most influencing, longer times are increasingly dominated by the influence of the gravity [37]. Samples frozen at higher velocity reach the saturation mass faster for all compositions. A higher freezing front velocity is connected to a smaller pore window size which results in faster wicking according to Equation 6.2. According to Equation 6.3, a smaller pore window size is also related to a lower permeability which decreases the wicking speed. However, the wicking results indicate that this decrease in permeability is not sufficient to compensate the increase in wicking speed caused by a small pore window size. The smaller the pore window size the higher the capillary force which is the driving force for wicking.

At short times, wicking curves of samples prepared at CFT conditions follow the behavior of fast frozen CFV samples. During the course of the experiment, the wicking speed significantly slows down to values which are smaller than samples frozen at slow CFV conditions. Besides the influence of the gravity, this can be mainly attributed to the gradient in pore window size along the axial height of the sample. Consequently, a gradient in pore window size creates a gradient in the driving force which changes the wicking speed additionally to the influence of gravity.

Figure 6.8 Mass divided by saturation mass in dependence on solvent and solid loading for all freezing conditions.

While at short times the viscosity of the liquid is most influencing, longer times are increasingly dominated by the influence of the gravity [37]. Samples frozen at higher velocity reach the saturation mass faster for all compositions. A higher freezing front velocity is connected to a smaller pore window size which results in faster wicking according to Equation 6.2. According to Equation 6.3, a smaller pore window size is also related to a lower permeability which decreases the wicking speed. However, the wicking results indicate that this decrease in permeability is not sufficient to compensate the increase in wicking speed caused by a small pore window size. The smaller the pore window size the higher the capillary force which is the driving force for wicking. At short times, wicking curves of samples prepared at CFT conditions follow the behavior of fast frozen CFV samples. During the course of the experiment, the wicking speed significantly slows down to values which are smaller than samples frozen at slow CFV conditions. Besides the influence of the gravity, this can be mainly attributed to the gradient in pore window size along the axial height of the sample. Consequently, a gradient in pore window size creates a gradient in the driving force which changes the wicking speed additionally to the influence of gravity.
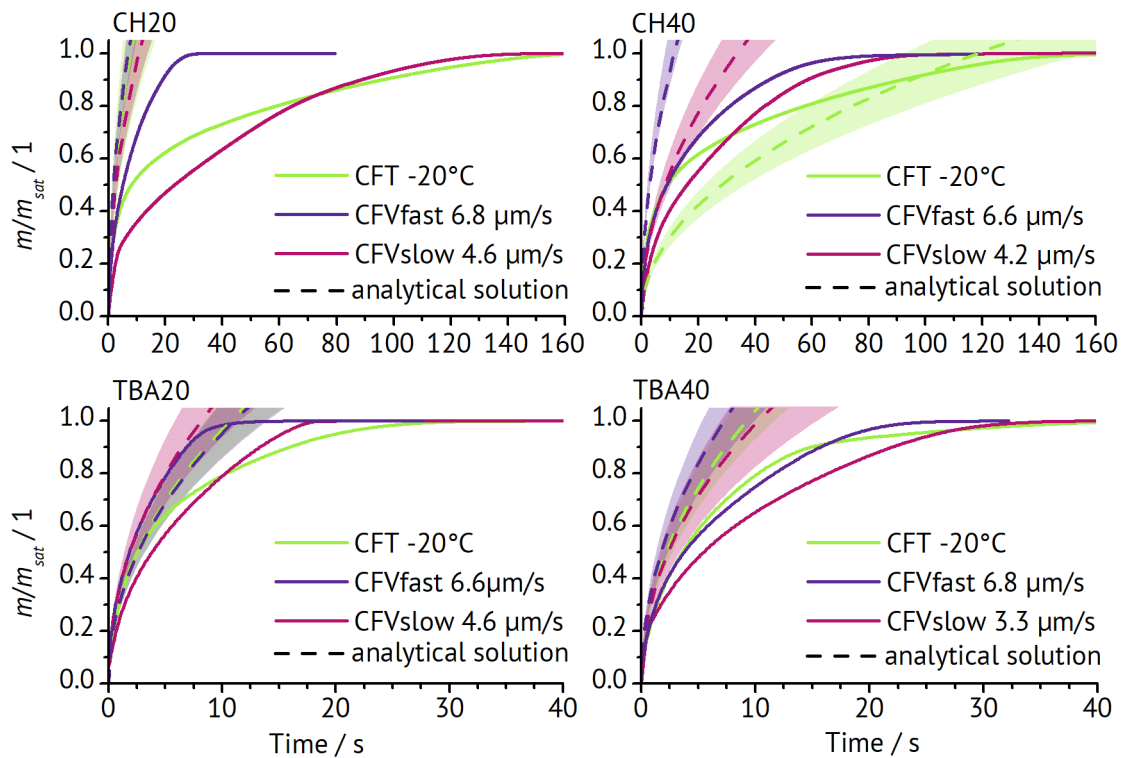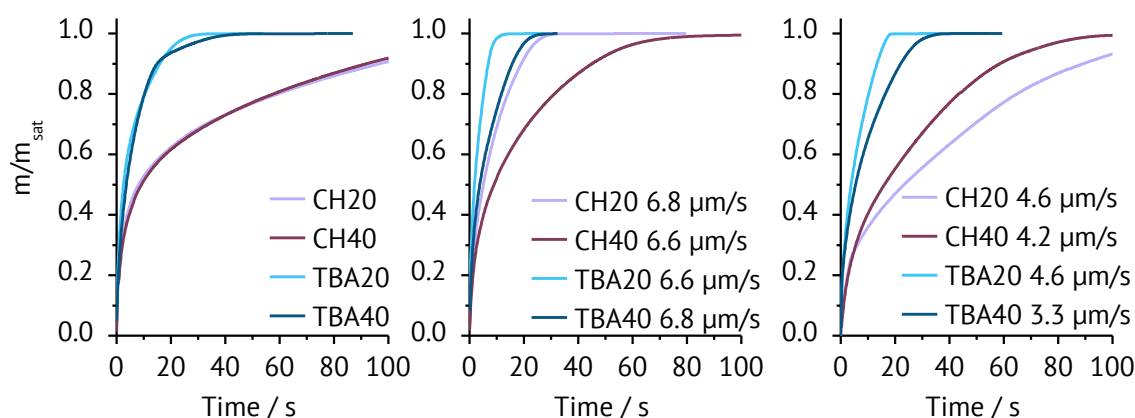
Figure 6.9 Wicking curves grouped by freezing condition in dependence on solvents and solid loading.

The influence of the porosity can be seen in Figure 6.9 which shows the wicking curves in dependence on solvent and solid loading grouped by freezing conditions. For all freezing conditions of TBA samples, higher porosity and larger pore window size caused by lower solid loading result in faster wicking. According to Equation 6.3, increasing porosity and pore window size translate into increasing permeability which can be attributed to be the main reason for faster wicking of samples with lower solid loading. For CH samples, this trend is not consistent.

The influence of the pore morphology becomes obvious when comparing CH20 samples with TBA samples. Although all three CH20 samples exhibit similar permeability, CH20-20 and CH20slow wick considerably slower than CH20fast. The reasons for this behavior are unclear at the moment. The wicking into the dendritic pore structure is generally slower than into the prismatic structure. Secondary dendrites which are perpendicular to primary ones need to be filled during wicking by flow through primary dendrites. Hence, in the dendritic pore morphology a higher pore volume has to be filled through smaller pores compared to the prismatic structure of the TBA samples. With a time of 10.9 s until saturation, TBA20fast exhibits the fastest wicking of all investigated samples, whereas CH20-20 shows the slowest wicking with 151.7 s. In between those limits, the wicking speed can be changed. Furthermore, a gradient in the driving force can be generated by a gradient of the pore window size. The knowledge of the factors influencing the wicking and the possibility to easily adapt the pore structure make it possible to precisely tailor materials for several applications in capillary transport.

Theoretical wicking curves were calculated according to the Lucas-Washburn equation as can be seen in Figure 6.8. The experimentally observed trend in wicking speed CFVfast > CFVslow is reflected in the analytical solution for all samples besides TBA20. The term ($\Phi \cdot K \cdot R_s^{-1}$) which describes the pore structure is significantly higher for TBA20slow compared to the other samples. Also, the ratio between permeability and static radius ($K \cdot R_s^{-1}$) is considerable larger for TBA20CFVslow. The potential overestimation of the permeability of TBA20 samples might be a reason for the high ratio. Concerning the influence of the porosity on wicking, the theoretical considerations confirm the experimental finding of faster wicking at higher porosity for both solvents. Except for TBA20, the analytical solution shows a significant deviation from the experiment for the following reason. The Lucas-Washburn equation assumes a bundle of aligned capillary tubes of the same radii. This assumption holds only for TBA20 which has a prismatic pore structure and an open porosity of approx. 75 %. Decreasing the porosity to approx. 60 % or even changing to a dendritic pore structure leads to a pronounced overestimation of the wicking speed by the analytical solution. Additionally, the analytical solution is not able to reflect gradients in the pore window size as they are present in the CFT samples. As a consequence, the prediction of wicking into complex pore structures by the Lucas-Washburn equation is only possible for pore structures which exhibit a very specific set of properties.

A previous study by the authors investigating the wicking of non-unidirectional frozen samples revealed a peculiar wicking behavior for the dendritic pore structure with a pronounced linear section in the wicking curve [23]. The authors suggested that limited interconnectivity between aligned pore areas is a potential explanation. In the present work, samples were frozen unidirectional and no linear section in the wicking tests was observed. Unidirectional freezing ideally provides a fully aligned pore structure with dendrites or prismatic pore channels running from bottom to top without any interruption. Hence, the absence of a linear section in wicking curves of the dendritic structures in the present study supports the assumption of limited interconnectivity causing the reported linear wicking behavior [23].

6.5 Conclusions

In this study, porous SiOC monoliths were prepared by solution-based freeze casting and the influence of different freezing conditions on the pore structure and on isothermal wicking was investigated. Constant freezing temperature results in a gradient of the pore window size, whereas constant freezing velocities between 6.8 μm·s^{-1} and 3.3 μm·s^{-1} lead to homogeneous pore structures. This was proved by characterizing the pore structure at three different positions of the monolith. The homogeneity holds for dendritic and prismatic pore structures and different porosities. In dependence on the solid loading, the solvent and the freezing front velocity, the pore window size varies between 10 μm and 59 μm. Maintaining solvent and solid loading constant, a higher freezing front velocity reduces the pore window size. The permeability varies in the range of 1.12×10^{-13} m^2 to 1.03×10^{-11} m^2 and is in good agreement with trends found for the pore window diameter and the porosity. Fastest wicking was observed for a prismatic pore structure at low freezing front velocity and high porosity, whereas slowest wicking occurred into the dendritic structure with high porosity and constant freezing temperature. The gradient of pore window size in samples prepared at constant freezing temperature is clearly reflected by a pronounced decrease in the wicking speed. In contrast, preparation at constant freezing front velocity results in wicking curves which have a shape closer to the prediction according to the Lucas-Washburn equation. The wicking of only the prismatic structure with a porosity of approx. 75 % can be sufficiently described by the Lucas-Washburn equation. Contrary, the simplification of reducing complex three-dimensional pore structures to the three parameters pore window size, porosity and permeability is not applicable for predicting the wicking behavior of the other investigated structures. The knowledge of the relationship between structural properties and the resulting wicking behavior combined with the flexibility of the solution-based freeze casting process enables to tailor porous media. A wide range of applications in capillary transport can be addressed by this powerful combination.

Acknowledgements

References

[1]   N.A. Ahmad, C.P. Leo, A.L. Ahmad, W.K.W. Ramli, Sep. Purif. Rev. 44 (2014) 109-134.

[2]   X. Zhu, S. Li, Y. Shi, N. Cai, Prog. Energy Combust. Sci. 75 (2019) 100784-100824.

[3]   S.K. Bhatia, R.K. Bhatia, J.-M. Jeon, G. Kumar, Y.-H. Yang, Renew. Sust. Energ. Rev. 110 (2019) 143-158.

[4]   F. Baino, E. Fiume, J. Barberi, S. Kargozar, J. Marchi, J. Massera, E. Verné, International Journal of Applied Ceramic Technology 16 (2019) 1762-1796.

[5]   J. Hartwig, *Liquid Acquisition Devices for Advanced In-Space Cryogenic Propulsion Systems*. 2016, Amsterdam: Elsevier Inc.

[6]   R. Masoodi, K.M. Pillai, *Wicking in Porous Materials*. 2013, Boca Raton: CRC Press.

[7]   N. Fries, K. Odic, M. Conrath, M. Dreyer, J Colloid Interface Sci 321 (2008) 118-29.

[8]   E.O. Einset, J. Am. Ceram. Soc. 79 (1996) 333-338.

[9]   S. Kumar, A. Kumar, R. Devi, A. Shukla, A.K. Gupta, J. Eur. Ceram. Soc. 29 (2009) 2651-2657.

[10]   K. Okada, S. Uchiyama, T. Isobe, Y. Kameshima, A. Nakajima, T. Kurata, J. Eur. Ceram. Soc. 29 (2009) 2491-2497.

[11]   H. Zhang, C.L. Fidelis, M. Wilhelm, Z. Xie, K. Rezwan, Mater. Des. 134 (2017) 207-217.

[12]   P. Colombo, G. Mera, R. Riedel, G.D. Sorarù, J. Am. Ceram. Soc. 93 (2010) 1805-1837.

[13]   C. Vakifahmetoglu, D. Zeydanli, P. Colombo, Mater. Sci. Eng., R 106 (2016) 1-30.

[14]   P. Colombo, J. Eur. Ceram. Soc. 28 (2008) 1389-1395.

[15]   B.-H. Yoon, C.-S. Park, H.-E. Kim, Y.-H. Koh, J. Am. Ceram. Soc. 90 (2007) 3759-3766.

[16]   M. Naviroj, S.M. Miller, P. Colombo, K.T. Faber, J. Eur. Ceram. Soc. 35 (2015) 2225-2232.

[17]   K.L. Scotti, D.C. Dunand, Prog. Mater Sci. 94 (2018) 243-305.

[18]   Y. Tang, S. Qiu, C. Wu, Q. Miao, K. Zhao, J. Eur. Ceram. Soc. 36 (2016) 1513-1518.

[19]   S.M. Miller, X. Xiao, K.T. Faber, J. Eur. Ceram. Soc. 35 (2015) 3595-3605.

[20]   S. Deville, E. Saiz, A.P. Tomsia, Acta Mater. 55 (2007) 1965-1974.

[21]   M. Naviroj, P.W. Voorhees, K.T. Faber, J. Mater. Res. 32 (2017) 3372-3382.

[22]   Y. Grebenyuk, H.X. Zhang, M. Wilhelm, K. Rezwan, M.E. Dreyer, J. Eur. Ceram. Soc. 37 (2017) 1993-2000.

[23]   D. Schumacher, D. Zimnik, M. Wilhelm, M. Dreyer, K. Rezwan, Sci. Technol. Adv. Mater. 20 (2019) 1207-1221.

[24]   Y. Grebenyuk, M.E. Dreyer, Cryogenics 78 (2016) 27-39.

[25]   E.W. Washburn, Phys. Rev. 17 (1921) 273-283.

[26]   R. Masoodi, K.M. Pillai, P.P. Varanasi, AlChE J. 53 (2007) 2769-2782.

[27]   R. Masoodi, K.M. Pillai, P.P. Varanasi. *Role of Hydraulic and Capillary Radii in improving the Effectiveness of Capillary Model in Wicking*. in *Proceedings of FEDSM2008 2008 ASME Fluids Engineering Conference*. 2008.

[28]   3MDeutschlandGmbH, *Product Information 3M Novec 7500 Engineered Fluid*. 2019: Neuss.

[29]   U.G. Wegst, M. Schecter, A.E. Donius, P.M. Hunger, Philos Trans A Math Phys Eng Sci 368 (2010) 2099-2121.

[30]   P. Andersson, J Phy. Chem. Solids 39 (1978) 65-68.

[31]   H. Watanabe, H. Kato, J. Chem. Eng. Data 49 (2004) 809-825.

[32]   Cameo Chemicals Database United States Government, *Datasheet Tert-Butyl Alcohol*. 1999.

[33]   S. Deville, Adv. Eng. Mater. 10 (2008) 155-169.

[34]   J. Hommel, E. Coltman, H. Class, Transport Porous Med 124 (2018) 589-629.

[35]   N. Nishiyama, T. Yokoyama, J. Geophys. Res. Solid. Earth 122 (2017) 6955-6971.

[36]   G. Mikl, R. Obmann, S. Schörpf, R. Liska, T. Konegger, Adv. Eng. Mater. 21 (2019) 1900052-1900062.

[37]   N. Fries, M. Dreyer, J. Colloid Interf. Sci. 320 (2008) 259-263.

In situ Formation of Ni Particles
for CO₂ Methanation

<div style="text-align:right">

7

</div>

The previous chapters have shown various possibilities to alter the pore structure of macroporous monoliths prepared by the solution-based freeze casting process and their application in capillary transport. The influence of solid loading, templating solvent, freezing conditions and the addition of filler particles was evaluated. Additionally, the ability to control the pore structure in a wide range of pore sizes, porosities and pore morphologies was proven. Besides the application in capillary transport, macroporous monoliths are also important for heterogeneous catalysis due to their superior heat- and mass transport properties compared to pellets in packed-bed reactors. Control over the pore structure is only one part of the challenge to design an effective monolithic catalyst. The other part is to introduce catalytic activity to initially inert supports. Supports with an inherent catalytic activity are of interest due to some drawbacks of the commercially applied method of using a washcoat. As the in situ generation of metallic nanoparticles is possible in polymer-derived ceramics, they are promising candidates for inherent catalytic active materials. With the development and testing of porous catalytic active structures, another field of application is opened up besides the capillary transport. However, before optimizing the pore structure of a monolithic catalyst, it has to be ensured that the underlying principles and processes of manufacturing a porous metal containing PDC monolith are understood and controllable. Additionally, the catalytic activity without the influence of the macroporous monolith has to be evaluated to generate a benchmark for the development of the monolithic catalyst. In the following chapter, the adaption of the in situ formation of nickel particles from reflux synthesis to solution-based freeze casting is studied. Four complexing and cross-linking agents (CLA) with amino functionality are screened according to their ability to generate small and well distributed nickel particles as schematically shown in Figure 7.1.

The content of this section was published in the following article. The style and numbering of the references, the figures, the tables, the nomination as well as further typographic aspects have been adapted to be consistent throughout the thesis and to fit the superordinate layout. Furthermore, the coloring of the figures was unified. The supplementary data can be found in the appendix A.4 on page 201.

7.1 Abstract

Micro- and macroporous monoliths with in situ formed nickel nanoparticles were prepared for the first time by the combination of solution-based freeze casting and preceramic polymers (polymethylsiloxane). This one-step process results in macroporous monoliths composed of microporous and catalytic active nickel containing polymer-derived ceramic. Four different complexing and cross-linking siloxanes with amino functionality were screened for their ability to create small nickel particles. TEM analysis confirmed (3-aminopropyl)triethoxysilane being most efficient. High BET specific surface areas of $344 \ m^2 \cdot g^{-1}$ to $461 \ m^2 \cdot g^{-1}$ were achieved. Increased ratio of complexing groups to nickel improves the dispersion of nickel to (3.61 ± 1.49) nm. The nickel size dependence of carbon dioxide conversion (maximum 0.49) and selectivity towards methane (maximum 0.74) in CO_2 methanation emphasizes the importance of controlling the nickel size. The hydrophobic surface characteristic is hypothesized to be the main reason polymer-derived catalysts having better catalytic activity compared to nickel impregnated silica. The promising catalytic activity combined with the versatile freeze casting process can prospectively address heat and mass transfer considerations in heterogeneous monolith catalysis.
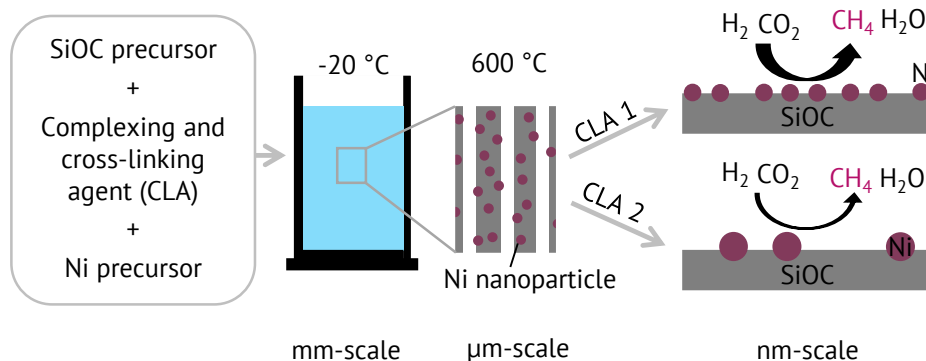
Figure 7.1 Schematic illustration of the screening of different complexing- and cross-linking agents (CLA) according to their ability to generate small and well distributed nickel particles.

7.2 Introduction

Nickel catalysts are the most intense studied catalysts for CO_2 methanation, also called Sabatier reaction $(CO_2 + 4H_2 \rightarrow CH_4 + 2H_2O, \Delta H_0 = -164\,\text{kJ·mol}^{-1})$ [1]. New concepts for energy storage such as "power-to-gas" and "power-to-liquid" require reactions like CO_2 methanation in order to generate methane and fuels from carbon dioxide and hydrogen.

Though, noble metal catalysts (rhodium, ruthenium, palladium) show superior performance especially at low temperatures, their high costs and limited abundance restrict their application in industrial processes compared to transitions metals (nickel, iron, cobalt) [1-5]. In heterogeneous catalysis, the support is very important to the performance with dispersing the active metal being its major role. High metal loading often results in aggregated metal particles with reduced catalytic activity [4]. Since water is a major product in CO_2 methanation a hydrophobic surface is claimed to avoid blocking of adsorption sites by water molecules [6]. Furthermore, weak interaction between the metal and the support was found to increase the activity due to a good reducibility of the metal [7].

The support influences the adsorption capability of the metal phase, its morphology, the metal-support interaction and finally the catalytic properties [8]. The preparation method effects the dispersion of the active phase and the metal-support interaction and hence strongly influences the overall catalytic behavior [9]. Numerous processes to prepare heterogeneous catalysts such as impregnation, sol-gel methods, co-precipitation and hydrothermal processes have been tested [1, 10].

Besides them, in situ formation of metal nanoparticles in a polymer-derived ceramics (PDCs) matrix proofed to result in small and very homogeneously distributed metal particles [11-13]. A great variety of metals such as nickel, iridium, platinum, palladium, iron, cobalt, copper, silver and gold were incorporated in PDC matrixes [13-16]. However, only some metal containing systems were fabricated for heterogeneous catalysis. Compared to conventional preparation processes, the in situ formation of metal particles and their reduction during inert-gas pyrolysis prevents the generation of hardly reducible oxides [16]. Furthermore, it has turned out that a complexing agent is strongly influencing the final metal size by complexing the nickel ions with e.g. amino groups. Complexing siloxanes were reported to be very efficient in creating a small and homogeneously distributed nickel nanoparticles [12, 13]. In addition, varying the process parameters such as pyrolysis temperature and chemical composition allows for the adjustment of properties like porosity, surface characteristics and metal dispersion [17].

Apart from the widely used reflux synthesis or polymeric shaping techniques, solution-based freeze casting of preceramic polymers allows for the generation of porous PDCs monoliths [18]. In solution-based freeze casting, pores are formed by thermally induced phase separation of a homogeneous polymeric solution during freezing. After completely frozen, the solvent is removed by sublimation resulting in a porous body with a pore structure reflecting the solvent crystals. The choice and the amount of the cross-linking agent has to be carefully adjusted in order to ensure sufficient cross-linking but prevent gelation before freezing [18]. Using cross-linking agents with amino groups adds the functionality of complexing metal ions to the cross-linking agent. Though metal containing PDCs have shown potential for catalytic applications and the fact that monolithic heterogeneous catalysis is supposed to overcome heat transport limitations no investigations were done on porous metal containing PDC monoliths, yet. Prior to optimizing such a monolithic catalyst in terms of pore structure, it has to be guaranteed that the underlying principles and processes of producing a porous metal containing PDC monolith are understood.

In this study, micro- and macro-porous catalytic active monoliths are prepared by solution-based freeze casting of polymethylsiloxane and in situ formation of nickel nanoparticles. In order to find an optimized cross-linking agent within the

restrictions of solution-based freeze casting, four different siloxanes with amino functionality are screened for their ability to generate small and homogeneous distributed nickel nanoparticles. Further variations were carried out for the most effective cross-linking agent. The amino to nickel ratio was increased, the pyrolysis temperature was altered and the nickel precursor was changed.

7.3 Experimental Section

7.3.1 Materials

Ni containing porous ceramic monoliths were prepared by solution-based freeze casting. A commercial polymethylsilsesquioxane (MK, Silres® MK, Wacker Chemie AG, Germany) and *tert*-butyl alcohol (TBA, > 99 %, Thermo Fisher GmbH, Germany) were used as preceramic polymer and solvent, respectively. Nickel(II) acetylacetonate (NiA, > 95 %, Sigma-Aldrich) and nickel(II) nitrate hexahydrate (NiN, 99.99 %, Sigma-Aldrich) acted as nickel precursor. NiN was chosen as a reference precursor. While NiN is reported to suffer from problems such as sintering and redistribution, such behavior is not known for NiA [8, 19]. Additionally, the better solubility of NiA in organic solvents provides a better compatibility with the presented approach of using polymeric solutions. To ensure complexing of nickel ions and provide cross-linking of the polymeric network, (3-aminopropyl)diethoxymethylsilane (APD, Sigma-Aldrich), (3-aminopropyl)triethoxysilane (APTES, abcr GmbH), (2-aminoethyl)-3-aminopropyltrimethoxysilane (AE, abcr GmbH) and Tetramethylethylenediamine (TMEDA, Sigma-Aldrich) were used. The complexing and cross-linking agents (CLAs) were chosen according to their ratio between complexing groups (R'NH$_2$, R'$_2$NH and R'$_3$N) and cross-linking active groups (OR). The ratio ranges from 0 (TMEDA) to 2/3 (AE) with APD (1/2) and APTES (1/3) being in between. Chemical structures and indication of complexing and cross-linking functionalities for all CLAs are shown in Figure 7.2. Additionally, the chemical structures are comprehensively listed on page 191. All raw materials were used without further treatment or purification.

7.3.2 Freeze Casting

The preparation of porous monolithic Ni containing samples by solution-based freeze casting is depicted in Figure 7.2. The overall solid loading was kept constant at 30 wt%. Whereby, the preceramic polymer, the Ni precursor and the CLA counted as solid fraction. For the preceramic polymer solution, MK was added to TBA under vigorous stirring. Meanwhile, the metal containing solution was prepared by adding the metal precursor and the CLA to TBA. Subsequently, the preceramic polymer solution was added to the metal containing solution.
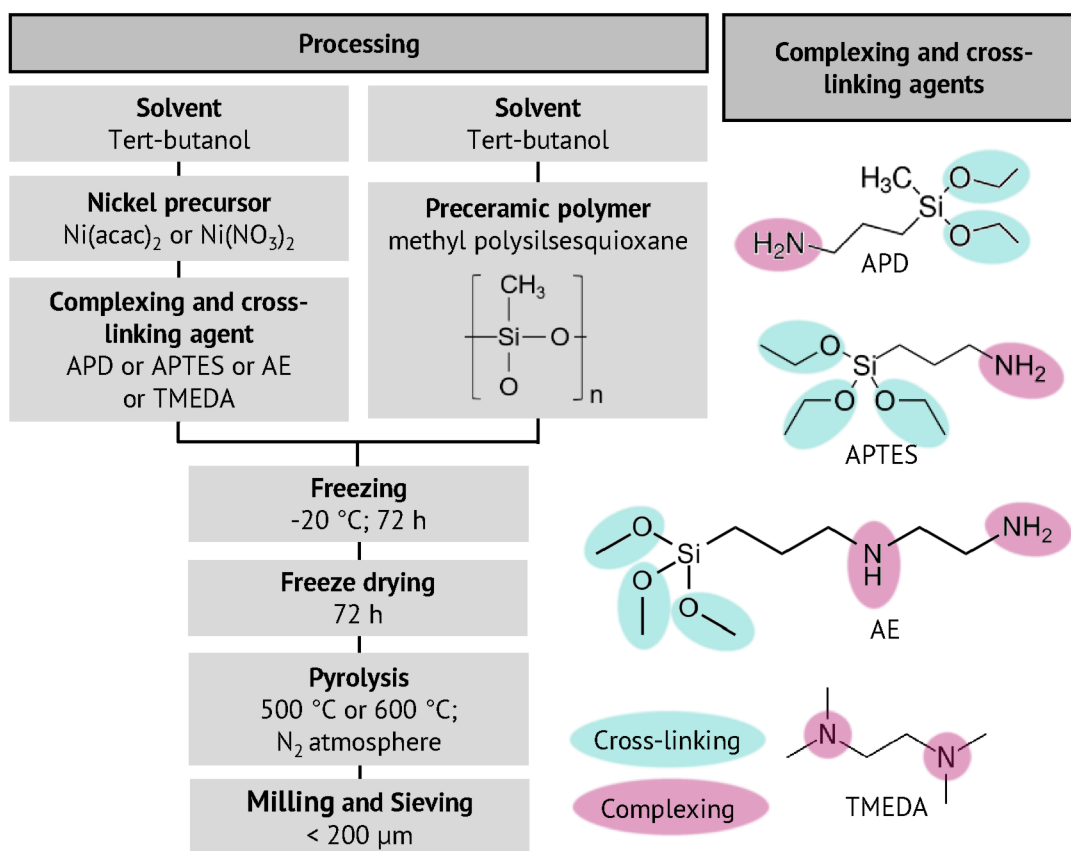
Figure 7.2 Process scheme and overview of complexing and cross-linking agents (CLAs) with indication of cross-linking and complexing functionalities.

The solution was poured into a mold, which consists of a PVC bottom and an aluminum rod with an inner diameter of 20 mm and a height of 60 mm. A silicon-coated PET film (Hostaphan RN 30 2SLK, Mitsubishi Polyester Film GmbH, Germany) was used as separation layer between solution and rod. After casting, the mold was transferred to a freezer at −20 °C for 72 h. After demolding, the solvent was sublimated in a freeze dryer for 72 h at −20 °C shelf temperature and a pressure of

1000 µbar. Finally, the monoliths were pyrolyzed at 500 °C or 600 °C under the flow of nitrogen with a heating rate of 2 K·min⁻¹ and a dwelling time of 4 h. Where required the monoliths were milled and subsequently sieved with a mesh size of 200 µm. The samples were labeled according to: [nickel precursor] [ratio of complexing groups to nickel ions] [CLA] / [pyrolysis temperature in °C]. Table 7.1 gives an overview of all samples and their compositions. For comparison of the catalytic activity, a reference catalyst was prepared by wet impregnation of commercial silica (1 µm, AngstromSphere, Fiber Optic Center Inc., USA) with nickel(II)nitratehexahydrate (99.99 %, Sigma-Aldrich). Subsequently, the catalyst was dried at 70 °C for 24 h and pyrolyzed at 600 °C.

Table 7.1 Denotation, composition and pyrolysis temperatures applied for all samples.

Denotation	Nickel precursor	Ratio complexing groups/Ni	Complexing agent	Pyrolysis temperature °C	Final metal loading wt%[a]
NiA2APD/600	Ni(acac)₂	2	APD	600	3.62
NiA2APTES/600	Ni(acac)₂	2	APTES	600	4.19
NiA2AE/600	Ni(acac)₂	2	AE	600	3.69
NiA2TMEDA/600	Ni(acac)₂	2	TMEDA	600	3.48
NiA4APTES/600	Ni(acac)₂	4	APTES	600	3.25
NiA4APTES/500	Ni(acac)₂	4	APTES	500	3.10
NiN4APTES/600	Ni(NO₃)₂	4	APTES	600	3.73
Ref Ni/SiO₂	Ni(NO₃)₂	–	–	600	5.00[b]

[a] according to TGA measurements
[b] calculated based on composition

7.3.3 Materials Characterization

The pore structure of the monolithic samples was investigated using scanning electron microscopy (SEM, field-emission SEM SUPRA 40, Zeiss, Germany) operating at 10.00 kV. Mercury intrusion measurements were conducted to reveal the open porosity and the mean pore window diameter (Pascal 140/440, POROTEC GmbH, Germany).

Specific surface area (SSA) was determined by evaluating nitrogen adsorption isotherms according to BET theory (Belsorp-Max, Bel Japan Inc., Japan). Measurements of vapor adsorption were performed by placing open vessels with ≈ 1 g

samples in closed Erlenmeyer flasks filled with liquids for 24 h. The adsorption of the liquids water and heptane was a measure of hydrophilic and hydrophobic surface characteristic, respectively. The liquids were at equilibrium with their vapor phase at 20 °C and atmospheric pressure. Prior to the measurement, the samples were dried at 70 °C for 24 h. Final metal loading in pyrolyzed samples was determined by thermogravimetric analysis in nitrogen atmosphere (STA 503, Bähr Thermoanalyse GmbH) assuming no loss of nickel during heat treatment. X-ray diffraction (XRD 3003, Seifert) was used to investigate the phase composition of pyrolyzed samples. Scans were performed with Cu-Kα radiation at diffraction angles 2θ of 5 ° to 80 ° at a step width of 0.025 ° and a time per step of 8 s. The size and dispersion of nickel nanoparticles was determined by the analysis of TEM images (Titan 80/300, FEI). To ensure statistically relevant results a minimum of nine images were captured of each sample and the average particle size of a minimum of 120 nickel particles was used for comparison.

CO_2 methanation in a fixed bed reactor was used as probe reaction to investigate the catalytic activity. 50 mg of sample were mixed with 300 mg of inert filler (alumina). The tubular reactor has an inner diameter of 9 mm and the total flow was set to 50 ml·min^{-1}, which gives a weight hourly space velocity (WHSV) of 60 l·g$_{cat}$$^{-1}$·h^{-1}. Whereby, the stoichiometric ratio of feed gases was H_2/CO_2/Ar = 16/4/5. Activation was conducted at 440 °C for 10 h at a flow of 20 ml·min^{-1} hydrogen with heating and cooling rates of 2 K·min^{-1}. To ensure steady state the temperature was hold at each measurement point for 40 min before the product stream was analyzed. Gas chromatography (5890 Series II, Hewlett-Packard) equipped with a thermal detector and a column to detect methane, carbon monoxide and carbon dioxide (Carboxen 1006 PLOT, 30 m × 0.53 mm, Supelco) were used to determine the carbon dioxide conversion X_{CO2} (Equation 7.1), the methane yield Y_{CH4} (Equation 7.2) as well as the methane selectivity S_{CH4} (Equation 7.3) according to following equations based on the assumption of carbon conservation:

$$X_{CO_2} = 1 - \frac{c_{CO_2,out}}{c_{CO_2,out} + c_{CH_4,out} + c_{CO_{out}}} \tag{7.1}$$

$$Y_{CH_4} = \frac{c_{CH_4,out}}{c_{CO_2,out} + c_{CH_4,out} + c_{CO_{out}}} \tag{7.2}$$

$$S_{CH_4} = \frac{Y_{CH_4}}{X_{CO_2}} \tag{7.3}$$

Additionally, the stability was exemplary evaluated on the sample NiA4APTES/600 at 400 °C for 10 h under reaction conditions.

7.4 Results

7.4.1 Pore Structure

SEM images were recorded and mercury intrusion experiments were conducted to investigate the pore structure of monolithic samples. Figure 7.3 (a – g) shows the characteristic pore structure.
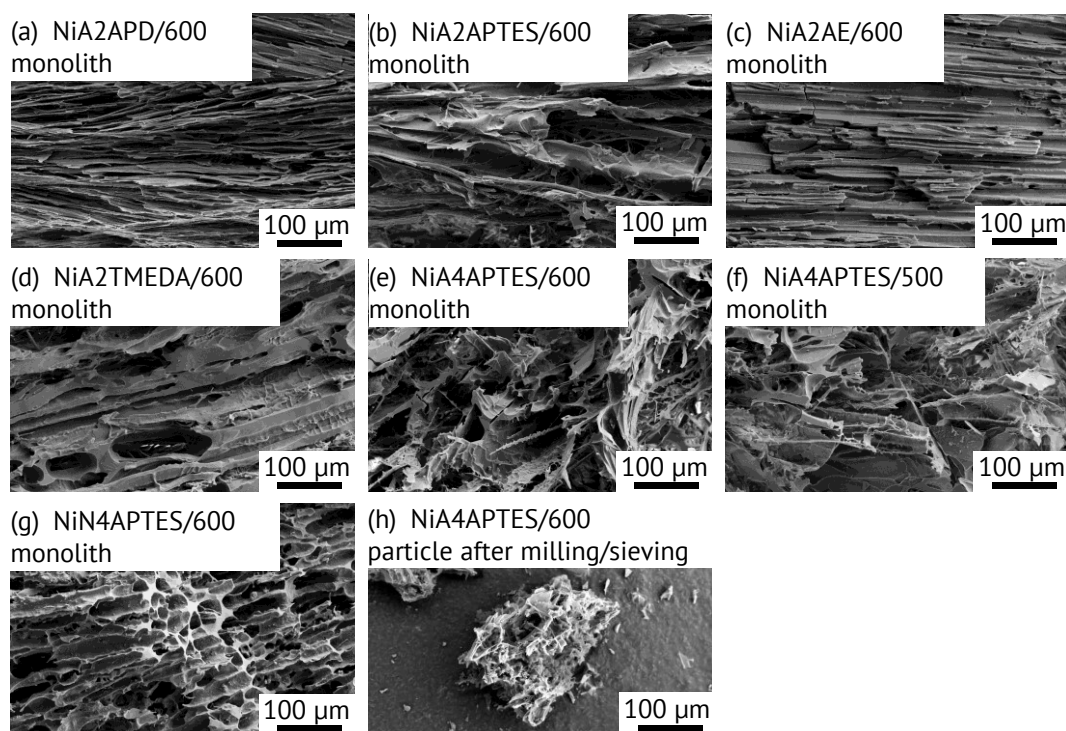
Figure 7.3 SEM images of the characteristic pore structure (a – g) of all samples and exemplary SEM image of a particle of sample AP4NiA/600 used in catalysis measurement (h).

The samples with a complexing group to Ni ratio of 2 (a – d) exhibit a prismatic like pore morphology with a pronounced orientation of the pore channels in radial direction. Orientation of the pores originates from the direction of freezing since the solvent crystals grow in the direction of heat transfer [20]. Additionally, mercury intrusion measurements reveal mean pore window diameters of 8.2 μm to 15.1 μm as

it can be seen in Figure A.4.1 on page 201. Changing the ratio of complexing groups to nickel from 2 to 4 results in a more unordered pore morphology with a channel like backbone superimposed by filigree details and interruptions of channels. Besides changes in the pore morphology, the mean pore window diameters significantly increase to values of 24.4 μm to 29.1 μm. Preliminary test revealed that the addition of metal precursors is not the reason for the change in pore morphology. Rather, these preliminary tests show that the increased amount of CLA is supposed to alter the pore morphology. Figure A.4.2 on page 201 clearly shows the change in pore morphology with increasing amount of the CLA AP. This finding indicates that high amounts of CLAs interfere the regular crystal growth. Figure 7.3 (h) shows a highly porous particle before the catalysis test.

7.4.2 Specific Surface Area and Surface Characteristic

Besides the pore structure, specific surface area and the surface chemistry with regards to hydrophilicity/hydrophobicity are important properties. Nitrogen adsorption isotherms were recorded to evaluate the specific surface area (SSA) according to BET theory. Figure 7.4 depicts the BET specific surface area.
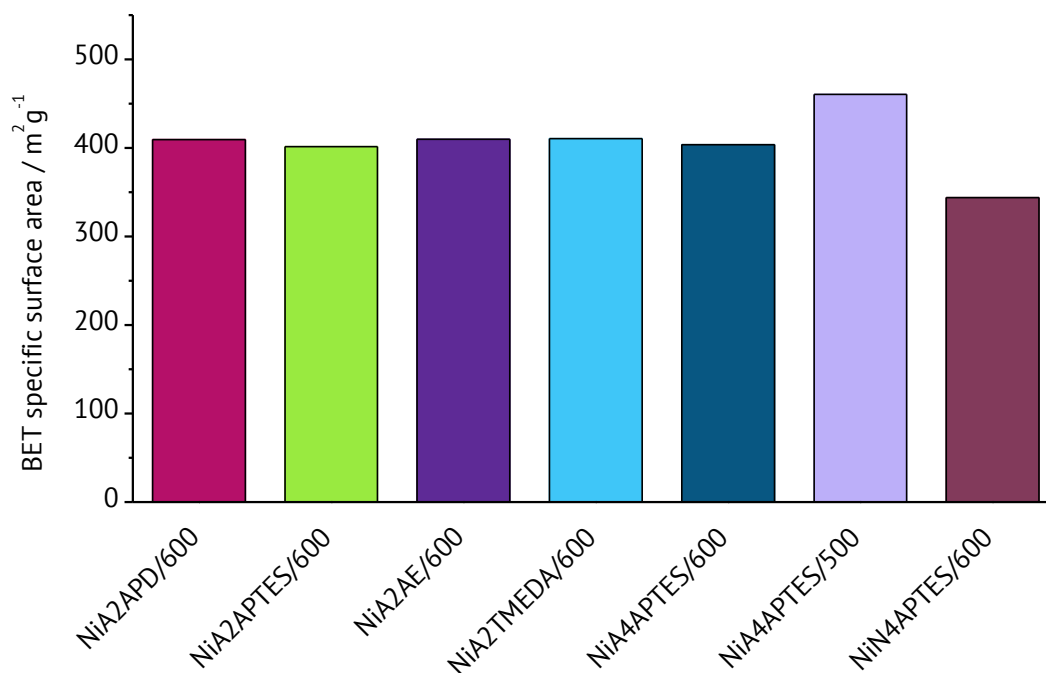

Figure 7.4 BET specific surface area determined by nitrogen adsorption for different cross-linking agents, nickel precursors and pyrolysis temperatures.

All samples exhibit type I isotherms indicating the presence of micropores as it can be seen in Figure A.4.3 on page 202. This is in accordance with the relatively high BET SSA in the range of 343 $m^2 \cdot g^{-1}$ to 461 $m^2 \cdot g^{-1}$. Micropores are formed during pyrolysis by the release of gaseous decomposition products. Mainly the decomposition of the CLAs and of the methyl group of MK contribute to the formation of micropores. Besides its positive effect in catalyzing the cross-linking, nickel is supposed to enhance the polymer-to-ceramic conversion. Consequently, the decomposition of the methyl group in MK is shifted to lower temperatures as it was observed in previous TGA measurements. This behavior of polysiloxanes has been reported in literature for nickel as well as for other metals [11, 17, 21, 22]. Studies using similar precursors found comparable BET SSA.

All samples with NiA as nickel precursor and a pyrolysis temperature of 600 °C show very similar BET SSA of 401 $m^2 \cdot g^{-1}$ to 410 $m^2 \cdot g^{-1}$. Hence, different CLAs are not influencing the BET SSA. Furthermore, also the ration between complexing groups and nickel ions does not affect the BET SSA as NiA2APTES/600 and NiA4APTES/600 show no significant difference in surface area. Reducing the pyrolysis temperature from 600 °C to 500 °C leads to a rise in BET SSA from 403 $m^2 \cdot g^{-1}$ to 461 $m^2 \cdot g^{-1}$. After the formation of micropores, further increase of the pyrolysis temperature typically results in the collapse of micropores as it is reported in literature [23, 24]. Changing the nickel precursor from NiA to NiN reduces the BET SSA from 403 $m^2 \cdot g^{-1}$ to 344 $m^2 \cdot g^{-1}$. In contrast to the polymer-derived catalysts, the reference catalyst shows a type III isotherm with a BET SSA of 2 $m^2 \cdot g^{-1}$ as it can be seen in Figure A.4.3 on page 202.

Apart from the specific surface area, the surface characteristic in terms of hydrophilicity/hydrophobicity is important when it comes to the interaction of molecules with the surface. Vapor adsorption measurements were performed with water and heptane as probe molecules for polar and unpolar surface characteristics, respectively. Figure 7.5 shows the ratio of adsorbed water to adsorbed heptane at 22 °C. Samples with ratios < 1 are considered to be hydrophobic. In contrast, a ratio of > 1 indicates hydrophilic surface characteristic.
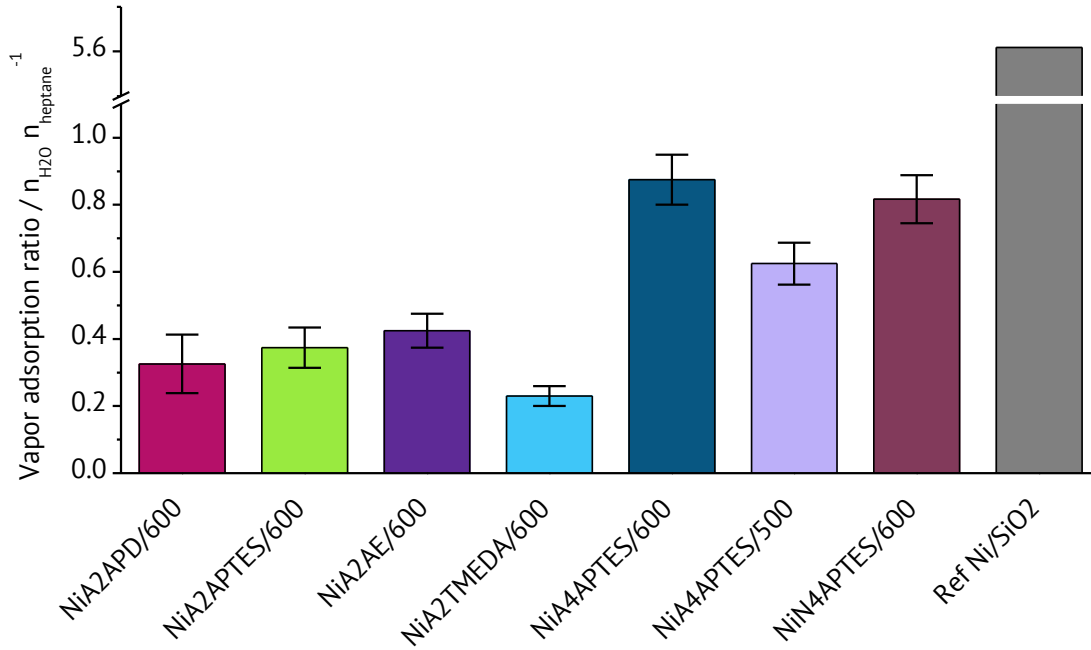
Figure 7.5 Vapor adsorption ratio of water to heptane at 22 °C for different cross-linking agents, nickel precursors and pyrolysis temperatures.

All samples exhibit a hydrophobic behavior. Two groups of samples can be distinguished: the one with a complexing group to nickel ratio of 2 and the other one with the increased ratio of 4. It is known that the metal-free preceramic polymer MK pyrolyzed at 600 °C itself is hydrophobic [25]. Since the amino groups of the CLA are almost completely decomposed at 600 °C, silicon containing CLAs mainly add additional hydrophilic SiO units to the pyrolyzed structure [26, 27]. The samples NiA2APD/600 and NiA2APTES/600 exhibit one silicon atom per complexing amino group. In contrast, NiA2AE/600 includes only 0.5 silicon atoms per amino group and NiA2TEMDA/600 has no silicon atoms at all. Therefore, the ratio of vapor adsorption is similar for NiA2APD/600, NiA2APTES/600 and NiA2AE/600 reaching values of 0.32 ± 0.09, 0.37 ± 0.06 and 0.42 ± 0.05, respectively. In contrast, NiA2TEMDA/600 without additional hydrophilic SiO units provided by TMEDA exhibits the lowest hydrophilicity with a value of 0.23 ± 0.03. Following this argumentation, samples with higher amount of CLA such as NiA4APTES/600, NiA4APTES/500 and NiN4APTES/600 show values of 0.87 ± 0.07, 0.62 ± 0.06 and 0.82 ± 0.07, respectively.

Decreasing the pyrolysis temperature from 600 °C to 500 °C results in less decomposition of organic groups and consequently in an increased hydrophobicity as it can be seen comparing NiA4APTES/600 and NiA4APTES/500 [25]. No significant

influence of the nickel precursor on the surface characteristic can be seen when comparing NiA4APTES/600 with NiN4APTES/600. According to TGA measurements both anions e.g. nitrate and acetylacetonate are decomposed at 500 °C. Hence, it can be assumed that they do not have an influence on the final surface characteristics.

7.4.3   Characterization of Ni Nanoparticles

XRD measurements were performed to gain knowledge on the crystal phase composition. Figure 7.6 shows X-ray diffractograms of pyrolyzed samples. In all samples, broad reflections between 10° and 30° are present indicating the formation of a silicon-based amorphous phase as it is characteristic for polysiloxanes at this pyrolysis temperature. Additionally, the peaks found around 45°, 52° and 77° are representing the cubic nickel structure. For NiA4APTES/600 also peaks correlated to nickel dioxide can be detected. The formation of nickel dioxide is assumed also in the other samples, but can't be detected by XRD due to low intensity of peaks. The absence of diffraction peaks related to other secondary phases such as nickel sulfide confirms that the samples are single phase consisting after pyrolysis. Metallic nickel particles are formed during pyrolytic conversion of the nickel containing poly-siloxanes under inert atmosphere. Released decomposition products such as hydrocarbons and hydrogen are creating reductive conditions within the sample and its pore network [16]. The absence of significant nickel peaks in NiN4APTES/600 due to superimposition by the background indicate very small nickel particles.

The presence and distribution of nickel nanoparticles were investigated by image analysis of TEM images. Figure 7.7 depicts representative TEM images and the average nickel size of all samples after pyrolysis (a – g) and of NiA4APTES/600 after 10 h stability test at 400 °C (h).
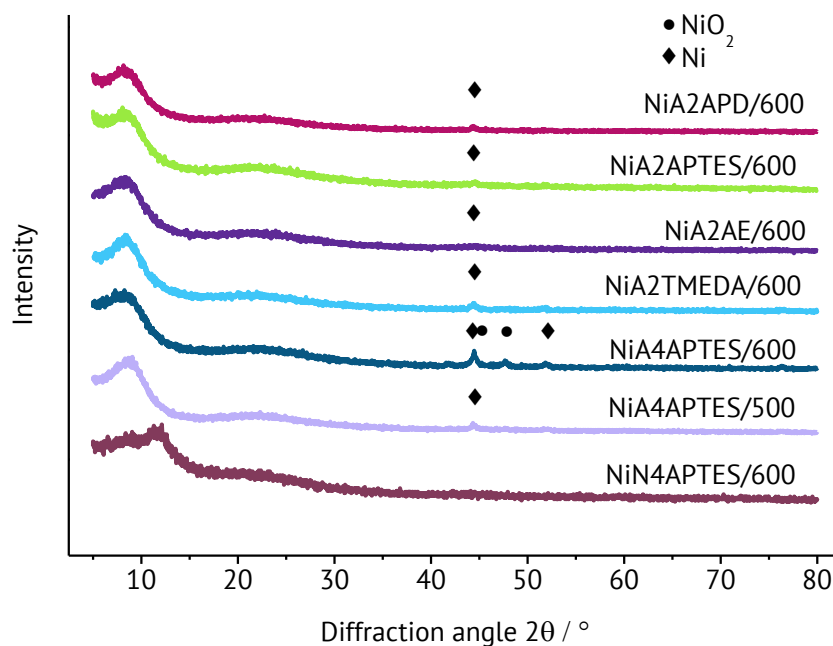
Figure 7.6 X-ray diffractograms of samples with different cross-linking agents, nickel precursors and pyrolysis temperatures.
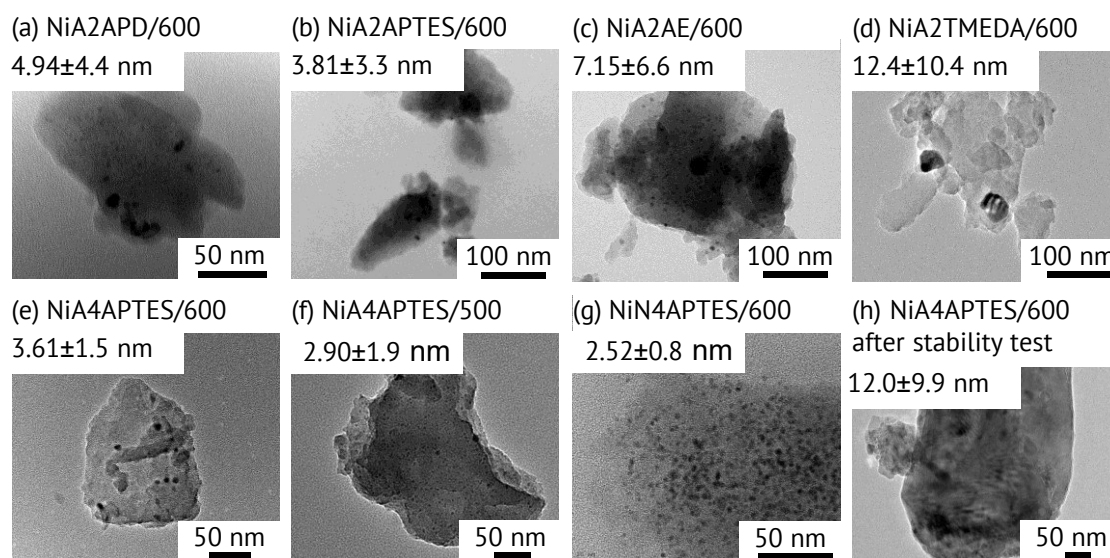
Figure 7.7 TEM images and Ni particle size of freshly pyrolyzed samples with different cross-linking agents, nickel precursors and pyrolysis temperatures (a – g) and sample after 10 h on stream at 400 °C (h).

When considering the samples with a complexing group to nickel ratio of 2, NiA2APD/600 and NiA2APTES/600 exhibit similar nickel particle sizes of (4.94 ± 4.42) nm and (3.91 ± 3.30) nm, respectively. Using AE and TMEDA as CLA lead to an increase in nickel particle size to (7.15 ± 6.65) nm and (12.4 ± 10.45) nm, respectively. While increasing the complexing group to nickel ratio from 2 to 4 only slightly decreases the nickel particle size, it significantly reduces the nickel particle

size distribution from (3.91 ± 3.30) nm to (3.61 ± 1.49) nm as it can be seen comparing NiA2APTES/600 and NiA4APTES/600. With a nickel particle size of (2.90 ± 1.91) nm NiA4APTES/500 shows smaller nickel particles compared to the same composition pyrolyzed at 600 °C. The smallest nickel particles and the most narrow particle distribution of (2.52 ± 0.82) nm was achieved by using nickel nitrate as nickel precursor. After the stability test of NiA4APTES/600 for 10 h at 400 °C under reaction conditions a considerable increase in the particle size by a factor of 3.33 to (12.02 ± 9.96) nm can be noticed. All observed particle sizes are in the range of reported nickel catalysts prepared by other methods [9, 28-33]. Evaluation of TEM images of the reference catalyst which are shown in Figure A.4.4 on page 202 reveals a nickel particle size of (37.15 ± 28.75) nm.

7.4.4 Catalytic Performance

CO_2 methanation was used as probe reaction in order to investigate the applicability of nickel containing polysiloxanes for catalytic purposes. The carbon dioxide conversion X_{CO2} and the methane selectivity S_{CH4} are shown in Figure 7.8.

Conversion as well as selectivity are maximized at the maximum reaction temperature of 400 °C for all samples except for NiA2TMEDA/600 which has its maximum selectivity at 250 °C. Since the thermodynamic equilibrium was not reached, the discussion of the data without considering underestimation of intrinsic activity is reasonable. Global maximum values of $C_{CO2} = 0.49$ and $S_{CH4} = 0.74$ are observed for NiA4APTES/600. Two groups can be identified when evaluating the conversion. For NiA2TMEDA/600 and NiA2AE/600 the conversion is very similar and exhibit with 0.18 and 0.19 the lowest measured values. In contrast, the other samples show considerable higher conversions ranging at 400 °C from 0.40 for NiA2APD/600 to 0.49 for NiA4APTES/600 in the order NiA2APD/600 – NiA2APTES/600 – NiA4APTES/500 – NiN4APTES/600 – NiA4APTES/600. However, at low reactions temperatures from 250 °C to 350 °C the sample NiN4APTES/600 is clearly most effective. Following trends can be observed: the conversion increases when using APTES as CLA; increasing the complexing to nickel ratio from 2 to 4 improves the activity; the pyrolysis temperature has no influence on the conversion; and finally, using nickel nitrate as nickel precursor leads to superior conversion at low temperatures.
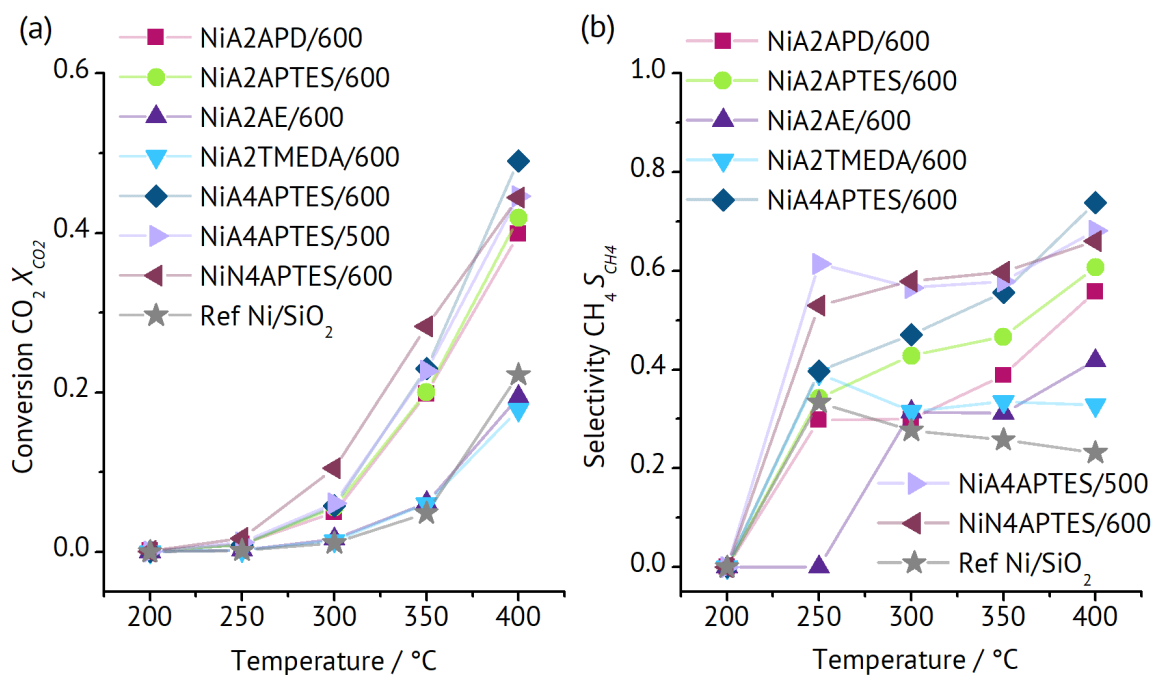
Figure 7.8 Conversion of carbon dioxide X_{CO2} (a) and selectivity towards methane S_{CH4} (b) tested in CO_2 methanation for different cross-linking agents, nickel precursors and pyrolysis temperatures.

In contrast to the conversion, clustering of samples into groups is not possible for the selectivity towards methane. Some trends are obvious for the selectivity: APTES shows the best selectivity of all investigated CLAs and increasing the complexing group to nickel ratio. Changing the nickel precursor to nickel nitrate as well as reducing the pyrolysis temperature to 500 °C leads to superior selectivity in the temperature range of 250 °C to 350 °C. Exemplary stability test of sample NiA4APTES/600 at 400 °C for 10 h under reaction conditions shows that 91 % and 88 % can be preserved for carbon dioxide conversion and methane selectivity, respectively.

7.5 Discussion

7.5.1 Influencing Factors on Ni Particle Size

Most obviously, the pyrolysis temperature influences the nickel particle size. Higher temperatures facilitate the growth of nickel particles by diffusion and mechanisms such as Ostwald ripening. Though the pyrolysis temperature has an effect on the particle size, it is not the strongest influencing factor. The binding of nickel ions to the polymeric Si-O chain might be the reason for the comparable small increase of particle size with increasing temperature. Bazarjani et al. synthesized nickel particles

of 2 nm to 3 nm using a nickel containing polysilazane precursor [34]. Covalent bonds of the nickel complex with the polysilazane were found. The presence of nickel has a strong impact on the resulting microstructure. By reducing the barrier for heterogeneous pore nucleation as well as reducing the viscous flow of the pores, nickel nanoparticles lead to the pronounced development of porosity (BET SSA of 215 $m^2 \cdot g^{-1}$). Furthermore, the formation of turbostratic carbon is catalyzed by nickel.

While Bazarjani et al. used polysilazanes which provide very active functional groups, in the present work relatively inactive polymethylsiloxane acts as precursor. Hence, the binding of the nickel to the polymeric network is only possible by the condensation reaction of cross-linking active OH-groups. However, this argument is only valid for samples where the functionality of complexing and cross-linking is combined in one molecule. Thus, a connection of the nickel ion to the polymeric chain can be assumed as it was reported previously [11, 13, 35]. This is not true for the sample NiA2TMEDA/600 where the complexing agent TMEDA has no cross-linking active groups. Consequently, binding of the complexed nickel ions to the polymeric chain is not possible. Consequently, the highest observed particle size and broadest particle size distribution among all studied samples was found for NiA2TMEDA/600.

In contrast, the CLAs APD, APTES and AE provide binding of the nickel ions to the polymeric chain. Among them, AE exhibits the largest nickel particles and APTES the smallest. Since each AE molecule has two complexing groups and according to the ratio complexing group/nickel of 2, each AE molecule is attributed to one nickel ion. Whereas two molecules of APD and APTES are attributed to one nickel ion, respectively. Additionally, attribution of two APTES and APD molecules to one nickel ion results in 6 and 4 cross-linking active groups per nickel ion, respectively. Compared to the 3 cross-linking active groups of AE, APD and APTES have a higher possibility to bind to the polymer chain. Furthermore, steric considerations suggest that it is more likely for APTES and APD complexed nickel ions to get bound to the polymer chain. A better distribution of cross-linking active groups around the ion is supposed to be the reason. Apparently, not only the complexing ability but also the capability to anchor the complex to the polymer chain is an influencing factor. By comparing the particle sizes of APTES ($d = (3.91 \pm 3.30)$ nm) and APD ($d = (4.94 \pm 4.42)$ nm) this becomes obvious. With 3 cross-linking active groups it is

more likely for APTES to bind to the polymer chain than it is for APD with only 2 groups.

Increasing the ratio of cross-linking active group to nickel from 2 to 4 in case of APTES as CLA decreases the nickel particle size. Usually, the coordination number of nickel is 6. Hence, it can be assumed that an increase of the ratio from 2 to 4 in case of APTES as CLA results in a more effective complexing and/or a more effective binding to the polymer chain leading to smaller nickel particles. The exact contribution of each single effect (complexing and binding) could not be clarified in this work.

Finally, also the nickel precursor influences the particle size. Organic ligands are reported to result in higher dispersion compared to nitrate in case of cobalt in impregnation methods [19, 36]. On the other hand, general problems of nitrate as precursor such as sintering and redistribution of nickel during calcination causing inferior dispersion which are reported for impregnation methods are not observed for the solution-based freeze casting method [8, 19]. The chelating character of the acetylacetonate anion provides the possibility for acetylacetonate to complex nickel ions and hence to block complexing sites even in solution. In contrast, nickel nitrate completely dissociates into ions when in solution. Consequently, complexing of nickel ions by the complexing agent is facilitated for the dissociated nickel nitrate. Thus, it is more likely that nickel ions are bound to the polymeric chain when using nickel nitrate compared to nickel acetylacetonate. Furthermore, nickel acetyl-acetonate is composed of 3 nickel ions complexed by 6 acetylacetonate ligands. Whereas nickel nitrate consists of a single nickel ion. Hence, the presence of single nickel ions might be an additional reason for the better dispersion observed for nickel nitrate.

7.5.2 Catalytic Performance

The nickel particle size and dispersion are found to be the most influencing factors on the carbon dioxide conversion at a constant metal loading. The order of conversion reflects very well the order of nickel particle size with smaller nickel particles enhancing the conversion. In contrast to the findings of Macedo et al. no influence of the pyrolysis temperature was found [17]. Furthermore, the increase of $50 \ m^2 \cdot g^{-1}$ in BET surface area was found to have no impact. Due to the presence of mainly

micropores generating the high BET surface area, diffusion limitation of reactants in micropores can be assumed.

For CO_2 hydrogenation, it is reported that the nickel particle size has an influence on the catalytic pathway and consequently on the selectivity [2]. In this study, a trend of increasing selectivity towards methane with decreasing nickel particle size was observed Most research found that increasing nickel size leads to higher selectivity towards methane [37-39]. Though, there are also studies reporting higher carbon monoxide selectivity with increasing nickel size [40]. The suggested mechanism bases on the carbon monoxide dissociation at highly uncoordinated sites present on steps of nickel [41]. While strong carbon monoxide adsorption at edges could enable direct methanation of carbon dioxide, nickel faces mainly produce carbon monoxide. On nickel faces carbon monoxide desorbs prior to methanation. Since smaller nickel particles are supposed to exhibit larger percentage of uncoordinated sites their selectivity towards methane is higher. This mechanism is in accordance with studies investigating nickel on supports with weak interaction [42, 43]. While supports with a strong support metal interaction such as titania and Nb_2O_5 are characterized by their reducibility, SiOC can be filed to the class of supports with weak support metal interaction such as silica [44].

The reference catalyst performs similar to the ones prepared using TMEDA and AE as cross-linking agent. The higher hydrophobicity and the smaller nickel particles of the polymer-derived catalysts are reasons for the better performance of the polymer-derived catalyst. Furthermore, the highly porous structure of the polymer-derived ceramic sample particles shown in Figure 7.3 (h) provides a higher number of accessible nickel sites compared to the dense silica particles.

The reduced conversion during the stability test is most likely due to the increased nickel size and carbon deposition [44]. Though moderate sintering is taking place, the confinement of the nickel within the matrix is supposed to help preventing severe sintering by suppressing the mobility of nickel atoms.

7.6 Conclusions

Micro- and macroporous nickel containing monoliths were prepared by solution-based freeze casting of polymethylsiloxanes. The screening of four different complexing and cross-linking siloxanes with amino functionality revealed that (3-aminopropyl)triethoxysilane (APTES) is most efficient in creating small and well dispersed nickel particles. The formation of micropores due to the decomposition of organic groups of the polymer gives reason for the high BET surface area of around 400 $m^2 \cdot g^{-1}$. Increasing the ratio of complexing groups to nickel improves the dispersion of nickel particles. The dispersion is further enhanced for changing the nickel precursor from nickel acetylacetonate to nickel nitrate. Catalytic tests of CO_2 methanation show a dependence of the carbon dioxide conversion and methane selectivity mainly on the nickel particle size. Furthermore, selectivity towards methane improves with decreasing particle size up to a value of 0.74. According to the mechanism, the adsorption of carbon monoxide is supposed to be stronger at nickel edges, whereas on faces carbon monoxide desorbs before methanation. Hence, methane generation is higher for smaller particles which exhibits more edges. Compared to nickel impregnated on silica, the polymer-derived catalysts show better conversion and selectivity. The highly porous structure of the polymer-derived ceramic samples might provide a better mass transport compared to the impregnated catalyst.

This research shows promising catalytic activity of nickel containing polymer-derived ceramics for CO_2 methanation tested in a packed bed reactor and opens up several potential approaches to further optimize monolithic metal containing polymer-derived ceramics, e.g. heat and mass transfer considerations can be easily addressed by adapting the pore structure.

References

[1]   X. Su, J. Xu, B. Liang, H. Duan, B. Hou, Y. Huang, J. Energy Chem. 25 (2016) 553-565.

[2]   W. Li, H. Wang, X. Jiang, J. Zhu, Z. Liu, X. Guo, C. Song, RSC Adv. 8 (2018) 7651-7669.

[3]   P. Panagiotopoulou, D.I. Kondarides, X.E. Verykios, Appl. Catal., A 344 (2008) 45-54.

[4]   M.A.A. Aziz, A.A. Jalil, S. Triwahyono, A. Ahmad, Green Chem. 17 (2015) 2647-2663.

[5]   W. Wei, G. Jinlong, Front. Chem. Sci. Eng. 5 (2010) 2-10.

[6]   M.A.A. Aziz, A.A. Jalil, S. Triwahyono, M.W.A. Saad, Chem. Eng. J. 260 (2015) 757-764.

[7]   A.Y. Khodakov, W. Chu, P. Fongarland, Chem. Rev. 107 (2007) 1692-1744.

[8]   W. Wang, S. Wang, X. Ma, J. Gong, Chem Soc Rev 40 (2011) 3703-3727.

[9]   X. Yan, Y. Liu, B. Zhao, Z. Wang, Y. Wang, C.-j. Liu, Int. J. Hydrogen Energy 38 (2013) 2283-2291.

[10]   A. Zhao, W. Ying, H. Zhang, H. Ma, D. Fang, Catal. Commun. 17 (2012) 34-38.

[11]   M. Schubert, M. Wilhelm, S. Bragulla, C. Sun, S. Neumann, T.M. Gesing, P. Pfeifer, K. Rezwan, M. Bäumer, Catal. Lett. 147 (2017) 472-482.

[12]   M. Wilhelm, M. Adam, M. Bäumer, G. Grathwohl, Adv. Eng. Mater. 10 (2008) 241-245.

[13]   M. Adam, M. Wilhelm, G. Grathwohl, Microporous Mesoporous Mater. 151 (2012) 195-200.

[14]   M. Zaheer, T. Schmalz, G. Motz, R. Kempe, Chem Soc Rev 41 (2012) 5102-16.

[15]   M. Wójcik-Bania, A. Krowiak, J. Strzezik, M. Hasik, Mater. Des. 96 (2016) 171-179.

[16]   T. Schmalz, T. Kraus, M. Günthner, C. Liebscher, U. Glatzel, R. Kempe, G. Motz, Carbon 49 (2011) 3065-3072.

[17]   H.P. Macedo, R.L.B.A. Medeiros, J. Ilsemann, D.M.A. Melo, K. Rezwan, M. Wilhelm, Microporous Mesoporous Mater. 278 (2019) 156-166.

[18]   M. Naviroj, S.M. Miller, P. Colombo, K.T. Faber, J. Eur. Ceram. Soc. 35 (2015) 2225-2232.

[19]   E. Marceau, M. Che, J.í. Cejka, A.t. Zukal, ChemCatChem 2 (2010) 413-422.

[20]   R. Liu, T. Xu, C. Wang, Ceram. Int. 42 (2016) 2907-2925.

[21]   M. Adam, M. Bäumer, M. Schowalter, J. Birkenstock, M. Wilhelm, G. Grathwohl, Chem. Eng. J. 247 (2014) 205-215.

[22]   M. Adam, S. Kocanis, T. Fey, M. Wilhelm, G. Grathwohl, J. Eur. Ceram. Soc. 34 (2014) 1715-1725.

[23]   C. Vakifahmetoglu, D. Zeydanli, P. Colombo, Mater. Sci. Eng., R 106 (2016) 1-30.

[24]   P. Colombo, J. Eur. Ceram. Soc. 28 (2008) 1389-1395.

[25]   T. Prenzel, M. Wilhelm, K. Rezwan, Microporous Mesoporous Mater. 169 (2013) 160-167.

[26]   H. Zhang, C.L. Fidelis, A.L.T. Serva, M. Wilhelm, K. Rezwan, J. Am. Ceram. Soc. 100 (2017) 1907-1918.

[27]   D. Schumacher, M. Wilhelm, K. Rezwan, Mater. Des. 160 (2018) 1295-1304.

[28]   S. He, X. Zheng, L. Mo, W. Yu, H. Wang, Y. Luo, Mater Res Bull 49 (2014) 108-113.

[29]   D. Liu, Y. Wang, D. Shi, X. Jia, X. Wang, A. Borgna, R. Lau, Y. Yang, Int. J. Hydrogen Energy 37 (2012) 10135-10144.

[30]   L. Li, S. He, Y. Song, J. Zhao, W. Ji, C.-T. Au, J. Catal. 288 (2012) 54-64.

[31]   M.V. Bykova, D.Y. Ermakov, V.V. Kaichev, O.A. Bulavchenko, A.A. Saraev, M.Y. Lebedev, V.A. Yakovlev, Applied Catalysis B: Environmental 113-114 (2012) 296-307.

[32]   M. Xue, S. Hu, H. Chen, Y. Fu, J. Shen, Catal. Commun. 12 (2011) 332-336.

[33]   W.-S. Xia, Y.-H. Hou, G. Chang, W.-Z. Weng, G.-B. Han, H.-L. Wan, Int. J. Hydrogen Energy 37 (2012) 8343-8353.

[34]   M. Seifollahi Bazarjani, H.-J. Kleebe, M.M. Müller, C. Fasel, M. Baghaie Yazdi, A. Gurlo, R. Riedel, Chemistry of Materials 23 (2011) 4112-4123.

[35]   A. Gorschinski, G. Khelashvili, D. Schild, W. Habicht, R. Brand, M. Ghafari, H. Bönnemann, E. Dinjusa, S. Behrens, Journal of Materials Chemistry 19 (2009) 2289-2238.

[36]   A. Śrębowata, W. Juszczyk, Z. Kaszkur, J.W. Sobczak, L. Kępiński, Z. Karpiński, Appl. Catal., A 319 (2007) 181-192.

[37]   H.C. Wu, Y.C. Chang, J.H. Wu, J.H. Lin, I.K. Lin, C.S. Chen, Catal. Sci. Tech. 5 (2015) 4154-4163.

[38]   J.H. Kwak, L. Kovarik, J. Szanyi, ACS Catalysis 3 (2013) 2449-2455.

[39]   J.H. Kwak, L. Kovarik, J. Szanyi, ACS Catalysis 3 (2013) 2094-2100.

[40]   G. Garbarino, P. Riani, L. Magistri, G. Busca, Int. J. Hydrogen Energy 39 (2014) 11557-11565.

[41]   J. Engbæk, O. Lytken, J.H. Nielsen, I. Chorkendorff, Surf. Sci. 602 (2008) 733-743.

[42]   M.A.A. Aziz, A.A. Jalil, S. Triwahyono, R.R. Mukti, Y.H. Taufiq-Yap, M.R. Sazegar, Appl. Catal., B 147 (2014) 359-368.

[43]   P.A.U. Aldana, F. Ocampo, K. Kobl, B. Louis, F. Thibault-Starzyk, M. Daturi, P. Bazin, S. Thomas, A.C. Roger, Catal. Today 215 (2013) 201-207.

[44]   Q. Fu, T. Wagner, Surf. Sci. Rep. 62 (2007) 431-498.

Summarizing Discussion

<div style="text-align: right; font-size: 3em;">8</div>

This section provides a summarizing discussion of the most important findings in a concise way. For detailed explanations, it is referred to the corresponding chapters. Additionally, aspects which spread over multiple publications and thus were not yet taken a closer look at are discussed.

In the first part of this work (see chapter 4 on pages 60 to 84), the fundamental relationships between the process parameters and the resulting pore structure and properties have been evaluated. This knowledge is crucial for the subsequent development of the pore structure according to the requirements of capillary transport and heterogeneous catalysis. The influence of the addition of preceramic (SiOC) and ceramic (silica, alumina) filler particles on the resulting pore structure and properties such as hydrophilicity, strength and specific surface area was investigated. Especially for the application in capillary transport, the increase of the mechanical strength was a key requirement.

To alter the specific surface area and the hydrophilicity, preceramic filler particles with widely differing properties were added. These altering properties were realized by controlling chemical composition of the filler particles. Due to micropores which are formed during pyrolysis by decomposition of organic groups, the preceramic fillers H1 (H44; 1 mol% AP), H50 (H44; 50 mol% AP) and M1 (MK; 1 mol% AP) show very high BET surface areas of (607 ± 3) m$^2 \cdot$g^{-1}, (546 ± 1) m$^2 \cdot$g^{-1} and (451 ± 1) m$^2 \cdot$g^{-1}, respectively. The phenyl group in the polymethylphenylsiloxane H44 (H1, H50) decomposes below 600 °C, whereas the methyl groups in H44 and MK (M1) are not decomposed at 600 °C [1]. Therefore, the use of phenyl containing H44 results in higher BET surface areas compared to polymethylsiloxane MK [2, 3]. Since pure APTES has a BET surface area of 350 m$^2 \cdot$g^{-1}, a decreasing BET surface area was found in literature for the addition of APTES to MK [4]. This can also be observed when comparing the fillers H1 (1 mol% AP) and H50 (50 mol% AP). Due to the absence of microporosity, the ceramic filler particles (silica spheres and alumina platelets) show a very low BET surface area and consequently the overall BET surface area of the monolithic samples is reduced.

Filler particles not only differ in BET surface area, but also in their hydrophilicity. Due to the decomposition of the hydrophobic phenyl groups at 600 °C, the preceramic fillers H1 and H50 show hydrophilic behavior [1, 5]. Additionally, an increase of the APTES concentration in the filler particles enhances the hydrophilicity. Almost all amino groups of APTES are decomposed at 600 °C, leading to the formation of hydrophilic silica [4]. In contrast to H1 and H50, M1 is not composed of phenyl groups, but of methyl groups which are thermally more stable and decompose at 600 °C to a lower extent [1]. Hence, M1 retains its hydrophobic surface character at 600 °C. As a result of the microporous matrix material, filler particles are not sealed by the surrounding matrix. Thus, highly precise tailoring of the BET surface area and the hydrophilicity in a wide range is possible by adjustment of the filler concentration and the filler composition. In addition, calculations based on a linear rule of mixture show very good agreement with the experimental results in the case of homogeneously distributed particles.

Besides influencing physical properties, filler particles with spherical and non-spherical shape have been used to increase the mechanical stability. As it is characteristic for cyclohexane, the usage of cyclohexane as solvent leads to a dendritic pore morphology [6, 7]. The mean pore window size and the open porosity is in the range of 13 µm to 21 µm and 60 % to 65 %, respectively. The consistency of these parameters indicate no influence of the addition of filler particles on the pore size distribution, the mean pore size and the open porosity. In the structure without filler particles, primary and secondary dendrites can be easily identified. Whereas with increasing content of filler particles, the isotropy of the structure is enhanced. Naviroj et al. assume that suspended particles are disrupting the dendritic solidification structure by inducing *noise* ahead of the freezing front [7]. Sufficient noise ahead of the freezing front disrupts the growth of the dendrite tips and affects the solidification microstructure [8]. Hence, fractal patterns are created instead of regular ones. By creating small temperature fluctuations and direct contact, particles located at the dendritic tip can act as noise.

Apart from porosity and pore size, the pore morphology directly influences the mechanical properties of freeze cast samples [9]. The addition of 25 vol% of filler M1 improves the compressive strength by a factor of 1.9 for a pyrolysis temperature of 1000 °C. Whereas, the increase of filler particles to 50 vol% leads to a decrease of

strength. The increase in strength is attributed to a change in the pore morphology showing enhanced isotropy. Another aspect is the reduction of elongated pores. Assuming a discrepancy between the axis of pores and the axis of the applied load, the resistance against load out of crystal axis is increased by both of these structural aspects. Load out of crystal axis results in shear stress between single pore channels. In filler free samples, the pore walls between elongated pore channels are rather thin leading to a low resistance. In contrast, addition of filler reduces this weak points by enhancing the isotropy and diminishing elongated pores. Changing the composition of the preceramic filler particles from M1 to H1 and H50 reduces the strengthening effect. Due to different decomposition of H1 and H50 compared to the matrix, crack formation around the filler particles during pyrolysis is assumed to result in less enhancement.

Comparing the manufactured solution-based structures of this work with polymer-derived ceramics prepared by suspension-based freeze casting reveals that the solution-based freeze casting process results in considerable superior mechanical stability. At very similar compositions, suspension-based structures show a compressive strength of 1.6 MPa to 5.9 MPa whereas the solution-based structures of this work lead to a strength of up to 67.5 MPa [10]. Two aspects are contributing to the drastically increased strength. First, the suspension-based samples are characterized by single particles with a small amount of binder which provides only a reduced contact between the particles. Contrary, in solution-based freeze casting the structure is composed of a homogeneous and continuous solid. Secondly, the pore morphology is different. The suspension-based samples were prepared with water whereas cyclohexane was used in solution-based freeze casting. Although it is difficult to exactly determine the impact of the pore morphology when comparing solution- and suspension-based freeze casting, it is reasonable to assume that the ramified dendritic structure of cyclohexane is superior to the lamellar and almost layered structure of water.

No well-known strengthening/toughening mechanisms, such as crack deflection and crack bridging are observed for the addition of alumina platelets. At low filler concentrations (1.7 vol%), the addition of platelets is more effective than the addition of spherical particles. Hence, at the same concentration the platelets manipulate the pore morphology to a greater extend. Besides having a slightly higher particle size,

the platelets exhibit a highly different shape compared to the spherical fillers. It can be assumed, that the platelet like shape creates more *noise* at the freezing front, resulting in higher disruption of the dendrite tips.

However, increasing the content of alumina platelets to 3.5 vol% induces crack formation as shown in chapter 4.4.1.2 on page 71. Crack formation is caused by the difference in the coefficient of thermal expansion between the matrix and the alumina platelets [11].

The knowledge of the possibilities to alter the pore structure by adding fillers is a great base to manufacture and test porous monoliths in two relevant fields of application: capillary transport and heterogeneous catalysis. In the context of the capillary transport, the relation between wicking performance and properties which are characterizing the porous structure such as porosity, pore window size and pore morphology is a key aspect which is elucidated in the second part of this work (see chapter 5 on pages 85 to 116). Besides filler-free and filler containing (50 vol%) samples which were produced with cyclohexane as solvent and already have been described in the first part of this work (see chapter 4 on pages 58 to 84), prismatic structures were obtained by using *tert*-butyl alcohol as solvent.

In general, the wicking behavior depends on the pore structure and the first time steps are mostly influenced by the viscous force, whereas for longer times the influence of the gravity becomes more significant [12]. The tested samples differ in pore window size (11 µm to 21 µm), porosity (60 % to 79 %) and pore morphology (dendritic and prismatic). The fastest wicking and the strongest influence of gravity was recorded for the sample with the highest porosity and the highest pore window size which equals to the highest permeability. Though exhibiting a very similar pore window size and porosity, the isotropic dendritic structure (CH40/50) wicks considerable faster than the prismatic structure (TBA40/0). The differences in pore morphology result in a higher permeability and consequently in a lower influence of the viscous force for the isotropic dendritic structure. This implies that the isotropic dendritic pore morphology has a higher ability of liquid flow compared to the prismatic pore morphology. Generally, it turns out that the sample with the highest viscous resistance has the slowest imbibition rate, while the smallest viscous resistance

results in a high imbibition rate. In addition, the samples with the highest influence of gravitation have the biggest change in the slope during wicking.

It has to be noted, that there is no general optimum of the wicking speed. Both, fast as well as slow wicking have application areas. While small pore sizes with slow wicking are beneficial for phase separation purposes e.g. separation of liquid fuels from vapor, fast wicking caused by high porosity and large pores is used in the context transport, e.g. transport of liquid fuel to the engine. In specific applications, both functions should be provided by one component. In this case, either a compromise has to be found or the component needs to be composed of multiple sections with different pore structures.

Prediction of the wicking was performed using the Lucas-Washburn equation. This approach simplifies the pore structure to a bundle of capillaries which is described by three macroscopic parameters: the open porosity, the permeability and the static radius [12-15]. In this study, the static radius equals the pore window radius. When considering the permeability which was obtained by the Darcy experiment K_{Darcy}, the prediction underestimates the wicking experiment. Thus, it can be concluded that, despite independently determined macroscopic parameters, the Lucas-Washburn equation does not predict the imbibition rate correctly. In contrast, the prediction which uses the permeability obtained by fitting the wicking curve $K_{wicking}$ shows a good accordance with the experimental data for the prismatic (TBA40/0), the isotropic dendritic (CH40/50) and the dendritic structure with a porosity of 79 % (CH20/0). This can be attributed to the fact, that in this case the permeability is a fitting parameter determined from the first mass increase of the imbibed mass of the wicking experiment. Thus, a match at initial wicking is ensured.

However, the dendritic structure with a porosity of 61 % (CH40/0) behaves differently compared to the prediction. The experimental curve does not show the typical Lucas-Washburn behavior. After an initial coincident mass increase, further progression is characterized by a linear mass increase. Furthermore, removing the closed external surface results in an increase of the imbibition rate of 20 %. Hence, the external open surface favors the imbibition of the liquid into the dendritic structure with a porosity of 61 % [15-18]. A linear wicking curve was observed in other wicking investigations, too [14]. The authors explained the linear course with an additional pressure created

in a superheated structure by the evaporating liquid, which could not escape fast enough from the pore network. However, the samples in the present work are not superheated and consequently the evaporation of liquid can be neglected. Thus, structural features are supposed to cause the abnormal wicking behavior. At higher magnifications of the SEM images in Figure 5.4 (see page 98), it can be observed, that some pores of the dendritic low porous structure (CH40/0) seem to be closed. As a result, the reduced available number of transport routes for the liquid slows down the wicking. Especially, the interface between clusters of internally aligned pores is supposed to be prone to reduced flow by the lack of interconnectivity.

Therefore, eliminating the interfaces between clusters by changing the freezing condition from non-unidirectional to unidirectional freezing was investigated (see chapter 6 on pages 117 to 140). Unidirectional freezing ideally provides a fully aligned pore structure with dendrites or prismatic pore channels running from bottom to top without any interruption. Wicking tests of prismatic and dendritic structures with two different porosities of approx. 80 % and 60 % revealed no linear section. Hence, the absence of a linear section in wicking curves of the dendritic structures with a low porosity (CH40-20, CH40fast and CH40slow) supports the assumption of limited interconnectivity causing the linear wicking behavior.

To qualitatively confirm the hypothesis of limited interconnectivity in dendritic structures, µ-CT scans of non-unidirectional and unidirectional frozen samples were performed. High resolution CT scans with a pixel size of 2 µm ensure a representative reconstruction of the pore structure. As the first step to judge the interconnectivity between aligned pore clusters, each primary dendrite with its corresponding direction and complete pore volume which includes secondary dendrites has to be identified. This allows to identify the interface between clusters of different orientation. And finally, the transition pore volume between different clusters which was defined as the measure of interconnectivity can be determined. Following image processing steps have been performed to implement this approach: binarisation thresholding, calculation of the Euclidean distance transform, discrimination of Euclidean distance transform, 3D skeletization via thinning algorithm, classification of vectors which are associated to the direction of primary dendrites, reconstruction of skeleton lines of primary dendrites which were separated due to the elimination of intersection points, calculation of average distance between dendrites in one cluster, successive dilation

of dendrites, seeded-watershed algorithm, multiplication of the watershed transform with the binary image, dilatation of the pore volume and summing up in one image.

The reconstruction of the CT-scans for a non-unidirectional and for an unidirectional frozen sample is shown in Figure 8.1 (a) and (b), respectively. Furthermore, the determined skeleton lines of the primary dendrites are displayed in Figure 8.1 (c) and (d). Even without any further anlysis of the data, it can be seen that the non-unidirectional frozen sample exhibits primary dendrites with various orientations. In contrast, the primary dendrites in the unidirectional frozen sample are fully aligned in only one direction.

(a)

(b)

Dimensions:
0.96 x 0.96 x 0.96 mm^3

Dimensions:
0.96 x 0.96 x 0.96 mm^3

(c)

(d)

Dimensions:
0.96 x 0.96 x 0.96 mm^3
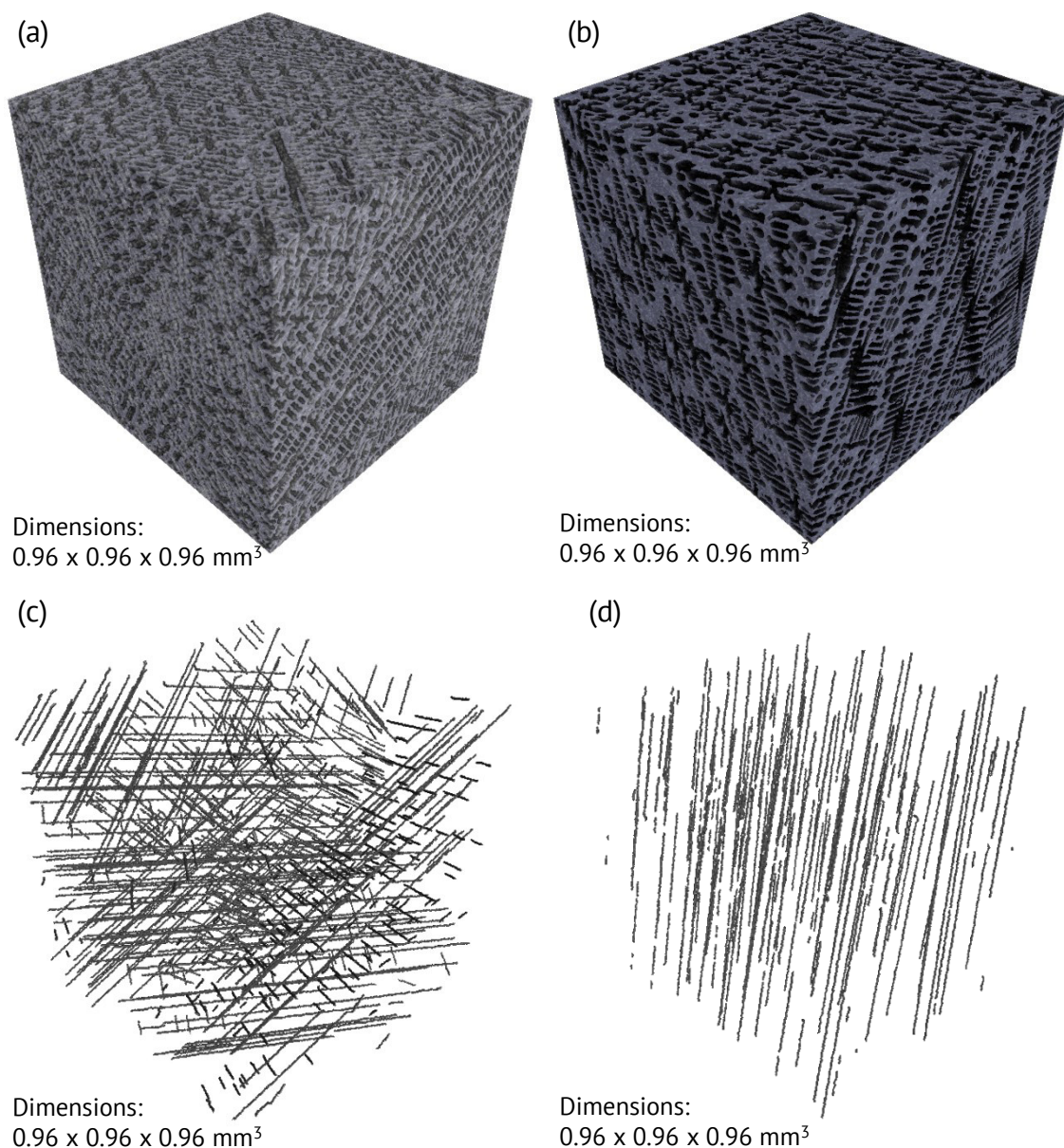
Dimensions:
0.96 x 0.96 x 0.96 mm^3

Figure 8.1 Reconstruction of the CT-scans of a (a) non-unidirection and of an (b) unidirectional frozen sample; skeleton lines of the primary dendrites in a (c) non-unidirectional and in a (d) unidirectional frozen sample.

The analysis of the orientation of the primary dendrites is shown in Figure 8.2. In case of the non-unidirectional frozen sample, the orientations of the primary dendrites are clustered. Each cluster is indicated by a red arrow. Hence, multiple orientations of primary dendrites exist which can be attributed to the presence of different clusters of aligned pore areas. In contrast, the unidirectional frozen sample exhibits only one single orientation. Hence, the pore structure is fully aligned and the primary dendrites running through the whole sample without any interruption. These findings on the alignment of pores and the difference between non-unidirectional and unidirectional freezing confirm the results presented in chapter 5 and 6 (see pages 85 to 116 and 117 to 140).
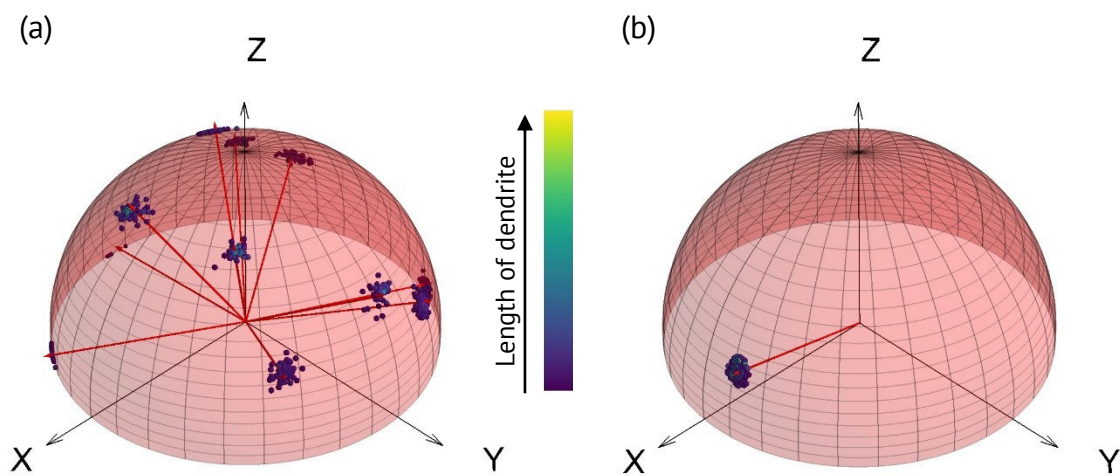
Figure 8.2 Representation of the orientation of the primary dendrites for the (a) non-unidirectional and (b) unidirectional frozen sample.

In order to determine the interface between clusters of aligned pores, the pore volume of each pore channel which consists of the primary dendrite and the corresponding secondary dendrites needs to be identified. The result of this segmentation is shown in Figure 8.3 for the non-unidirectional frozen sample.
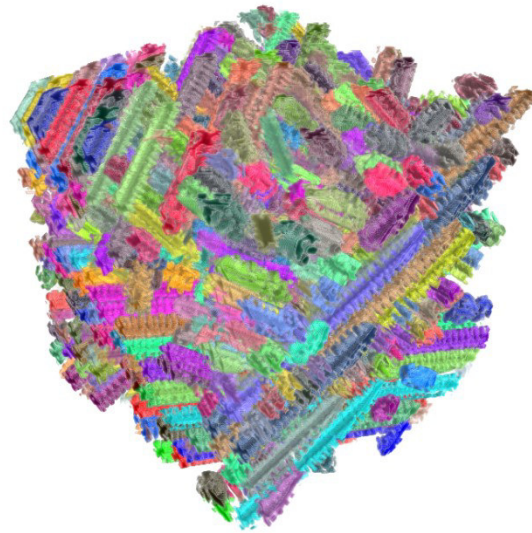
Dimensions:
0.96 x 0.96 x 0.96 mm^3

Figure 8.3 Segmentation of the pores in the non-unidirectional frozen sample.

Since the unidirectional structure does not show an interface between clusters, the pore volume at the interface which can be attributed to two different clusters (red) is shown in Figure 8.4 (a) only for the non-unidirectional frozen sample. For a better comprehensibility, Figure 8.4 (b) depicts only three clusters with the corresponding transition volume (red). It becomes clear that distinct transition volumes between the clusters exist throughout the whole structure. Hence, different clusters of aligned pores are connected with each other. But as it can be seen especially in Figure 8.4 (b), the connection between clusters is limited to distinct points. There is no continuous transition of the pore structure from one cluster to another. Consequently, porosity of the interface is reduced and it acts as a throttle in mass transport applications. These findings are in accordance with experimental results of a wicking test at non-unidirecetional and unidirectional structures which show a significantly slower wicking for the non-unidirectional sample (see chapters 5 and 6 on pages 85 to 116 and 117 to 140).

As these investigations are preliminary, only qualitative and no quantitative statements are reasonable. Nevertheless, the presented data proves that the interconnectivity between clusters with different pore orientations is an influential feature of freeze cast monoliths. Especially, for mass transport applications this aspect should not be neglected as it can have a significant impact on the performance.
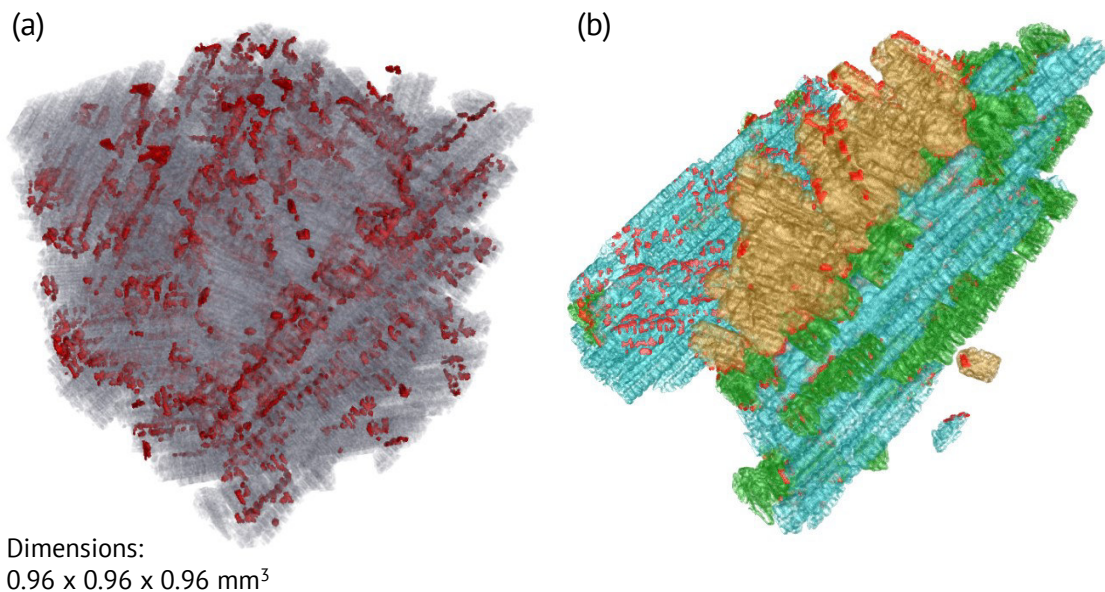
(a)

(b)

Dimensions:
0.96 x 0.96 x 0.96 mm³

Figure 8.4 (a) Transition volume between clusters of different orientation (red) for the non-unidiectional frozen sample; (b) three extracted clusters with the corresponding transition volume (red).

Additionally to the unidirectionality, gradients in the pore window size have been avoided by changing the freezing conditions from constant freezing temperature (CFT) to constant freezing velocity (CFV). Furthermore, the influence of both freezing conditions on the wicking was investigated. Constant freezing temperature conditions are characterized by a clear decrease of freezing front velocity with time. The thermal resistance increases with progressing freezing front and leads to a decrease of the thermal gradient at the freezing front [19]. Consequently, the freezing front velocity decreases with time and results in an increasing pore window size from bottom to top of factors between 1.2 and 3.5. This correlation was also reported in literature for suspension-based freeze casting using water as liquid phase [20]. Furthermore, a gradient in pore window size creates a gradient in the driving force for wicking which changes the wicking speed additionally to the influence of gravity. When adapting the temperature program, two different constant freezing front velocities were achieved indicated by an almost constant slope. The realized freezing front velocities are influenced by the composition of the solution and differ from $3.3\ \mu m \cdot s^{-1}$ to $6.8\ \mu m \cdot s^{-1}$. Constant freezing front velocities over the complete height of the sample are easier to achieve for slow freezing front velocities. Depending on the solvent, the freezing front velocity deviates to higher or lower velocities. Due to different melting points of TBA (T_m = 23 °C to 26 °C) and CH (T_m = 6.5 °C) the thermal gradient at initial freezing (0 °C) is higher for TBA compared to CH.

A constant freezing front velocity generates a homogeneous pore window size as observed for most of the samples frozen at CFV conditions. Deviations from the constant pore window sizes in CFV conditions are caused by locally different freezing front velocities. Following theoretical considerations, decreasing the freezing front velocity from CFV slow to CFV fast conditions results in an increase of the pore window diameter by 14 % to 67 %. In addition, samples with higher solid loading are more sensitive to variations in freezing front velocity and allow for a larger range of achievable pore window sizes. At low solid loadings which are connected to large pore window sizes, the thermodynamics of crystal growth are assumed to reduce the increase of pore window size with decreasing freezing front velocity. Furthermore, small pore window sizes at low solid loading are difficult to achieve due to the dependence of the pore window size on the solid loading. In contrast, decreasing the freezing front velocity to obtain larger pores at high solid loading is easily possible.

In wicking tests, samples frozen at higher velocity reach the saturation mass faster for all compositions. A higher freezing front velocity is connected to a smaller pore window size which results in faster wicking according to Equation 6.2. In agreement with Equation 6.3, a smaller pore window size is also related to a lower permeability which decreases the wicking speed. However, the wicking results indicate that this decrease in permeability is not sufficient to compensate the increase in wicking speed caused by a small pore window size. In general, the wicking into the dendritic pore structure is slower than into the prismatic structure. Secondary dendrites which are perpendicular to primary ones need to be filled during wicking by flow through primary dendrites. Hence, in the dendritic pore morphology a higher pore volume has to be filled through smaller pores compared to the prismatic structure of the TBA samples. As already described above, the Lucas-Washburn equation assumes a bundle of aligned capillary tubes of the same radii. This assumption only holds for the prismatic pore structure and an open porosity of approx. 75 %. Decreasing the porosity to approx. 60 % or even changing to a dendritic pore structure leads to a pronounced overestimation of the wicking speed by the analytical solution. In addition to the findings on non-unidirectional structures (see chapter 5 on pages 85 to 116), also the wicking of unidirectionally solidified structures can be predicted by the Lucas-Washburn equation only for pore structures which exhibit a very specific set of properties.

The second part of this work has shown that the knowledge of the relationship between structural properties and the resulting wicking behavior combined with the flexibility of the solution-based freeze casting process enables to tailor porous media in a wide range (see chapter 5 and 6 on pages 85 to 140). This knowledge is fundamental when applying solution-based freeze cast structures. Consequently, a large variety of applications correlated to mass transport (e.g. filtration, storage, adsorption) can be approached and optimized structures can be developed when considering the fundamental findings of this work. Especially, the precise control of the pore structure by means of composition as well as freezing conditions gives many degrees of freedom in designing optimized and very specific structures. Besides in capillary transport applications, control of the pore structure is also essential for monolithic catalysts. Nevertheless, the efficient design of the pore structure is only one task on the way to a monolithic catalysts. First, it has to be ensured that the underlying principles and processes of manufacturing a porous metal containing PDC monolith are understood and controllable. Additionally, the catalytic activity without the influence of the macroporous monolith has to be evaluated to generate a benchmark for the optimization of the monolithic catalyst.

These basic investigations are described in the third part of this work (see section 7 on pages 141 to 162). The first aspect was the adaption of the one step in situ formation of nickel particles from the known reflux synthesis to solution-based freeze casting by selecting an effective complexing- and cross-linking agent. The applied complexing and cross-linking agents (CLAs) differ in the ratio between complexing groups (R'NH$_2$, R'$_2$NH and R'$_3$N) and cross-linking active groups (OR). The ratio ranges from 0 (Tetramethylethylenediamine, TMEDA) to 1/2 ((3-aminopropyl)diethoxy-methylsilane, APD), 1/3 ((3-aminopropyl)triethoxysilane, AP) and 2/3 ((2-aminoethyl)-3-aminopropyltrimethoxysilane, AE). In the case of catalytic reactions involving water such as the CO$_2$ methanation, the hydrophilicity of the structure is influencing the catalytic performance. As Si containing CLAs mainly add additional hydrophilic SiO units to the pyrolyzed structure, the choice of the CLA impacts on the hydrophilicity [4, 21]. APD and APTES exhibit one silicon atom per complexing amino group. In contrast, AE includes only 0.5 silicon atoms per amino group and TMEDA has no silicon atoms at all. Therefore, the ratio of vapor adsorption

is similar for samples with APD and AP. In contrast, the sample with TMEDA which has no additional hydrophilic SiO units exhibits the lowest hydrophilicity.

Most obviously, the pyrolysis temperature influences the nickel particle size. Higher temperatures facilitate the growth of nickel particles by diffusion and mechanisms such as Ostwald ripening. Besides the pyrolysis temperature, further aspects influence the nickel particle size. The binding of Ni ions to the polymeric Si-O chain might be the reason for the comparable small increase of particle size with increasing temperature. This argument is only valid for samples where the functionality of complexing and cross-linking is combined in one molecule. Thus, a connection of the nickel ion to the polymeric chain can be assumed as it was reported previously [22-24]. This is not true for the sample with TMEDA where the complexing agent TMEDA has no cross-linking active groups. Consequently, binding of the complexed nickel ions to the polymeric chain is not possible. As a result, the highest observed particle size and broadest particle size distribution among all studied samples is present for TMEDA. In contrast, the CLAs APD, APTES and AE provide binding of the nickel ions to the polymeric chain. Among them, AE exhibits the largest nickel particles and APTES the smallest. Since each AE molecule has two complexing groups and according to the ratio complexing group to nickel of 2, each AE molecule is attributed to one nickel ion. Whereas two molecules of APD and APTES are attributed to one nickel ion, respectively. Additionally, the attribution of two APTES and APD molecules to one nickel ion results in 6 and 4 cross-linking active groups per nickel, respectively. By comparing the particle sizes of APTES (d = (3.91 ± 3.30) nm) and APD (d = (4.94 ± 4.42) nm), the impact of the available cross-linking active groups becomes obvious. Compared to the 3 cross-linking active groups of AE per nickel ion, APD (4 cross-linking active groups per nickel) and APTES (6 cross-linking active groups per nickel) generally have a higher possibility to bind to the polymer chain. Furthermore, steric considerations suggest that it is more likely for nickel ions which are complexed by APTES and APD to get bound to the polymer chain. A better distribution of the cross-linking active groups of the CLA (2 molecules of APD/APTES per nickel vs. 1 molecule of AE per nickel) around the ion is supposed to be the reason. Apparently, not only the complexing ability but also the capability to anchor the complex to the polymer chain is an important factor.

The second aspect in this thematic area was the improvement of the catalytic activity by adapting following process parameters: increasing the ratio of nickel to complexing groups from 2 to 4, changing the nickel ligand from acetylacetonate to nitrate and decreasing the pyrolysis temperature from 600 °C to 500 °C. As already mentioned, lower pyrolysis temperatures lead to smaller nickel particles due to suppressed diffusion. Also increasing the ratio of nickel to complexing agent facilitates the formation of smaller nickel particles. More complexing and cross-linking groups provide a better complexing and simultaneously increase the probability of a complexed nickel ion to be bound to the polymeric chain. The chelating character of the acetylacetonate anion provides the possibility for acetylacetonate to complex nickel ions and hence to block complexing sites even in solution. In contrast, nickel nitrate completely dissociates into ions when in solution. Consequently, complexing of nickel ions by the complexing agent is facilitated for the dissociated nickel nitrate.

The catalytic activity was assessed in a packed-bed reactor on sample powders. Concerning the carbon dioxide conversion, the nickel particle size and dispersion are the most influencing factors. The order of carbon dioxide conversion and methane selectivity reflects very well the order of the nickel particle size with smaller nickel particles enhancing the conversion and the selectivity. For carbon dioxide hydrogenation, it is reported that the nickel particle size has an influence on the catalytic pathway and consequently on the selectivity [25]. Most research states that increasing nickel size leads to higher selectivity towards methane [26-28]. Though, there are also studies which report higher selectivity towards carbon monoxide with increasing nickel size [29]. The suggested mechanism bases on the dissociation of carbon monoxide at highly uncoordinated sites present on steps of nickel [30]. While the strong adsorption of carbon monoxide at edges could enable direct methanation of carbon dioxide, nickel faces mainly produce carbon monoxide due to the desorption of carbon monoxide prior to methanation. Since smaller nickel particles are supposed to exhibit a larger percentage of uncoordinated sites, their selectivity towards methane is higher. This mechanism is in accordance with studies investigating nickel on supports with weak interaction [31, 32]. While supports with a strong support metal interaction such as titania and Nb_2O_5 are characterized by their reducibility, SiOC can be filed to the class of supports with weak support metal interaction like

also silica [33]. In general, the in situ formation of nickel particles in polymer-derived ceramics shows promising carbon dioxide conversion (up to 0.49) and methane selectivity (up to 0.74) in CO_2 methanation assessed in a packed bed reactor.

Although supports such as samarium(III) oxide or ceria outperform SiOC as support, the feature of inherent catalytic activity of the presented catalysts is a reasonable advantage compared to a support which requires a coating. Especially at varying temperatures together with differences in the thermal expansion coefficient between support and washcoat flake-off of the catalytic layer is a very critical aspect. Degradation of the catalyst performance and the damage of downstream equipment are potential harmful consequences [34-36]. Additionally, abrasive conditions such as high gas velocities or the presence of particles in the stream may cause erosion of the washcoat and consequently dropping catalytic conversion [37]. As a result, the inherent catalytic activity of metal containing SiOC structures makes them a highly promising alternative for reactions at specific severe conditions such as largely varying temperatures or abrasive conditions.

Due to the superior heat- and mass transport properties, monolithic heterogeneous catalysts are high potential alternatives to packed-bed reactors. Although the catalytic performance of a monolithic catalyst was not assessed within this work, the macroporous structure of the catalyst particles provides a relatively large accessible surface area. As compared to dense particles with a mesoporous washcoat, hampering of the reaction due to mass transport limitation is very unlikely and needs no consideration. In order to take full advantage of the monolithic catalysts a multi-objective optimization problem has been solvend and the resulting design guidelines have been reported in the literature [38]. Since the catalysts needs to be optimized according to the specific reaction and the actual operating conditions, only general guidelines are given in the following. Small pore window diameters below 1 mm provide large specific surface area. Hence, a high space-time yield can be obtained. To prevent thermal runaway in exothermic reactions due to a lack of thermal conductivity of the structure the porosity needs to be carefully adapted. Despite the small pore windows, high pressure losses are avoided due to the relatively high porosity. For example, in case of carbon dioxide methanation in porous sponges it was found that at a constant pore window size of 200 μm, the porosity should decrease from 90 % to 70 % in the radial direction core to shell [38]. All the mentioned

guidelines can be addressed in solution-based freeze casting with the knowledge of the fundamental relationship between processing parameters and resulting pore structure as it is presented in the first and second part of this work (see chapter 4, 5 and 6).

A further and very common applications of porous structures is the use as membranes. Although this important field of application is not presented in detail in this work, research was done on the manufacturing of electrical conductive membranes as gas diffusion layer for zinc air batteries [39]. This study bases on the fundamental findings which have been presented in chapter 5. Solution-based freeze tape casting resulted in flat membranes with a thickness of 390 µm to 450 µm, a porosity of 55 % and an average pore window diameter of 3 µm to 10 µm. Graphite particles were added as filler according to the findings presented in the first part of this work (see chapter 4 on pages 60 to 84) to provide electrical conductivity. As shown in Figure 8.5, the membranes are characterized by a bilayered structure with a thin denser top layer and a sponge like bottom layer. Evaporation of the solvent after the tape casting and before complete freezing leads to the formation of the dense top layer. The electrical conductivity increased by five orders of magnitude due to the addition of graphite particles. After coating the membrane with PTFE to increase the hydrophobicity and applying a commercial platinum/ruthenium catalyst the membrane outperforms the commercial electrode with longer discharge times. Enhanced oxygen exchange rates and short pathways for the oxygen ion/-electron kinetics are supposed to be the reason. Additionally, stability up to 200 cycles proofs excellent cycling stability. However, the relatively low electrical conductivity results in reduced discharge voltage compared to the reference electrode. In summary, solution-based freeze tape casting provides a new strategy to design gas diffusion layers for energy conversion and storage devices. These findings show once more that the optimization of structures obtained by solution-based freeze casting according to results presented within this work offers a very high potential to tackle challenges in several applications.
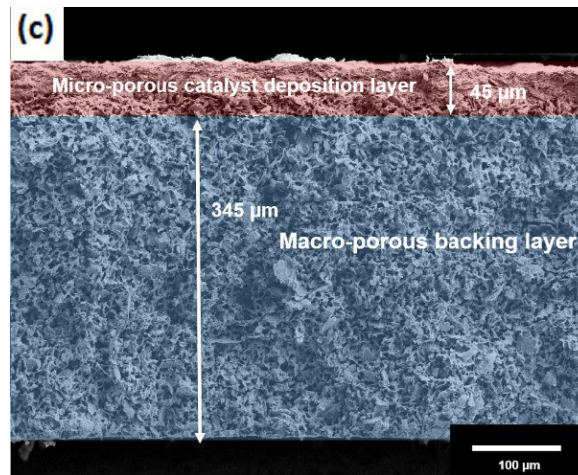
Figure 8.5 Cross sectional image of the pore structure of the bilayered gas diffusion layer membrane with a dense top layer (red) and a sponge-like bottom layer (blue) [39].

References

[1]   M. Scheffler, T. Gambaryan-Roisman, T. Takahashi, J. Kaschta, H. Muenstedt, P. Buhler, P. Greil, Ceram Trans 115 (2000) 239-250.

[2]   T. Prenzel, M. Wilhelm, K. Rezwan, Chem. Eng. J. 235 (2014) 198-206.

[3]   T. Prenzel, M. Wilhelm, K. Rezwan, Microporous Mesoporous Mater. 169 (2013) 160-167.

[4]   H. Zhang, C.L. Fidelis, A.L.T. Serva, M. Wilhelm, K. Rezwan, J. Am. Ceram. Soc. 100 (2017) 1907-1918.

[5]   F. Xue, K. Zhou, N. Wu, H. Luo, X. Wang, X. Zhou, Z. Yan, I. Abrahams, D. Zhang, Ceram. Int. 44 (2018) 6293-6299.

[6]   M. Naviroj, S.M. Miller, P. Colombo, K.T. Faber, J. Eur. Ceram. Soc. 35 (2015) 2225-2232.

[7]   M. Naviroj, P.W. Voorhees, K.T. Faber, J. Mater. Res. 32 (2017) 3372-3382.

[8]   E. Brener, H. Muller Krumbhaar, D. Temkin, Phys Rev E 54 (1996) 2714-2722.

[9]   S. Deville, S. Meille, J. Seuba, Sci. Technol. Adv. Mater. 16 (2015) 43501-43516.

[10] H. Zhang, C.L. Fidelis, M. Wilhelm, Z. Xie, K. Rezwan, Mater. Des. 134 (2017) 207-217.

[11] T. Rouxel, G. Massouras, G.-D. Soraru, J. Sol-Gel Sci. Technol. 14 (1999) 87-94.

[12] N. Fries, M. Dreyer, J. Colloid Interf. Sci. 320 (2008) 259-263.

[13] N. Fries, K. Odic, M. Conrath, M. Dreyer, J Colloid Interface Sci 321 (2008) 118-29.

[14] Y. Grebenyuk, M.E. Dreyer, Cryogenics 78 (2016) 27-39.

[15] Y. Grebenyuk, H.X. Zhang, M. Wilhelm, K. Rezwan, M.E. Dreyer, J. Eur. Ceram. Soc. 37 (2017) 1993-2000.

[16] E.W. Washburn, Phys. Rev. 17 (1921) 273-283.

[17]   R. Masoodi, K.M. Pillai, P.P. Varanasi, AlChE J. 53 (2007) 2769-2782.

[18]   R. Masoodi, K.M. Pillai, P.P. Varanasi. *Role of Hydraulic and Capillary Radii in improving the Effectiveness of Capillary Model in Wicking*. in *Proceedings of FEDSM2008 2008 ASME Fluids Engineering Conference*. 2008.

[19]   U.G. Wegst, M. Schecter, A.E. Donius, P.M. Hunger, Philos Trans A Math Phys Eng Sci 368 (2010) 2099-2121.

[20]   S. Deville, E. Saiz, A.P. Tomsia, Acta Mater. 55 (2007) 1965-1974.

[21]   D. Schumacher, M. Wilhelm, K. Rezwan, Mater. Des. 160 (2018) 1295-1304.

[22]   M. Adam, M. Wilhelm, G. Grathwohl, Microporous Mesoporous Mater. 151 (2012) 195-200.

[23]   M. Schubert, M. Wilhelm, S. Bragulla, C. Sun, S. Neumann, T.M. Gesing, P. Pfeifer, K. Rezwan, M. Bäumer, Catal. Lett. 147 (2017) 472-482.

[24]   A. Gorschinski, G. Khelashvili, D. Schild, W. Habicht, R. Brand, M. Ghafari, H. Bönnemann, E. Dinjusa, S. Behrens, Journal of Materials Chemistry 19 (2009) 2289-2238.

[25]   W. Li, H. Wang, X. Jiang, J. Zhu, Z. Liu, X. Guo, C. Song, RSC Adv. 8 (2018) 7651-7669.

[26]   H.C. Wu, Y.C. Chang, J.H. Wu, J.H. Lin, I.K. Lin, C.S. Chen, Catal. Sci. Tech. 5 (2015) 4154-4163.

[27]   J.H. Kwak, L. Kovarik, J. Szanyi, ACS Catalysis 3 (2013) 2449-2455.

[28]   J.H. Kwak, L. Kovarik, J. Szanyi, ACS Catalysis 3 (2013) 2094-2100.

[29]   G. Garbarino, P. Riani, L. Magistri, G. Busca, Int. J. Hydrogen Energy 39 (2014) 11557-11565.

[30]   J. Engbæk, O. Lytken, J.H. Nielsen, I. Chorkendorff, Surf. Sci. 602 (2008) 733-743.

[31]   M.A.A. Aziz, A.A. Jalil, S. Triwahyono, R.R. Mukti, Y.H. Taufiq-Yap, M.R. Sazegar, Appl. Catal., B 147 (2014) 359-368.

[32]   P.A.U. Aldana, F. Ocampo, K. Kobl, B. Louis, F. Thibault-Starzyk, M. Daturi, P. Bazin, S. Thomas, A.C. Roger, Catal. Today 215 (2013) 201-207.

[33]   Q. Fu, T. Wagner, Surf. Sci. Rep. 62 (2007) 431-498.

[34]   A. Cybulski, J.A. Moulijn, *Structured Catalysts and Reactions*. 2006, Boca Raton: CRC/Taylor and Francis.

[35]   V. Tomašić, F. Jović, Appl. Catal., A 311 (2006) 112-121.

[36]   D. Wu, H. Zhang, Ind Eng Chem Res 52 (2013) 14713-14721.

[37]   P. Avila, M. Montes, E.E. Miró, Chem. Eng. J. 109 (2005) 11-36.

[38]   L. Kiewidt. *Solid Sponges as Support for Heterogeneous Catalysts in Gas-Phase Reactions*. 2017. thesis in Production Engineering at University of Bremen. Dr.-Ing.

[39]   P. Moni, A. Deschamps, D. Schumacher, K. Rezwan, M. Wilhelm, Chem. Eng. J. (submitted) (2020)

Conclusions

<div style="text-align: right; font-size: 3em;">9</div>

As a base for the subsequent development of structures according to the requirements of capillary transport and heterogeneous catalysis, this work investigated on the first part the fundamental influence of the addition of filler particles on the pore structure and further properties. The addition of preceramic and ceramic filler particles proved to be effective in significantly altering important properties of SiOC monoliths such as the pore morphology, the mechanical strength, the specific surface area and the hydrophilicity. The different decomposition behavior of the preceramic fillers which is determined by the chemical composition gives rise to varying BET surface area and hydrophilicity. As a result of the microporous matrix material, the filler particles are accessible though being embedded in the surrounding matrix. Adjustment of the filler concentration as well as the filler composition enables precise tailoring of the BET surface area and the hydrophilicity in a wide range. In addition, calculations based on a linear rule of mixture show very good agreement with the experimental results in the case of homogeneously distributed particles.

While no influence of the filler particles on the mean pore window diameter, the porosity and the pore size distribution was found, the dendritic pore morphology was altered by the addition of filler particles. With increasing content of filler particles, the isotropy of the dendritic structure increases and the structure is called isotropic dendritic. Particles are supposed to induce temperature fluctuations and hence disrupt the dendritic solidification. The remarkable increase in compressive strength is attributed to the change in the pore morphology showing enhanced isotropy. Especially for the capillary transport, the enhancement of the mechanical strength was a key requirement. At low filler concentrations (1.7 vol%), the addition of alumina platelets which exhibit a low aspect ratio is more effective in improving the strength than the addition of spherical particles. Hence, at the same concentration the platelets manipulate the pore morphology to a greater extend.

The knowledge of the possibilities to influence the pore structure by adding fillers is an excellent base to manufacture porous monoliths with different structural motifs and test these pore structures on their capillary transport ability. Isothermal wicking experiments in axial direction at room temperature reveal the fastest wicking for the

sample with the highest permeability (highest porosity and pore window size). Though having similar pore window size and porosity, the differences in pore morphology between isotropic dendritic and prismatic result in a higher permeability and consequently faster wicking for the isotropic dendritic structure. This implies that the isotropic dendritic pore morphology has a higher ability of fluid flow compared to the prismatic pore morphology. Generally, the sample with the highest viscous resistance has the slowest imbibition rate. The wicking of the dendritic structure with a low porosity is characterized by a linear mass increase which deviates from the typical wicking behavior. Due to the presence of an increased number of dead-end pores, the available number of transport routes for the liquid is suggested to be reduced and the wicking is slowed down. Especially, the interface between clusters of internally aligned pores is supposed to be prone to reduced flow by the lack of interconnectivity. In the case of unidirectional freezing which provides a fully aligned pore structure without any interruption, no linear section is present in the wicking curves of the dendritic structure. This supports the assumption of limited interconnectivity causing the linear wicking behavior.

In addition to the unidirectionality, the freezing front velocity was altered. Due to increasing thermal resistance, constant freezing temperature conditions (CFT) are characterized by a clear decrease of freezing front velocity with time. The resulting gradient in pore window size creates a gradient in the driving force for wicking which changes the wicking speed additionally to the influence of gravity. In contrast, a constant freezing front velocity (CFV) generates a homogeneous pore window size observed for most of the samples frozen at CFV conditions. Decreasing the freezing front velocity from CFV slow (approx. $3.3\ \mu\mathrm{m}\cdot\mathrm{s}^{-1}$) to CFV fast (approx. $6.8\ \mu\mathrm{m}\cdot\mathrm{s}^{-1}$) conditions results in an increase of the pore window diameter by 14 % to 67 %. Furthermore, samples with a higher solid loading are more sensitive to variations in freezing front velocity and allow for a larger range of achievable pore window sizes. In general, the wicking into unidirectional dendritic pore structures is slower than into unidirectional prismatic structures. Secondary dendrites which are perpendicular to primary ones need to be filled during wicking by flow through primary dendrites. Hence, in the dendritic pore morphology a higher pore volume has to be filled through smaller pores compared to the prismatic structure of the TBA samples.

The wicking of all non-unidirectional structures is underestimated by the prediction using the Lucas-Washburn equation with gravity effects. In the case of directionally aligned pore structures, only the prismatic structure with an open porosity of approx. 60 % exhibit a good agreement with the prediction. Decreasing the porosity to approx. 60 % or even changing to a dendritic pore structure leads to a pronounced deviation between the experimental data and the analytical solution. As a result, the wicking of solution-based freeze cast structures can be predicted by the Lucas-Washburn equation only for pore structures which exhibit a very specific set of properties. The assumptions made by the Lucas-Washburn equation are too restrictive to allow for a reliable prediction of wicking in such complex three dimensional structures.

Besides the application in capillary transport, macroporous monoliths have a high potential in heterogeneous catalysis due to their superior heat- and mass transport properties compared to conventional packed-bed reactors. Because of some drawbacks of the commercially applied method of using a washcoat, supports with an inherent catalytic activity are of substantial interest. With the development and testing of novel porous catalytic active structures in this work, another field of application for solution-based freeze cast PDCs is opened up besides the capillary transport. However, before optimizing the pore structure of a monolithic catalyst, it has to be ensured that the underlying principles and processes of manufacturing a porous metal containing PDC monolith are understood and controllable. By adapting the in situ formation of nickel particles from reflux synthesis, porous metal containing solution-based freeze cast PDCs were prepared. Four complexing and cross-linking agents with amino functionality were screened according to their ability to generate small and well distributed nickel particles. Not only the complexing ability but also the capability to anchor the complex to the polymer chain is an important factor. The binding of nickel ions to the polymeric Si-O chain might be the reason for the comparable small increase of particle size with increasing pyrolysis temperature. This argument is only valid for samples where the functionality of complexing and cross-linking is combined in one molecule. In this case, a connection of the nickel ion to the polymeric chain can be assumed. (3-aminopropyl)triethoxy-silane as complexing and cross-linking agent, a ratio of complexing groups to nickel of 4 and nickel nitrate as nickel source formed the smallest nickel particles of (2.52 ± 0.82) nm. The catalytic activity was tested in a packed-bed reactor using the

CO$_2$ methanation as probe reaction. The nickel particle size and dispersion are the most influencing factors on the carbon dioxide conversion of nickel containing SiOC. The order of carbon dioxide conversion and methane selectivity reflects very well the order of nickel particle size with smaller nickel particles enhancing the conversion and selectivity. In general, the in situ formation of nickel particles in polymer-derived ceramics shows carbon dioxide conversion (up to 0.49) and methane selectivity (up to 0.74).

In short, this work reveals the fundamental relationships between the process parameters (e.g. the addition of fillers or the freezing conditions) and the resulting pore structure of solution-based freeze cast PDCs. These findings represent a toolbox which enables the efficient development of the pore structure according to the requirements of various applications. Furthermore, this work demonstrates the adaption and development of the structure for two relevant applications: capillary transport and heterogeneous catalysis. Regarding capillary transport applications, the determined relationship between structural properties and the resulting wicking behavior combined with the flexibility of the solution-based freeze casting process results in a high potential of tailoring porous media for capillary transport. Additionally, the underlying principles and processes of manufacturing an inherent catalytic active porous metal containing PDC monolith by solution-based freeze casting were elucidated. The combination of these findings with the knowledge of the precise tailoring of the pore structure is a powerful approach towards inherent catalytic active PDCs by solution-based freeze casting for heterogeneous catalysis.

Outlook

<div style="text-align: right; font-size: 2em;">10</div>

Recalling the results of this work, further research on several aspects is promising. Three main categories of future work can be defined. Firstly, broadening the set of properties which can be achieved by the combination of solution-based freeze casting and the addition of fillers in order to meet the requirements of further applications. Another aspect in this context is the tackling of the limited flexibility of solution-based freeze casting in terms of pore size. Secondly, perform wicking test at cryogenic conditions. And lastly, increasing the metal loading and performing investigations on the catalytic activity and heat- and mass transfer of monolithic catalysts with optimization of the pore structure.

Concerning the broadening of the set of properties, the fillers which were used in this work varied only in the BET surface area, the hydrophilicity and the aspect ratio. However, applications of porous media such as electrode materials and magnetic membranes require electrical conductivity and magnetic properties, respectively. In general, the possibility to control the pore structure by adapting the freeze casting process is crucial for applications like electrode materials. One example of an electrical conductive membrane by solution-based freeze casting was briefly touched in the summarizing discussion: gas diffusion layer for zinc air batteries (see page 178). Although showing a very promising performance, the relatively low electrical conductivity is the major limiting factor. To further enhance the electrical conductivity, fillers with very low or very high aspect ratios should be incorporated. Such fillers are supposed to generate a percolation path at lower filler concentrations and result in higher conductivity at constant concentrations, respectively. Hence, structures such as carbon nanotubes and graphene oxide flakes should be preferred. In principle, also metallic filler particles can provide electrical conductivity. But due to their higher density compared to the carbon allotropes, sedimentation during the freezing process is more likely for metallic fillers. In suspension-based freeze casting, magnetic particles were already used to align the particles according to an external magnetic field. Also magnetic SiFeOC nanocomposites were already synthesized using a single-source-precursor. Nevertheless, the promising combination of a

porous monolith formed by solution-based freeze casting and magnetic SiOC or the addition of magnetic particles such as iron(III)oxide was not yet investigated.

Furthermore, a very general and severely limiting aspect of solution-based freeze casting should be addressed. Though the porosity and pore morphology can be widely altered, up to now the pore size is restricted to a range between a few micrometers to approx. 70 µm. This excludes many applications from being tackled with solution-based freeze casting as larger pore sizes are widely required in e.g. waste water filtration (> 80 µm). One approach to solve this problem is to manipulate the crystal growth by surface active molecules at low freezing velocities. In suspension-based freeze casting with water as dispersing medium, this approach was successfully implemented. The pore size of the highly uniform pores was increased up to 100 µm by the addition of ice structuring compounds such as zirconium acetate or cryoprotectants, e.g. glycerol and antifreeze proteins. Due to the lower surface tension of organic solvents compared to water, finding suitable molecules for solution-based freeze casting of preceramic polymers is supposed to be more challenging. So far no research is published on this aspect. Nevertheless, research on this field is worthwhile as it would highly extend the potential applicability of solution-based freeze cast structures.

Regarding the application in capillary transport, wicking tests at cryogenic conditions would push porous SiOC monoliths closer to the application of propellant management devices. Until now, wicking was only evaluated at room temperature which excludes the relevant impact of the beneficial thermal properties of SiOC as well as neglects vapor formation due to superheated structures. Due to its low thermal conductivity, SiOC has a high potential to improve the capillary transport of cryogenic liquids.

With regard to heterogeneous catalysis, this work investigated the catalytic activity on sample powder in a packed-bed reactor. Although the particles themselves exhibit a hierarchical pore structure, the influence of the macroporous structure obtained by freeze casting on the catalytic performance of a monolith was not investigated yet. In order to use the entire potential of the in situ formation of nickel particles in solution-based freeze casting, the catalytic activity needs to be assessed on monoliths. Once tested as monolith, the pore structure of the samples can be designed according to

reported design guidelines in order to improve mass and heat transfer properties. These guidelines state that radially graded structures significantly improve important parameters such as pressure loss and temperature increase. Low porosity close to the wall was found to promote heat conductivity and results in efficient conversion of the reactants. Furthermore, a low porosity induces low superficial velocities and leads to long residence times and thus high yields. On the other hand, high porosity in the center provides low pressure loss. As a result, it is worthwhile to manufacture structures with graded properties e.g. porosity and pore size. Depending on the property, the gradient can be continuously or discontinuously. For discontinuous gradients, multiple step freeze casting is necessary which was already reported for suspension-based freeze casting. By multiple step freeze-casting, layered as well as core-shell structures can be manufactured. In contrast to suspension-based freeze casting and to avoid collapse of the first structure, particular attention has to be paid to the degree of cross-linking in multiple step solution-based freeze casting. This can be achieved by e.g. thermal cross-linking prior to the second freeze-casting step.

Additionally, a straightforward approach to increase the catalytic performance is to increase the metal loading. The maximum metal loading is given by the solubility of the metal salt in the solvent. By carefully adjusting the compositions of the metal containing solution and of the preceramic polymer containing solution according to the limits of solubility it is possible to increase the metal loading. According to preliminary results, an increase of at least 50 % is possible without further adaption of the process. A higher metal loading not only enhances the conversion, but also facilitates investigations on the interaction between the nickel and the SiOC support. This includes the determination of potential intermediate species. The knowledge of the intermediates and the interaction of nickel with SiOC would significantly contribute to the comprehensive understanding of the catalytic activity in nickel containing SiOC. Preliminary measurements with surface sensitive methods such as in-situ XPS have been turned out to be difficult within this work due to the relatively low metal content at the surface of the samples.

Nomination

List of Abbreviations

Abbreviation	Name
A	Alumina platelets
AE	(2-aminoethyl)-3-aminopropyltrimethoxysilane
APTES	(3-aminopropyl)triethoxysilane
APD	(3-aminopropyl)diethoxymethylsilane
BET	Brunauer-Emmett-Teller method
CFV	Constant freezing velocity
CH	Cyclohexane
CLA	Complexing and cross-linking agent
CVT	Constant freezing temperature
DMSO	Dimethyl sulfoxide
EC	Experimental closed
EDX	Energy-dispersive X-ray spectroscopy
EO	Experimental open
FFV	Freezing front velocity
GC	Gas chromatography
H1	Preceramic filler particle, H44 1 mol% AP
H44	Silres® H44, polymethylphenylsiloxane
H50	Preceramic filler particle, H44 50 mol% AP
HFE	Hydrofluoroether
M1	Preceramic filler particle, MK 1 mol% AP
MK	Silres® MK, polymethylsiloxane
N	Numerical
NiA	Nickel(II) acetylacetonate
NiN	Nickel(II) nitrate hexahydrate
PDC	Polymer-derived ceramic
PET	Polyethylene terephthalate
PVC	Polyvinylchloride
RT	Room temperature
S	Silica particles
SEM	Scanning electron microscopy
SSA	Specific surface area
STA	Simultaneous thermal analysis
TBA	*Tert*-butyl alcohol
TEM	Transmission electron microscopy
TGA	Thermogravimetric analysis
TMEDA	Tetramethylethylenediamine
WHSV	Weight hourly space velocity
XRD	X-ray diffraction

List of Symbols

Symbol	Quantity	Unit
A	Cross section area	m^2
a_{spec}	Specific surface area	$m^2 \cdot g^{-1}$
BET_{calc}	Calculated BET specific surface area	$m^2 \cdot g^{-1}$
BET_{Ref}	BET specific surface area of the matrix	$m^2 \cdot g^{-1}$
BET_{Filler}	BET specific surface area of the filler	$m^2 \cdot g^{-1}$
b	Parameter, describing the influence of the viscous friction	$s \cdot m^{-2}$
C	Constant in BET equation	1
c	Parameter, describing the influence of the gravity	m^{-1}
c_{geo}	Geometrical factor, describing the pore structure	1
D	Diameter of the sample	m
d	Particle size of metal particles	m
d_{50}	Mean particle size of filler particles	m
g	Gravitational acceleration	$m \cdot s^{-2}$
H	Height of the sample	m
H_{Darcy}	Height of samples for Darcy test	m
h	Wicking height	m
$\dot{h}$	Interstitial velocity	$m \cdot s^{-2}$
h_{CHP}	Height of water column in constant head permeability test	m
h_{eq}	Equilibrium height	m
j	Water flux through lateral surface	$kg \cdot s^{-1} \cdot m^{-2}$
K	Permeability	m^2
K_{Darcy}	Permeability obtained by Darcy test	m^2
$K_{Wicking}$	Permeability obtained from a wicking experiment	m^2
M_{N2}	Molecular mass of nitrogen	$mol \cdot g^{-1}$
m	Mass	kg
m_{eq}	Equilibrium mass	kg
m_{sat}	Mass of the completely saturated sample	kg
$m_{w, Darcy}$	Mass of permeated water in Darcy test	kg
N_A	Avogadro constant	1
p	Pressure in nitrogen adsorption measurment	Pa
p_0	Saturated vapor pressure in nitrogen adsorption measurement	Pa
R	Pore radius	m
R_{Darcy}	Radius of samples for Darcy test	m
R_{merc}	Mean pore window radius obtained by mercury intrusion	m
R_s	Static radius	m
r	Radial direction according to coordinate system	1

Symbol	Quantity	Unit
S_0	Average area occupied by an adsorbed nitrogen molecule	m^2
S_{CH4}	Selectivity towards methane	1
T_M	Melting point	°C
t	Time	s
t_{Darcy}	Measurement time in Darcy test	s
u_s	Superficial velocity	$m·s^{-1}$
$\dot{V}$	Volumetric flow rate	$m^3·s^{-1}$
X_{CO2}	Conversion of carbon dioxide	1
x	Volume fraction	1
Y_{CH4}	Yield of methane	1
z	Axial direction according to coordinate system	1
α	Coefficient of thermal expansion	K^{-1}
$\Delta_R G_{298}$	Gibbs free energy at 298.15 K	$kJ·mol^{-1}$
$\Delta_R H_{298}$	Reaction enthalpy at 298.15 K	$kJ·mol^{-1}$
ΔL	Length	m
Δp	Pressure difference	Pa
Δp_{Darcy}	Pressure difference in Darcy test	Pa
Θ	Contact angle	°
μ	Dynamic viscosity	Pa·s
μ_l	Dynamic viscosity of test liquid	Pa·s
μ_W	Dynamic viscosity of water	Pa·s
ν	Specific adsorbed volume	m^3
ν_m	Specific volume of a mono-layer	m^3
ρ	Density	$kg·m^{-3}$
ρ_l	Density of test liquid	$kg·m^{-3}$
ρ_{N2}	Density of nitrogen	$kg·m^{-3}$
ρ_W	Density of water	$kg·m^{-3}$
σ	Surface tension	$N·m^{-1}$
σ_l	Surface tension of test liquid	$N·m^{-1}$
σ_{lp}	Surface tension of interface liquid-particle	$N·m^{-1}$
σ_{sl}	Surface tension of interface solid-liquid	$N·m^{-1}$
σ_{sp}	Surface tension of interface solid-particle	$N·m^{-1}$
ϕ	Open porosity	1

Materials and Chemical Structure

Abbreviation	Name	Structure
AE	(2-aminoethyl)-3-aminopropyltrimethoxy-silane	
APTES	(3-aminopropyl)-triethoxysilane	
APD	(3-aminopropyl)-diethoxymethylsilane	
CH	Cyclohexane	
H44	Silres® H44 Polymethylphenylsiloxane	
MK	Silres® MK Polymethylsiloxane	
NiA	Nickel(II) acetylacetonate	Ni(acac)$_2$
NiN	Nickel(II) nitrate hexahydrate	Ni(NO$_3$)$_2$
TBA	*tert*-Butyl alcohol, *tert*-Butanol	
TMEDA	Tetramethylethylenediamine	

Appendix

A.1 Supplementary Data for Chapter 4
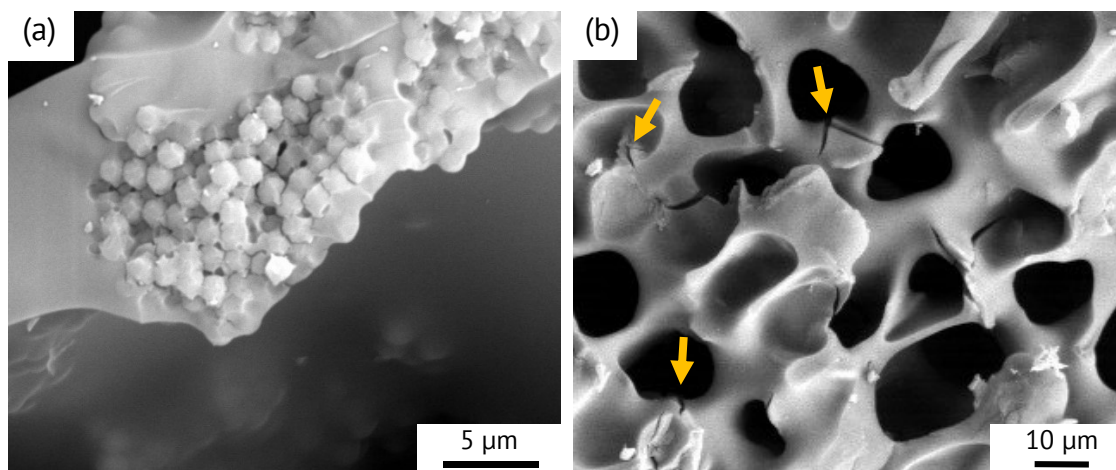
Figure A.1.1 SEM images of (a) agglomerated silica filler particles at sample 25S/600 and (b) cracks around alumina at sample 3.5A/1000.
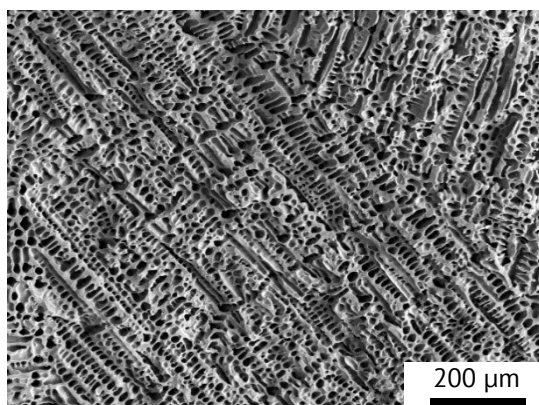
Figure A.1.2 SEM image of 1.7A/1000 with increased isotropy of the pore structure compared to Ref/1000.
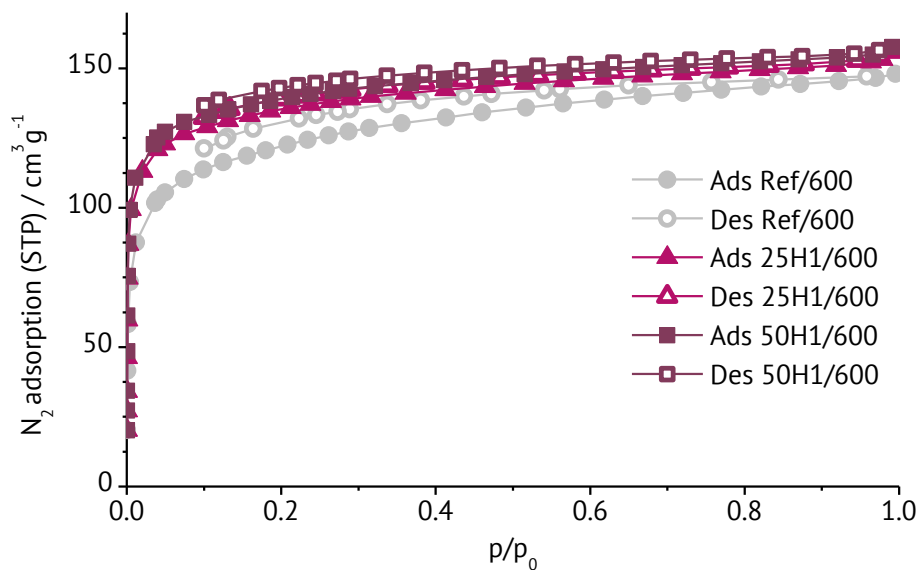
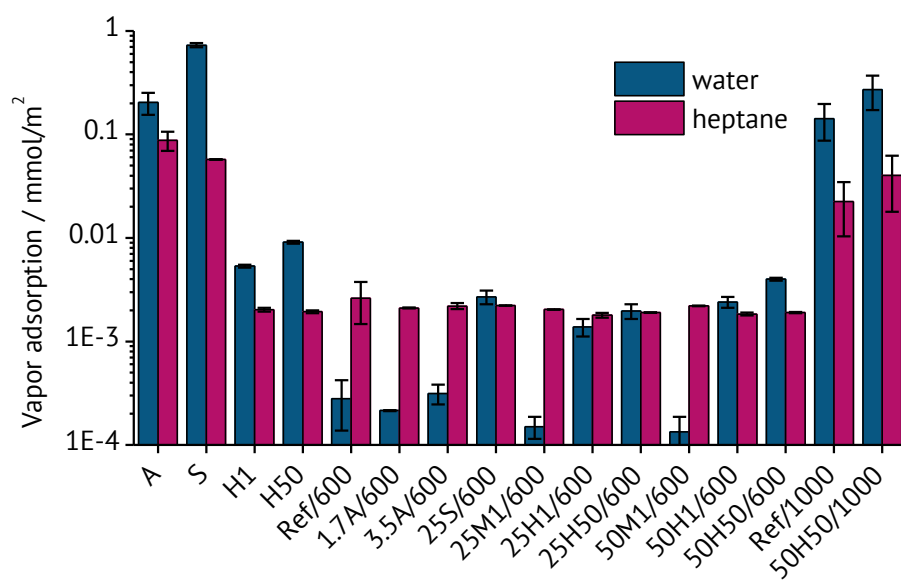**Figure A.1.3** Nitrogen adsorption and desorption isotherms exemplary for samples Ref/600, 25H1/600 and 50H1/600.

Figure A.1.4 Water and heptane adsorption at 22 °C for polymeric and inorganic filler particles and samples with different filler particles content at different pyrolysis temperatures.

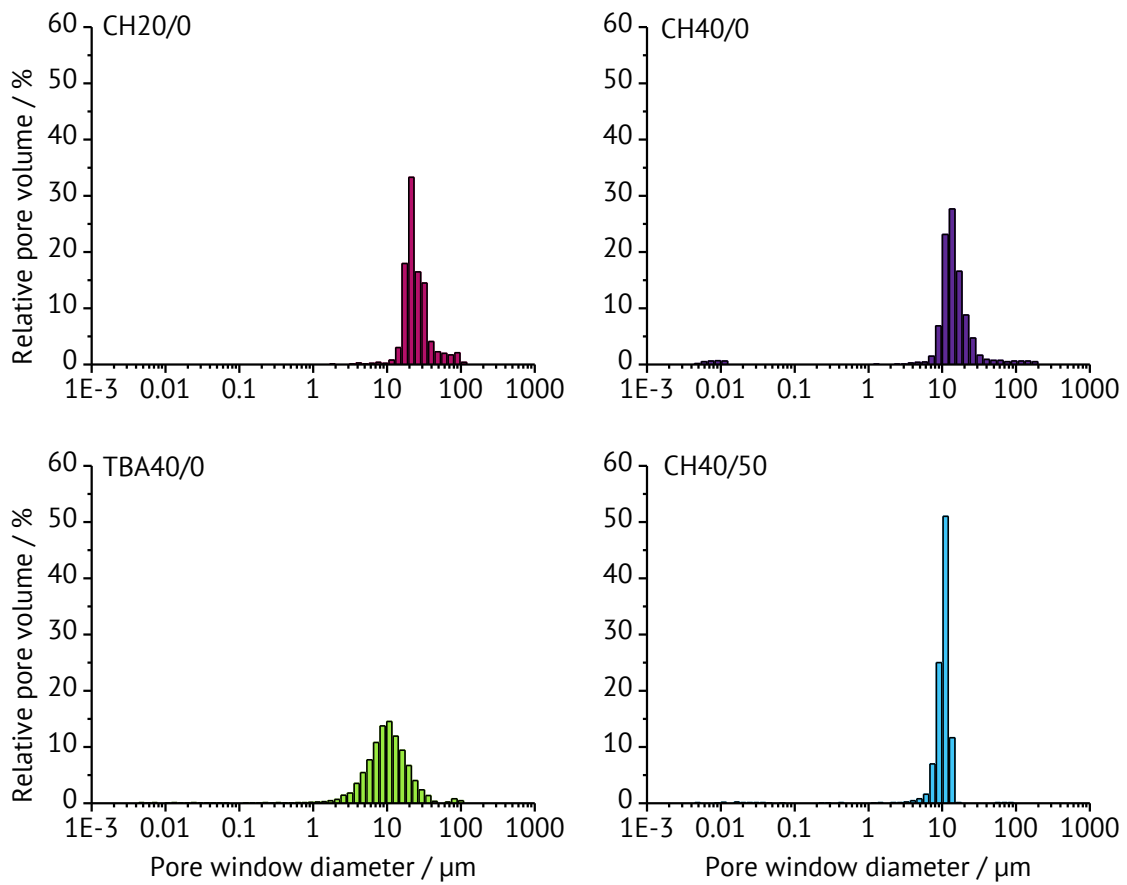## A.2 Supplementary Data for Chapter 5

Figure A.2.1 Relative pore volume obtained by mercury porosimetry for all investigated samples; exemplary only one measurement out of the three tests of each sample is shown.

A.2.1 Derivation of the Lucas-Washburn equation for Porous Media

Permeability K is the ability of a porous material to allow fluids to pass through it. It is a property of the porous material and is commonly defined by the Darcy law [1].

Different methods are proposed to determine the permeability of a porous structure in literature. Thus, the permeability can be determined for example by constant head permeability measurements, or as a fitting parameter of the viscous dominated part of the wicking experiment [2-4]. Both methods base on the Darcy law, which is given by

$$\frac{\Delta p}{\Delta L} = -\frac{\mu}{K} u_s. \tag{A.2.1}$$

To facilitate an overview all symbols used in equations are listed on page 189. The permeability describes how easily a liquid can flow through a porous medium. The permeability is the parameter of the structure, which is related to the porosity, as well as to the shape of the pores. The superficial velocity u_s can be expressed in terms of the mass of liquid per unit time per unit area

$$u_s = \frac{\Delta m}{\rho A \Delta t} \tag{A.2.2}$$

with the cross section area

$$A = \frac{\pi}{4} D^2 \tag{A.2.3}$$

and an expression for the length $\Delta L = h_s$, the permeability can be determined from a flow measurement using

$$K = \frac{\mu h_s}{\Delta p} \frac{m}{\rho \frac{\pi}{4} D^2 t}. \tag{A.2.4}$$

Another method would be to fit the permeability to the viscous dominated part of the wicking experiment. This approach is also based on the Darcy equation A.2.1 (see page 195). The superficial velocity is replaced by the interstitial velocity $\dot{h}$ within the porous structure, given by

$$u_s = \phi \dot{h} \tag{A.2.5}$$

Furthermore, the length in the Darcy equation is replaced by the height of the wicking process $\Delta L = h$, which results in the following notation of the Darcy law.

$$\frac{\Delta p}{h} = \frac{\mu}{K} \phi \dot{h} \tag{A.2.6}$$

The driving force for the capillary rise is the capillary pressure resulting from the curvature of the liquid-vapor interface. It is expressed by the Young-Laplace equation

$$\Delta p = \frac{2\sigma \cos \theta}{R_s} \tag{A.2.7}$$

Rearranging Equation A.2.6 and Equation A.2.7, one obtains the Lucas-Washburn equation for porous materials [5, 6]

$$\dot{h}h = \frac{2\sigma \cos \theta \, K}{\phi \mu R_s}. \tag{A.2.8}$$

After separation of variables and the subsequent integration with $h(t = 0) = 0$ leads to

$$\frac{h^2}{t} = \frac{4\sigma \cos \theta \, K}{\phi \mu R s}. \tag{A.2.9}$$

Since the weight-measurement technique was used in this work, the height in Equation A.2.9 on page 196 was converted into a mass equation using the following equation.

$$m = \phi \rho A h \tag{A.2.10}$$

with

$$A = \frac{\pi}{4} D^2. \tag{A.2.11}$$

It follows

$$\frac{m^2}{t} = \frac{4\sigma \cos \theta \rho_l^2 A^2 \phi}{\mu_l} \frac{K}{R_s}. \tag{A.2.12}$$

With knowledge of the parameters of the porous structure and liquid parameters, the permeability can be determined using this equation. For this, the knowledge of $m^2 \cdot t^{-1}$ is required, which can be determined from the wicking experiment.

A.2.2 Formation of Lateral Surface

In the past, a lot of research was conducted on suspension-based freezing using different solvents as well as particles [7-10]. Only few studies also investigated as part of the research the morphology of the lateral surface [11, 12]. They found porous lateral surfaces with slightly reduced permeability of a factor of 1.7 due to reduced pore sizes [11]. As demonstrated in Figure 5.6, the water flux $j(EC)$ of the as prepared surface varies in dependence on the composition of the sample. But all samples show a larger ratio between open and closed surface as well as significantly lower water flux j in case of closed lateral surface compared to literature. Though a direct comparison with literature is not possible due to different pore morphology, pore size and porosity, it can be stated, that the lateral surface is significantly less permeable for samples presented in this work compared to previous studies.

Two main determining factors for the formation of a less permeable lateral surface should be described in the following. The first is the use of a silicon-coated PET film between mold and solution. Its very smooth and anti-adhesive surface prevents the formation of critical nuclei due to an absence of crystallization sites. Consequently, significantly less crystals are formed at the interface solution – film. The second factor is the difference in segregation mechanism between literature and this work. Previous research was conducted using suspended particles, hence suspension-based freeze casting with the segregation process of particle rejection and entrapment between solvent crystals [11, 12]. In contrast, polymeric solutions which are used in this work segregate according to thermally induced phase separation [13, 14]. In suspension-based freeze casting it can be assumed, that the particles can still be rejected and entrapped in between the crystals even though the crystals had approached already very close to the wall. Though the interaction of particles with the advancing solidification front is strongly influenced by parameters such as particle size, particle shape and freezing front velocity, this assumption is reasonable due to findings that the particles are for most cases displaced only by a fraction of their diameter in direction of freezing [15, 16]. This results in a very limited increase of particle concentration in front of the crystal tip and hence in the possibility that the crystal reaches the wall by rejecting all particles between the crystal tip and the wall. This is in correlation with previous studies showing open lateral surfaces for suspension-based freeze casting [11]. In contrast to the segregation mechanism of

particle rejection and entrapment, thermally induced phase separation results in a pronounced concentration profile with increased polymer concentration in front of the crystal tip [14]. Consequently, a dense solid layer is formed at the interface solution – wall. As a result, it can be stated that the prevention of nucleation on the interface solution – wall by a silicon-coated film and the segregation mechanism of thermally induced phase separation are supposed to be main influential factors for the formation of a dense lateral surface

References

[1]   H. Darcy, *Les Fontaines Publiques de la ville de Dijon*. 1856: Dalmont.

[2]   N. Fries, K. Odic, M. Conrath, M. Dreyer, J Colloid Interface Sci 321 (2008) 118-29.

[3]   Y. Grebenyuk, H.X. Zhang, M. Wilhelm, K. Rezwan, M.E. Dreyer, J. Eur. Ceram. Soc. 37 (2017) 1993-2000.

[4]   J.F. Siau, *Transport processes in wood*. 1984, Berlin: Springer.

[5]   R. Lucas, Kolloid Z. 23 (1918) 15-22.

[6]   E.W. Washburn, Phys. Rev. 17 (1921) 273-283.

[7]   R. Liu, T. Xu, C. Wang, Ceram. Int. 42 (2016) 2907-2925.

[8]   S. Deville, J. Mater. Res. 28 (2013) 2202-2219.

[9]   S. Deville, Materials 3 (2010) 1913-1927.

[10]   W.L. Li, K. Lu, J.Y. Walz, International Materials Reviews 57 (2013) 37-60.

[11]   J. Seuba, J. Leloup, S. Richaud, S. Deville, C. Guizard, A.J. Stevenson, J. Eur. Ceram. Soc. 37 (2017) 2423-2429.

[12]   J.-W. Moon, H.-J. Hwang, M. Awano, K. Maeda, Materials Letters 57 (2003) 1428 - 1434.

[13]   M. Naviroj, S.M. Miller, P. Colombo, K.T. Faber, J. Eur. Ceram. Soc. 35 (2015) 2225-2232.

[14]   P.v.d. Witte, P.J. Dijkstra, J.W.A.v.d. Berg, J. Feijen, J. Membr. Sci. 117 (1996) 1-31.

[15]   R. Asthana, S.N. Tewari, J. Mater. Sci. 28 (1993) 5414 - 5425.

[16]   A.W. Rempel, M.G. Worster, J Cryst Growth 205 (1999) 427 - 440.
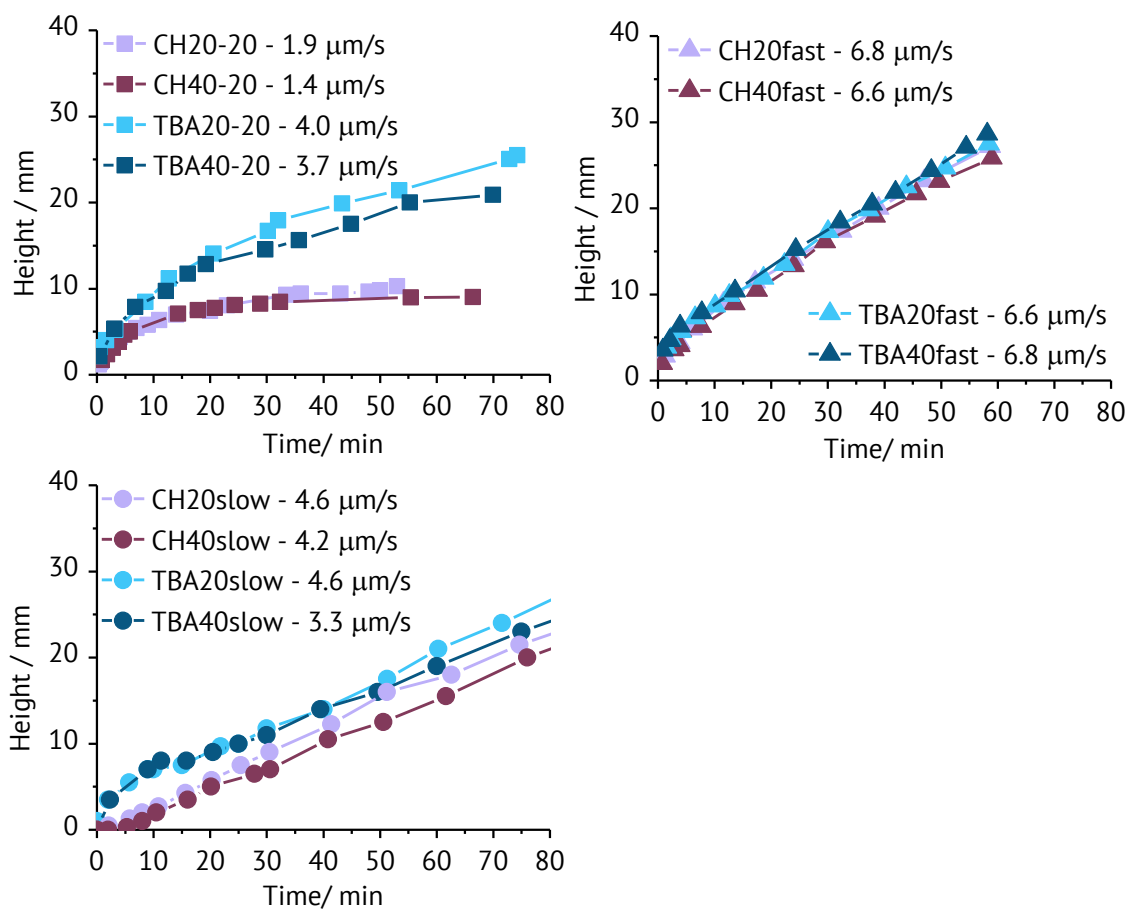
A.3 Supplementary Data for Chapter 6

Figure A.3.1 Experimental and modeled position of freezing front during freeze casting in dependence on solvent, solid loading and freezing conditions grouped by the freezing conditions.
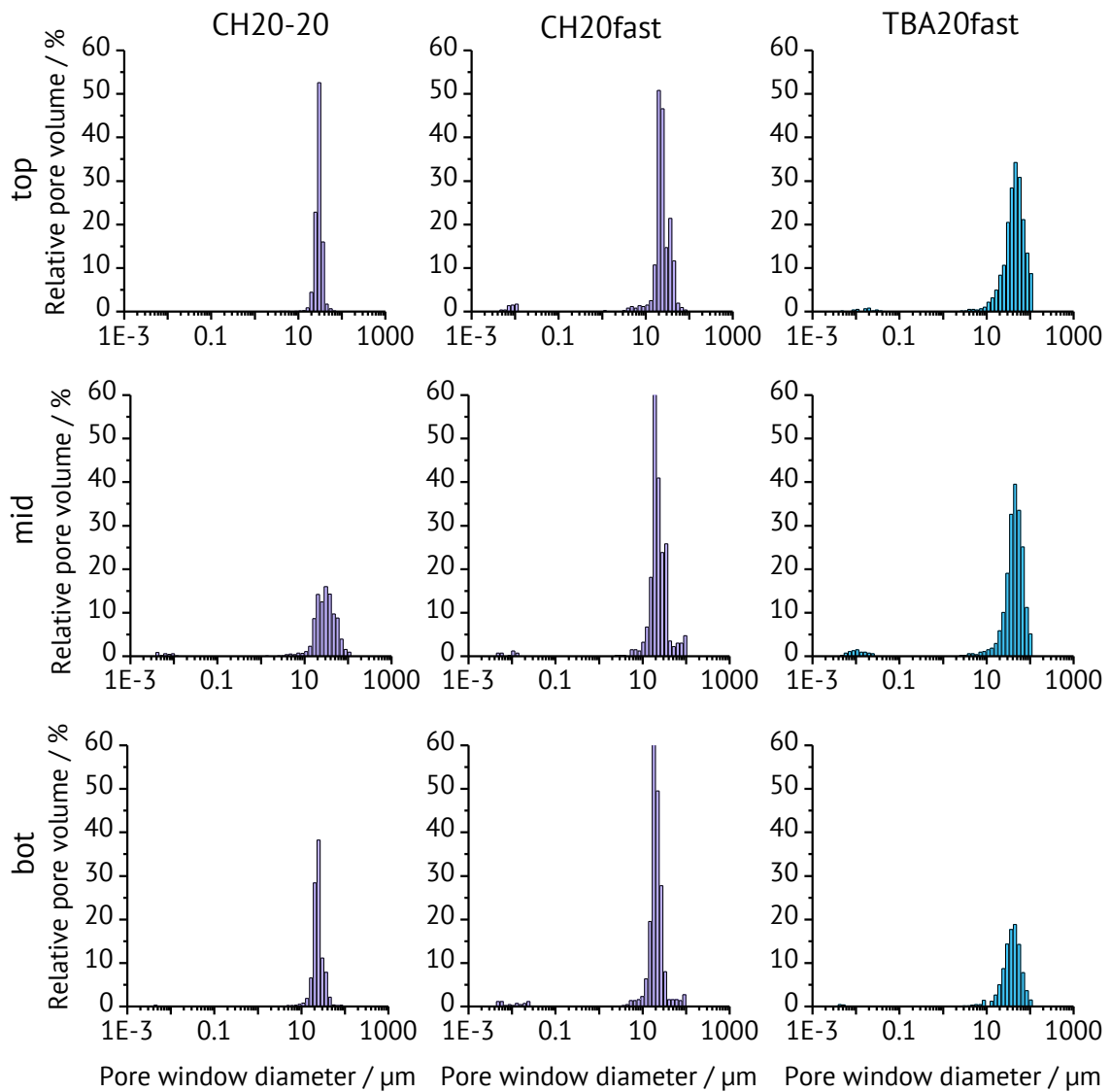
Figure A.3.2 Exemplary pore window size distribution in dependence on the position obtained by mercury intrusion porosimetry.

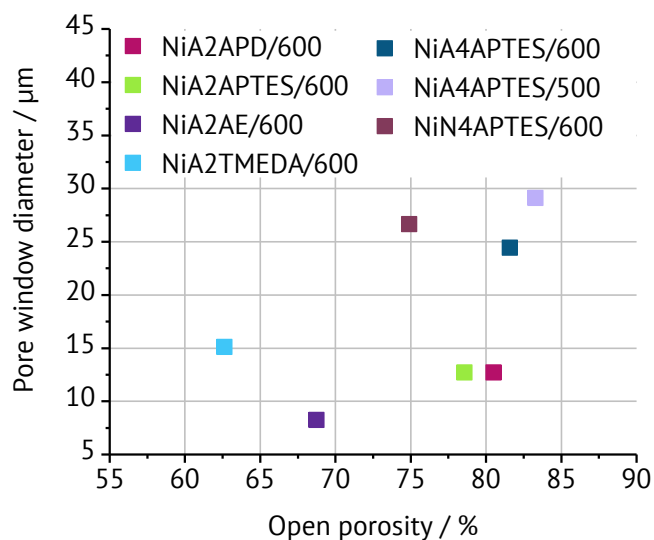# A.4 Supplementary Data for Chapter 7

Figure A.4.1 Open porosity and mean pore window diameter for samples with different cross-linking agents, nickel precursors and pyrolysis temperatures.
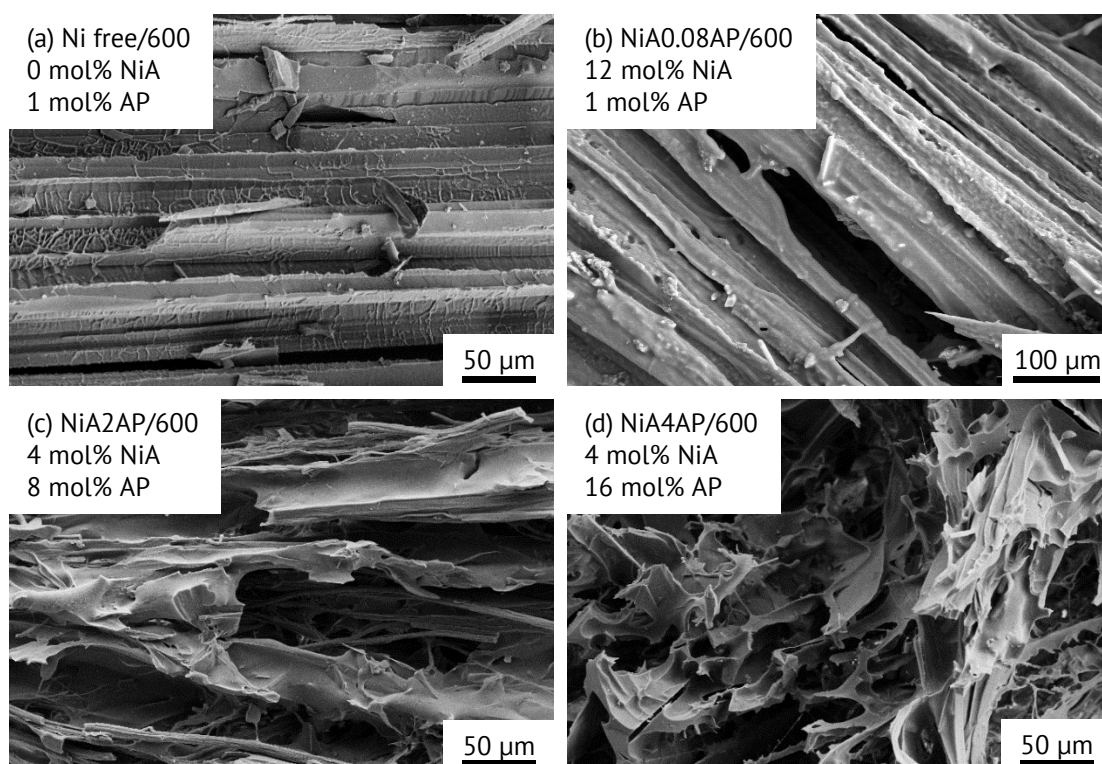

Figure A.4.2 SEM images of samples with increasing amount of APTES from (a) and (b) 1 mol% to (b) 8 mol% and (c) 16 mol%; (a) was prepared without the addition of nickel and represents the characteristic prismatic pore morphology obtained by TBA; (b) exhibits an increased nickel content with a very low nickel to APTES ratio and represents the influence of high nickel at comparable low APTES contents.
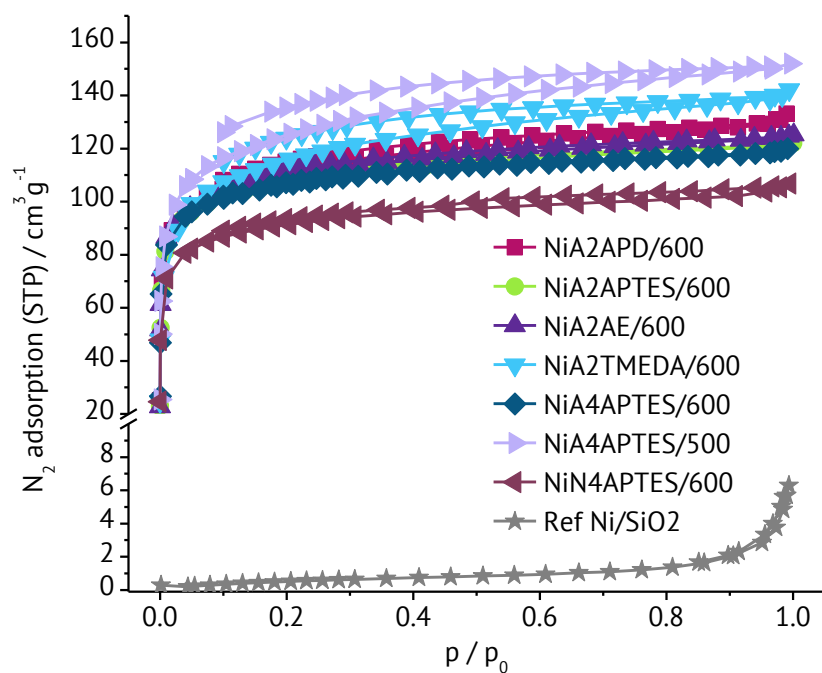
Figure A.4.3 Nitrogen adsorption and desorption isotherms for samples with different cross-linking agents, nickel precursors and pyrolysis temperatures.
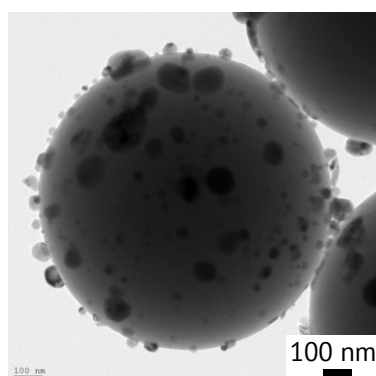

Figure A.4.4 TEM image of the reference catalyst prepared by wet impregnation of silica with nickel nitrate.

Curriculum Vitae

Surname	Schumacher
First name	Daniel
Date of birth	21.09.1989
Place of birth	Fürth, Germany

Education

10/2013 – 05/2016	M.Sc. Materials Science with emphasis on glass and ceramics, Thesis "Electrical properties of MAX-phase – ceramic composites" in cooperation with Nagoya Institute of Technology, FAU Erlangen-Nuremberg, Erlangen, Germany
10/2010 – 09/2013	B.Sc. Materials Science, Thesis "Manufacturing of partially stabilized ZrO_2-substrates via tape casting", FAU Erlangen-Nuremberg, Erlangen, Germany

Research Experience

10/2016 – 03/2020	Ph.D. Student, Advanced Ceramics Group, University of Bremen, Bremen, Germany
10/2016 – 09/2019	Member of the research training group "Micro-, meso- and macroporous nonmetallic Materials: Fundamentals and Applications (MIMENIMA)", University of Bremen, Bremen, Germany
06/2016 – 09/2016	Research Assistant, Institute of Glass and Ceramics, FAU Erlangen-Nuremberg, Erlangen, Germany
03/2012 – 05/2015	Student Assistant, Institute of Glass and Ceramics, FAU Erlangen-Nuremberg, Erlangen, Germany

List of Publications and Conference Contributions

List of Publications (peer-reviewed)

L. Luhede, B. Besser, *D. Schumacher*, M. Wilhelm, U. Fritsching, Continuous multi-step encapsulation process for the generation of multiple emulsions, (2020) submitted

P. Moni, A. Deschamps, *D. Schumacher*, M. Wilhelm, K. Rezwan, A new silicon oxycarbide based gas diffusion layer for zinc-air batteries, (2020) submitted

D. Schumacher, M. Wilhelm, K. Rezwan Porous SiOC monoliths with catalytic activity by in situ formation of Ni nanoparticles in solution-based freeze casting, Journal of the American Ceramic Society 103 (2020) 2991-3001, DOI: 10.1111/jace.16988

D. Schumacher, P. da Rosa Braun, M. Wilhelm, K. Rezwan, Unidirectional solution-based freeze cast polymer-derived ceramics: influence of freezing conditions and templating solvent on capillary transport in isothermal wicking, Journal of Material Science, Journal of Material Science 55 (2020) 4157-4169, DOI: 10.1007/s10853-019-04310-0

D. Schumacher[†], D. Zimnik[†], M. Wilhelm, M. Dreyer, K. Rezwan, Solution-based freeze cast polymer-derived ceramics for isothermal wicking - relationship between pore structure and imbibition, Science and Technology of Advanced Materials 20 (2020) 1207-1221, DOI: 10.1080/14686996.2019.1699766
[†] Equal authorship

D. Schumacher, M. Wilhelm, K. Rezwan, Modified solution-based freeze casting process of polysiloxanes to adjust pore morphology and surface functions of SiOC monoliths, Materials and Design 160 (2018) 1295-1304, DOI: 10.1016/j.matdes.2018.10.048

Author Contributions for the Publications presented in this Work

Publication Presented in Chapter 4

D. Schumacher, M. Wilhelm, K. Rezwan, Modified solution-based freeze casting process of polysiloxanes to adjust pore morphology and surface functions of SiOC monoliths, Materials and Design 160 (2018) 1295-1304, DOI: 10.1016/j.matdes.2018.10.048

Author	Contribution
Daniel Schumacher	Concept and planning of work, fabrication of samples, samples preparation for characterizations, nitrogen adsorption/desorption measurements, SEM, vapor adsorption measurements, data analysis and interpretation, manuscript preparation (design, editing, writing)
Michaela Wilhelm	Gave scientific input and conceptual advice, discussed data, edited manuscript
Kurosch Rezwan	Gave scientific input and conceptual advice, discussed data, edited manuscript

Publication Presented in Chapter 5

D. Schumacher*, D. Zimnik*, M. Wilhelm, M. Dreyer, K. Rezwan, Solution-based freeze cast polymer-derived ceramics for isothermal wicking - relationship between pore structure and imbibition, Science and Technology of Advanced Materials 20 (2020) 1207-1221, DOI: 10.1080/14686996.2019.1699766
* Equal authorship

Author	Contribution
Daniel Schumacher	Concept and planning of work, fabrication of samples, samples preparation for characterizations, SEM, water flux permeability measurements, data analysis and interpretation, manuscript preparation (design, editing, writing)
Dawid Zimnik	Concept and planning of work, wicking measurements, numerical modelling, data analysis and interpretation, manuscript preparation (writing)
Michaela Wilhelm	Gave scientific input and conceptual advice, discussed data, edited manuscript
Michael Dreyer	Gave scientific input and conceptual advice, discussed data, edited manuscript
Kurosch Rezwan	Gave scientific input and conceptual advice, discussed data, edited manuscript

Publication Presented in Chapter 6

D. Schumacher, P. da Rosa Braun, M. Wilhelm, K. Rezwan, Unidirectional solution-based freeze cast polymer-derived ceramics: influence of freezing conditions and templating solvent on capillary transport in isothermal wicking, Journal of Material Science 55 (2020) 4157-4169, DOI: 10.1007/s10853-019-04310-0

Author	Contribution
Daniel Schumacher	Concept and planning of work, fabrication of samples, samples preparation for characterizations, mercury porosimetry, SEM, permeability measurements, data analysis and interpretation, manuscript preparation (design, editing, writing)
Pedro Braun	Fabrication of samples, samples preparation for characterizations, wicking measurements, theoretical prediction, data analysis, edited manuscript
Michaela Wilhelm	Gave scientific input and conceptual advice, discussed data, edited manuscript
Kurosch Rezwan	Gave scientific input and conceptual advice, discussed data, edited manuscript

Publication Presented in Chapter 7

D. Schumacher, M. Wilhelm, K. Rezwan, Porous SiOC monoliths with catalytic activity by in situ formation of Ni nanoparticles in solution-based freeze casting, Journal of the American Ceramic Society (in press) DOI: 10.1016/j.matdes.2018.10.048

Author	Contribution
Daniel Schumacher	Concept and planning of work, fabrication of samples, samples preparation for characterizations, nitrogen adsorption/desorption measurements, SEM, Mercury porosimetry, vapor adsorption measurements, XRD measurements, TEM analysis, catalytic tests, data analysis and interpretation, manuscript preparation (design, editing, writing)
Michaela Wilhelm	Gave scientific input and conceptual advice, discussed data, edited manuscript
Kurosch Rezwan	Gave scientific input and conceptual advice, discussed data, edited manuscript

List of Oral and Poster Presentations

D. Schumacher, M. Wilhelm, K. Rezwan, Porous catalytic active SiOC monoliths by in situ formation of Ni nanoparticles in solution-based freeze casting, Oral presentation, 10th International Conference on High Temperature Ceramic Matrix Composites, 2019, Bordeaux, France

D. Schumacher, M. Wilhelm, K. Rezwan, Multifunctional precursor derived ceramics prepared by freeze casting technique, Oral presentation, conference organization and session chair, MIMENIMA summer school "Mass transport in porous media with special consideration of imaging methods" 2018, Etelsen, Germany

D. Schumacher, M. Wilhelm, K. Rezwan, Modified solution-based freeze casting process of polysiloxanes to add functional and structural properties, Oral presentation, 12th Conference on Ceramic Materials and Components for Energy and Environmental Applications, 2018, Singapore, Singapore

List of Student Projects

The presented work includes results which were obtained as a part of following supervised student projects.

Gustavo Hamann	Unidirectional Solution-Based Freeze Casting of Polysiloxanes for Capillary Transport Internship (6 months), 2019
Catherine Yokan, Nantje Steinberg	Nickel-Containing Polymer-Derived Ceramics Prepared by Solution-Based Freeze Casting Master Project, 2019
Pedro Henrique da Rosa Braun	Solution-Based Freeze Casting of Polysiloxane for Capillary Transport Applications Diploma Thesis, 2018
Tuoi Hoang	Solution-Based Freeze Casting Fabricating Nickel Containing Polymer-derived Ceramics Internship (3 months), 2018
Matheus Neves Olivan	Polymer-derived SiOC Ceramics by Solution-Based and a Combination of Solution- and Suspension-Based Freeze Casting Process Using *Tert*-Butyl Alcohol as Solvent Diploma Thesis, 2017